**Technische Universität München**
**Fakultät für Physik**
**Physics of Energy Conversion and Storage**

# In-Depth Characterization of Electrified Solid/Liquid Interfaces with the Laser-Induced Current Transient Technique

## Daniel Scieszka

# Abstract

According to the classical perspective of chemical physics, the properties of the electrified solid/liquid interfaces are crucial for the behavior of multiple systems, especially those which are envisaged to play the key role in so-called sustainable energy provision schemes. The interface structure and, related to it, energy barriers for the charge and mass transfer significantly affect, e.g., the electrocatalyzed processes. While the rate of the electrocatalytic reactions was typically attributed to the properties of the electrode, i.e., the surface structure and composition, it turns out that the resulting system performance depends also on the electrolyte composition. Numerous studies show that various species present in the solution can modify both the kinetics and the mechanism of the interfacial reactions. Particularly interesting is the influence of the seemingly inert ions (e.g., alkali-metal cations) frequently found in the electrolytes. As reported in the literature, the activity towards an electrocatalytic reaction often exhibits sensitivity to the nature of these species. Another interesting aspect is the effect of the concentration of certain electrolyte constituents. For instance, the effect of the $H^+$ concentration (expressed as pH) on the activity which, in many situations, does not show obvious trends.

Whereas the electrolyte composition is an important factor affecting the electrocatalytic activity, the explanation of its effect is often challenging. The incomprehension of the electrolyte influence results from the limited number of the experimental methods that allow the in-depth analysis of the role played by certain constituents for the electrocatalyzed reactions. Thus, the focus of this thesis lays on developing the experimental methodology enabling a thorough investigation of the effect mentioned above. For this purpose, several different systems were studied using the so-called laser-induced current transient (LICT) technique. This in situ technique uses a high-power laser beam to probe the electrode/electrolyte interface. The utilization of the LICT together with other commonly known electrochemical methods appears as a powerful tool of the system examination.

In this work, the usefulness of the aforementioned methodology is elaborated for electrocatalytic and battery systems (important for energy applications). The catalytic systems included pure noble metal (i.e., Pt and Au) electrodes as well as electrodes consisting of non-precious metal compound (i.e., $Mn_2O_3$) immersed in various acidic electrolytes of different pH, near-to-neutral $Na^+$ and $K^+$ salt solutions, or in the alkaline electrolytes of NaOH. In all the systems under study, one can see a direct correlation between the interface structure and the

activity of the electrodes towards the hydrogen evolution or oxygen reduction reactions. Interestingly, the proposed methodology can also be successfully used to investigate battery cells. As shown by the example of model aqueous Na-ion battery systems utilizing $Na_2Ni[Fe(CN)_6]$ and $Na_2Co[Fe(CN)_6]$ as the electrode material, the laser technique augmented by the other electroanalytical methods could deliver unique information about the interfacial charge and mass transfer.

Owing to its simplicity and ability to investigate the effect of the electrolyte on the resulting performance of various systems, the LICT is expected to open up new opportunities for more efficient studies of the electrified solid/liquid interfaces.

# Zusammenfassung

Gemäß der klassischen Perspektive der chemischen Physik sind Eigenschaften der elektrisierten Fest-Flüssig-Grenzflächen entscheidend für das Verhalten der elektrochemischen Systeme, insbesondere derjenigen, die die Schlüsselrolle in sogenannten nachhaltigen Energieversorgungssystemen spielen sollen. Die Struktur der Grenzfläche und die damit verbundenen Energiebarrieren zum Ladungs- und Massentransport beeinflussen z.B. die elektrokatalysierten Prozesse erheblich. Während die Geschwindigkeit der elektrokatalytischen Reaktionen typischerweise auf die Eigenschaften der Elektrode, d.h. die Oberflächenstruktur und Zusammensetzung, zurückgeführt wurde, stellt sich heraus, dass die resultierende Systemleistung auch von der Elektrolytzusammensetzung abhängt. Zahlreiche Studien zeigen, dass verschiedene in der Lösung vorhandene Spezies sowohl die Kinetik als auch den Mechanismus der Grenzflächenreaktionen verändern können. Besonders interessant ist der Einfluss der scheinbar inerten Ionen (z.B. Alkalimetallkationen), die häufig in den Elektrolyten vorkommen. Wie in der Literatur berichtet, zeigt die Aktivität gegenüber einer elektrokatalytischen Reaktion oft eine Sensibilität für die Art dieser Spezies. Ein weiterer interessanter Aspekt ist der Effekt der Konzentration bestimmter Elektrolytbestandteile. Beispielsweise die Auswirkung der $H^+$-Konzentration (ausgedrückt als pH-Wert) auf die Aktivität, die in vielen Situationen keine offensichtlichen Trends aufweist.

Während die Elektrolytzusammensetzung ein wichtiger Faktor für die elektrokatalytische Aktivität ist, ist die Erklärung ihrer Wirkung oft schwierig. Das Unverständnis des Elektrolyteinflusses ergibt sich aus der begrenzten Anzahl der experimentellen Methoden, die eine eingehende Analyse der Rolle bestimmter Bestandteile für die elektrokatalysierten Reaktionen ermöglichen. Daher liegt der Schwerpunkt dieser Arbeit auf der Entwicklung der experimentellen Methodik, die eine gründliche Untersuchung der oben genannten Effekte ermöglicht. Zu diesem Zweck wurden mehrere verschiedene Systeme mit der sogenannten laserinduzierten Stromtransienten (englisch: laser-induced current transient, LICT) Technik untersucht. Diese in-situ-Technik verwendet einen Hochleistungslaserstrahl, um die Elektrode-Elektrolyt-Grenzfläche zu sondieren. Die Verwendung des LICT zusammen mit anderen allgemein bekannten elektrochemischen Methoden erscheint als ein leistungsfähiges Werkzeug der Systemprüfung.

In dieser Arbeit wird der Nutzen der oben genannten Methodik für Elektrokatalytische- und Batteriesysteme (wichtig für Energieanwendungen) erarbeitet. Zu den Katalysatorsystemen gehörten sowohl reine Edelmetallelektroden (d.h. aus Pt und Au) als auch Elektroden aus Nichtedelmetallverbindung (d.h. aus $Mn_2O_3$), die in verschiedene saure Elektrolyte mit unterschiedlichem pH-Wert, nahezu neutrale $Na^+$- und $K^+$-Salzlösungen oder in die alkalischen Elektrolyte von NaOH eingetaucht waren. In allen untersuchten Systemen kann man einen direkten Zusammenhang zwischen der Grenzflächenstruktur und der Aktivität der Elektroden in Richtung Wasserstoffentwicklung oder Sauerstoffreduktionsreaktionen sehen. Interessanterweise kann die vorgeschlagene Methode auch erfolgreich zur Untersuchung von Batteriezellen verwendet werden. Wie das modellhafte Beispiel wässriger Na-Ionen-Batteriesysteme mit $Na_2Ni[Fe(CN)_6]$ und $Na_2Co[Fe(CN)_6]$ als Elektrodenmaterial zeigt, könnte die durch die anderen elektroanalytischen Verfahren erweiterte Lasertechnik einzigartige Informationen über den Grenzflächen vermittelten Ladungs- und Massentransfer liefern.

Aufgrund seiner Einfachheit und Fähigkeit den Einfluss des Elektrolyten auf die resultierende Leistung verschiedener Systeme zu untersuchen, wird erwartet, dass das LICT neue Möglichkeiten für effizientere Untersuchungen von elektrisierten Fest-Flüssig-Grenzflächen eröffnet.

# Acknowledgment

The accomplishment of this thesis would have been not possible without the help and support received from many people. Therefore, I would like to thank…

… **Prof. Dr. Aliaksandr Bandarenka** for giving me the opportunity to work on this interesting project. I would also like to thank him for his supervision during my Ph.D. studies.

… **Prof. Dr. Frédéric Maillard** for being the second reviewer of my thesis.

… **Prof. Juan Feliu** for accepting me as a visitor scientist at the beginning of the scientific project at the University Alicante where I could have gained a lot of knowledge about electrochemistry. I would also like to express my gratefulness to **Valentín Briega-Martos**, **Sara Lopez Bernabeu**, **Ricardo Martínez Hincapié**, **Juan Victor Perales**, and **Carlos Busó Rogero** for taking care of me during my stay in Spain.

… **Christian Sohr** and **Mathias Rehm** for their great contribution to the development of the experimental methodology.

… **Dr. Faheem Butt** for his scientific and non-scientific support during his stay in our group.

… **Philipp Marzak**, **Dr. Batyr Garlyyev**, **Johaness Fichtner**, **Jeongsik Yun**, **David McLaughlin**, **Yunchang Liang**, **Regina Kluge**, **Song Xue**, and **Sebastian Watzele** for their constructive feedback on this thesis as well as for their support and great atmosphere during my stay in the ECS group. It was a big pleasure to work with you!

… all the former and current members and guests of the ECS and neighboring groups: **Dr. Viktor Čolić**, **Dr. Marcus Pohl**, **Enggar Wibowo**, **Christoph Csoklich**, **Jonas Pfisterer**, **David Reinisch**, **Bianca Paulitsch**, **Jeongsik Yun**, **Jongho Kim**, **Philipp Moser**, **Richard Haid**, **Dr. Wei-Jin Lin**, **Swaroopa Ganti**, **Namitha Rajendran**, **Xing Ding**, **Prof. Tharamani**, **Florian Schieg**, **Radu Bors**, **Alexander Wieczorek**, **Paul Scheibenbogen**, **Pascal Hauenstein**, **Angus Laurenson**, **Mike Dao**, **Johannes Figueiredo**, **Marc Kosiahn**, **Muhammad Umair Ul Hassan**, **Felix Kemmeth, Nasim Tavakoli,** and **Borja Pano** (random order) for making my stay at the TUM enjoyable.

… **Siegfried Schreier** and **Markus Haß** for their professional technical assistance during realization of this project. I would also like to thank Siegfried that he never gave up on my German skills. Danke schön!

… our secretaries **Manuela Ritter** and **Susanne Tillich** for taking care of all the bureaucratic cases during my stay at the TUM.

… my **local church community** for being my second family in Munich, for their spiritual and physical support.

… my **family** without whom I would not have been there where I am now.

… my girlfriend **Sosena** for all love and support which I could have received from her during the time of writing this thesis.

# Table of Contents

# 1. Publications and Conference Attendance

## 1.1 Publications

1. M.D. Pohl, V. Čolić, <u>D. Scieszka</u>, A.S. Bandarenka. *Elucidation of Adsorption Processes at the Surface of Pt(331) Model Electrocatalysts in Acidic Aqueous Media.* Phys. Chem. Chem. Phys., 2016, 18, 10792. DOI: 10.1039/C5CP08000B

2. V. Čolić, M.D. Pohl, <u>D. Scieszka</u>, A.S. Bandarenka, *Influence of the Electrolyte Composition on the Activity and Selectivity of Electrocatalytic Centers.* Catal. Today, 2016, 262, 24. DOI:10.1016/j.cattod.2015.08.003

3. <u>D. Scieszka</u>,[1] J. Yun,[1] A.S. Bandarenka. *What Do Laser-Induced Transient Techniques Reveal for Batteries? Na- and K-Intercalation from Aqueous Electrolytes as an Example.* ACS Appl. Mater. Interfaces, 2017, 9, 20213. DOI: 10.1021/acsami.7b03923

4. J. Yun,[1] F. Schiegg,[1] Y. Liang, <u>D. Scieszka</u>, B. Garlyyev, A. Kwiatkowski, T. Wagner, A.S. Bandarenka. *Electrochemically Formed $Na_xMn[Mn(CN)_6]$ Thin Film Anodes Demonstrate Sodium Intercalation and De-Intercalation at Extremely Negative Electrode Potentials in Aqueous Media.* ACS Appl. Energy Mater., 2018, 1, 123. DOI: 10.1021/acsaem.7b00022

5. B. Garlyyev, S. Xue, S. Watzele, <u>D. Scieszka</u>, A.S. Bandarenka. *Influence of the Nature of the Alkali Metal Cations on the Electrical Double Layer Capacitance of Model Pt(111) and Au(111) Electrodes.* J. Phys. Chem. Lett., 2018, 9, 1927. DOI: 10.1021/acs.jpclett.8b00610

6. R. Bors, J. Yun, P. Marzak, J. Fichtner, <u>D. Scieszka</u>, A.S. Bandarenka. *Chromium(II) Hexacyanoferrate-Based Thin Films as a Material for Aqueous Alkali Metal Cation Batteries.* ACS Omega, 2018, 3, 5111. DOI: 10.1021/acsomega.8b00273

7. <u>D. Scieszka</u>,[1] C. Sohr,[1] P. Scheibenbogen, P. Marzak, J. Yun, Y. Liang, J. Fichtner, A.S. Bandarenka. *Multiple Potentials of Maximum Entropy of a $Na_2Co[Fe(CN)_6]$ Battery Electrode Material: Does the Electrolyte Composition Control the Interface?* ACS Appl. Mater. Interfaces, 2018, 10, 21688. DOI: 10.1021/acsami.8b03846

8. <u>D. Scieszka,</u> S. Watzele, S. Xue, X. Ding, B. Garlyyev, A.S. Bandarenka, *Why Electrolytes Control the Catalytic Activity*, In preparation.

9. A. Tiwari, V. Singh, <u>D. Scieszka,</u> A.S. Bandarenka, T.C. Nagaiah, *In-situ Exploration of Mn$_2$O$_3$ Activation Towards Oxygen Reduction Electrocatalysis*, In preparation.

## 1.2   Conference Attendance

### 1.2.1   Oral Presentations

1. 6$^{th}$ Colloquium of the Munich School of Engineering, Garching, Germany, 7$^{th}$ of July 2016, *Elucidation of Adsorption Processes at the Surface of Pt(331) Model Electrocatalysts in Acidic Aqueous Media.*

2. Nanosystems Initiative Munich Summer Retreat, Herrsching, Germany, 27$^{th}$ – 29$^{th}$ of July 2016, *Elucidation of Adsorption Processes at the Surface of Pt(331) Model Electrocatalysts in Acidic Aqueous Media.*

3. International Conference on Materials Science and Nanotechnology, Lahore, Pakistan, 25$^{th}$ of September 2016, *Elucidation of Adsorption Processes at the Surface of Pt(331) Model Electrocatalysts in Acidic Aqueous Media* – Video Presentation.

4. 6$^{th}$ Regional Symposium on Electrochemistry of South-East Europe, Balatonkenese, Hungary, 11$^{th}$ – 15$^{th}$ of June 2017, *What Do Laser-Induced Transients Techniques Reveal for the Electrochemical Systems?*

5. European Materials Research Society Fall Meeting, Warsaw, Poland, 18$^{th}$ – 21$^{st}$ of September 2017, *What Do Laser-Induced Transients Techniques Reveal for the Electrochemical Systems?*

### 1.2.2 Poster Presentations

1. Symposium Electrochemical Energy Conversion and Storage in honor of Prof. Ulrich Stimming's 70th Birthday, Garching, Germany, 20th October 2016, *Battery Systems Analysis Using Laser Induced Current Transient Measurement.*

2. 7th Colloquium of the Munich School of Engineering, Garching, Germany, 13th of July 2017, *What Do Laser-Induced Transients Techniques Reveal for the Electrochemical Systems?*

3. Nanosystems Initiative Munich Conference on Nanostructured functional Materials for sustainable Energy Provision, Munich, Germany, 26th – 28th of July 2017, *What Do Laser-Induced Transients Techniques Reveal for the Electrochemical Systems?*

# 2. Introduction

## 2.1 Global Energy Production: Current Situation, Limitations, and Challenges

A global population growth coupled with dynamic industrialization of developing countries results in a continuous rise in energy demand.[1,2,3,4] According to the forecast of the International Energy Agency (IEA), by 2040 this demand is going to further increase by another 50%.[5] Current energy production largely depends on fossil fuels. In 2017, 85% of produced energy came from oil (34%), coal (28%), and natural gas (23%).[6] However, the consumption of these resources has two significant drawbacks. First, it generates greenhouse gases recognized as the primary cause of climate changes. Second, the remaining reserves of the non-renewable resources are predicted to diminish within the next few decades. Thus, one can see that addressing the global need for energy necessitates the development of alternative energy sources.[7]
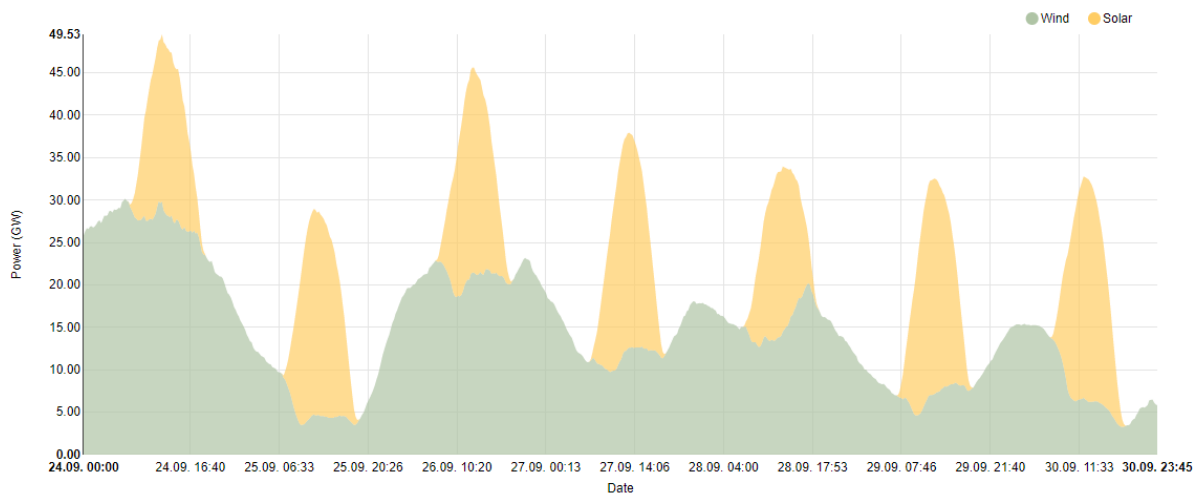


***Figure 2.1***. *Diagram representing the combination of the power output of wind and solar power plants in Germany during the time period between the 24th and 30th of September 2018. Note the fluctuation in the power production. Taken from reference 8.*

Solar and wind, often recognized as the most promising examples of renewable energy sources, already contribute to about 3% of global energy provision.[6,9,10,11] However, their stochastic nature frequently results in temporary excess or deficiency of the generated energy (see **Figure 2.1**). This appears to be one of the biggest challenges causing the so-called "generation vs consumption" problem.[12] Therefore, one can see that efficient, widespread utilization of renewable energy requires viable methods of its provision and storage.

## 2.2 Hydrogen: Energy Carrier of the Future

One of the most suitable candidates to store energy produced from renewable sources is hydrogen. In this respect, energy can be stored in the form of chemical bonds, transported, and eventually converted back to the electricity using fuel cells (FCs) or combustion systems (see **Figure 2.2**). Undoubtedly, the utilization of $H_2$ would fit well into the worldwide "decarbonization" trend.[13] On earth, however, hydrogen does not occur in its molecular form. Rather, it is found in water and hydrocarbons. Currently, the steam reforming of the latter is the primary source of $H_2$. Nevertheless, producing hydrogen from fossil fuels does not solve the problems related to the consumption of non-renewable energy resources. Instead, it only shifts the fossil fuels from end-use to earlier production steps.[14]
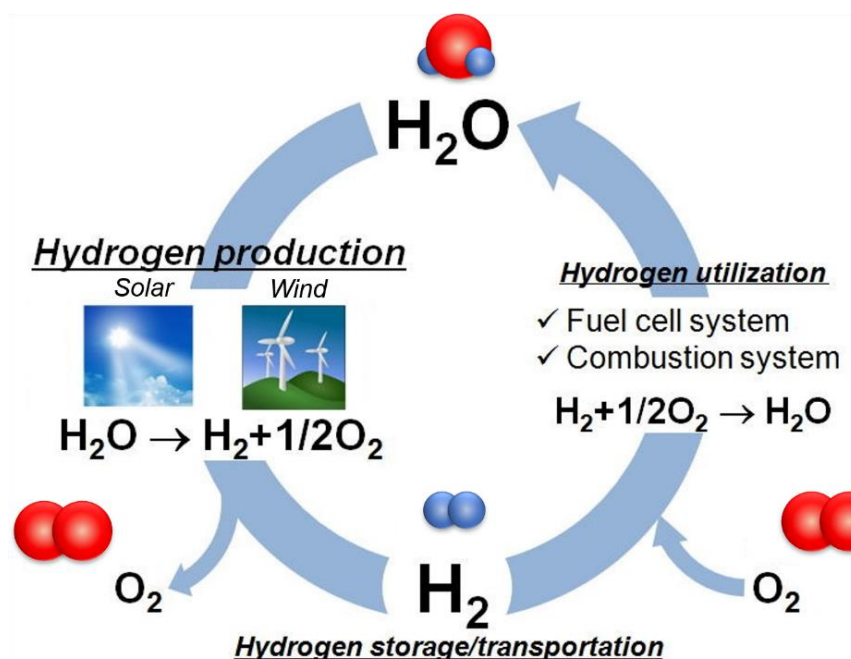


***Figure 2.2.*** *Schematic representation of the hydrogen energy cycle. Adapted from reference 15.*

Electrolytic water splitting is likely a viable route of clean hydrogen acquisition. This process, performed in the so-called water electrolyzers (WELs), uses electric energy to split water molecules.[16,17,18,19] This method of hydrogen gas production has recently garnered massive attention along with high expectations to fulfill demands for environmentally friendly energy.[20,21,22] However, to make this technology financially rewarding, it is still necessary to improve the efficiency of the processes essential for electrocatalytic production and utilization of gas $H_2$.

Although the "hydrogen technologies" are mainly based on $H_2$ reactions, their biggest bottlenecks are the oxygen evolution reaction and oxygen reduction reaction taking place in WELs and FCs, respectively.[23] Hence, many efforts are made to improve the sluggish kinetics of these processes. Furthermore, the aggressive electrolytes used in these electrocatalytic systems narrow down the choice of catalysts to expensive noble metals. Thus, the optimization of the catalyst activity would additionally allow decreasing the loading of the pricey materials and, as a consequence, reduce the operational costs.
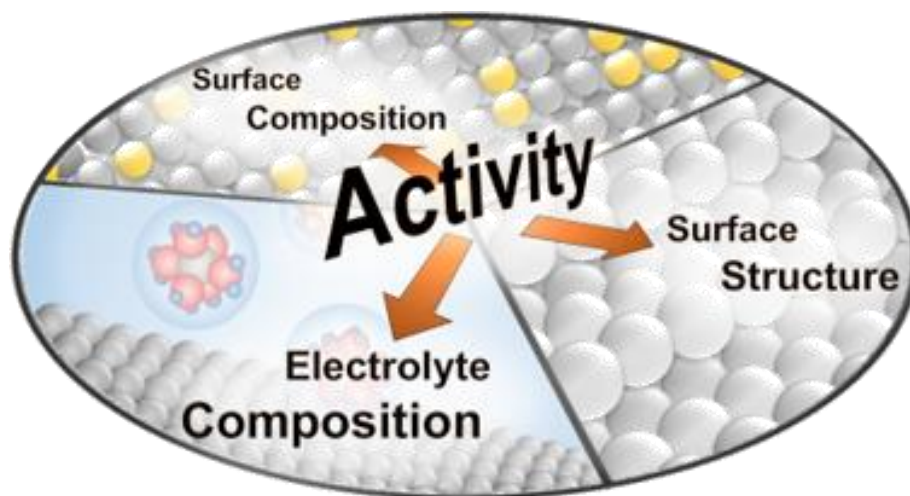


*Figure 2.3. Three major factors influencing the electrocatalytic activity: surface composition, surface structure, and electrolyte composition.*

Studies of the optimization of the WELs and FCs performance typically concentrate on the electrode materials and electrode structure. However, there is a growing body of evidence that, in many cases, the activity of a certain electrocatalyst drastically depends on the electrolyte composition. Moreover, the consideration of the "inert" electrolyte species often appears to be the only possible way to fully explain an electrocatalytic behavior of numerous systems.[24] Thus,

it is now clear that the activity of a given electrode surface should be found as a combination of three essential components, namely: (i) surface composition, (ii) surface structure, and (iii) electrolyte composition (see **Figure 2.3**).

## 2.3 Batteries: Old Ideas, New Applications

Utilization of rechargeable batteries is another solution for storing the intermittent surpluses of renewable energy in the form of chemical energy.[25,26] Currently, Li-ion batteries are the most popular type of rechargeable cells. Because of their large operational voltage and high energy density, they find application in numerous types of portable devices or plug-in hybrid vehicles.[27] Furthermore, due to their relatively simple maintenance and ability to provide high energy conversion, these devices are also often presented as a promising choice for the large-scale energy storage systems.[9,11,28,29] However, there are a few major drawbacks that characterize this technology. One of them is associated with the low abundance of Li deposits on earth. Additionally, the reserves of lithium are located in distant places or in countries, which are nowadays not politically stable.[30] These factors affect the costs of the key materials hindering the widespread upscaling of this kind of storage systems. Moreover, flammable organic electrolytes, typically used in this type of battery cells, can raise safety issues. Therefore, the utilization of batteries consisting of cheaper materials and safe electrolytes would largely simplify the grid-scale application of battery systems.[31,32] Aqueous Na-ion batteries could be an answer to this problem. Unlike lithium, sodium is the 6th most abundant element in the earth's crust occurring in ocean water[33] and various minerals.[34,35] The resemblance between the electrochemical behavior of the Na and Li elements additionally enables to transfer advanced technologies of Li-ion cells to Na-based batteries.[30] For these reasons, Na-ion batteries have drawn a lot of interest from the scientific community.

There have been numerous studies dedicated to developing electrode materials that could be implemented in aqueous Na-ion batteries.[36,37,38] The majority of reported studies on this type of battery cells focuses on properties, such as energy and power densities, or the stability of the electrode materials upon their exploitation.[39,40,41,42,43] Nonetheless, still relatively little is known about the kinetics of the interfacial processes governing their performance, such as intercalation and deintercalation of metal cations. Particularly interesting is the role of the electrolyte

composition for the mechanism of (de)intercalation. Apparently, the influence of the electrolyte species on the performance of the battery cells (both cations and anions) might have also been underestimated in the case of battery systems.[12,44,45,46]

## 2.4 Objective of the Thesis

In spite of its importance, the determination of the electrolyte effect on the behavior of electrochemical systems remains a challenge. The difficulties arise from the shortage of techniques, which allow the profound study of the electrified solid/liquid interfaces and processes taking place at them.[45] Therefore, there is a great need for elaborating new characterization methods, which would allow a more in-depth analysis of the systems. In this work, the influence of the electrolyte composition on interfacial processes is examined. The interfaces formed between solid electrodes and liquid electrolytes in various systems crucial for sustainable energy provision are investigated with the so-called laser-induced current transient (LICT) technique complemented by other commonly known methods of electroanalysis (i.e., cyclic voltammetry, impedance spectroscopy, or electrochemical nanogravimetry). Using this unique tool, the following aspects are addressed:

1. The pH effect and the influence of alkali-metal cations on the electrocatalytic activity of noble metal electrodes. The oxygen reduction reaction and the hydrogen evolution reaction are used as model energy relevant processes.
2. The kinetics of the electrocatalytic reactions on electrodes consisting of non-precious metal compounds.
3. The effect of alkali-metal cations and anions on the kinetics and mechanism of intercalation and deintercalation processes in systems relevant to aqueous Na-ion batteries.

# 3. Theoretical Considerations

## 3.1 Catalysis and Electrocatalysis

By definition, catalysis is a phenomenon of enhancing the rate of a chemical reaction as a result of adding a material, which does not get consumed during the entire process and can be used repetitively. The introduced material, known as a catalyst, alters the kinetics of the reaction without modifying its thermodynamics.[47,48]

Probably one of the oldest examples of catalytic reactions is the production of ethanol. This process, known already in antiquity, utilizes the enzymes supplied by yeast to convert sugar to alcohol during fermentation. Notwithstanding, the first reported catalytic operation in modern history was decomposition of ammonia on hot metals performed in 1813 by the French professor L. J. Thenard. Still, it took about two decades until the official term "catalysis" was used for the first time. It was done by J. J. Berzelius who in 1836 published an extensive report on the systematic studies of this phenomenon.[49,50] This opened a new field of scientific research enabling the development of numerous branches of the chemical industry.[51]

The catalysis can be divided into two main fields:[47,50]

➢ Homogeneous catalysis; in this type of catalysis, the catalyst exists in the same phase as the reactants and products of the catalyzed reaction.

➢ Heterogeneous catalysis, which is related to all catalytic systems, where the catalyst and the reactants are in different phases.

Heterogeneous catalysis is the most common type of catalysis. In the literature, it typically refers to the processes in which the catalyst is in a solid state, while the substrates and products of the catalyzed reaction are gases or liquids. The popularity of such a "combination" comes from the ease of separation and cleaning of the catalytic material.[50]

The idea behind the catalytic process can be explained as follows. In order for a reaction to occur, a certain energy barrier (i.e., activation energy) must be overcome. The role of the catalyst is to lower this barrier by bonding the reaction substrates and creating a complex characterized by a decreased demand for energy. Such a complex undergoes the chemical reaction forming products which, in the end, can be separated from the catalyst.[51]

In search for an optimal catalytic material, three factors should be considered: (i) the activity of the catalyst, (ii) its selectivity, and (iii) stability.[52] The activity is described using the rate of the reaction turnover expressed as the overall number of catalytic conversions of reactants taking place at one active center in a given amount of time.[53] In turn, the selectivity can be defined as the ability of a catalyst to promote a particular reaction pathway to achieve a preferred outcome.[54] Finally, the catalytic material should exhibit high stability in often harsh reaction conditions without getting less active or damaged.[55,56]

Electrocatalysis is a special type of catalysis focusing on the enhancement of the rate of chemical reactions occurring at the electrode surface. At a certain current density, the simplest indicator of the rate enhancement is a decrease in the overpotential. The overpotential can be defined as the difference between the experimentally observed potential at which a reaction takes place and the thermodynamic equilibrium potential value.[47] Electrocatalysis covers all the cases in which the applied potential can govern the reactions. The use of the external voltage provides another adjustable parameter affecting the chemical processes. This gives an additional possibility to control the catalytic reactions more effectively which appears as a clear advantage over the "classical" catalysis.[57,58]

## 3.2    Sabatier Principle

The so-called Sabatier principle formulated at the beginning of the 20th century by the French chemist P. Sabatier is one of the fundamentals of heterogeneous catalysis.[59] According to this tenet, the binding energy between the intermediates of a catalytic reaction and the active sites of the catalyst should be neither too strong nor too weak. Too strong interactions would simply block the catalyst surface, while too weak interactions would not allow the species to stay at the surface long enough to react. On the basis of this principle, it is possible to say that for each catalytic reaction there is optimal binding energy for which the reaction proceeds the most efficiently.[60]

It has become a common practice to depict activity trends using the so-called volcano plots. They illustrate the relation between the electrocatalyst activity and the surface reactivity. The activity shows how fast the catalytic process takes place at the surface, while the reactivity measures the intensity of the interactions between the catalyst surface and the adsorbing species.

The catalytic activity can be represented as, for instance, current density, overpotential, or ''half-wave potential'', while the reactivity is typically quantified by the strength of the bonds estimated from the heat of hydride formation, the heat of oxide formation, etc. (**Figure 3.1**). An optimal catalyst for a particular reaction is located at the top of the volcano plot.[61,62] The activity of the catalysts placed on the left from the top is limited by the desorption of the products. In contrary, the activity of the catalysts from the right side of the plot is limited by the poor activation of the reactant.[60] The volcano plots constructed in such a way are useful in designing efficient catalytic materials.[61]
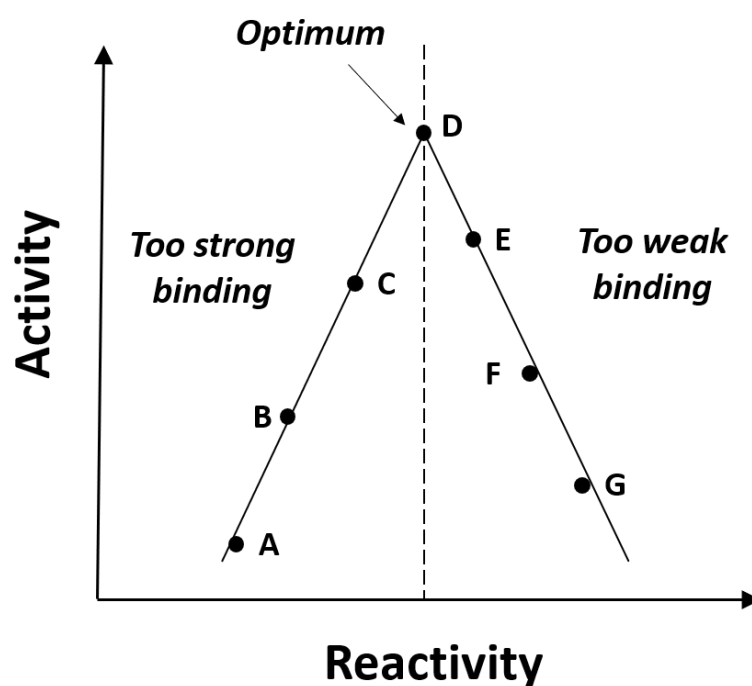


*Figure 3.1. Schematic illustration of the volcano plot. The catalyst depicted as D is an optimal one. The catalysts located on the left side of the optimum bind the reaction species too strongly, while the catalysts on the right bind them too weakly.*

## 3.3   Active Sites

The Sabatier principle and its volcano plot quantification (**Section 3.2**) could answer questions regarding the species-catalyst interaction. However, they did not provide information about the location of the active sites at the catalyst surface. It was Langmuir who was the first who concluded that adsorption of gas molecules at the surface is not even. According to this

statement, the catalyst surface contains a finite number of ''spaces'' which can be covered by the adsorbate, while the rest of the spaces stay unoccupied. This idea was further developed by H. S. Taylor. According to Taylor, a catalytic chemical reaction is not catalyzed over the entire solid surface of the heterogeneous catalyst but only at certain centers: so-called ''active sites''.[63] The reactions remarkably dependent on the distribution of the catalytic active sites are known as structure-sensitive.[64] Identification of active sites, as well as their structure, relative surface abundance, and electronic properties, plays a vital role in the process of optimization and development of new catalysts.[65,66]

## 3.4 Reactions Important for Energy Conversion and Storage and their Applications

### 3.4.1 Hydrogen Evolution Reaction

Hydrogen gas can be produced in the cathodic half-reaction of water splitting. This reaction, known as the hydrogen evolution reaction (HER), is undeniably among the most studied electrochemical processes. It is of great importance for a number of energy conversion devices, such as artificial photosynthetic cells or WELs.[17,18,19,67] Depending on the pH of the electrolyte used, the HER proceeds through the following half-reactions:[68]

In acidic media:

$$2H_{(aq)}^+ + 2e^- \rightarrow H_{2(g)} \qquad\qquad \textit{Eq. 3.1}$$

In alkaline solutions:

$$2H_2O + 2e^- \rightarrow H_{2(g)} + 2OH_{(aq)}^- \qquad\qquad \textit{Eq. 3.2}$$
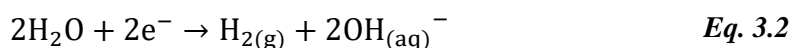
The thermodynamic equilibrium potential for the HER is given as $E^o{}_{H^+/H_2} = 0.00\ \text{V}$ vs reversible hydrogen electrode (RHE).[69]

The kinetics of the HER strongly depends on its reaction pathway (**Figure 3.2**). In acidic media, the HER consists of the following steps:[68,70]

- Volmer reaction (also known as the discharged reaction) is usually considered to be the fastest one.[71] During this step, the electron transfer takes place at the catalyst surface. As a consequence, an intermediate hydrogen atom gets adsorbed:

$$H_{(aq)}^+ + e^- \rightarrow H_{(ads)}$$
*Eq. 3.3*

- Heyrovsky reaction (also known as electrochemical desorption) occurs subsequently to the Volmer reaction. In this step, another electron transfer takes place. The adsorbed hydrogen atom reacts with a proton from the solution forming molecular hydrogen:

$$H_{(ads)} + H_{(aq)}^+ + e^- \rightarrow H_{2(g)}$$
*Eq. 3.4*
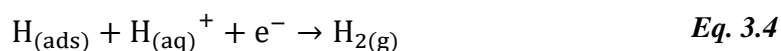
- Tafel reaction (also known as the recombination reaction) is a process alternative to the Heyrovsky reaction. In this step, molecular hydrogen is formed by two adsorbed hydrogen atoms:

$$H_{(ads)} + H_{(ads)} \rightarrow H_{2(g)}$$
*Eq. 3.5*
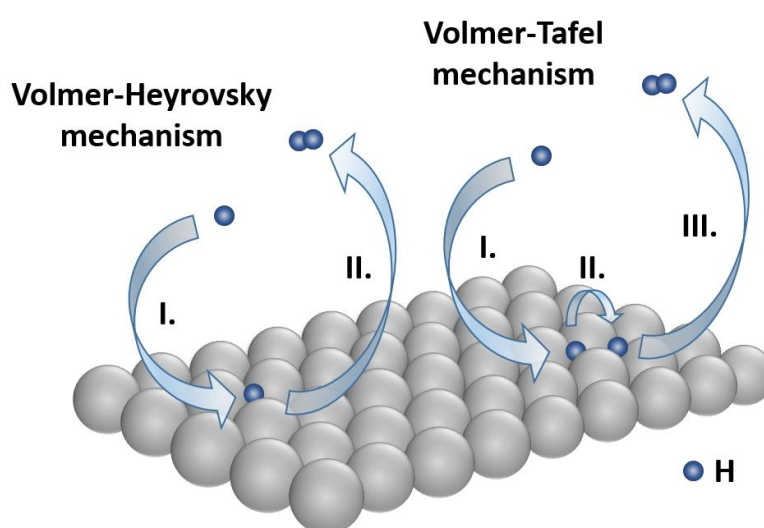


***Figure 3.2.*** *HER mechanisms on the electrode surface in acidic media. Roman numerals show the order of the subsequent steps. Adapted from reference 70.*

The aforementioned reaction pathways can be both potential- and catalyst-dependent. In some cases, the multiple pathways can be simultaneously operative. This can happen due to the structure sensitivity of the HER. The existence of different surface crystal facets on a single electrocatalyst can cause the reaction to undergo more than one pathway.[68]

### 3.4.2 Oxygen Evolution Reaction

The anodic half-reaction of water splitting is the oxygen evolution reaction (OER).[67] Similar to the HER, the OER is one of the most important processes for production and storage of renewable energy in chemical form.[72,73] During this reaction, molecular oxygen is generated through several proton-electron coupled processes. As for the HER, the mechanism of the OER is also strictly related to the acidity of the environment. Depending on pH of the electrolyte, one can distinguish two reaction pathways:[67,74,75,76,77,78]

In acidic solutions:

$$2H_2O \rightarrow 4H^+ + O_2 + 4e^-$$    *Eq. 3.6*

In alkaline solutions:

$$4OH^- \rightarrow 2H_2O + O_2 + 4e^-$$    *Eq. 3.7*
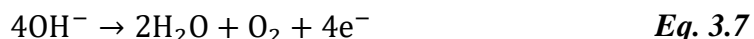
### 3.4.3 Water Electrolyzers

As mentioned above, the process of water electrolysis can be carried out in WELs.[79] These devices utilize the external direct current (DC) to split $H_2O$ into hydrogen and oxygen.[80] The concept of water decomposition using electric current dates back to the beginning of the 19th century when Nicholson and Carlise performed this process for the first time.[81] Since then, the electrolysis faced many ups and downs finally becoming one of the most promising solutions for the future sustainable energy provision.[82]

Consider the simplest WEL consisting of an anode and a cathode submerged in an acidic ion conductive solution and connected with a power source (see **Figure 3.3**). In such a system,

water molecules are oxidized at the anode side producing $O_2$ in the OER (**Eq. 3.6**). Then, the released protons migrate through the diaphragm (preventing the mixing of the gases) towards the cathode where they undergo the HER forming $H_2$ (see **Eq. 3.1**). The generated gases are captured in collectors located near the electrodes.
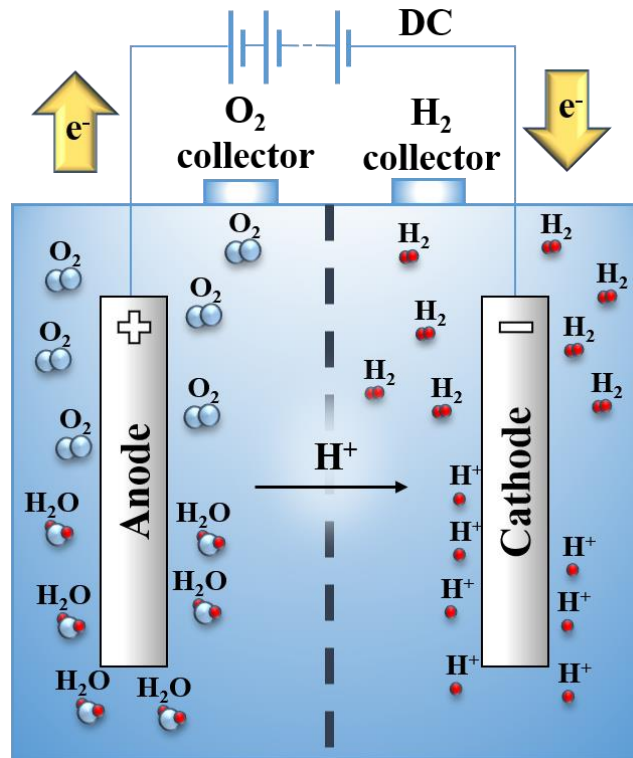


***Figure 3.3.*** *Scheme of a water electrolysis unit working in an acidic media. Yellow arrows show the direction of the electrons flow. Water molecules are reduced at the anode, while protons are transported to the cathode where they get oxidized to $H_2$. Adapted from reference 83.*

Regardless of the electrolyte pH, the sum of both half-reactions can be expressed as:

$$H_2O \rightarrow H_2 + \frac{1}{2}O_2 \qquad \textit{Eq. 3.8}$$

In general, one can distinguish three main types of electrolysis systems: (i) alkaline water electrolyzers, (ii) polymer electrolyte membrane (PEM) electrolyzers, and (iii) solid oxide electrolyzers (SOE). The technology using the alkaline water electrolyzers is the most mature. Such electrolyzes typically utilize the 20 %-30 % aqueous solution of KOH as an electrolyte. Thus, their main drawback is related to the high risk of corrosion caused by the aggressive media. The second, PEM devices are so far meant for small-scale applications. As the name

suggests, the PEM electrolyzers contain a proton exchange membrane usually made of Nafion®. The presence of the solid membrane results in a separation of oxygen and hydrogen gases, as well as in faster transportation of ions. Furthermore, due to an absence of the highly alkaline electrolyte, the PEM electrolysis assures longer durability and higher safety. High costs of the membrane and electrode materials in these systems is an obvious shortcoming of this technology. The third type of the electrolyzers listed above, namely the SOE, utilizes electricity to perform the conversion of steam or $CO_2$ into $H_2$ and CO. These devices operate at high temperatures. This is a clear advantage considering the fact that water electrolysis is an endothermic process. The high temperatures increase the rate of the redox reaction and, as a consequence, decrease the amount of electricity used. Therefore, it is believed that application of the SOEs to the hydrogen production could significantly reduce the price of the final product.[84,85]

### 3.4.4 Hydrogen Oxidation Reaction

Next to the HER, the hydrogen oxidation reaction (HOR) is a reaction of fundamental importance for electrocatalysis. Many basic laws in this field have been developed and verified using these two hydrogen reactions.[86] The HOR is also essential for FCs in which it occurs at the anode. In opposite to the ORR (the cathode reaction in FCs), this reaction exhibits rather fast kinetics.[23] Especially on Pt-based catalysts, the oxidation of hydrogen occurs quickly and its rate in a FC is usually controlled by mass-transport limitations.[87] Because of that, during the optimization of the performance of these devices, the overpotential of the HOR is often neglected.[88]

Despite the importance of the HER/HOR in both acidic and alkaline media (especially for alkaline electrolyzers and alkaline fuel cell systems), the mechanism and kinetics of this reaction have been more often studied in the acidic electrolytes. As in the case of the HER, the HOR is also believed to follow the Tafel-Heyrovsky-Volmer mechanism (see **Section 3.4.1**). However, depending on the electrode material, the rates of the Tafel and Heyrovsky reaction can vary.[89,90]

Although the HOR proceeds fast on Pt-based catalysts, it exhibits sensitivity to impurities. For instance, the CO impurity can block the active sites at the catalyst surface. Thus, hydrogen used

in this reaction should be pure. This can cause problems, making the reactant expensive and difficult to store.[87]

### 3.4.5 Oxygen Reduction Reaction

Similarly to the OER, the ORR is a multielectron process. It may include multiple elementary steps involving different intermediates. The complicated reaction pathway of $O_2$ reduction at the surface is usually described by the scheme proposed by Wroblowa et al. shown in **Figure 3.4**.[91,92]
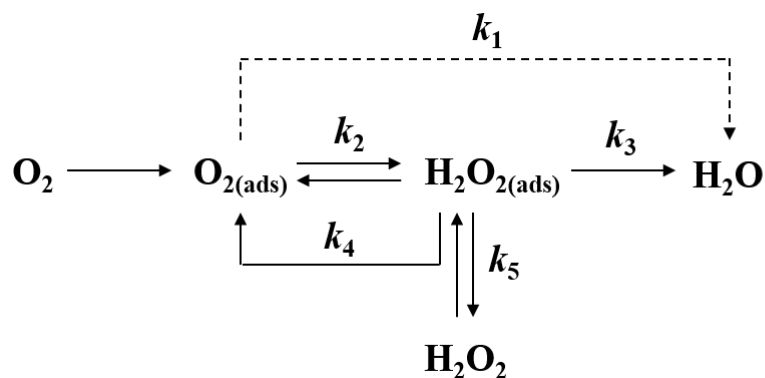


***Figure 3.4.*** *Schematic representation of the most plausible ORR mechanism. Adapted from reference 91.*

According to this reaction scheme, an oxygen molecule can be electrochemically reduced directly to water with the rate constant $k_1$. This reaction known as ''direct'' reduction requires four electrons and proceeds without the $H_2O_{2(ads)}$ intermediate formation. Another possibility is ''series'' reduction taking place with the rate constant $k_2$. In this reaction, $O_2$ is firstly reduced to $H_2O_{2(ads)}$. The generated intermediate can be further electroreduced to water (rate constant $k_3$), catalytically decomposed at the electrode surface (rate constant $k_4$), or desorbed into the bulk of the electrolyte (rate constant $k_5$). Based on the literature, the ORR on Pt and Pt-bimetallic electrocatalysts is believed to most likely undergo the pathway of four-electron reduction.[93]

The first step of four-electron reduction of oxygen (hereunder presented the so-called dissociative mechanism in acidic media) includes oxygen molecule adsorption. This process can be shown as follows:[23,93,94]

$$\frac{1}{2} O_2 \rightleftarrows O_{(ads)} \qquad \textit{Eq. 3.9}$$

The $O_{(ads)}$ further undergoes the reductive transition according to the kinetic equation:

$$O_{(ads)} + H^+ + e^- \rightleftarrows OH_{(ads)} \qquad \textit{Eq. 3.10}$$
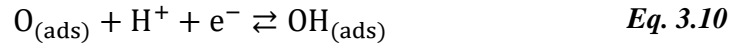
Finally, the $OH_{(ads)}$ gets reduced to water through the reductive desorption step:

$$OH_{(ads)} + H^+ + e^- \rightleftarrows H_2O \qquad \textit{Eq. 3.11}$$
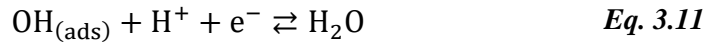
For transition metal catalysts less active than Pt (i.e., Au, Hg), it was reported that the oxygen molecule is more likely to be subjected to the two-electron pathway.[93] In this scenario, the $O_2$ is reduced to $H_2O_2$. During this process, the $HOO_{(ads)}$ intermediate is generated:[95]

$$O_2 + H^+ + e^- \rightleftarrows HOO_{(ads)} \qquad \textit{Eq. 3.12}$$

$$HOO_{(ads)} + H^+ + e^- \rightleftarrows H_2O_2 \qquad \textit{Eq. 3.13}$$
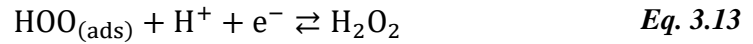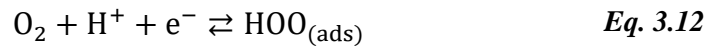
The standard reduction potential for the ORR is given as $E^o{}_{O_2/H_2O} = 1.23$ V vs RHE.[69]

### 3.4.6   Fuel Cells

The hydrogen generated in the HER can be utilized as a fuel in a FC. By definition, the FC is a galvanic cell converting the chemical energy of a fuel to electrical energy (via an electric current) without fuel combustion.[87,96] This is undoubtedly one of the oldest electrical energy conversion technologies. The idea of using these apparatuses as energy conversion systems dates back to the middle of the 19$^{th}$ century. Since that time, due to the increase in the global energy consumption and the urge to look for a replacement for fossil fuels, the FCs have been recognized as one of the main candidates for the future energy provision.[97,98,99]

A scheme of a typical FC is depicted in **Figure 3.5**. Hydrogen (fuel) and oxygen (oxidant) are introduced into the system where, at electrode surfaces, they undergo redox reactions resulting in electricity production.[100]
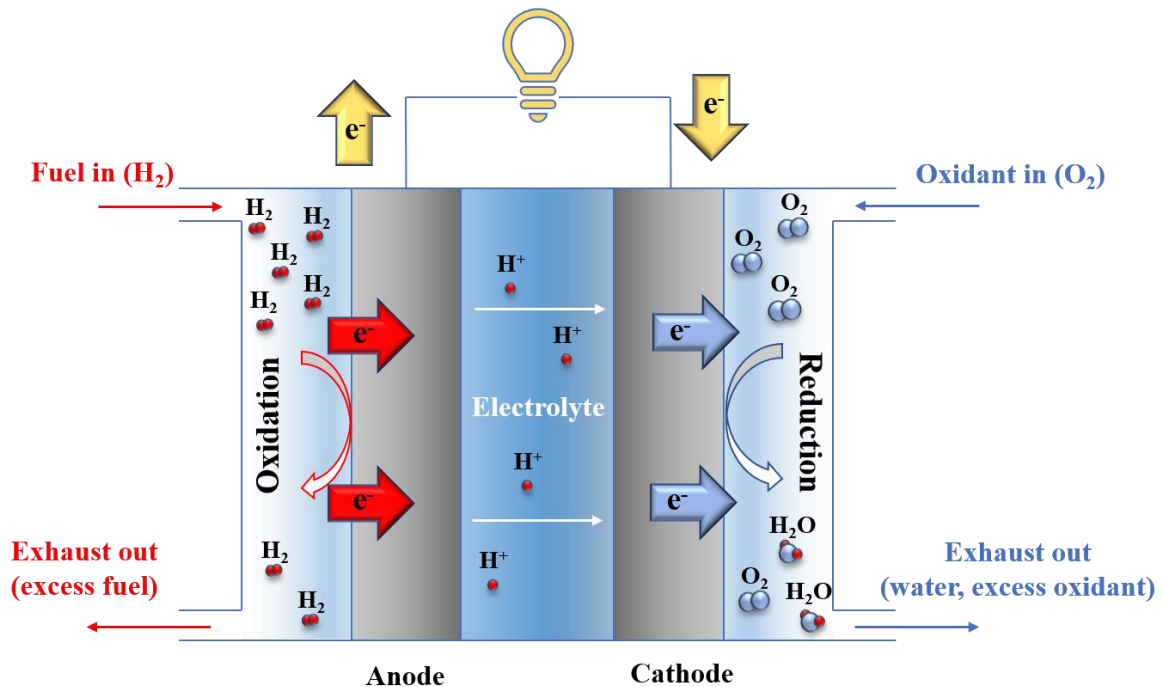


***Figure 3.5.*** *Scheme of a fuel cell containing an acidic electrolyte and utilizing hydrogen as a fuel. The fuel ($H_2$) gets oxidized at the anode, while the oxidant ($O_2$) is reduced at the cathode side. The redox reaction results in the electric current flow through the external circuit. Adapted from reference 101.*

The fuel ($H_2$) introduced into the FC gets oxidized at the anode side (the HOR takes place), whereas the oxidant ($O_2$) is transferred to the cathode where it is reduced (during the ORR). The whole process takes place with high conversion efficiency, high power density, and quiet operation. Although various types of fuels can be utilized (i.e., methanol, ethanol, methane, etc.), hydrogen appears to be the most environmentally friendly choice. Besides the electrical energy, utilization of this gas results in the generation of only water and heat as side products.[96,102]

Depending on the electrolyte pH, the mechanism of the reactions occurring in the FCs can be presented as follows:[96]

In acidic electrolytes:

$$\text{Anode: } H_2 \rightarrow 2H^+ + 2e^- \qquad \textit{Eq. 3.14}$$

$$\text{Cathode: } O_2 + 4H^+ + 4e^- \rightarrow 2H_2O \qquad \textit{Eq. 3.15}$$

In alkaline electrolytes:

$$\text{Anode: } H_2 + 2OH^- \rightarrow 2H_2O + 2e^- \qquad \textit{Eq. 3.16}$$

$$\text{Cathode: } O_2 + 4e^- + 2H_2O \rightarrow 4OH^- \qquad \textit{Eq. 3.17}$$
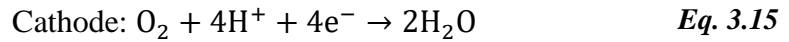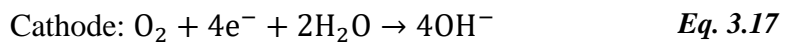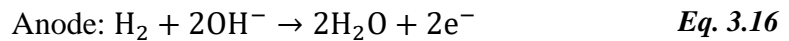
In both cases, the half-reactions can be combined and expressed as the following general reaction of the cell:

$$2H_2 + O_2 \rightarrow 2H_2O \qquad \textit{Eq. 3.18}$$

There are various ways of the FCs classification. Typically, these devices are categorized according to parameters related to their construction or operation. One of the most common criteria is based on the electrolyte used. The electrolyte can exist in the solid and liquid state. A solid oxide ion-conducting ceramic is an example of the former. The FC containing the ceramic material is known as the solid oxide FC (SOFC). The liquid electrolytes can be further divided according to their pH value of the electrolyte. For instance, $H_3PO_4$ finds an application in phosphoric acid FCs (PAFCs). In turn, solutions from the other side of the pH scale, such as KOH, can be applied in the so-called alkaline FCs (AFCs). Another common way of grouping these devices is based on their working temperatures. One can distinguish low-temperature and high-temperature FCs. Direct methanol FCs (DMFCs), polymer electrolyte FCs (PEMFCs), or AFCs and PAFCs mentioned above belong to the group of the low-temperature FCs. By contrast, SOFCs are an example of the high-temperature FCs. A typical operating temperature range of such a cell is ca. 600-1000 °C.[87,103]

## 3.5    Na-Ion Battery Systems

### 3.5.1    Fundamentals of Batteries

From the scientific viewpoint, batteries are defined as galvanic cells that generate direct current as a consequence of converting chemical energy into electrical one. A schematic illustration of a battery is displayed in **Figure 3.6**. A battery cell consists of an anode and a cathode. During the discharge, the anode material undergoes oxidation processes. Electrons generated during oxidation move through the external circuit towards the cathode which, in turn, undergoes reduction processes. Both reactions occur simultaneously which results in the electron flow through the external circuit. Electrolytes used in batteries can be a liquid, gel, or even a solid material exhibiting ionic conductivity. An important part of a battery cell is a separator, which can be also an ion-selective membrane. It is used to prohibit the physical contact between the two electrodes. The physical contact between the electrodes would lead to their short circuiting and, as a further consequence, to the so-called ''thermal runaway'' often resulting in the cell destruction.[104,105,106,107]
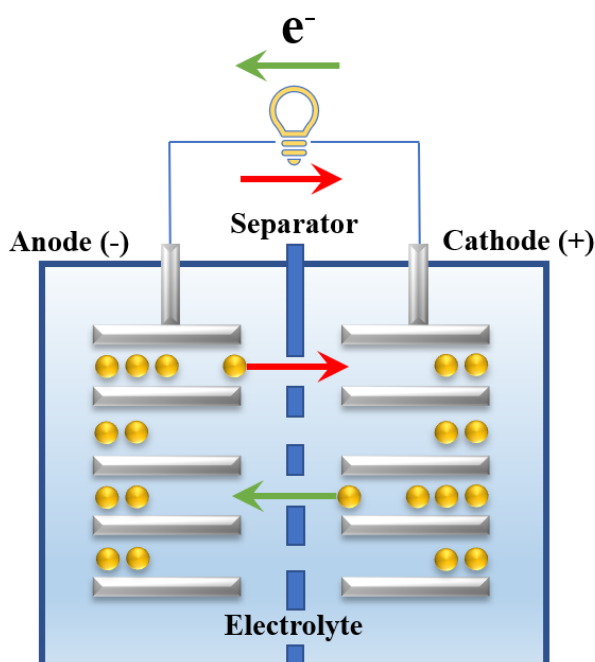


***Figure 3.6.*** *Schematic image of a battery system utilizing intercalation and de-intercalation of alkali-metal cations. Yellow spheres symbolize metal cations. Arrows show the direction of the cations and electrons movement during discharge (depicted as red arrows) and charge (depicted as green arrows).*

There are several different ways of battery classification. One of the most general divides these devices according to their capability to get recharged. Batteries, which are not designed to be repetitively used are known as primary batteries, while the cells, which can be periodically charged and discharged are called secondary batteries. The battery systems can be also grouped according to the type of the electrolyte used. One can distinguish cells utilizing the electrolyte in a solid or liquid state. The latter can be further split into non-aqueous and aqueous solutions.[104] A common practice of naming different types of battery directly refers to electrolytes, which they contain, charge carriers which they use, or material which they are made of.[108,109,110,111,112] In this thesis, a focus is put on the aqueous Na-ion batteries using the so-called Prussian Blue Analogs (PBAs) as the electrode material.

### 3.5.2 Prussian Blue Analogs as Electrode Materials for Na-Ion Batteries

Prussian Blue is known as one of the oldest synthetic chemicals. Its general chemical formula can be depicted as $AM[Fe^{III}Fe^{II}(CN)_6]$, where AM stands for alkali-metal cations. This coordination compound forms a face-centered cubic (fcc) open framework structure with iron(III) and iron(II) ions placed on the alternate corners. The Fe ions in the corner-shared octahedra are linked by conjugated cyanide anions $(C{\equiv}N^-)$, where the high-spin ferrous ions $(Fe^{II})$ and the low-spin ferric ions $(Fe^{III})$ are connected to the N and C atoms, respectively. The $Fe^{II}$ centers can be replaced with other transition metal $M^{II}$ ions (e.g., Ni, Co, Cu, Mn) or even with whole compounds (e.g., $VO_x$) (see **Figure 3.7**).[113,114,115,116,117,118,119] The materials obtained this way are classified as PBAs.
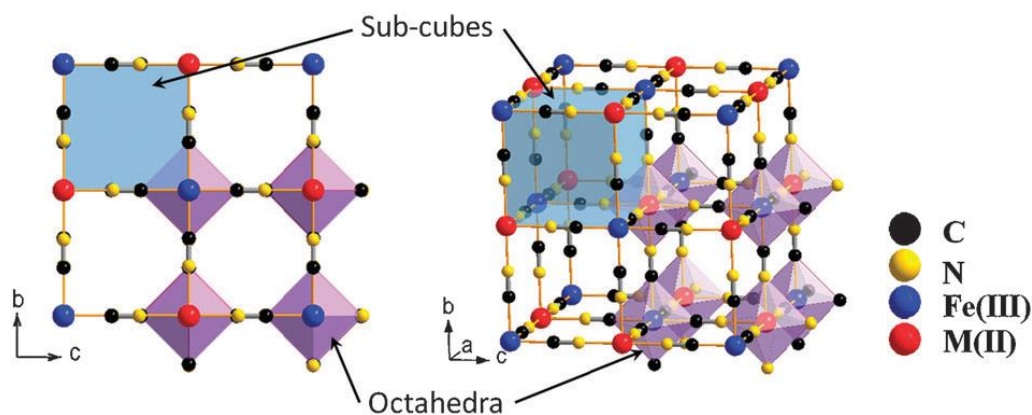


**Figure 3.7.** *Schematic representation of the framework of a Prussian Blue Analog. Taken from reference 114.*

The particular arrangement in the structure of both the Prussian Blue and its analogs results in a formation of relatively huge, open ionic channels. This allows alkali-metal cations to move into and from the material structure. The quasi-reversible insertion and extraction of cations (or other guest molecules) into and from the structure of host solids are known as intercalation and deintercalation, respectively.[120,121] Intercalation and deintercalation are of crucial importance for the Na-ion battery systems. Generally speaking, while charging a battery cell, the cations are deintercalated from the structure of the cathode material. Then, they move towards the anode side where they get intercalated again. The process is reversed during discharging (**Figure 3.6**).[122] Both intercalation and deintercalation take place as a result of reduction/oxidation of $Fe^{III}/Fe^{II}$ ions in the framework of PBAs. The occurrence of the electrochemical reaction and the resulting electron flow make it possible to use this type of compounds as battery electrode materials.[113,123,124,125,136] The technology utilizing the PBAs as the electrode material appears to be particularly beneficial among the other known alternatives.[126,127,128,129,130,131] The main benefits of the batteries containing these compounds are that they are relatively cheap and simple in production, have good energy density and high durability.[32,132,133,134,135,136,137]

### 3.5.3   Intercalation Mechanism

The general scheme of the electrochemical reaction taking place in a typical PBA may be expressed as follows:[12,126]

$$AMNi[Fe^{III}(CN)_6] + AM^+ + e^- \rightleftarrows AM_2Ni[Fe^{II}(CN)_6] \qquad \textit{Eq. 3.19}$$
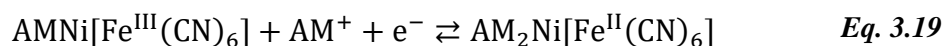
The one-step mechanism presented above can briefly explain the electrochemical reasons for the insertion and extraction of the cation into and from the structure of the PBA electrode discussed in **Section 3.5.2**. One can see that in this very simple model, electrolyte constituents are not considered to have any remarkable contribution to the entire course of the processes. However, the simplicity of (de)intercalation was recently brought into question. As shown by Yun et al. and Ventosa et al., the real mechanism of cation (de)intercalation in the systems utilizing the PBA as a cathode material consists of at least three quasi-reversible stages.[12,138]

Based on the impedance studies, the authors propose the following scenario of the whole process (hereunder presented for deintercalation):[12]

(i) In the first step, $Fe^{II}$ gets oxidized. Because of the high electronic conductivity of the PBA, this stage can be considered as relatively fast:

$$AM_2Ni[Fe^{II}(CN)_6] - e^- \rightleftarrows AM_2Ni[Fe^{III}(CN)_6]^+ \qquad \textit{Eq. 3.20}$$
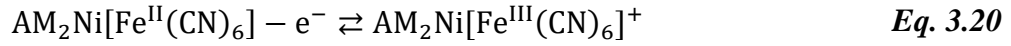
(ii) As actual deintercalation of the alkali-metal cations occurs quite slowly, the short-time excessive positive charge is generated at the electrode surface. This results in the specific adsorption of the counter electrolyte species, such as anions (depicted as AN), compensating the excess surface charge:

$$n(AM_2Ni[Fe^{III}(CN)_6]^+) + AN^{n-} \rightleftarrows (AM_2Ni[Fe^{III}(CN)_6])_nAN \qquad \textit{Eq. 3.21}$$
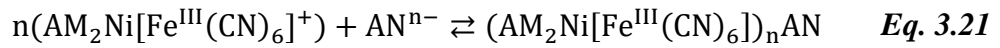
(iii) Finally, as a part of the last step, the alkali-metal cations and the specifically adsorbed anions leave the electrode surface:

$$(AM_2Ni[Fe^{III}(CN)_6])_nAN \rightleftarrows nAM^+ + AN^{n-} + nAMNi[Fe^{III}(CN)_6] \qquad \textit{Eq. 3.22}$$

Unlike the scheme depicted in **Eq. 3.19**, the three-stage mechanism presented above underlines the vital role played by the electrolyte components during the entire course of the alkali-metal cation (de)intercalation.[126] A careful examination of the multiple-step process reveals that some kinetic characteristics of cation insertion into and removal from the electrode structure might show sensitivity towards the nature of the species present in the electrolytes. As further shown by Yun et al., this is indeed the case for the Na-ion battery systems. Different properties of both the negatively and positively charged species have a significant impact on the interfacial charge and mass transfer. According to the authors, the observed changes likely originate from the different hydration energies of dissimilar electrolyte constituents. This clearly shows that the composition of the solution used in battery cells has a substantial effect on their overall performance.[12]

## 3.6 Electrified Solid/Liquid Interface

### 3.6.1 General Model

It has been experimentally proven that the behavior of the interface formed between the electrode and electrolyte resembles the behavior of a capacitor. Hence, after applying a potential to the system, the charge typically separates between the metal electrode ($q_M$) and the solution ($q_S$). Regardless of the actual sign of the excess charge at the metal electrode surface (being a function of the potential, the electrode material, and the electrolyte composition), the following expression is valid:[47]

$$q_M = -q_S \qquad \textit{Eq. 3.23}$$

The charge at the metal surface can be interpreted as an excess or deficiency of electrons. Because of the high conductivity inside the metal, the extended (or contracted) space charge-region is located in the outer thin layer of the metal electrode. An excess of ions carrying a charge with the sign opposite to the sign of the electrode surface charge (expressed as $q_S$) will be localized on the electrolyte side of the formed phase boundary. Assuming full hydration of the ions, the separation of the charged layers is equal to one half of the diameter, $d$, of the hydrated ions (see **Figure 3.8A**). This model of the electrochemical interface was proposed by Helmholtz and is commonly recognized as the Helmholtz layer model.[139]

Considering the thermal motions of the ions and their consequences in terms of loosening the compact ion layer, the Helmholtz model appeared to be insufficient. The issue regarding the temperature-driven movement of the ions near the electrode surface was considered by L. G. Gouy and D. L. Chapman. According to the model developed by them, positively and negatively charged ions coexist in an extended region nearby the electrode surface, in the so-called diffuse layer. Furthermore, near to the surface, there is a surplus of the ions carrying the charge opposite to the electrode charge in comparison to the scarcity of ions of the same charge (**Figure 3.8B**). This image of the interface, however, does not consider the existence of the Helmholtz layer.[139]
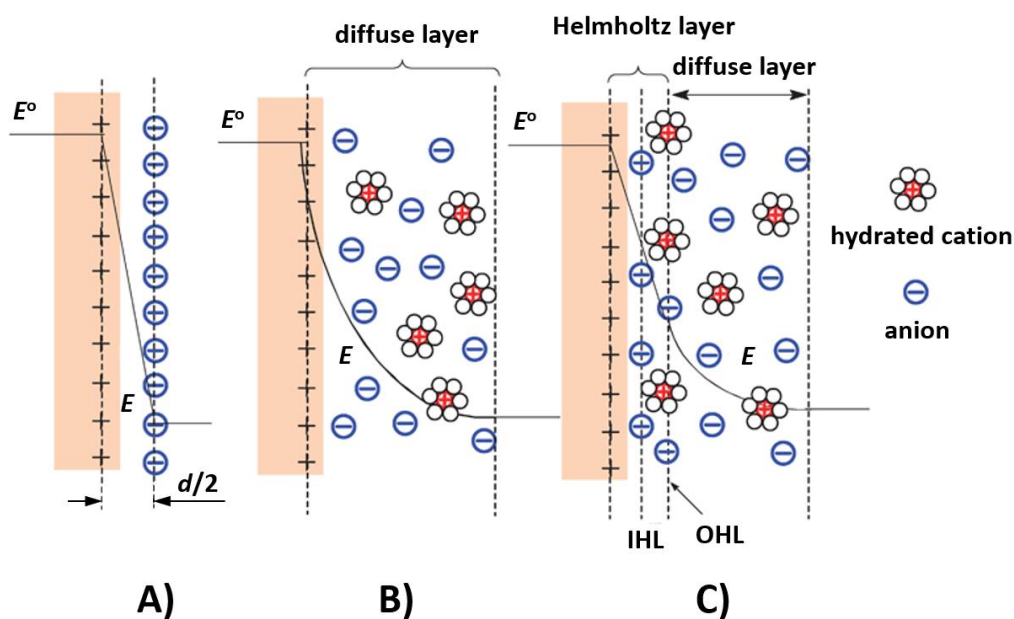
***Figure 3.8.*** *Schematic illustration of the electrified solid/liquid interface: (A) Helmholtz layer model, (B) diffuse layer model, (C) combination of Helmholtz and diffuse layers. The thickness of the interface depends on the ionic strength of the solution, and is inversely proportional to the electrolyte concentration. Adapted from reference 140.*

It was O. Stern who suggested that the most plausible model of the interface is a combination of the two mutually exclusive models. Moreover, according to Stern, some ions may (partially or entirely) lose their hydration shell and, as a consequence, get very close to the electrode surface (**Figure 3.8C**). Such a phenomenon is called specific adsorption, and it can take place through van der Waals forces, Coulombic forces, or even by establishing strong chemical bonds (chemisorption). The plane consisting of the specifically adsorbed ions is defined as the inner Helmholtz layer (IHL). Adequately, the outer Helmholtz layer (OHL) will be constituted by the ions (strictly speaking their centers), which stayed hydrated. Species adsorbed in such a way are known as non-specifically adsorbed. Because of the solvent sheath, the interactions between these species and the charged metal surface are limited to the long-range electrostatic forces.[139]

In reality, all the species present in the electrolyte can undergo the specific adsorption. Its strength, however, can vary depending on the alteration in the electrode potential. Nonetheless, because the anions tend to interact with the electrode through the van der Waals forces, they can adsorb at the surface even if its net charge is negative (**Figure 3.9**). As the specific adsorption of an anion requires at least partial removal of its hydration shell, one can expect that the metal-anion interactions will be stronger for the species with lower hydration

energies.[139] The entire arrangement of solvent molecules and charged ions present in the electrified solid/liquid interface is known as the electric double layer (EDL).[47]
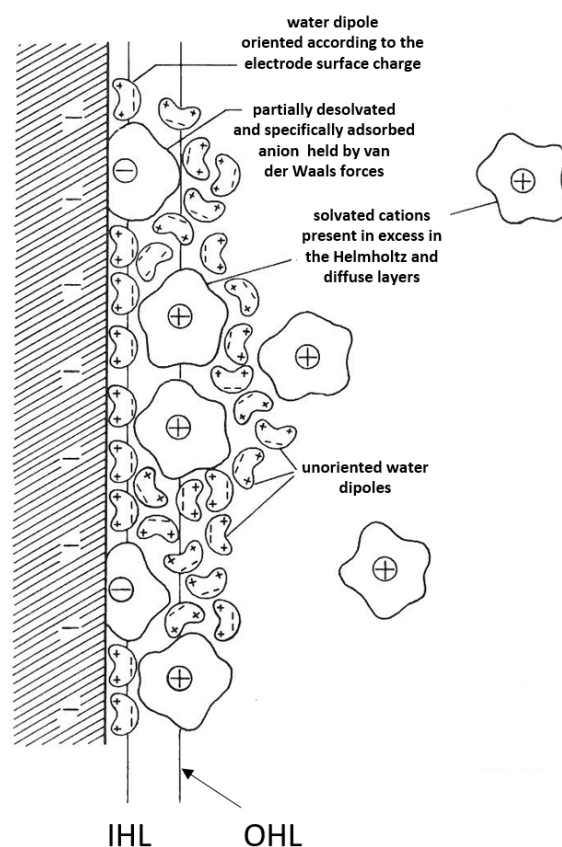


*Figure 3.9. Representation of the generally accepted model of the electrified solid/liquid interface depicting ions and solvent molecules. Adapted from reference 139.*

### 3.6.2 Interfacial Water Layer

In the absence of the specifically adsorbed ions, solvent molecules present at the electrode surface constitute the first layer of the EDL.[141] Thus, the water-electrode interplay is one of the key factors influencing the behavior of the electrochemical systems.[45] Over the decades, the topic concerning the interactions between water and metal surfaces has gathered particular attention of the scientific community both from the fundamental and applied perspective.[142,143,144] To this date, the comprehension of this subject is of crucial importance for various disciplines involving physics, chemical physics, heterogeneous catalysis, biochemistry, electrochemistry, surface science, or corrosion.[145,146,147,148]

In fact, metal surfaces interact with water molecules relatively weakly. Based on DFT calculations performed for single water molecules on monocrystalline (111) surfaces, the calculated energy values are between -0.1 and -0.4 eV. Furthermore, according to the DFT studies, the adsorption energies of the most commonly used metals increase according to the following order: Au < Ag < Cu < Pd <Pt < Ru < Rh. A single $H_2O$ molecule tends to bind to a metallic surface through its oxygen atom at a top site. Also, the distance between such a molecule and the topmost metal layer is much bigger than distances usual for chemically adsorbed species.[149]

It has been found that on the hexagonally close-packed surfaces of transition metals, which strongly interact with the solvent molecules (i.e., Ru, Rh, or Ni), water tends to form an ice-like structure (**Figure 3.10A**).[145,147] It is a bilayer structure similar to the layer of ice.[149] In this network, every second solvent dipole is aligned parallel to the surface, while its oxygen atom is bound to a top site of the metal. The other dipoles can orient themselves either with the H atom pointed towards or away from the metallic surface.[145] These structures are commonly known as ''H-down'' and ''H-up'', respectively. On the close-packed metals, both configurations are energetically alike. Interestingly, at the surfaces of less noble metals interacting more strongly with the water molecules (e.g., Ru), a half-dissociated solvent layer is supposed to be more stable. In such a configuration, every second dipole is dissociated to OH.[149,150,151] However, in the light of substantial barriers inhibiting its formation, the existence of the half-dissociated bilayer might be called into question.[152,153] In opposite to the aforementioned metal/water interfaces, the ice-like structure is not expected to be observed at the surfaces of weakly interacting metals (i.e., Au or Ag).[145,147] Due to its wide application in electrocatalysis, the Pt-water interface is especially important. In this case, the electronic structure of platinum is barely affected by the presence of water.

Because of the presence of the strong electric field, adsorption of ions, as well as differences in temperature and pressure, the solvent structure becomes even more complex in the electrochemical interfaces.[154] On the basis of the existing models, the water dipoles in the EDL exhibit an ''oxygen-up'' and ''oxygen-down'' average orientation. The former exists on negatively charged surfaces, while the latter on the positively charged ones. According to the classical perspective on the electrochemical interface, at the potentials lower than the potential of zero charge (PZC; potential at which the net electrode charge changes its sign, see **Section 3.6.3**), the $H_2O$ molecules orient their dipoles directly towards the electrode interacting with its

surface through hydrogen atoms.[155] This model was further complemented by including water-water (i.e., H-bonds) and water-metal interactions.[156,157,158] As suggested by Thiel et al., the actual molecule-surface interplay at the potentials below the PZC is more complex.[145] Admittedly, each $H_2O$ molecule is oriented with both H-atoms somewhat closer to the electrode surface than the O atoms. However, the oxygen atoms still interact with the metal via lone-pair electrons (see **Figure 3.10B**). Interestingly, at the potential values around the PZC, solvent dipoles lay nearly flat at the surface (**Figure 3.10C**).[159,160] This is the reason why at these potentials and at the potentials slightly higher than the PZC, interfacial water can also form the ice-like structure (see **Figure 3.10A**). However, as for the uncharged surfaces, the ability of the solvent adlayer to rearrange this way depends strongly on the electrode material.[154] Finally, at the potentials significantly higher than the PZC, water dipoles orient themselves with the oxygen part towards the electrode and the hydrogen atoms directed opposite to the surface (see **Figure 3.10D**).[161]
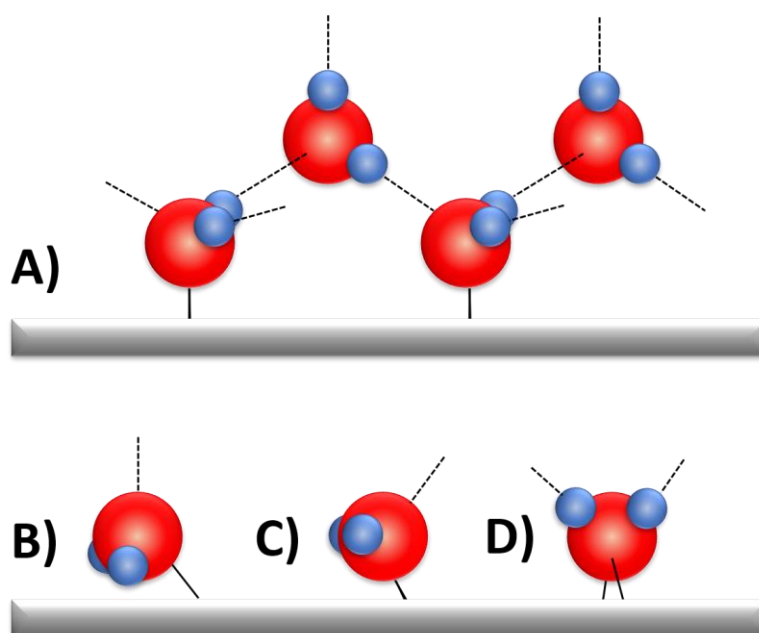


***Figure 3.10.*** *Orientation of interfacial water molecules. (A) Ice-like water structure and the most plausible orientation at potentials: (B) lower than the PZC, (C) around the PZC, (D) more positive than the PZC (for more information regarding the PZC see **Section 3.6.3**). Adapted from references 161 and 162.*

### 3.6.3 Potential of Zero Charge and Potential of Maximum Entropy

The PZC mentioned in the previous section is one of the most important energetic parameters characterizing the metal electrode interface. It is commonly defined as a potential at which the electrode surface exhibits no excess charge.[104,163,164,165] The PZC was introduced by Frumkin in 1928,[166] and since then it is vital for a detailed understanding of phenomena taking place at the EDL (e.g., adsorption of charged and uncharged species) and their kinetics.[163,164,165] It also plays an important role in physicochemical mechanics of solids, photoemission, and electron transfer at the interface. Introduction of the concept of the PZC enabled to, for instance, measure or compute the absolute electrode potential.[104] For transition metals, the PZC is closely related to their work function. The relation can be expressed in the following equation:[167]

$$E_{\text{PZC}} = \frac{\Phi}{e_0} + K_{\text{S}}$$

*Eq. 3.24*

where $\Phi$ stands for the work function, $e_0$ is the electron charge, and $K_{\text{S}}$ is a constant representing the influence of the solvent on the $E_{\text{PZC}}$ of a given electrode. The existence of the direct dependence between the PZC and the work function builds a direct connection between electrochemical surface science and classical surface science.[164,168] The value of the PZC depends on the electrode and electrolyte composition, as well as on electrode surface crystallography and defectiveness.[104]

Although the definition of the PZC seems to be clear, one can encounter difficulties arising from the ambiguity of the concept of the electrode charge. The problem becomes particularly complex in the presence of adsorption processes involving charge transfer which can occur at the electrode/electrolyte interface (a phenomenon commonly observed for Pt and Pt-group metals). In order to overcome this issue, definitions of two PZC types have been introduced:[163,164,165,169]

1. The potential of zero free charge (PZFC), defined as a potential at which the free, electronic net charge density of the electrode surface is zero.
2. The potential of zero total charge (PZTC), defined as a potential at which the sum of the free, electronic net charge density, as well as the charge density transferred during reversible adsorption processes, are zero.

Clearly, for an ideally polarizable electrode, both concepts coincide. This is because of the fact that no charge transfer associated with adsorption takes place. However, for the Pt-group metal electrodes, these two values differ from each other. Hence, in cases of metals adsorbing hydrogen or oxygen, the PZTC exhibits a pH dependence.[104,165] Noteworthy, only the PZTC can be obtained experimentally (thus, in the following sections of this thesis, the PZC stands for the PZTC).[164]
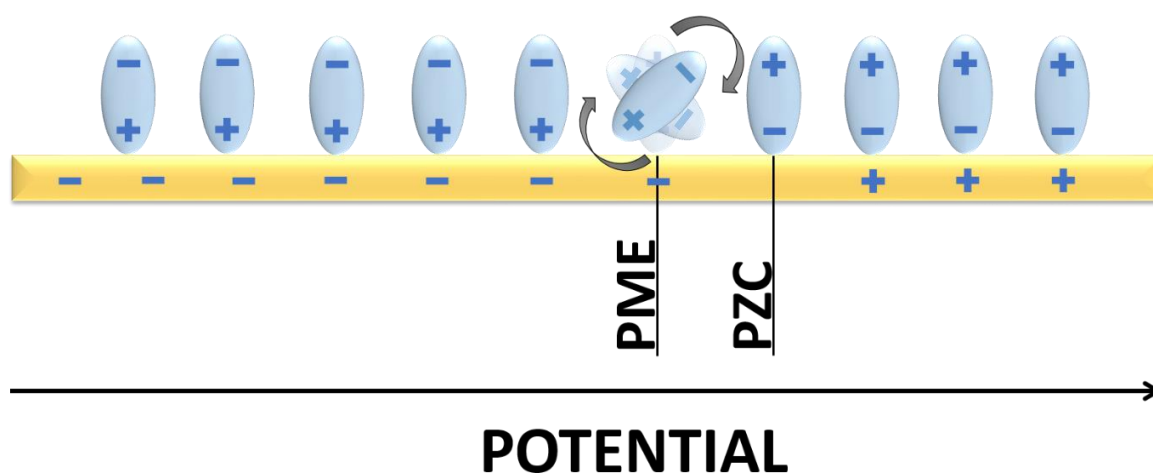


*Figure 3.11*. *Simplified schematic of the water dipoles orientation towards the metal surface according to the surface charge in aqueous electrolytes. The potential at which there is a maximum disorder in the interfacial layer corresponds to the PME, while the PZC represents the potential at which the net surface charge equals zero. In most cases, the PZC and PME of metal electrodes are located close to each other. Adapted from reference 45.*

The potential of maximum entropy (PME) is another parameter of paramount importance for the electrode/electrolyte interface and processes taking place at it. The PME is commonly defined as a potential at which the entropy of the double layer formation reaches its maximum. This state is achieved when there is maximum disorientation in the solvent layer at the electrode surface. The PME is expected to be located close to the PZC (see **Figure 3.11**). For instance, for mercury or gold electrodes immersed in aqueous solutions, the PME has a slightly more negative value than the PZC.[170] The observed difference between PZC and PME results from the specific interactions between water molecules and (uncharged) metal surfaces preventing solvent dipoles from a full reorientation.[141] This phenomenon occurs most likely due to a strong directional bond formed between the oxygen atom and unoccupied d-orbitals of the transition

metal surface.[144] Thus, a negative charge at the electrode surface is necessary in order to reach a maximum disorder in the double layer.[171] The knowledge of the PME is especially useful in the assessment of stiffness of the interfacial water layer. For instance, this is found to be the main cause of energy barriers affecting the charge and mass transfer through the interface.[46,172]

Interestingly, species specifically adsorbed at the electrode surface may also affect the water-metal interactions. Hence, up to a certain extent, the PME is also expected to exhibit sensitivity to the PZC.[141]

## 3.7    Modification of the Electrocatalytic Activity

Understanding the behavior of electrode/electrolyte interfaces is of great importance for applications in various branches of chemistry.[173] The idea that the interface structure governs the activity towards a certain electrocatalytic reaction dates back already to the middle of the last century when Breiter[174] and Frumkin[175] published first articles on this topic. Since that time, numerous studies have been conducted in order to better comprehend interactions between the electrode surface and the reaction intermediate, as well as their consequences for the kinetics and mechanism of electrocatalyzed processes.[99,176,177,178,179,180,181] This often complex interplay appears to be crucial for the activity and selectivity of the reactions taking place in electrochemical systems. In the following sections, special attention is paid to three main parameters having a massive impact on the system performance, namely the electrode composition, the electrode surface structure, as well as the composition of the electrolyte.

### 3.7.1    Influence of the Electrode Structure

Since Taylor's statement was published (see **Section 3.3**),[63] the identification of the active sites at which certain reactions take place became one of the main goals in the heterogeneous electrocatalysis. It turned out that the successful recognition of these centers would likely allow further optimization of electrocatalysts, as well as the development of new electrocatalytic materials with the highest possible density of the active sites at the surface. On the basis of the aforementioned ideas, two main ways of boosting the electrocatalytic activity have been

developed: (i) modification of the electrode morphology and (ii) modification of the electrode composition.[182] The first approach focuses on maximizing the number of active centers by introducing certain facets or defects (i.e., steps, kinks, vacancies) into the structure of the electrode surface.[66,183] This plays a vital role for the structure-sensitive reactions. Studies aiming at the identification of active sites usually focus on single-crystal surfaces. The choice of model surfaces with a known surface atoms arrangement makes it easier to assess the contribution of different facets to the observed activity. This is of crucial importance for the further development of the "real-world electrocatalysts", which are typically used in the form of extended porous surfaces or nanoparticles immobilized on an electronically conductive carbon support.[99,184] The second approach to increase the activity of an electrocatalytic material is based on the alteration of its composition by creating alloys of various metals.[62,65] This way of increasing the electrocatalyst activity is discussed in **Section 3.7.2**.
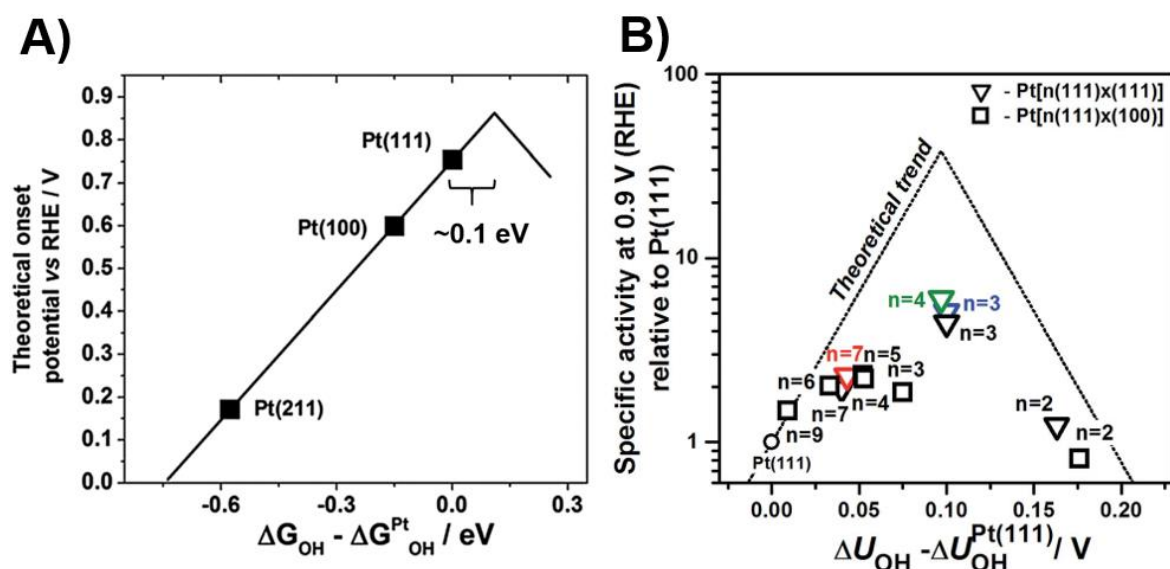


*Figure 3.12. (A) ORR on Pt(111), Pt(100), and Pt(211): theoretical volcano plot. Adapted from reference 66. (B) Experimental volcano plot recorded for Pt(111) (depicted as a circle), Pt[n(111) × (111)] (depicted as triangles), and Pt[n(111) × (100)] (depicted as squares) electrodes. The plot is taken from reference 185; however, the data points shown in black are taken from reference 66.*

Consider the oxygen reduction reaction. Using the binding energy of the $OH_{(ads)}$ as the reactivity descriptor in the Sabatier-type volcano plot, one can see that, for the pure Pt(111) surface, its value is almost optimal.[23,186] Nonetheless, in order to reach the tip of the activity plot, the binding energy of the active sites, situated mainly on-top of the Pt(111) surface atoms,[187,188,189,190,191] should be decreased by ~0.1 eV (**Figure 3.12A**).[66,192,193] It has been

shown that for some platinum stepped monocrystalline surfaces, the ORR activity increases in comparison to Pt(111). For instance, the ORR activity exhibited by some stepped surfaces, such as Pt(221) or Pt(331), highly outperforms the activity of the low-index platinum electrocatalyst in acidic media (**Figure 3.12B**),[66,194] surpassing even some platinum alloys.[194] This appears surprising considering that reduction of the surface atom coordination typically increases the binding energy.[195] In other words, undercoordinated sites (e.g., steps) are supposed to bind the reaction intermediates more strongly than sites located at (111) terraces (see **Figure 3.12A**).[66]

The increased electrocatalytic activity of stepped surfaces might suggest that the defects are responsible for the improvement in the overall electrocatalyst performance.[194,196,197,198] The activity of these surfaces, however, does not rise linearly with step density. For instance, as shown in **Figure 3.12B,** the Pt(110) surface (depicted as Pt[n(111) × (111)] with n = 2), known for having the highest step density, shows the activity only slightly higher than that recorded for Pt(111).[66] Furthermore, the activity of Pt(110) is much lower than those recorded for the aforementioned Pt(221) and Pt(331) surfaces (depicted as Pt[n(111) × (111)] with n equal to 4 and 3, respectively) characterized by lower step densities.[188]

These seemingly contradicting experimental findings can be understood through the prism of increased destabilization of $OH_{(ads)}$ on stepped surfaces. While in the ORR the effect of strongly adsorbing oxygen on the structure of hydroxyl adsorbate appears to be negligibly small, the interplay between $OH_{(ads)}$ and $H_2O_{(ads)}$ is significant.[66] As reported by Casalongue et al., one can distinguish two phases of hydroxyl species coexisting at the surface: hydrated and non-hydrated ones.[199] The latter phase is characterized by a weaker bonding of the hydroxyl species at terraces. Furthermore, the $OH_{(ads)}$-$H_2O_{(ads)}$ interactions exhibit sensitivity to the surface structure. That is to say, the tendency of the system to form a certain OH-array depends on the width of the surface terraces. At narrow terraces, there is simply not enough space to form an extended network of hydrated OH. As a consequence, an increased quantity of the non-hydrated hydroxyl species can be detected which results in the improvement of the surface activity towards the ORR.

In search for the explanation of these activity trends, it should not be overlooked that the formation of undercoordinated sites is not the only consequence of generating the surface defects. Instead, by introducing, for instance, steps, one also creates highly coordinated sites located at the bottom of these defects. As suggested by Calle-Vallejo et al., exactly the sites characterized by high coordination numbers are responsible for the observed increase in the

electrode activity. The authors support their statement using the so-called generalized coordination numbers ($\overline{CN}$) – a weighted average of the common coordination numbers of every nearest neighbor atom. This geometric descriptor correlates the electrode activity with the morphology of the electrode surface bridging the gap between the Sabatier principle and the theory proposed by Taylor (see **Section 3.2** and **3.3**).[191,200] The resulting coordination-activity plots provide information about optimal electrode surface sites (see **Figure 3.13**). Interestingly, by using this means, it is possible to explain not only the outstanding ORR activity of the aforementioned stepped surfaces[65,185] but also the activities towards other reactions, such as the HER[200] or CO oxidation.[201]
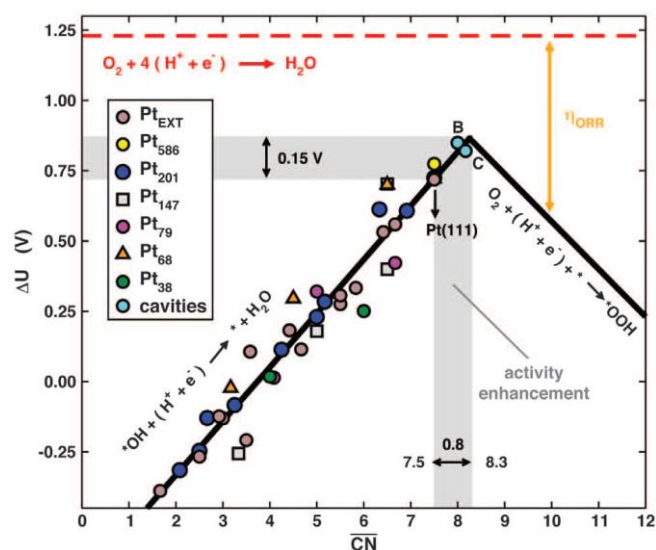


***Figure 3.13.*** *Coordination-activity plot for the ORR on the extended Pt surface and various Pt nanoparticles. The plot represents the $\overline{CN}$ in relation to the potentials of the limiting step of oxygen reduction. The overpotential, $\Delta U$, stands for the difference between the thermodynamic equilibrium of the ORR (1.23 V vs RHE) and potential values recorded for the various Pt electrocatalysts. Note that the optimal catalysts for the ORR possess the $\overline{CN} \approx 8.3$ and adsorb the OH intermediate ~0.15 eV more weakly than Pt(111) (blue points B and C represent two different cavities on Pt(111)). Taken from reference 191.*

Considering the influence of the electrode surface structure on its electrocatalytic activity, it should also be noted that the presence of defects is not beneficial for all kinds of structure-sensitive reactions. For some processes taking place at (100) facets, the existence of steps, kinks, or vacancies will have the opposite effect leading to a decrease in the electrocatalytic activity. Especially, it is the case in reactions proceeding through breaking or forming O-O,

C-O, N-O, or N-N bonds.[181] Ammonia oxidation on Pt can be given as an example. As shown by Rosca and Koper, this reaction involves the formation of ''NH$_2$ fragments''.[202] According to the same authors, the exceptionally high stability of these fragments adsorbed at (100) facets results in the superior activity of Pt(100).[203]

### 3.7.2 Influence of the Electrode Composition

Modifying the electrode composition is another approach to alter its electronic structure and, as a consequence, to tailor the electrocatalytic activity. A common way of changing the electrocatalyst composition is to create its alloys.[62,204,205,206] In the literature, special attention is paid to alloys of Pt with 3d metals and rare earth elements.[193,207,208,209,210,211,212,213] Such a combination can boost the activity by even an order of magnitude in comparison to Pt(111). Due to their excellent performance during the ORR and relatively high stability, bimetallic electrocatalysts are especially promising for applications in FCs.[193,214,215,216] Additionally, the possibility to adjust the content of certain electrocatalyst constituents is another advantage over pure metals.[62,217] This additional degree of freedom appears to be especially important in the process of the catalyst design. A good example showing the usefulness of this approach is the case of the Toyota MIRAI FC car. The optimization of the PtCo catalyst utilized in this car resulted in the ORR activity increase by a factor of 1.8 in comparison to the former model.[218] This improvement allowed the further commercialization of this vehicle.

The changes in the performance of the bimetallic catalysts are mainly recognized as results of three effects:[48,62,204,207,219,220]

> ➢ Ligand effect- arising from the coexistence of two different neighboring metal atoms interacting with each other. As a consequence of these interactions, the electronic structure of the atoms alters affecting the activity of the electrocatalyst.
> ➢ Strain effect- originating from the different arrangement of dissimilar metal atoms present in the crystal structure. The strain can be either compressive or tensile. Its intensity depends mainly on the radius and content of the solute element.
> ➢ Ensemble effect- coming from different characteristics of individual surface atoms or their ensembles. Different atomic arrangements result in different surface properties influencing, for instance, the specific adsorption of electrolyte species.

In most cases, the effects listed above occur simultaneously and co-contribute to the electrode activity. For this reason, it is often complicated to separate them from one another.[207]

As mentioned in the previous chapter, the use of model single-crystal surfaces can be very useful in gaining fundamental knowledge about the system behavior. The simplicity of the low-index planes allows to better predict and comprehend the activity of electrocatalysts. **Figure 3.14** displays a volcano plot representing the relation between the relative activity of the Pt alloy fcc(111) surfaces and the binding energy of the $OH_{(ads)}$ intermediate. One can see that $Pt_3Ni(111)$ exhibits the best performance towards the ORR among the presented surfaces, being about ten times more active than Pt(111). Furthermore, this surface binds the intermediate approximately 0.13 eV more weakly than the monocrystalline Pt surface. In general, it can be seen that creating Pt alloys decreases the OH-binding energy.[62]
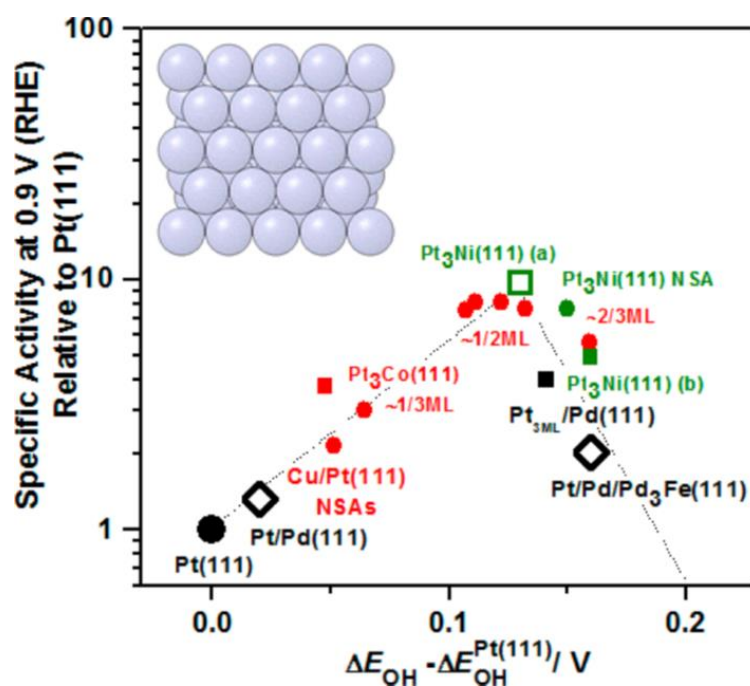


***Figure 3.14.*** *Volcano plot showing the relative ORR activity of different Pt alloy (111) monocrystalline surfaces (at 0.90 V vs RHE) plotted as a function of $OH_{(ads)}$ intermediate in 0.1 M $HClO_4$. Taken from reference 62.*

Consider Pt alloy stepped monocrystalline surfaces. It is not difficult to predict that modification of the surface structure of the bimetallic catalysts will have further impact on their activity. Again, one could expect that introduction of periodic defects into the electrode surfaces is supposed to increase their OH-binding energy and, as a consequence, move the binding

energy values far from the optimum of the volcano plot. However, as displayed in **Figure 3.15**, the platinum alloy stepped surfaces do not exhibit such simple trends. Instead, one can see that the surface activities of the alloy-electrodes increase together with the step density, reaching the optimum value. Then, the activity starts decreasing for surfaces containing a higher number of steps. The elucidation of origins of the presented dependence is not trivial. The issue arises from the difficulty in the distinction between the influence of the introduced defects and the ligand and strain effects. Thus, unlike for low-index alloy planes and stepped pure Pt surfaces (see **Section 3.7.1**), determination of the binding energies of the active sites located at stepped alloy surfaces can be, in many cases, performed only experimentally.[62]
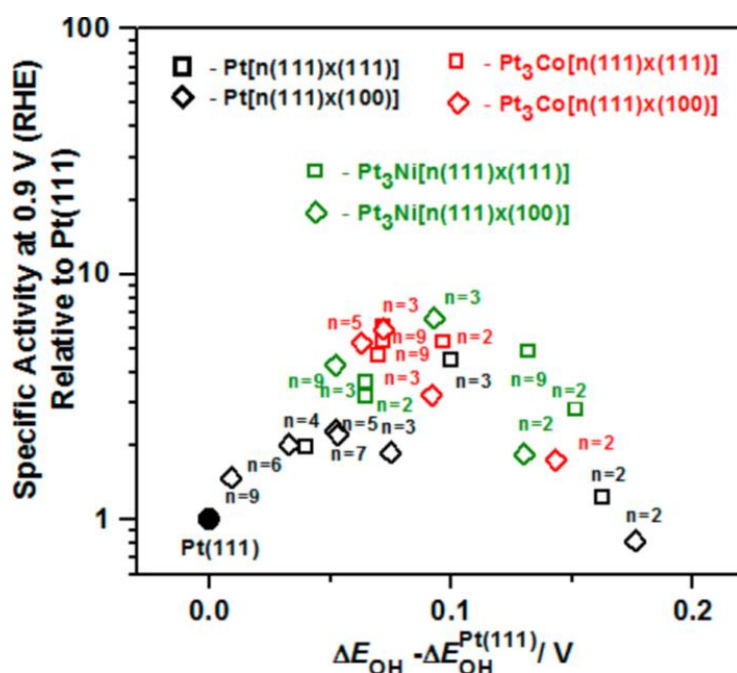


***Figure 3.15.*** *Volcano plot representing the relative ORR activities of various stepped surfaces of Pt alloys (at 0.90 V vs RHE) shown as a function of the binding energy of the hydroxyl intermediate in 0.1 M HClO4. Taken from reference 62.*

In order to accommodate expectations regarding the commercial utilization of electrocatalysts, it is necessary to address the activity of polycrystalline alloy-surfaces and nanoparticles. Unfortunately, the multiplicity of randomly distributed facets, steps, and kinks makes the comprehension of their catalytic behavior much more complicated. Moreover, the existence of numerous defects in these surfaces negatively influences their lifetime. The decreased stability of the catalysts stems from the selective dissolution of less noble metals from their structures generating compressive strains in surface and near-to-surface layers.[221,222] As a consequence, the electrode surface binds the oxygen intermediates more weakly, which affects its activity.[62]

The successful assessment of the electrocatalytic behavior of this type of systems would require a descriptor associated with the binding energies of the reaction intermediates. One of such means could be the so-called "double volcano" plot. In this type of plot, maximal activities of bimetallic catalysts are shown in dependence on the atomic radii of solute elements (see **Figure 3.16**). By creating platinum alloys with various metals of different radii, one alters the strains in the material structure. The existence of two maxima in the double volcano (at smaller and larger atomic radii) implies that there are two optimal atomic radii at which the surface binding energies and, as a consequence, the activities reach their optima. It must be, however, noted that to be able to present the activities in such a way, their values should be related to pure platinum electrocatalysts. Furthermore, to avoid the influence of the electrolyte or the nanoparticle shape, the experimental data should be acquired in solutions containing non-adsorbing species, whereas the utilized nanostructures should exhibit simple forms.[62]
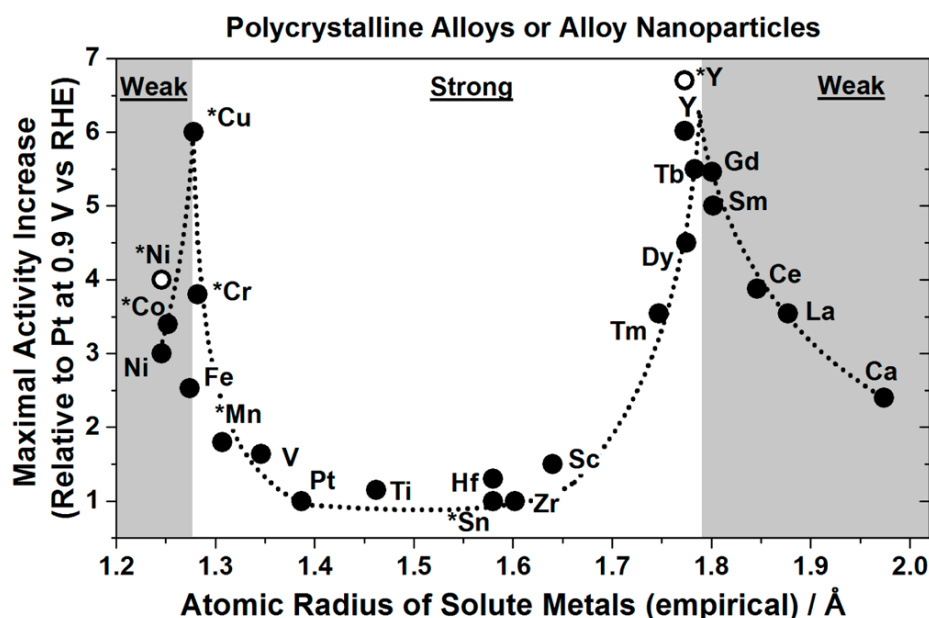


***Figure 3.16.*** *Double volcano plot depicting the ORR activities of polycrystalline platinum alloy catalysts and alloy nanoparticles at 0.90 V vs RHE in 0.1 M HClO₄ relative to pure platinum shown as a function of the radii of solute metals. Asterisks depict nanoparticles. Taken from reference 62.*

### 3.7.3  Influence of the Electrolyte Composition

- **Influence of Alkali-Metal Cations**

Latest studies, both experimental and theoretical, concordantly reveal that the electrolyte composition should be considered as an additional factor influencing the behavior of the electrochemical interface.[223,224,225,226,227] Especially, the effect of alkali-metal cations, such as $Na^+$ or $K^+$, might have been highly underestimated for a long time.[228,229,230,231,232,233] These cations, very often considered as ''spectator species'', are common constituents of aqueous electrolytes widely used in laboratory and industrial syntheses.[234,235,236,237] Already in 1930 Herasymenko and Slednyk observed that the hydrogen overpotential on Hg electrodes depends on the concentration and nature of the metal cations present in the electrolyte.[238] The importance of the cation effect has been further addressed by, for instance, Tokuoka,[239] Frumkin,[240] or Heyrovsky.[241] However, despite remarkable observations resulting from their studies, the subject has not attracted prominent attention of the scientific community. It is only recently that further development of experimental methodologies and a gain in the fundamental understanding of electrocatalytic processes have brought the focus back to the effect of alkali-metal cations.[242,243,244,245,246,247,248,249] It is now clear that the unexpected influence related to the electrolyte composition cannot be interpreted only through the prism of the ''unknown contaminations''.

A good example illustrating the cation effect is the ORR performed on a Pt(111) electrode in various alkaline solutions. One can see that in this case the activity towards the ORR changes in the presence of different alkali-metal cations according to the following trend: $Li^+ < Na^+ < K^+ < Cs^+$ (see **Figure 3.17**).[24]
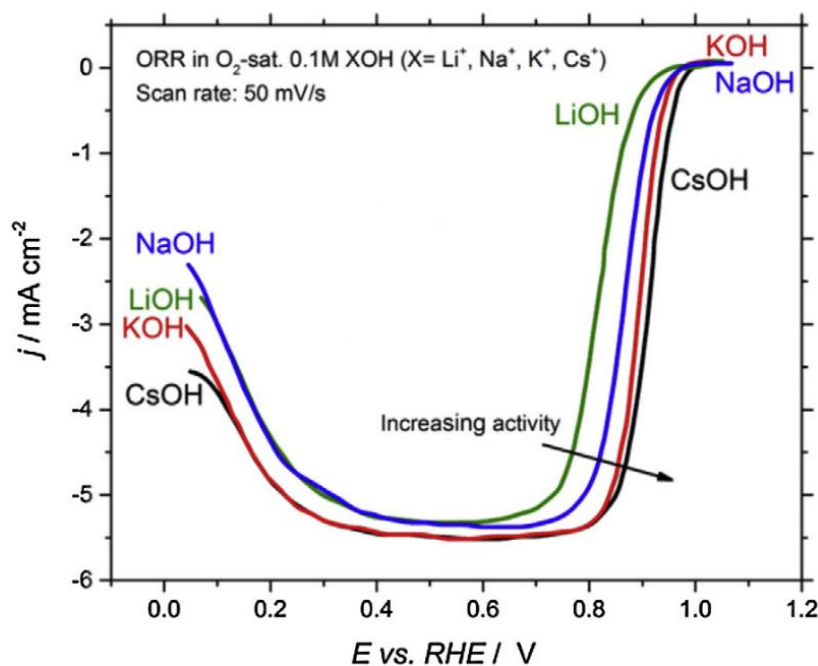
***Figure 3.17.*** *Voltammograms illustrating the influence of various alkali-metal cations on the electrocatalytic activity of the Pt(111) electrode towards the ORR in $O_2$-saturated 0.1 M XOH (X= Li, Na, K, Cs). Adapted from reference 24; original data taken from reference 242.*

The obtained tendency can be explained in the light of $OH_{(ads)}$-Pt interactions. According to Strmcnik et al., the hydroxyl is expected to be stabilized at the platinum surface by the increased charge density between the cations and metal.[244] Then, the hydrated cations interact non-covalently with $OH_{(ads)}$ creating a cluster and stabilizing the adsorbate. The intensity of the cation-hydroxyl strength will, in turn, depend on the hydration energy of the positively charged species. This can explain why the observed activity is the lowest in the case of $Li^+$-containing electrolytes and the highest for the solutions that contain $Cs^+$ cations. Interestingly, the hydration energy can be used as a quantitative descriptor of the cation effect not only in the ORR but also in such reactions as the HOR or methanol oxidation.[24,242,248]

Quite surprisingly, the activity of the Pt(111) surface towards the HER exhibits an opposite cation effect than the activity towards the ORR. As shown by Xue et al., the rate of hydrogen evolution on the monocrystalline platinum electrode is the highest in the electrolyte containing $Li^+$ cations (**Figure 3.18A**).[250] Then, the recorded electrode activity continuously diminishes in the presence of $Na^+$, $K^+$, and $Rb^+$, reaching the minimum in the $Cs^+$-containing solution. As further presented by the authors, the same tendencies are observed for the Pt(221) and $Pt_{pc}$ surfaces with the exception for the RbOH electrolyte in the presence of which the rate of the HER on the Pt(221) electrode is the lowest. The electrolyte effect can be explained in light of

51

the H-binding describing the energy of the surface adsorption of the hydrogen intermediates. According to this theory, different alkali-metal cations interact with the adsorbate more or less strongly, altering the aforementioned H-binding energy.[250]
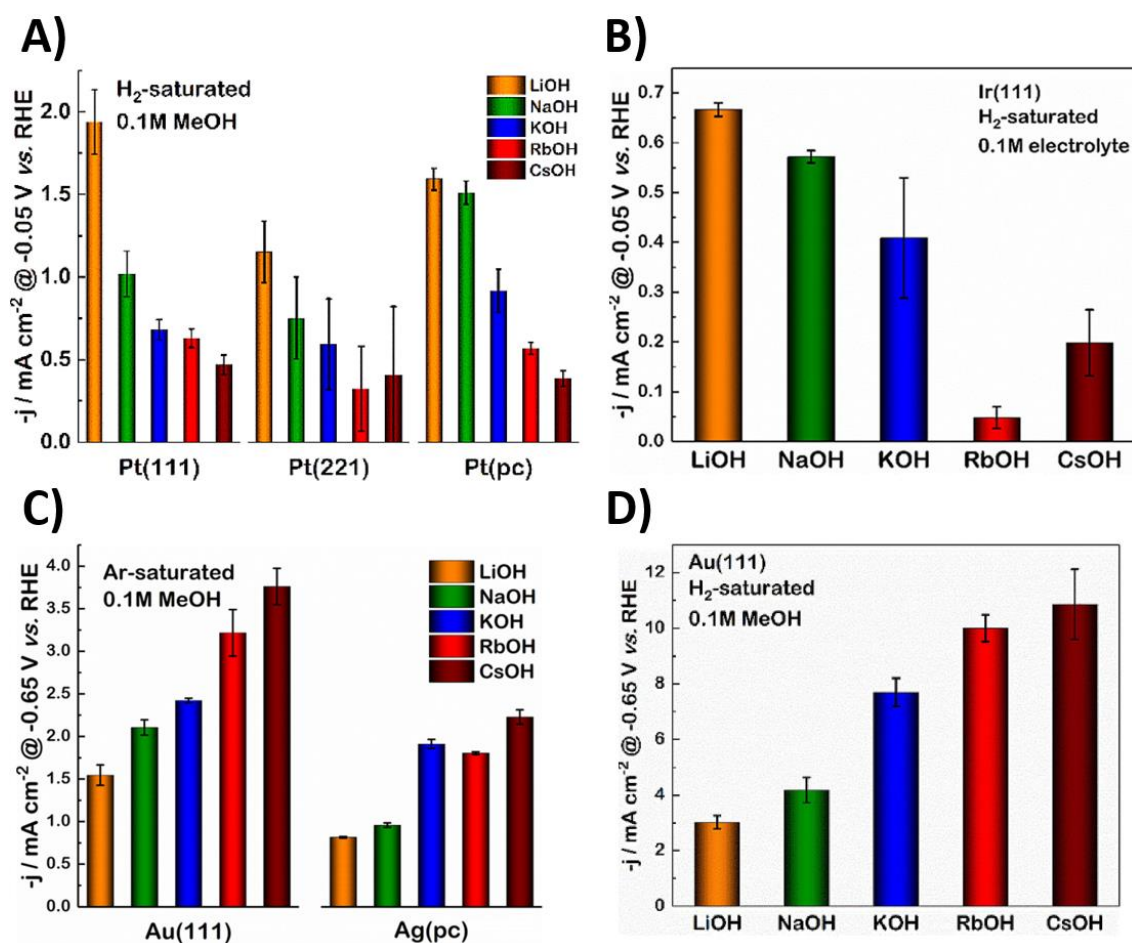


***Figure 3.18.*** *HER activities at -0.05 V vs RHE recorded for the (A) Pt(111), Pt(221), Pt$_{pc}$ surfaces, and (B) for the Ir(111) electrode, as well as at -0.65 V vs RHE for (C) Au(111), Ag$_{pc}$, and (D) Au(111) metal surfaces in (A,B,D) H$_2$-saturated and (C) Ar-saturated 0.1 M alkaline XOH solutions (where X= Li, Na, Rb, Cs). Taken from reference 250.*

Interestingly, the effect appears to change for different electrode materials. While the activity towards hydrogen evolution on the Ir(111) surface follows the same trends as those observed for Pt(221) (**Figure 3.18B**), the analogous measurements performed on Au(111) and Ag$_{pc}$ revealed that the activity towards hydrogen evolution is the lowest in the presence of lithium cations (**Figure 3.18C** and **D**). Then, the activity increases in sodium, potassium, and rubidium hydroxide solutions, reaching the maximum value in the cesium-containing electrolyte. In this case, the electrode-dependent activity variations can also be explained through the prism of the H-binding energies. As reported in the literature, different metals are characterized by different

strength of the reaction intermediate adsorption at the surface.[251,252] Pt and Ir are known for adsorbing the intermediates too strongly, which would place them on the opposite side of an activity volcano plot than Au or Ag characterized by too weak binding energies. As a result, the activity trends will alter for different electrode materials.[250]

The concept that the alkali-metal cations affect the adsorption of reaction intermediates on metal electrodes can be additionally revealed from the blank voltammograms recorded for the Pt(111) electrode. Interestingly, adsorption and desorption of hydrogen occurring at the potentials lower than 0.40 V vs RHE do not appear to be significantly influenced by the nature of the cations. Instead, the effect is noted only at the electrode potentials higher than 0.60 V vs RHE (see **Figure 3.19**) at which hydroxyl and oxygen adsorption takes place. While the onset potential for hydrogen adsorption/desorption is not changed in series from $Li^+$ to $Cs^+$, the peaks representing OH-adsorption and metal surface oxidation (~1.00 V vs RHE) alter.[24,253] The former shifts towards more negative potential values, while the latter one exhibits an opposite tendency.
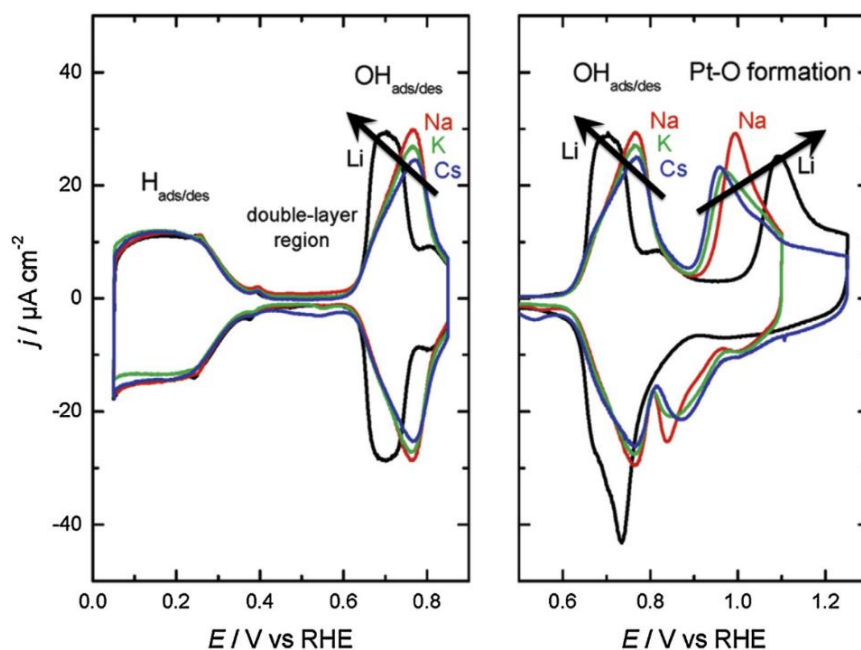


***Figure 3.19.*** *Cyclic voltammograms of Pt(111) immersed in the Ar-saturated 0.1 M XOH (X= Li, Na, K, Cs) solutions. Scan rate: dE dt $^{-1}$ = 20 mV s$^{-1}$. Black arrows depict the peak shift associated with the stabilization of OH$_{(ads)}$. Taken from reference 246.*

Unlike the alkaline electrolytes, the activity of metal electrodes immersed in acidic electrolytes does not exhibit straightforward tendencies. This non-trivial electrocatalytic behavior is attributed to the fact that the acidic solutions often contain species specifically adsorbing at platinum surfaces (e.g., (bi)sulfate anions) and blocking the active sites.[247] The alkali-metal cations can interact with adsorbates, which can generate difficulties in the interpretation of the origin of the electrocatalytic activities. **Figure 3.20** depicts the relation between the nature of the alkali-metals and the electrocatalytic activity towards the HER, ORR, and OER. One can clearly see that the presented relations significantly deviate from those typical for the systems containing alkaline media (see **Figure 3.18**). Furthermore, although there are visible alterations in the shape of the blank CVs obtained in the sulfate solutions (**Figure 3.21**), there is no obvious correlation between the obtained changes and measured activities.[24]
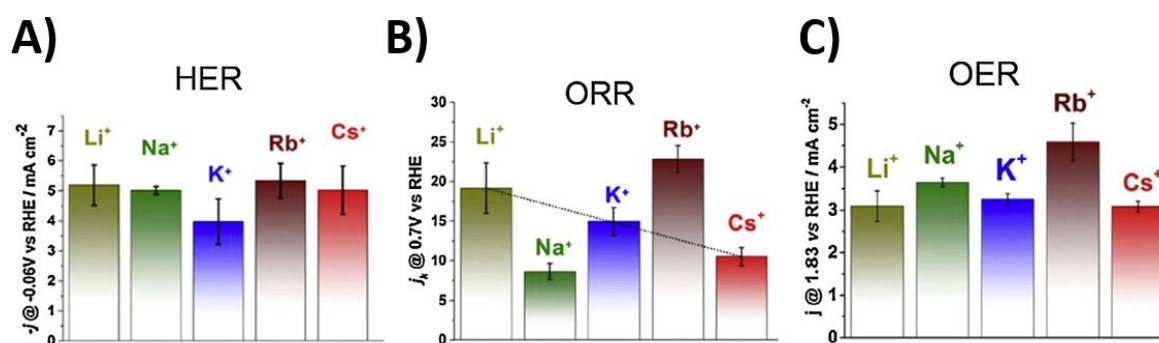


***Figure 3.20.*** *Pt(111) electrodes activity towards the (A) HER, (B) ORR, and (C) OER in electrolytes consisting of 0.05 M $H_2SO_4$ + 0.05 M $X_2SO_4$ (X = Li, Na, K, Rb, Cs). Taken from reference 247.*

The presence of different alkali-metal cations in acidic media also seems to have a minor effect on the $H_{upd}$ and the double layer regions of the recorded voltammograms (**Figure 3.21**). One can, however, notice that in the different sulfate solutions, the potential at which the phase transition in the adsorbed (bi)sulfate layer occurs (visible at ~0.50 V vs RHE) "moves" towards more positive values. The intensities of the corresponding current peaks increase in the presence of dissimilar cations according to the following trend: $Cs^+ < Rb^+ < K^+ < Na^+ < Li^+$. Furthermore, different cations seem to differently influence the layer of the specifically adsorbed (bi)sulfates. The re-arrangements in the adsorbate structure can be seen as a current alteration between 0.60 V and 0.80 V vs RHE (indicated by "*"). Its shift towards more negative potential values reveals the destabilization of the anion adlayer caused by the cations with increasing size.[247]
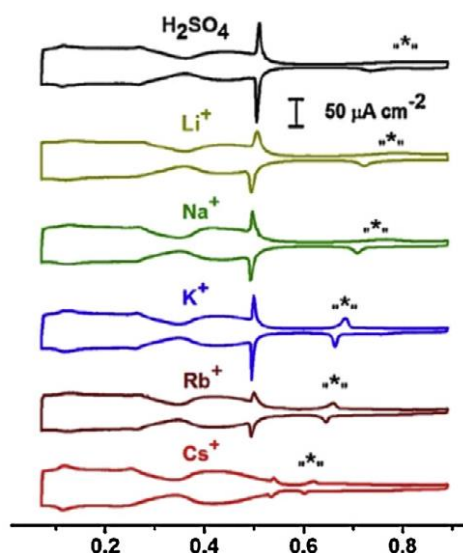
**Figure 3.21.** *CVs obtained for Pt(111) in Ar-saturated solution of 0.05 M $H_2SO_4$ + 0.05 M $X_2SO_4$ (where X = Li, Na, K, Rb, Cs). Taken from reference 247.*

It should be noted that also in the systems containing acidic solutions, the intensity of the cation effect depends on the electrode material. For instance, Strmcnik et al. show that the influence of the electrolyte species on the ORR activity decreases at the monocrystalline gold electrodes. As further claimed by the authors, the observed effect originates from the smaller coverage by hydroxyl at the gold surface, which makes the electrolyte influence less noticeable.[173]

- **Anion and pH Effect**

Since many types of anions have been identified to be poisonous to the catalytic centers, it is often easier to notice their effect in heterogeneous catalysis.[254,255,256,257,258,259] For instance, species, such as $SO_4^{2-}$, are known for their ability to specifically adsorb at the active sites of the platinum surfaces lowering their activity towards many reactions.[260,261,262] The influence of the anions can be seen in **Figure 3.22** representing the HER and OER in acidic media in the presence of $SO_4^{2-}$ and $ClO_4^-$ at Pt and Ir electrodes. While the presence of different anions does not affect the former reaction,[263] it alters the catalytic activity towards the latter one.[264] One can see that perchlorates, known for their weaker adsorption on the metal surfaces, enable better performance of the Ir electrocatalyst during the OER.
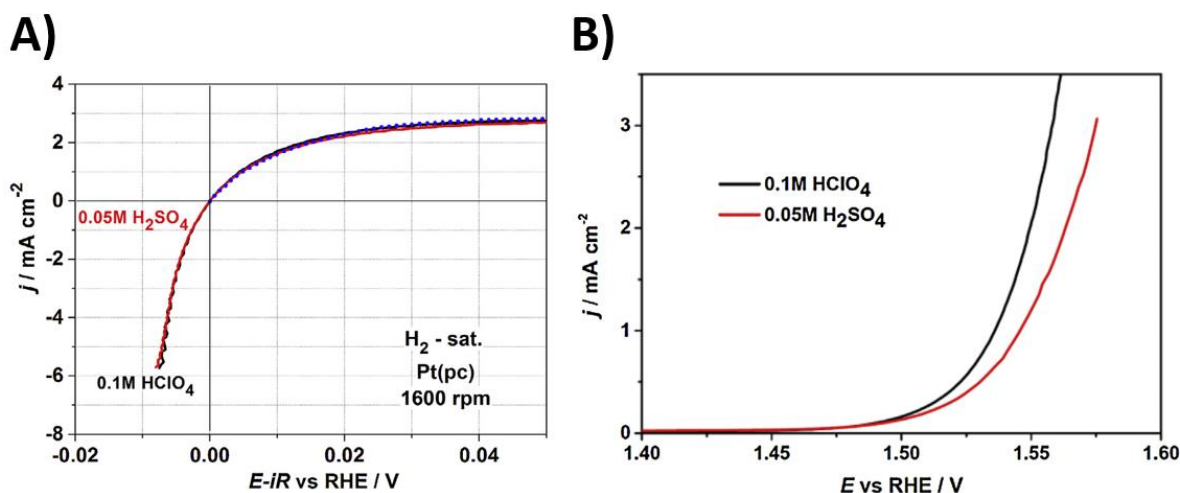
*Figure 3.22. (A) Polarization curves obtained for $Pt_{pc}$ electrodes immersed in $H_2$-saturated 0.05 M $H_2SO_4$ and 0.1 M $HClO_4$ solutions. The dotted blue line represents a theoretical curve for the HOR. (B) OER curves recorded at Ir-oxide thin films in the 0.05 M $H_2SO_4$ and 0.1 M $HClO_4$ electrolytes (pH 1). Taken from reference 263.*

While in many cases the influence of the anions can be foreseen, the interpretation of the pH effect is more complicated.[265,266] Predictably, basic principles portrayed by the Nernst equation should describe processes directly involving hydrogen or hydroxyl species (e.g., HER or ORR).[267] In reality, however, in many reactions crucial for the energy conversion and storage, this basic tenet often does not explain the observed trends.[268,269] For instance, it has been shown that in alkaline solutions, OH-adsorption occurs at more negative potentials than it had been expected.[270] As a consequence, the alkali-metal cations present in the electrolyte interact with $OH_{(ads)}$ more easily leading to an increase in the cation concentration in the vicinity of the surface. This should further hinder the transport of the protons to the interface where the HER takes place and, as a consequence, decrease the reaction rate. Interestingly, the non-trivial pH dependence can be seen both for the HER and HOR. As shown by Sheng et al., the HER gets impeded at higher pH levels (**Figure 3.23A**).[88] A similar effect is observed for the HOR (see **Figure 3.23B**). Also in that manuscript, the authors explain the effect through the prism of the hydrogen binding energies, which likely change for different pHs. The differences in the activity towards hydrogen evolution and hydrogen oxidation might also originate from the changes in the local pH taking place in the near-to-neutral solutions in the vicinity of the electrode surface. As claimed by Auinger et al., in such electrolytes, the supply of $H^+$ gets slower resulting in a lower rate of the reactions.[271] While that theory has been originally developed for the near-to-neutral pH solutions, Li et al. further proved that it could also be

applied for more acidic electrolytes.[272] Interestingly, the change in the local proton concentration has been also recognized as the reason of the pH influence on the ORR activity. As claimed by Briega-Martos et al., in solutions with pH < 7, the onset potential for oxygen reduction at the basal surface gets more positive upon decreasing the concentration of hydrogen.[273]
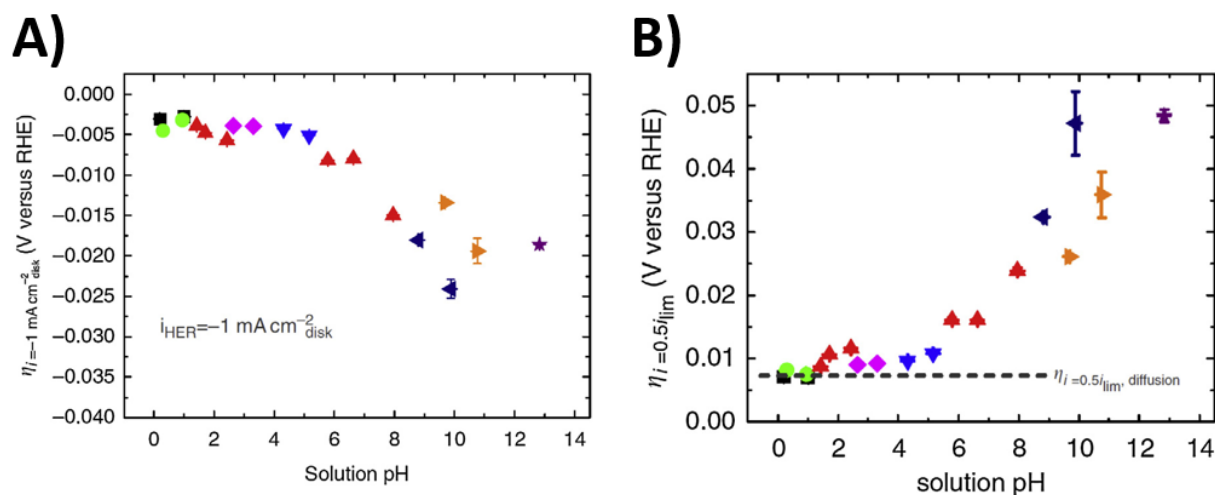


*Figure 3.23. Overpotentials as a function of pH for the (A) HER and the (B) HOR at polycrystalline Pt electrodes. Black squares depict results for 0.1 M and 1 M HClO₄; green circles – 0.1 M and 1 M H₂SO₄; red up-triangles – 0.1 M H₃PO₄ and phosphate buffers; blue down-triangles represent results for acetate buffers; purple diamonds – citrate buffers; navy left-triangles – borate buffers; orange right-triangles – (bi)carbonate buffers; purple stars correspond to values obtained in the 0.1 M KOH solution. Taken from reference 88.*

The pH effect on the electrode activity can also vary for different electrode surface structures. Particularly interesting is the influence of the pH on the activities towards the ORR at stepped platinum surfaces. For example, it was reported that Pt(221) and Pt(331) exhibit the highest activities towards this reaction in the acidic solution (0.1 M HClO₄).[194] Quite surprisingly, however, after immersing the same electrodes in the alkaline media (0.1 M NaOH), their surfaces becomes comparatively least active.[274] The exceptionally outstanding performance of the stepped Pt electrodes in the acidic media can be understood using the binding energies of the hydroxyl intermediate as a descriptor (see **Section 3.7.1**). However, the origin of the decreased activity of the electrode immersed in the alkaline solution might be related to the higher surface coverage by reaction intermediates (i.e., $O_{(ads)}$ and $OH_{(ads)}$) occurring in alkaline electrolyte.[244] An alternative explanation of this effect draws attention to the structure of the

surface water layer, which changes according to the pH level and, as a consequence, affects the electric field.[275]

It should also be noted that, in most cases, model high-pH systems contain alkali-metal hydroxides. Therefore, it is not always easy to differentiate between the pH effect and the influence resulting from the alkali-metal cations. The performance of such systems can be affected by the nature of the cations or by the pH level of the electrolyte used. Nonetheless, the development of relatively simple models describing the observed behaviors is necessary for further comprehension of electrocatalytic processes.[24]

## 3.8 Determination of the Potential of Zero Charge

### 3.8.1 Capacitance Method

The double-layer capacitance method utilizes the fact that the electrode/electrolyte interface can be modeled as a capacitor (see **Section 3.6.1**).[47] As the name suggests, this technique is based on the analysis of the double layer capacitance ($C_{dl}$) as a function of the applied potential. Examination of the $C_{dl}$ can answer specific questions about the structure of the double layer.[276] The sought value can be obtained by performing the electrochemical impedance measurements (**Section 3.9.2**).[277] According to the Gouy-Chapman-Stern model, the reciprocal of the $C_{dl}$ on surfaces of metal electrodes can be shown as:

$$\frac{1}{C_{dl}} = \frac{1}{C_i} + \frac{1}{C_d}$$

*Eq. 3.25*

where $C_i$ is the inner layer capacitance, while $C_d$ stands for the diffuse layer capacitance. The former value is constant, whereas the latter one varies for different potentials applied. In the vicinity of the PZC, the polarization of the interface is small, which results in a parabolic dependence between the $C_d$ and the potential. The potential value at which the capacitance reaches its local minimum corresponds to the PZC (see **Figure 3.24**).[47,276,278] The characteristic "well" is not observed at the potential located far from the PZC where the curve gets flattened.

Furthermore, the presented method of the PZC determination cannot be used for highly concentrated solutions.[47]
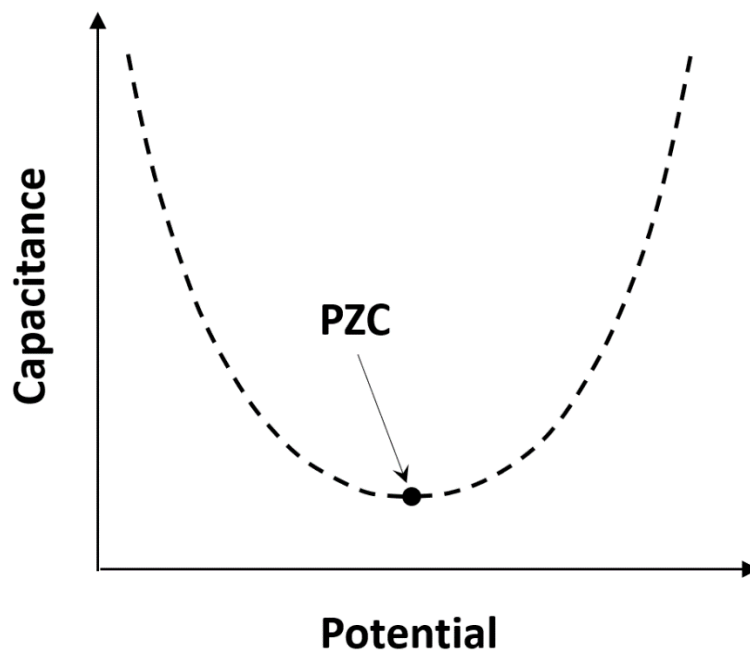


***Figure 3.24***. *Schematic illustration of an $C_d(E)$ graph. The black arrow points to the local minimum in the capacitance which corresponds to the PZC of the system.*

### 3.8.2 CO Displacement

This technique of the PZC determination utilizes the phenomenon of strong CO molecules adsorption on Pt substrates.[279] In this experiment, the potential-dependent charge is measured during the displacement of the EDL with the inert adsorbate.[280]

At the beginning of the measurement, a constant potential is applied to the system, and the solution is purged with CO. Once the saturation coverage is achieved, the current falls to zero. Then, the excess CO is removed from the electrolyte by purging it with Ar. A CV measurement allows testing the degree of surface blockage. Finally, CO molecules are voltammetrically stripped from the electrode. The process of CO adsorption takes place without changing the oxidation state of the adsorbate. Therefore, the charge measured during the adsorption of CO ($q_a$) can be expressed as a difference between the total electrode charges before ($q_i$) and after ($q_f$) adsorption:

$$q_\mathrm{a} = q_\mathrm{f} - q_\mathrm{i} \qquad\qquad \textit{Eq. 3.26}$$

The initial charge is the total charge of the CO-free surface at a given potential of the experiment. In order to determine it, the knowledge of the final charge is required. However, determination of the $q_\mathrm{f}$ is usually far from straightforward. Nevertheless, this value is negligibly small when compared with the initial charge present at the electrode surface before the monoxide adsorption. Therefore, as the first approximation, one can express **Eq. 3.26** as:[281]

$$q_\mathrm{a} \approx -q_\mathrm{i} \qquad\qquad \textit{Eq. 3.27}$$

With such an approximation, the CO displacement can be seen as a direct measurement of the total charge of the electrode surface at an applied potential. By repeating the experiment at different constant potentials (within a regime of $CO_{(ads)}$ stability), or integrating the voltammetric current, a $q$ vs $E$ curve can be plotted.[279,281,282] The point at which $q_\mathrm{i}$ is equal to zero correlates with the value of the PZC.[280]

The CO displacement method can be successfully used to evaluate the relationship between the PZC and different step densities[165,283] or electrolyte pHs.[284] However, as mentioned above, its application is limited to the platinum substrates. Furthermore, the assessment of different local contributions to the PZC coming from terraces and defects is problematic. The total charge measured with this technique can be seen as an average value of positive and negative local values of the charge.[281]

### 3.8.3   N₂O Reduction

As reported by Ebert et al., the irreversible N₂O reduction reaction at monocrystalline Pt surfaces exhibits sensitivity to the structure of the electrode/electrolyte interface.[285] In that work, the adsorbed hydrogen was considered as an essential intermediate species of the reaction taking place according to the following equation:

$$N_2O_{(ads)} + H_{(ads)} \longrightarrow N_{2(g)} + OH_{(ads)} \qquad\qquad \textit{Eq. 3.28}$$
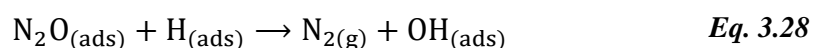
Further studies performed by Attard et al. on different transition metals in various electrolytes refuted this statement.[286] Additionally, they showed that $N_2O$ can be utilized for probing the local surface charge of the electrode. According to the mechanism proposed by that group, the reduction reaction on Pt-group metals is initiated by the adsorption of the $N_2O$ molecule at the metal surface:[281,285]

$$Pt + N_2O \overset{K}{\rightleftarrows} Pt - N_2O_{(ads)} \qquad \textit{Eq. 3.29}$$
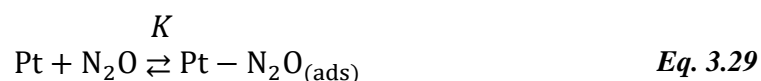
The adsorption step is followed by adsorbate reduction:

$$Pt - N_2O_{(ads)} \overset{k_1}{\rightarrow} Pt - O + N_{2(g)} \quad \text{(slow)} \qquad \textit{Eq. 3.30}$$

$$Pt - O + 2H^+ + 2e^- \overset{k_2}{\rightarrow} Pt + H_2O \quad \text{(fast)} \qquad \textit{Eq. 3.31}$$
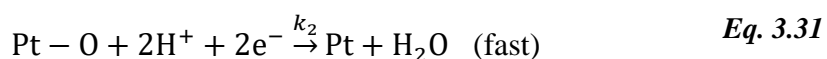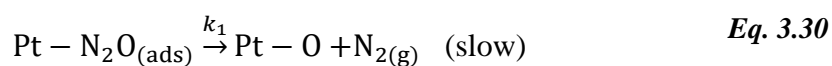
Assuming competitive adsorption of hydrogen, anions, and water at the surface, the rate of the $N_2O$ reduction will be the highest when the amount of free sites available for its adsorption reaches the maximum. Interestingly, on many transition metals (i.e., Pt, Ir, Pd, Rh), the potential at which such a situation occurs is equal or close to the PZC. It should be also noted that adsorption of the $N_2O$ molecules on the Pt surface is extremely weak (~20 kJ mole$^{-1}$).[287] Thus, the existence of the oxide at the surface does not influence adsorption of the other species (i.e., hydrogen and anions). For these reasons, reduction of $N_2O$ can serve as a probe sensitive to the total surface charge.[286]

The method described above is especially useful in the case of the existence of multiple local PZCs. The obtained value can be found as the net sum of dissimilar contributions coming from different parts of the surface.[281]

### 3.8.4 Laser-Induced Current Transients

Application of intense laser light pulses is of crucial importance for electroanalysis. It plays a special role both in activating of the surfaces towards electron transfer, as well as in elucidating the interfacial structure. For instance, McCreery et al. have reported pioneering studies focusing on the application of high-intensity pulses of 1064 nm irradiation to activate the surface of highly ordered pyrolytic graphite (HOPG),[288] glassy carbon,[289,290,291] and platinum.[292] The high power densities remove adsorbed contaminants and restructure the electrode material. In turn, Watanabe et al. have applied the high-intensity pulses of infrared laser light in order to clean gold electrode surface by removing their top layer during the potential sweep.[293]

Probing the electrode/electrolyte interface with short, powerful laser pulses is also a convenient way of analyzing the electrochemical systems.[45,294,295] This method was developed and widely described in the 1980's by Benderskii et al.[296,297,298] In those studies, the authors, for the first time, applied the so-called temperature jump effect to probe the EDL formed between an aqueous electrolyte and a mercury electrode.[299] More recently Feldberg et al. used a similar approach in order to investigate the kinetics of the electrochemical processes occurring on platinum electrodes.[299,300] Climent et al. have also adopted this method; however, they used a lower density light with a wavelength of 532 nm to study the surface charge of Au(111)[295,301] and Pt(111)[302] electrodes. Applying the laser to experiments on the interface rapidly shifts the thermodynamic equilibrium which enables to study the dynamics of interfacial processes. This technique also allows separating the double layer response from the charge transfer processes. This is possible because the high power illumination results in a rapid temperature jump, which is simply too fast for the charge transfer to proceed.[302] Independent studies have shown that for particularly quick processes (e.g., hydrogen adsorption), very high frequencies up to 1 MHz would be needed in order to reach such a separation using the impedance spectroscopy.[303] Taking into account the aforementioned facts, the application of the temperature effect in the examination of the interface of electrochemical systems appears to be particularly useful.

A proper selection of the beam energy and the wavelength of the laser light are important factors to be considered while probing the solid/liquid interface. While too strong laser beams can extensively heat the electrode up or even damage its surface, an incorrectly selected wavelength can result in side effects, such as photoemission of electrons.[301]

Assuming a negligible penetration depth of the light, the temperature change of the electrode surface after a laser illumination can be given as:[295,297,302]

$$\Delta T(t) = \frac{1}{\sqrt{\pi \kappa c \rho} - \sqrt{\pi \kappa_1 c_1 \rho_1}} \int_0^t p(t - t') - \frac{1}{\sqrt{t'}} dt' \qquad \textit{Eq. 3.32}$$

where $\kappa$ and $\kappa_1$, $c$ and $c_1$, as well as $\rho$ and $\rho_1$, are the thermal conductivities, thermal capacities, and densities of the metal electrode (without the subscript) and the aqueous electrolyte (with the subscript "1"). The parameter $p$ represents the power density absorbed by a metal electrode. It depends on the temporal shape of the laser pulse. This relation can be expressed as:

$$p(t) = (1 - \delta)\epsilon(t) \qquad \textit{Eq. 3.33}$$

where $\epsilon$ is the time-dependent energy flux per unit area (considered spatially uniform), and $\delta$ stands for the reflectivity of the surface.

For a uniform laser pulse, **Eq. 3.32** can be integrated resulting in the following formulas:

$$\Delta T(t) = \frac{2(1-\delta)\epsilon}{\sqrt{\pi \kappa c \rho} - \sqrt{\pi \kappa_1 c_1 \rho_1}} \sqrt{t} \quad t \leq t_0 \ \text{(heating)} \qquad \textit{Eq. 3.34}$$

$$\Delta T(t) = \frac{2(1-\delta)\epsilon}{\sqrt{\pi \kappa c \rho} - \sqrt{\pi \kappa_1 c_1 \rho_1}} \left[\sqrt{t} - \sqrt{t - t_0}\right] \quad t > t_0 \ \text{(cooling)} \qquad \textit{Eq. 3.35}$$

If time is long enough, one can expand the $\sqrt{t - t_0}$ term, keeping only the lower terms in the series. After applying the approximation, the temperature decreases in time as:

$$\Delta T(t) = \frac{1}{2} \Delta T_0 \sqrt{\frac{t_0}{t}} \qquad \textit{Eq. 3.36}$$

**Figure 3.25** illustrates the temperature alteration assessed from **Eq. 3.32** for a uniform as well as for a particular non-uniform laser pulse shape (as depicted in the inset). Additionally, the figure shows the temperature obtained with a simulation for the same non-uniform shape. One can see that the difference in pulse shapes is visible only at times shorter than ca. 0.02 µs.

Furthermore, the different functions become indistinguishable after ca. 0.1 µs which justifies the use of **Eq. 3.36**.[295]
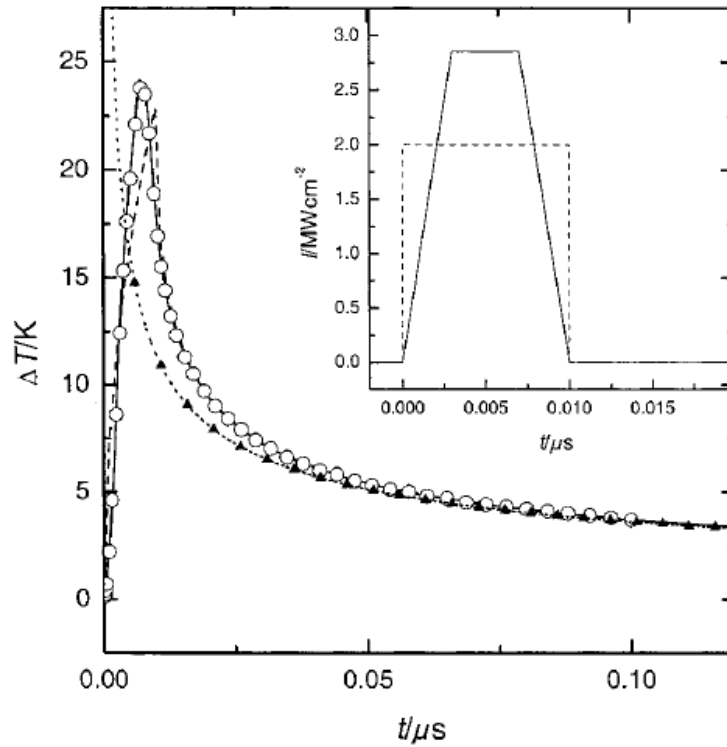


***Figure 3.25.*** *Theoretical temperature change resulting from a laser pulse of 20 mJ cm*$^{-2}$ *on a gold electrode. Solid and dashed lines represent non-uniform and uniform temporal pulse shape, respectively (for a negligible penetration depth); circles depict the non-uniform temporal pulse shape (finite penetration depth); dotted line with triangles are related to the approximated temperature decay proportional to the reciprocal of* $\sqrt{t}$. *The inset presents temporal pulse shapes used for the calculations. Taken from reference 295.*

If the temperature change is small enough to allow a linear variation of the potential with the temperature, it is possible to write:

$$\Delta E = \left(\frac{\partial E}{\partial T}\right)_q \Delta T = \left(\frac{\partial E}{\partial T}\right)_q \frac{1}{2} \Delta T_0 \sqrt{\frac{t_0}{t}} \qquad \textbf{\textit{Eq. 3.37}}$$

The temperature coefficient of the open circuit potential can be determined from the slope of the plot showing the relation $\Delta E$ vs $\frac{1}{\sqrt{t}}$. Furthermore, based on the electrocapillary equation, one can show:[304,305]

$$\left(\frac{\partial E}{\partial T}\right)_q = -\left(\frac{\partial \Delta S}{\partial q}\right)_T \qquad \text{Eq. 3.38}$$

where $\Delta S$ stands for the interfacial entropy of formation of the electrified interface. A plot of $\Delta S$ can be obtained by integration of a plot of the $\Delta E$ vs $\frac{1}{\sqrt{t}}$ as a function of the double layer charge. Moreover, from **Eq. 3.38**, one can see that if the curve $\Delta S$ vs $q$ reaches its maximum, the term $\left(\frac{\partial \Delta S}{\partial q}\right)_T$ will be zero. As a consequence, the potential drop resulting from the electrode heating will also be zero.

In general, the response of the system to the rapid increase in the temperature is due to three contributions:[171]

- ➤ temperature coefficient of the potential drop through the EDL $\left(\frac{\partial E}{\partial T}\right)_q$;
- ➤ thermo-diffusion potential caused by the existence of the temperature difference between the electrolyte in contact with the working electrode, and the electrolyte in contact with the reference electrode;
- ➤ temperature gradient in the metal electrode.

The thermo-diffusion potential can be estimated from the so-called Eastman entropy of transfer of the ions involved. This can be expressed as:[295,306]

$$\frac{\Delta E_{\text{TD}}}{\Delta T} = -\frac{1}{F}\sum \frac{\vartheta_n}{q_n}\hat{S}_n \qquad \text{Eq. 3.39}$$

where $\vartheta_n$ and $\hat{S}_n$ stand for the transport number and the Eastman entropy of transport of the ion n, respectively. The correction resulting from the thermo-diffusion potential is very small and often can be neglected. Furthermore, it has been demonstrated that the contribution related to the temperature gradient is also negligible in comparison with the other two.[297,300] Therefore, the system response after the laser pulse comes largely from the double layer.

According to the traditional understanding of the double layer, the potential drop at the interface can be divided into two parts related to the diffuse and inner layers (see **Section 3.6.1**). It was also pointed out that, due to additional processes, such as electron spillover, the contribution of

the inner layers can be further split into two other ones.[307] Therefore, the temperature coefficient of the potential drop through the EDL can be represented as follows:[141,302]

$$\left(\frac{\partial E}{\partial T}\right)_q = \left(\frac{\partial \Phi}{\partial T}\right)_q + \left(\frac{\partial E^2}{\partial T}\right)_q + \left(\frac{\partial E^w}{\partial T}\right)_q \qquad \textit{Eq. 3.40}$$

where $\Phi$ stands for the work function at a given charge $q$, $E^2$ is the potential drop at the diffuse layer, and $E^w$ represents the potential drop due to the solvent structuring. The thermal coefficient of the work function can only be measured at $q = 0$. According to Kaack et al., the temperature coefficient of the work function is $\frac{\Delta \Phi}{\Delta T}$ =1.5 x 10$^{-4}$ eV K$^{-1}$.[308] Even though this value is valid only for $q = 0$, it shows the order of magnitude of this contribution. The potential drop at the diffuse layer can, in turn, be estimated from the Gouy-Chapman-Stern theory. Both the thermal coefficient of the work function and the potential drop at the diffuse layer are negligible in comparison to the values obtained for the potential drop coming from the solvent structuring. Therefore, it can be assumed that the potential drop through the double layer results mainly from the effect of the temperature increase on the structure of the interfacial solvent layer.[302]

As the potential changes, the orientation of the interfacial water molecules alters from ''oxygen-up'' to ''oxygen-down'' (see **Section 3.6.2**).[161,309,310] The orientation of the solvent molecules is governed by the interactions between the molecules' dipole moment and the electric field generated by the electrode surface charge ($E_{charge}$). Because of the large dipole moment, the potential drop of the electrode mainly originates from the water molecules ($E_{dipole}$). Hence, the potential between the electrode and the solution ($E_{M-S}$) can be expressed as:[311,312]

$$E_{M-S} = E_{charge} + E_{dipole} \qquad \textit{Eq. 3.41}$$

The rapid temperature jump introduces a disorder into the water layer for a very short period of time. This results in the change of $E_{dipole}$ and alters the $E_{M-S}$ according to **Eq. 3.41**. As a consequence, one can reveal the charge of the electrode surface. This phenomenon is utilized in the so-called laser-induced current transient (LICT) technique. During the laser measurement, the laser-induced potential drops are observed as current transients representing the relaxation of the electrified interface. The orientation of the recorded transients is, in turn, related to the electrode surface charge. Thus, the negative and positive charge will result in the

negatively and positively oriented current spikes, respectively. However, at the potentials equal to the PME (closely related to the PZC), the system response will not be prominent (**Figure 3.26**).[295]
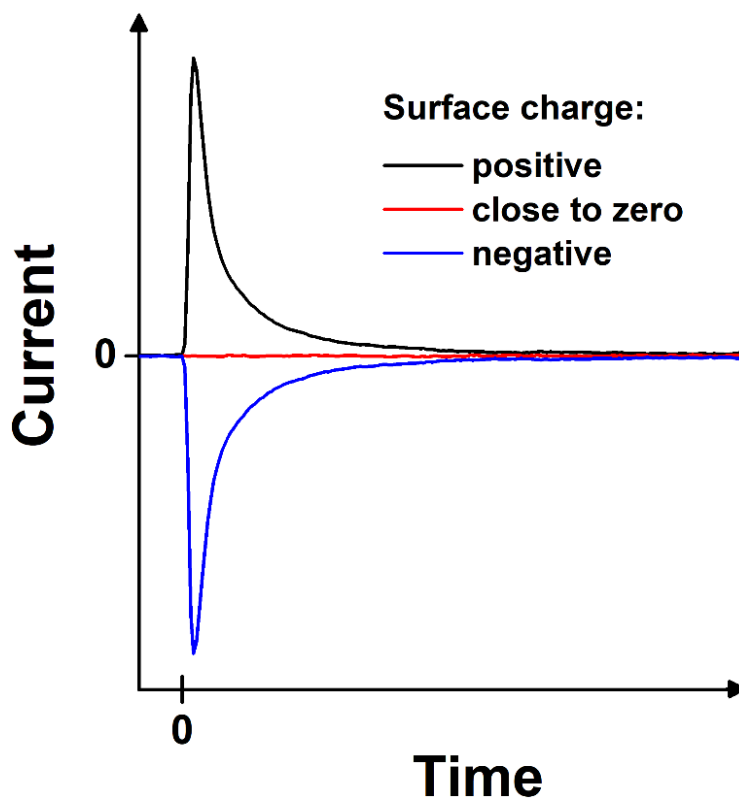


*Figure 3.26. Orientation of the LICTs according to the excess surface charge of the electrode. The sign of the current transient is strictly related to the sign of the net surface charge.*

In spite of its ability to reveal the electrode surface charge and, as a consequence, its PZC,[301] the LICT is also a convenient method of evaluating a mechanism and kinetics of Faradaic processes.[313] The possibility of combining it with other commonly used techniques is another big advantage over the other methods of the PZC/PME determination making the LICT particularly useful for a detailed characterization of electrochemical systems.[45]

## 3.9   Other Techniques Used in this Work

### 3.9.1   Cyclic Voltammetry

Cyclic voltammetry (CV) is an electroanalytical technique, in which the current associated with the electrode processes is measured as a function of time and an applied potential. During the measurement, the voltage changes linearly, while the potential inversion results in a cycle. This versatile method finds application in many branches of science, such as electrochemistry, chemical physics, biochemistry, organic and inorganic chemistry. Because of its simplicity and ability to provide valuable information even about complex electrode reactions, the CV is frequently used as the initial characterization method in analyses of new systems.[47,314,315,316,317]
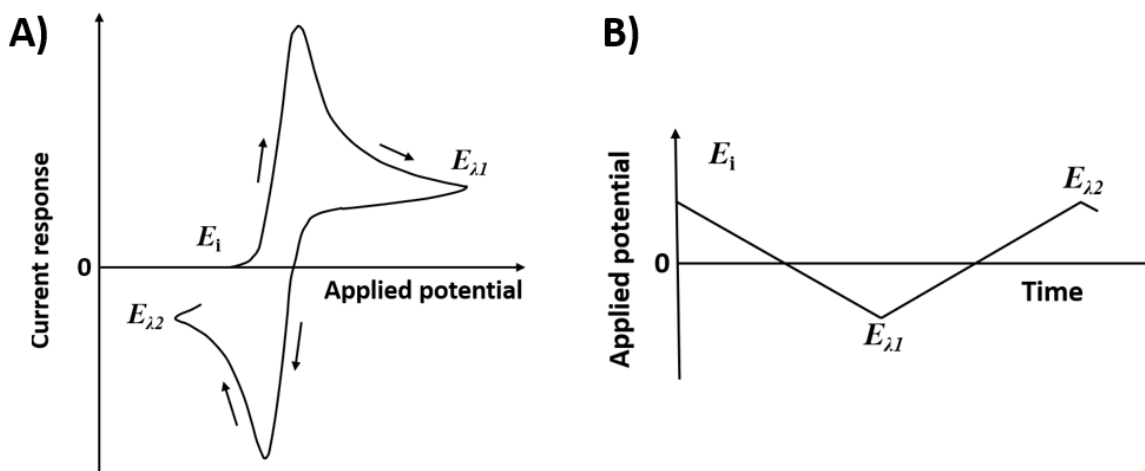


***Figure 3.27.*** *(A) Schematic representation of a cyclic voltammogram. Black arrows indicate the scan direction. (B) Potential change in time during CV measurements. $E_i$- initial potential value; $E_{\lambda 1}$ and $E_{\lambda 2}$- switching potentials. Adapted  from reference 47.*

The plot obtained in a CV experiment, known as a voltammogram (**Figure 3.27A**), displays the change of the current (vertical axis) as a function of the applied voltage (horizontal axis). Due to the linear change of the potential, the horizontal axis can also represent time. Depicting the current response as a function of time can be particularly useful in comprehending the fundamental principles of the technique.[316] During the CV measurement, the potential of the working electrode is swept linearly from a set initial value, $E_i$, up to a so-called switching potential, $E_{\lambda 1}$. After reaching the $E_{\lambda 1}$, the scan direction gets reversed approaching another

preselected value, $E_{\lambda 2}$ (see **Figure 3.27B**). The cycle within the preset voltage range can be repeated as many times as needed.[315]

The shape of the consecutive cycles can differ from the shape of the first scan. These changes, however, carry information about mechanisms of the reactions taking place in a studied electrochemical system.[315] Notably, the alteration of the obtained voltammograms can also originate from the scan rate, $\upsilon$, of an experiment. The increase in its value usually results in the increase in the recorded peak currents.[47] Therefore, the $\upsilon$ is usually provided as an important parameter of the CV measurements.

### 3.9.2   Impedance Spectroscopy

The electrochemical impedance spectroscopy (EIS) is a method of an electrochemical characterization of materials and interfaces formed between them and electronically conductive electrolytes.[318] Its application dates back to the end of the 19th century when Nernst for the first time used this method in his work.[319] Further studies conducted by Warburg made it possible to employ the EIS to the analysis of redox reactions.[320]

During an EIS experiment, the signal is measured as a frequency function at a constant potential. This undoubtedly makes this technique special among the other methods of electrochemical analysis which typically present the evolution of the measured current, electrode voltage, or charge as a function of time.[321] The general idea during the EIS experiment is to apply an electrical stimulus to the electrodes and record the system answer. The former is a periodically altered potential or current, while the latter is the resulting current or potential, respectively. The amplitude of alternating current (AC) signals ought to be as small as possible. The application of sufficiently small signals allows considering the examined systems as pseudo-linear.[318]

During the electrode probing, a sinusoidal voltage is used:[322,323]

$$E(\omega, t) = E_0 sin\,(\omega t) \qquad \textit{Eq. 3.42}$$

with an amplitude $E_0$ and an angular frequency $\omega$. The relation between the frequency, $f$, and $\omega$ can be expressed as:

$$\omega = 2\pi f \qquad\qquad \text{Eq. 3.43}$$

In a linear system, the response current, $i$, is measured with a different amplitude than the current signal, $i_0$, and is shifted in phase by an angle $\theta$:

$$i(\omega, t) = i_0 sin(\omega t + \theta) \qquad\qquad \text{Eq. 3.44}$$

The impedance of the system, $Z(\omega, t)$, can be determined from an expression analogous to Ohm's law:

$$Z(\omega, t) = \frac{E(\omega, t)}{i(\omega, t)} \qquad\qquad \text{Eq. 3.45}$$

Both the numerator and the denominator of **Eq. 3.45** can be described using the complex number notation. Taking $j$ as the imaginary unit, one can rewrite this equation as follows:

$$Z(\omega, t) = \frac{E(\omega, t)}{i(\omega, t)} = \frac{E_0}{i_0}e^{j\theta} = |Z(\omega)|e^{j\theta} \qquad\qquad \text{Eq. 3.46}$$

where $|Z|$ stands for the impedance modulus. By employing Euler's formula, one can express **Eq. 3.46** as:

$$Z(\omega, t) = |Z(\omega)|(cos\,\theta + j\,sin\,\theta) = Z_{Re}(\omega) + jZ_{Im}(\omega) \qquad\qquad \text{Eq. 3.47}$$

$Z_{Re}$ is the real part, while $Z_{Im}$ represents the imaginary part of the impedance. The modulus of the impedance can be calculated from:

$$|Z(\omega)| = \sqrt{Z_{Re}^2(\omega) + Z_{Im}^2(\omega)} \qquad\qquad \text{Eq. 3.48}$$

whereas the following equation can be used to evaluate the phase angle:

$$\theta(\omega) = tan^{-1}\left[\frac{Z_{Im}(\omega)}{Z_{Re}(\omega)}\right] \qquad\qquad \text{Eq. 3.49}$$

The impedance data are usually represented in two ways. The first one, known as the Nyquist plot, displays the imaginary parts, $Z_{Im}$, as a function of the corresponding real parts, $Z_{Re}$, for different frequency values (see **Figure 3.28A**). Even though the Nyquist plots are found to be the most compact, they have one significant drawback, namely they do not clearly display the frequency dependence. The other possibility of representing the data is the so-called Bode plot. Here, the logarithm of the impedance modulus, $\log|Z|$, and the phase angle, $\theta$, are plotted against the logarithm of frequency, $\log f$ (see **Figure 3.28B** and **C**).[322,323]
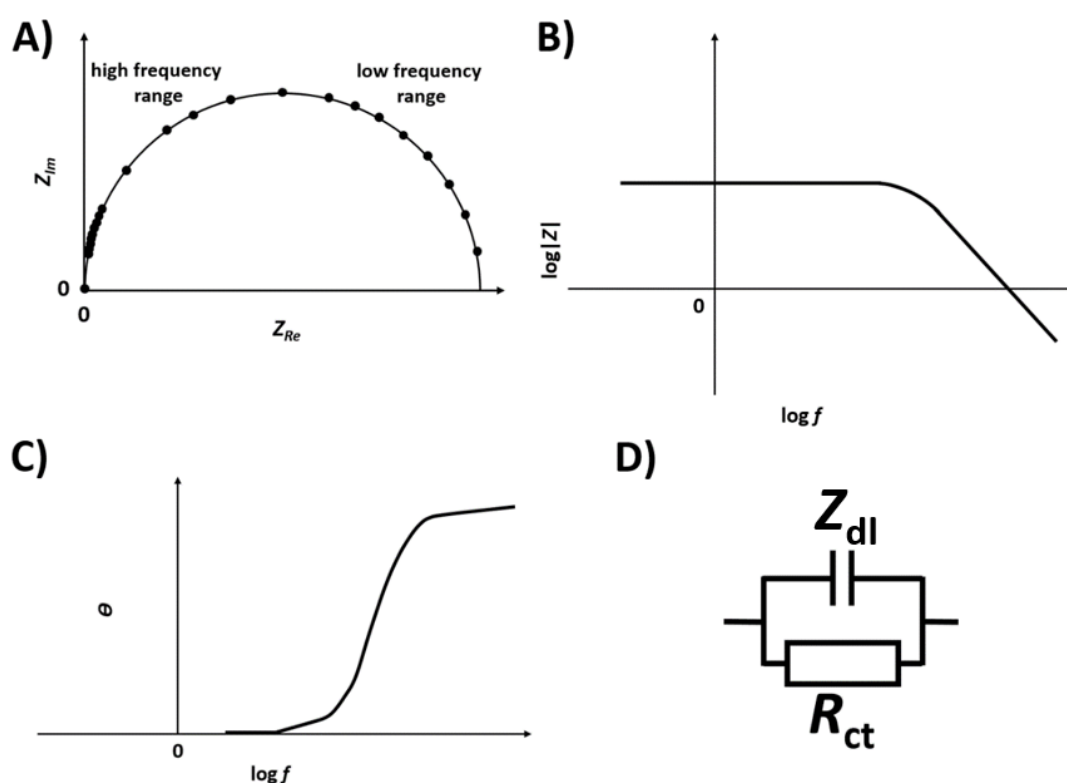


***Figure 3.28.*** *Schematic representations of: (A) Nyquist plot, (B) impedance Bode plot, and (C) phase Bode plot together with the (D) corresponding circuit representing the impedance behavior of the investigated electrochemical reaction. Adapted from 47.*

To simplify the study of the electrochemical systems, they are usually modelled with equivalent electric circuits (EECs) consisting of various elements describing the system behavior. **Figure 3.28D** shows an example of a simple EEC. Typically the circuits can contain resistances, $R$, capacitances, $C$, inductances, $L$, or diffusion Warburg impedance, $W$. Another frequently used element is the constant phase element (CPE, depicted in **Figure 3.28D** as $Z_{dl}$) which describes

the capacitances existing in porous systems in which the energy of the probing signal is noticeably dissipated.[322]

In order to acquire reliable results, the EIS measurement should be performed in accordance with three fundamental requirements: (i) causality, (ii) stability, and (iii) finiteness. According to the first requirement, the answer of the studied system has to come exclusively from the applied AC stimulus. To satisfy the stability criterion, it is necessary to ensure that during the measurement, the properties of the examined system do not change. Finally, the finiteness condition means that within the set frequency regime the real and imaginary parts of the impedance should have finite values.[322] There are a few methods allowing the validity assessment of the impedance analysis. One of them is the Kramers-Kronig transformations.[324]

The EIS is a sensitive technique providing a lot of information about the system behavior. As a very universal technique, the EIS can provide information about the dynamics of the mobile and bound charge at any region of electrochemical systems. It is usually utilized to evaluate the kinetics and mechanisms of the processes. Furthermore, it can be used to determine capacitances, resistances, or even real surface areas of electrodes. It can serve in the examination of almost any physicochemical system. It finds an application in fuel cell tests, characterization of batteries, electrochemical capacitors, semiconductors, as well as in corrosion and biomolecular studies. Although the big amount of information obtained from the EIS measurement is an obvious advantage, it can also generate ambiguities in the interpretation of the obtained data. This can be a case during the characterization of more complex electrochemical systems. In such situations, prior characterization studies including DC electrochemical measurements are necessary.[318,321,325]

### 3.9.3   Quartz Crystal Microbalance

The electrochemical quartz crystal microbalance (EQCM) is a simple, cost-effective, and non-destructive technique used to monitor changes of the electrode mass on the ng to μg scale.[326,327,328] The observed changes are usually caused by deposition of a material at the electrode or its removal from the surface. It finds application in many kinds of electroanalytical studies, such as underpotential deposition of metals, intercalation/deintercalation of ions, or adsorption/desorption of species.[47,329] The working principle of this technique is based on the

piezoelectric nature of a precisely cut slab of monocrystalline quartz, which undergoes slight deformation in the presence of an electric field.[47,330] Initially developed by Sauerbray to control mass changes in a vacuum and gas-phase measurements, the EQCM has been successfully adapted to experiments in liquid environments.[326,330]
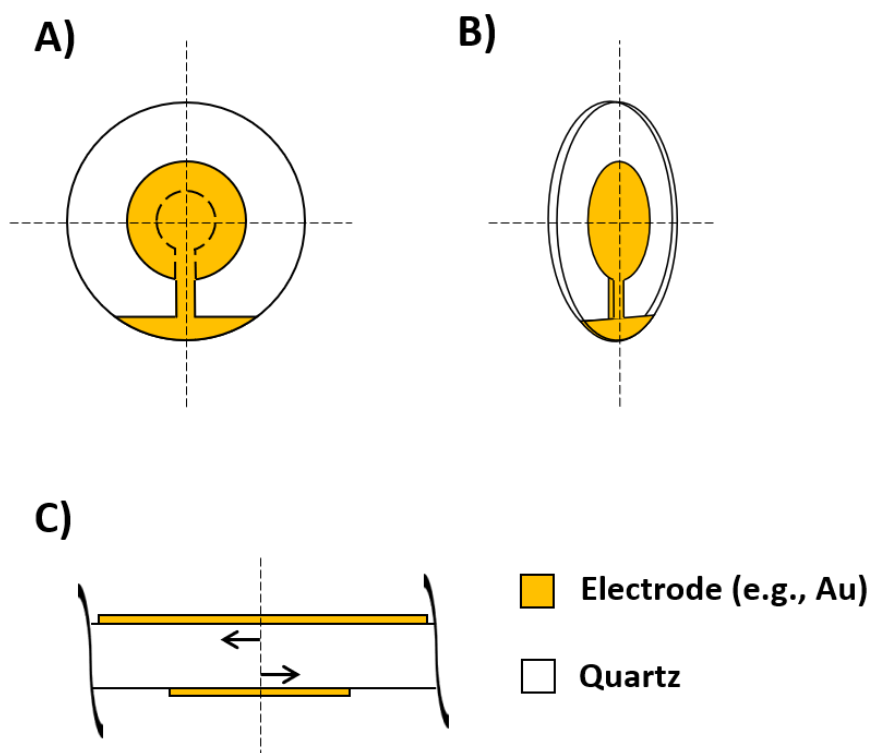


**Figure 3.29**. *Schematic depiction of an EQCM crystal wafer with metal electrodes. (A) Top view; (B) ''3/4'' view; (C) cross-section of a chip. A EQCM crystal wafer is usually a thin round slab with a diameter of 1 inch and thickness of 331 μm. After applying an electric field, the electrodes get displaced. Black arrows show the direction of the shear deformation.*

A quartz wafer is typically sandwiched between two electrodes deposited on its surfaces (**Figure 3.29**) and placed in an O-ring joint with only one side exposed to the solution. The applied sinusoidal electric signal generates a mechanical oscillation in the bulk of the quartz slab. The resonant mode is a specific feature of the crystal. Depending on its shape, size, and thickness, the quartz crystal oscillates at a given frequency $f_0$. For a conventional wafer having a diameter of 1 inch and a thickness of 331 μm this frequency is ca. 5 MHz. The direction of the oscillation is related to the orientation of the crystal structure. In the AT-cut quartz wafers used in the EQCM the shear wave oscillations dominate.

The parameter $f_0$ exhibits a sensitivity to mass changes occurring at the wafer surface. The alteration of the $f_0$ can be given as:[47,326,328,330]

$$\Delta f = \frac{-2\Delta m n f_0^2}{\sqrt{\rho_Q \mu}} = -C_S \Delta m \qquad\qquad \textit{Eq. 3.50}$$

In this expression, known as the Sauerbrey equation, $\Delta f$ represents the change in the frequency resulting from the increase or decrease in mass (per unit area) depicted as $\Delta m$, $n$ stands for the harmonic number of the oscillation (for a 5 MHz crystal, this value is equal to unity), $\rho$ represents the density of quartz (2.648 g cm$^{-3}$), while $\mu$ is the shear modulus (2.947·10$^{11}$ g cm$^{-1}$s$^{-2}$). The constant values can be grouped together and shown as $C_S$. The $C_S$ is known as the sensitivity factor. Both $f_0$ and $C_S$ vary for different media in which the crystal operates. Even though the AT-cut quartz crystal exhibits a low-temperature coefficient preventing temperature-driven changes in frequency, its behavior can be still indirectly affected by this physical parameter. This can happen due to the alteration in the viscosity and density of a solution affecting the oscillation frequency of the wafer.

A typical EQCM device allows the frequency measurements with a precision up to 1 Hz. On the basis of **Eq. 3.50**, higher sensitivities could be achieved by operating at higher harmonics or using crystals with a higher $f_0$ value. Such crystals, however, are usually very thin and fragile. Furthermore, using thinner wafers requires the application of more complex equipment. Thus, the use of 5 MHz crystal is the most common practice in laboratories nowadays.

Even though the presented technique gives a broad spectrum of possibilities to apply in the investigation of various systems, it might be limited by the thickness and the nature of the deposited materials. Particularly problematic are the viscoelastic effects which appear to play a role in experiments with certain kinds of polymers.[47]

### 3.9.4 Atomic Force Microscopy

The atomic force microscopy (AFM) is a technique used to probe and image surface structures with exceptionally high accuracy and resolution. It was developed as a variation of the scanning tunneling microscopy. Unlike its predecessor, the AFM does not require electrical conductivity of the investigated surfaces. Its operation is based on measuring forces or interatomic interactions occurring between a sharp probing tip and a sample originating from electrostatic and van der Waals forces. The tip, usually made from $SiO_2$ or $Si_3N_4$, is supported by the elastic

Si cantilever which gets bent as a result of tip-surface forces. The analyzed sample is placed on the piezo scanner. The sample holder moves in the $x$-, $y$-, and $z$-direction. During a surface scan, changes in the cantilever deflection are measured. This measurement is typically performed by monitoring the reflection of the laser beam from the back of the cantilever. The position of the reflected laser beam at the detector alters together with the motion of the cantilever.[47,331]

The surface analysis can be carried out in a few modes. For instance, in the so-called contact mode, the distance between the tip and the sample surface is reduced to the minimum. In such a setting the acting forces are mainly repulsive. During the measurement, the beam deflection is kept at a certain value (known as a set-point), and the tip moves in the $z$-direction. The altering piezo voltage is recorded in a function of the position. The contact mode ensures high resolution; however, in some cases, the direct contact between the tip and the surface can cause problems including the damage of the sample. Analogously, if the cantilever is located far away from the surface, the measurements are performed in the non-contact mode. In this mode, the measured net forces are only attractive. The use of the non-contact AFM eliminates the issues related to the direct tip-surface interactions. The increased sensitivity of this AFM type results, however, in a decreased resolution of acquired topographical information of examined surfaces. The tapping mode, in turn, combines features of both modes presented above. During the measurements with this kind of the AFM, the cantilever oscillates at or close to its natural resonance frequency with the oscillation amplitude set at the fixed value. While approaching the surface at the bottom of an oscillation, the tip taps the sample. As a consequence, the swinging amplitude alters. Depending on the surface topography, the vibration amplitude can either decrease or increase reaching its free air amplitude. By recording changes in oscillation amplitude, one can obtain an AFM image.[47,139,331,332,333,334,335,336,337]

# 4. Experimental Part

## 4.1 Electrochemical Cells

The measurements reported in this work were performed using three different electrochemical cells. Prior to the measurements, the whole glassware was cleaned with a mixture of a concentrated 96% solution of $H_2SO_4$ and a 30% solution of $H_2O_2$, and abundantly rinsed with ultrapure water. Subsequently, each cell compartment was boiled several times in ultrapure water.

### 4.1.1 Cell for Voltammetric, Impedance, Nanogravimetric, and Laser Experiments

The CV experiments (on the quartz crystal wafer electrodes) and the corresponding EIS, EQCM, and LICT measurements were performed in a custom-built electrochemical glass cell using a three-electrode configuration. As presented in **Figure 4.1**, the cell consisted of two main parts: (1) the preconditioning compartment and (2) the working compartment. The solution in the preconditioning part was purged with gases which flushed the chamber through the separated inlet and outlet. Depending on the experiment, Ar or $O_2$ was used. The preconditioned electrolyte was further introduced into the working compartment, where actual measurements were performed. This part of the cell was additionally equipped with a flat, laser light transmittable glass window located on the side of the cell. The window was mounted in order to ensure that the laser beam would reach the electrode surface with the possibly smallest perturbation. The additional gas inlet and outlet allowed to control the atmosphere inside the working compartment during the experiments. AT-cut quartz crystal wafer EQCM electrodes served as working electrodes. Depending on the experiment, they consisted of platinum, gold, or indium tin oxide (ITO) materials. A Pt wire was employed as a counter electrode, while mercury-mercury sulfate (MMS) and silver-silver chloride (SSC) electrodes were used as the reference electrodes (REs). Each RE was placed in a Luggin capillary including a ceramic insert conductive for ions. Bringing its tip as close as possible to the WE surface allowed to maximally decrease the ohmic potential drop.[338] All the potentials measured versus the MMS and reported in this work were converted to the RHE scale.
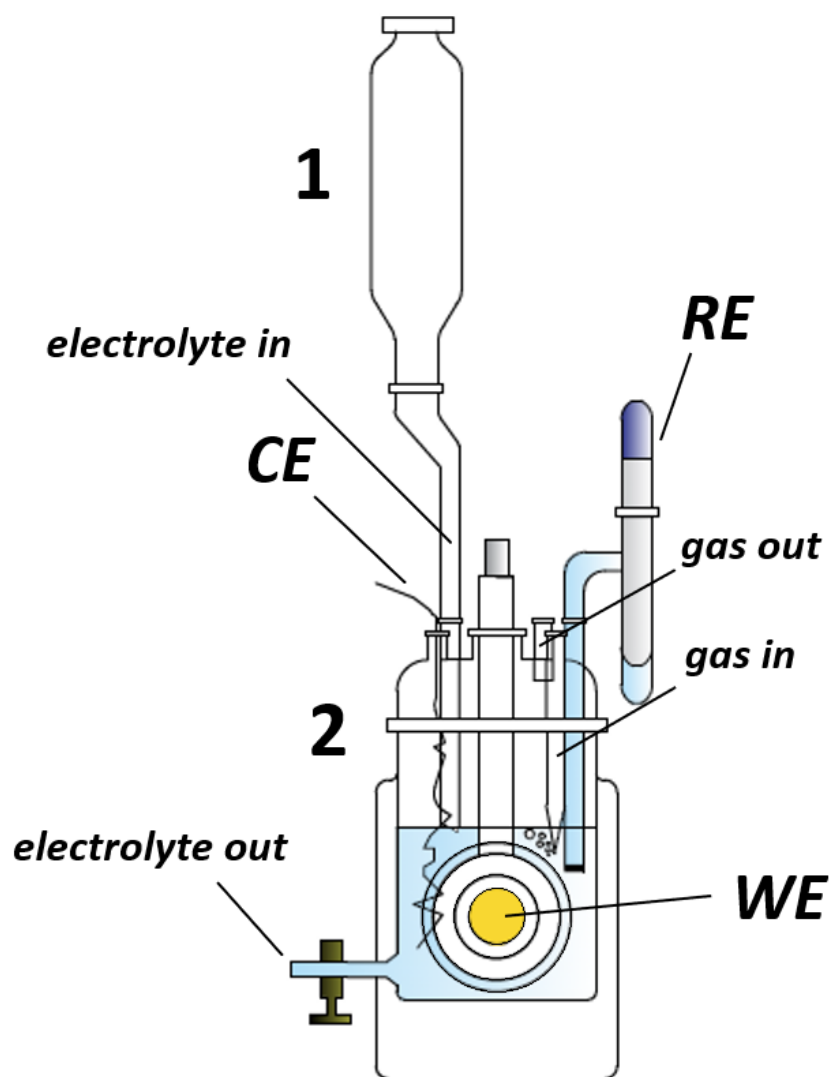
***Figure 4.1.*** *Scheme of the electrochemical cell used for the CV, EIS, EQCM, and LICT measurements of the quartz crystal wafer electrodes. 1- preconditioning compartment; 2- working compartment.*

### 4.1.2   Cells for Activity Measurements

The HER and ORR activity measurements of the polycrystalline metal electrodes were performed using two different electrochemical cells. Their schematic illustrations are depicted in **Figure 4.2A** and **Figure 4.2B**.
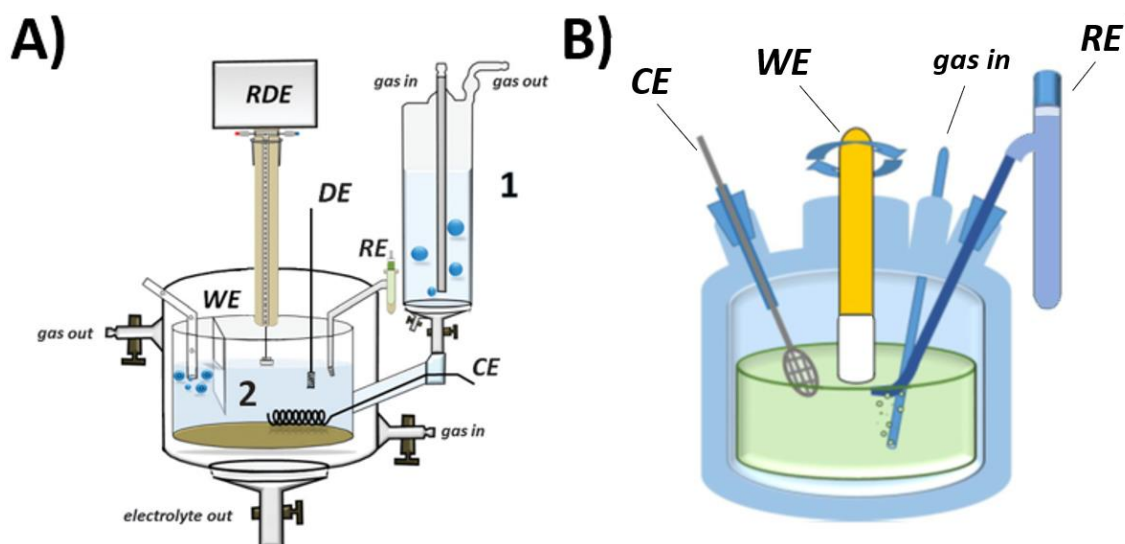
*Figure 4.2. Scheme of the cells used for the activity measurements of metal electrodes. 1- preconditioning compartment; 2- working compartment. Part A was adapted from reference 339.*

Similar to the cell described in the previous section, the first cell used for the activity measurements consisted of two main parts (see **Figure 4.2A**), namely (1) the preconditioning and (2) working compartments. The presence of separated inlets and outlets in both parts allowed to flush them with gases during the preparation of electrolytes as well as during actual measurements. The WE was inserted into the working compartment using the hanging meniscus rotating disk electrode (HMRDE) configuration which ensured a better mass transport during the measurement.[340] A movable shaft enabled to vertically adjust the position of the WE. By using the shaft, it was possible to bring the WE into contact with the solution and form the optimal shape of the meniscus. A Pt wire served as the CE, while the MMS electrode was used as the RE. Similar as for the other cell, the RE was introduced into the system through a Luggin capillary with a ceramic insert conductive for ions. The working compartment additionally contained a dummy electrode (DE) made of a Pt wire. The DE was connected in parallel with the WE. Using the DE ensured the control of the WE potential during the replacement of the electrolyte.[339] The working chamber was equipped with separated gas inlet and outlet allowing to continuously purge the solution with gases during measurements.

The second cell (**Figure 4.2B**) consisted of a single glass compartment. It contained a gas inlet through which Ar, $H_2$, or $O_2$ gases were supplied into the investigated systems. In the described cell, a platinum mesh served as the CE. The use of the metal mesh ensured a large surface area of the electrode. A MMS electrode was employed as the RE. It was introduced into the cell

through a Luggin capillary. As in the case described before, the WE was placed into the cell using the HMRDE configuration. The vertically movable shaft controlled the position of the WE.

## 4.2 Preparation of Electrolytes

Aqueous electrolytes of $HClO_4$ and $H_2SO_4$ used for cleaning the electrodes and performing further electrocatalytic measurements were prepared by diluting concentrated acid solutions in ultrapure water. To prepare aqueous solutions of $Na_2SO_4$, $K_2SO_4$, $K_3[Fe(CN)_6]$, $NiCl_2$, $CoCl_2$, $NaCl$, $NaClO_4$, as well as $NaOH$ and $KOH$ used to adjust the pH of electrolytes, appropriate amounts of salt powders or base flakes were dissolved in ultrapure water.

Whereas the obtained solutions of most of the compounds were directly employed in the experiments, pHs of 0.5 M $Na_2SO_4$ and 0.5 M $K_2SO_4$ were set to arbitrarily selected values using diluted bases and sulfuric acid. The final pH levels were checked using a portable pH meter. Depending on the subsequent experiment, the measured electrolytes were pre-purged with Ar, $H_2$, or $O_2$ for at least 10 min.

The detailed list of the chemicals used can be found at the end of this chapter.

## 4.3 Preparation of Electrodes

### 4.3.1   Preparation of AT-cut Pt and Au Quartz Crystal Wafers

AT-cut polycrystalline platinum and gold quartz crystal wafer electrodes with the surface area of 1.37 cm$^2$ were used. Prior to the measurements, the Pt and Au surfaces were electrochemically cleaned by cycling them in Ar-saturated 0.1 M $HClO_4$ and 0.1 M $H_2SO_4$, respectively. In the case of Pt, the chosen voltage range was between 0.00 V and 1.40 V vs RHE, which, after obtaining a stable CV, was narrowed down to 0.06 V and 1.00 V vs RHE. In turn, the Au electrodes were cycled within the set potential regime of -0.20 V – 1.40 V vs SSC. The CVs were performed at a scan rate of 50 mV s$^{-1}$. In order to ensure the desired quality

of the surface, the obtained voltammograms were further compared with the CVs available in the literature. After the electrochemical cleaning, the electrodes were abundantly rinsed with ultrapure water.

### 4.3.2 Preparation of Pt Microelectrodes and Pt Disk Electrodes

Analogous electrochemical cleaning procedure was used in the case of the platinum microelectrodes with a diameter of 25 μm, and platinum disk electrodes with a diameter of 5 nm. The metal surfaces were cycled between -0.10 V and 1.80 V vs RHE in Ar-saturated 0.1 M $HClO_4$. The processes were performed until stable voltammograms were recorded. In the next step, the potential ranges were narrowed down to the regimes of 0.10 V – 0.80 V vs RHE. The CVs were performed at a scan rate of 50 mV s$^{-1}$. The voltammograms recorded this way were compared with voltammograms available in the literature.

### 4.3.3 Preparation of the Polycrystalline Bead Au Electrode

A homemade polycrystalline gold electrode with a surface area of 0.136 cm$^2$ was utilized. Before the measurements, the gold electrode was electrochemically cleaned by cycling its surface in the 0.1 M $H_2SO_4$ solution within a potential range of 0.30 V – 1.50 V vs RHE. The CVs were performed at a scan rate of 50 mV s$^{-1}$. Then, the resulting voltammograms were compared with those available in the literature.

### 4.3.4 Preparation of AT-cut ITO Quartz Crystal Wafers

AT-cut ITO quartz crystal wafer electrodes with the surface area of 1.37 cm$^2$ were additionally used as support electrodes for $Mn_2O_3$ films. The ITO is an n-type semiconductor exhibiting excellent electrical conductivity.[341] Due to the wide gap (3.3 – 4.3 eV which corresponds to the wavelength range of ca. 375 – 290 nm) and high transparency to the visible light,[342,343,344] the pure ITO electrode itself did not show any response to the laser illumination. Prior to the

experiments, the ITO surfaces were rinsed with 0.1 M KOH and a generous amount of ultrapure water.

### 4.3.5    Preparation of $Mn_2O_3$ Electrodes

A $Mn_2O_3$ ink was prepared by dispersing 1.5 mg of $Mn_2O_3$ in 1 ml of water and ultrasonicating the obtained mixture for 30 min. Then, a small amount of the resulting slurry was drop-casted at the surfaces of freshly cleaned AT-cut ITO quartz crystal wafers and dried. The dried electrode chip was mounted in the EQCM holder and carefully placed in the electrochemical cell.

### 4.3.6    $Na_2Ni[Fe(CN)_6]$ (NiHCF) and $Na_2Co[Fe(CN)_6]$ (CoHCF) Films Deposition

Both the $Na_2Ni[Fe(CN)_6]$ (NiHCF) and the $Na_2Co[Fe(CN)_6]$ (CoHCF) thin films were electrodeposited on a clean Au quartz crystal electrode from Ar-saturated aqueous solutions based on the procedure described in reference 12. The utilized electrolytes were mixtures of 0.25 M $Na_2SO_4$, 0.5 mM $K_3Fe(CN)_6$ and, depending on the type of the film, 0.5 mM $NiCl_2$ (for NiHCF) or 0.5 mM $CoCl_2$ (for CoHCF) solutions. The thin films were deposited via cycling the electrode potential within the set ranges at a scan rate of 50 mV $s^{-1}$. The potential regimes were 0.12 V – 0.92 V vs SSC and -0.20 V – 1.10 V vs SSC for Ni- and Co-containing films, respectively. During deposition, the mass alteration of the WE was simultaneously recorded using the EQCM. The cycling of the electrodes was continuously repeated until the desired mass value was reached.

## 4.4 Setup for Voltammetric, Impedance, Nanogravimetric, and Laser Experiments

The CV experiments (on the quartz crystal wafer electrodes) and the corresponding EQCM, EIS, and LICT measurements were performed using a specially designed setup consisting of a VSP-300 potentiostat, a QCM 200 EQCM device, and a Quanta-Ray INDI-Series pulsed Nd:YAG laser (**Figure 4.3**). A VA-CB-532-CONEX motorized high-energy variable beam

splitter connected with a BD-7 passively air-cooled beam dump additionally served to regulate the power of the laser beam. Connecting all the components to a PC allowed a real-time control of the performed measurements.
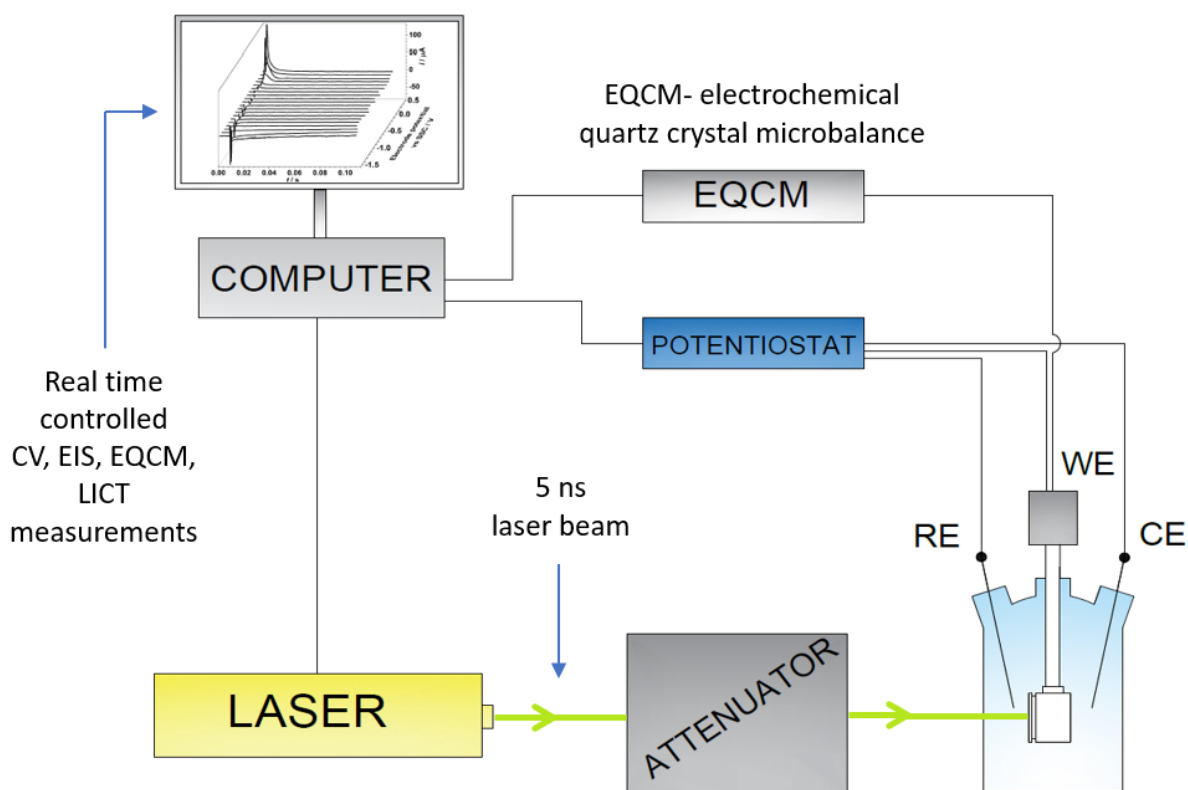


***Figure 4.3.*** *Scheme of the experimental setup used to perform voltammetric, impedance, nanogravimetric, and laser measurements.*

### 4.4.1 Laser Measurements

The laser measurements were performed using a Quanta-Ray INDI-Series pulsed Nd:YAG laser. The repetition rate of the device was 10 Hz, while its pulse width and wavelength were 5-8 ns and 532 nm, respectively. This laser beam wavelength value is commonly used in studies employing laser-induced transient techniques. The choice of this value is typically motivated by the desire to avoid side effects, such as photoemission of electrons,[295] as for numerous materials the photoemission threshold oscillates between 200 and 300 nm.[172,301,306,312] The laser beam diameter was equal to ~9 mm, which was slightly smaller than the diameter of the WE.

Along with the distance between the laser output and the WE, the beam diameter was kept constant. The energy of the laser beam directly at its output was ~200 mJ, which resulted in the energy density of more than 300 mJ cm$^{-2}$. This value was far above the damage threshold of most of the electrode materials. In order to reduce it, the beam was passed through the attenuator. Transients were acquired by recording current alterations over time right after illuminating the electrode surface. The representative LICTs were further plotted as a function of the WE potential.

## 4.5 Characterization of Electrodes

### 4.5.1 Characterization of AT-cut Pt and Au Quartz Crystal Wafer Electrodes

Freshly cleaned AT-cut polycrystalline Au quartz crystal wafers were introduced into the Ar-saturated 0.25 M Na$_2$SO$_4$ and 0.25 M K$_2$SO$_4$ electrolytes. Then, the LICT method was used to investigate the effective charge of the electrode surfaces. The laser experiments were conducted within the potential ranges of -1.50 V – 0.50 V vs SSC (-1.10 V – 0.90 V vs RHE) and -1.50 V – 1.50 V vs SSC (-0.90 V – 2.10 V vs RHE) in the 0.25 M Na$_2$SO$_4$ and 0.25 M K$_2$SO$_4$ electrolytes, respectively. All the measurements were performed with a positive scan direction using 20 mV potential steps. The energy of the laser beam was kept at ~12 mJ (energy density: ~19 mJ cm$^{-2}$).

In turn, clean AT-cut polycrystalline Pt quartz crystal wafers were introduced into the Ar-saturated 0.5 M Na$_2$SO$_4$ and 0.5 M K$_2$SO$_4$ electrolytes at the various pH values (see **Table 4.1**). The quality of the electrode was additionally checked by performing a voltammetric scan within a potential range of 0.06 V – 1.00 V vs RHE. The interfaces formed between the metal surfaces and the aqueous solutions were further examined using the LICT technique. The electrodes were probed with the laser beam with energy of ~10 mJ (energy density: ~16 mJ cm$^{-2}$). The Pt surfaces in 0.5 M Na$_2$SO$_4$ were investigated within a potential range of 0.04 V – 0.96 V vs RHE. In turn, the initial potential range used to examine the electrodes in 0.5 M K$_2$SO$_4$ (pH 1 and pH 3) was 0.06 V – 0.74 V vs RHE; however, in the following experiments with the K$^+$-containing solution, the wider voltage regime of 0.06 V – 0.94 V vs RHE was used. It should be also noted that in some solutions (e.g., pH 6), the potential ranges were further extended

towards more negative potentials, as it allowed a more precise estimation of the resulting PMEs. The potential step used during the measurements was 20 mV, while the scan direction at each series of measurements was positive.

*Table 4.1. Electrolytes used for the LICT characterization of AT-cut polycrystalline Pt quartz crystal wafers together with their adjusted pH values.*

| Electrolyte | pH values |
| --- | --- |
| 0.5 M $Na_2SO_4$ | 1, 2, 3, 4, 5, 6, 7, 8, 9, 9.50, 10, 11, 12, 12.40, 13, 13.30 |
| 0.5 M $K_2SO_4$ | 1, 1.70, 2, 3, 4, 5, 6, 7, 8, 9, 10.20, 11, 13, 13.70 |

### 4.5.2 Characterization of Pt and Au Electrodes

The HER and ORR activities of the polycrystalline Pt microelectrode, Pt disk electrode, and Au bead electrode in different $H_2$- or $O_2$-saturated solutions were measured using the CV. The freshly cleaned Pt microelectrode was immersed in the working electrolyte and cycled within the set potential range. The Pt disk and Au bead electrodes, in turn, were introduced into the cell under the constant potential of 0.00 V vs RHE under the HMRDE configuration. During the voltammetric measurements, the disk and bead electrodes were rotated with a rotation speed of 400 rpm. The electrolytes used in the experiments and the potential ranges chosen for the HER and ORR activity measurements are shown in **Table 4.2** and **Table 4.3**, respectively.

***Table 4.2.*** *Electrodes, electrolytes, corresponding potential ranges, and scan rates used during the HER activity measurements.*

| Electrode | Electrolyte | $E$ range vs RHE | Scan rate |
|---|---|---|---|
| $Pt_{pc,ME}$ | 1 M $HClO_4$, $H_2$ | -0.10 – 0.10 V | 10 mV s$^{-1}$ |
| $Pt_{pc,ME}$ | 0.1 M $HClO_4$, $H_2$ | -0.10 – 0.10 V | 10 mV s$^{-1}$ |
| $Pt_{pc,ME}$ | 0.01 M $HClO_4$, $H_2$ | -0.10 – 0.10 V | 10 mV s$^{-1}$ |
| $Pt_{pc}$ | 0.5 M $Na_2SO_4$ (pH 6), $H_2$ | -1.20 – 0.20 V | 50 mV s$^{-1}$ |
| $Pt_{pc}$ | 0.5 M $K_2SO_4$ (pH 6), $H_2$ | -1.20 – 0.20 V | 50 mV s$^{-1}$ |
| $Au_{pc}$ | 0.25 M $Na_2SO_4$, $H_2$ | -1.60 – 0.20 V | 50 mV s$^{-1}$ |
| $Au_{pc}$ | 0.25 M $K_2SO_4$, $H_2$ | -1.60 – 0.20 V | 50 mV s$^{-1}$ |

***Table 4.3.*** *Electrodes, electrolytes, corresponding potential ranges, and scan rates used during the ORR activity measurements.*

| Electrode | Electrolyte | $E$ range vs RHE | Scan rate |
|---|---|---|---|
| $Pt_{pc,ME}$ | 1 M $HClO_4$, $O_2$ | 0.10 – 1.20 V | 10 mV s$^{-1}$ |
| $Pt_{pc,ME}$ | 0.1 M $HClO_4$, $O_2$ | 0.10 – 1.20 V | 10 mV s$^{-1}$ |
| $Pt_{pc,ME}$ | 0.01 M $HClO_4$, $O_2$ | 0.15 – 1.20 V | 10 mV s$^{-1}$ |
| $Pt_{pc}$ | 0.5 M $Na_2SO_4$ (pH 6), $O_2$ | -0.05 – 1.20 V | 50 mV s$^{-1}$ |
| $Pt_{pc}$ | 0.5 M $K_2SO_4$ (pH 6), $O_2$ | 0.05 – 1.20 V | 50 mV s$^{-1}$ |
| $Au_{pc}$ | 0.25 M $Na_2SO_4$, $O_2$ | 0.05 – 1.20 V | 50 mV s$^{-1}$ |
| $Au_{pc}$ | 0.25 M $K_2SO_4$, $O_2$ | 0.05 – 1.20 V | 50 mV s$^{-1}$ |

### 4.5.3   Characterization of $Mn_2O_3$ Electrodes

$Mn_2O_3$ electrodes were initially characterized in $O_2$-saturated 1 M NaOH solutions with the CV without rotating. The electrode potential was cycled within the range between -0.20 V

and 1.20 V vs RHE at a scan rate of 50 mV s$^{-1}$. In the next step, the electrochemical interface of the electrodes was probed by the LICT technique. In this case, due to the extremely low stability of the electrode, the laser beam energy was decreased to ~8 mJ (energy density of ~13 mJ cm$^{-2}$). The experiments were carried out with a scan direction from the negative voltages towards the positive ones using 20 mV steps.

Subsequently, the electrodes were studied with the EIS using an AC probing signal amplitude of 10 mV over the frequency range between 900 kHz and 10 Hz. The measurements were carried out in the following potentials: 0.14 V, 0.74 V, 0.84 V, 1.09 V, and 1.14 V vs RHE. The resulting spectra were fitted using the homemade ''EIS Data Analysis 1.1''and ''EIS Data Analysis 1.2'' software. The validation process of the impedance analysis was performed following the concepts and algorithms described in references 345 and 346. For example, the Kramers-Kronig test did not reveal any problem regarding the quality of the impedance fitting.

### 4.5.4   Characterization of Battery Films

The electrodes were characterized during intercalation and deintercalation in various Ar-saturated aqueous solutions. The WEs were cycled with the scan rate of 50 mV s$^{-1}$ within the voltage regimes at which different alkali-metal cations intercalate into and deintercalate from the film structures. The simultaneous EQCM measurements made it possible to control the electrode mass change during insertion and extraction of the ions. The electrolytes as well as the potential regimes used to study the PBA films are presented in **Table 4.4**. It should be mentioned that the potential range in the experiments with CoHCF in sodium chloride was narrowed down in order to avoid chlorine evolution.

*Table 4.4. Electrolytes and potential ranges utilized to characterize battery films.*

| Film compound | Electrolyte used | $E$ range vs SSC |
|---|---|---|
| **NiHCF** | 0.25 M $Na_2SO_4$ | 0.12 V – 0.92 V |
| **NiHCF** | 0.25 M $K_2SO_4$ | 0.22 V – 1.02 V |
| **CoHCF** | 0.25 M $Na_2SO_4$ | -0.20 V – 1.10 V |
| **CoHCF** | 0.25 M $NaClO_4$ | -0.20 V – 1.10 V |
| **CoHCF** | 0.25 M NaCl | -0.20 V – 0.80 V |

The morphology of the deposited NiHCF and CoHCF films was imaged with the AFM. The AFM measurements were carried out in tapping mode at a scan rate of 0.5 Hz using a multimode EC-STM/AFM instrument equipped with a Nanoscope IIID controller. The whole device was controlled by Nanoscope 5.31r1 software. The acquired surface images were further analyzed with WSxM 5.0 Develop 8.0 software.[45,46,347]

The processes in the interfaces of the battery films were also investigated with the EIS. The EIS measurements were conducted within the potential ranges of cation (de)intercalation presented in **Table 4.4** using a 10 mV amplitude of AC probing frequency ranging from 10 kHz to 500 mHz and from 250 kHz to 300 mHz for the NiHCF and CoHCF electrodes, respectively. Also in these cases, the Kramers-Kronig test did not reveal any problem regarding the quality of the impedance fitting.[345,346]

In order to reveal the surface charge, the electrodes were probed with the laser beam. The LICT measurements were conducted within the voltage ranges listed in **Table 4.4** with the scan direction from lower potentials towards more positive ones. Subsequently, the scan voltage ranges used in the studies of the NiHCF electrode were extended towards more negative values reaching -0.38 V and -1.20 V vs SSC in sodium and potassium sulfate, respectively. This was done due to the absence of the PME within the initially set ranges. All the LICT experiments were conducted using 20 mV potential steps. The energy of the laser beam used to probe the NiHCF film was reduced to ~12 mJ (energy density: ~19 mJ $cm^{-2}$). In the case of Co-containing electrode, the pulse energy was decreased even more to ~10 mJ (energy density: 16 mJ $cm^{-2}$). Both the values were far below the damage threshold of the electrodes.[45,46]

## 4.6 List of Equipment, Materials, and Chemicals Used in this Work

**Equipment:**

AFM: MultiMode EC-STM/EC-AFM with a Nanoscope IIID controller- Veeco Instruments Inc., USA.

Beam dump: BD-7- Newport Corporation, USA.

Beam splitter: VA-CB-532-CONEX- Newport Corporation, USA.

EQCM: QCM 200- Stanford Research Systems, USA.

LICT: Quanta-Ray INDI-Series Nd:YAG laser, repetition rate: 10 Hz, pulse width: 5-8 ns, wavelength: 532 nm- Spectra-Physics Lasers, USA.

Potentiostat: VSP-300- Bio-Logic, France.

pH meter: Economical pH Meter or pH/mV Meter- Omega, USA

RDE/RRDE: Pine RDE 710 RDE with MSR rotator- Pine Research Instruments, USA.

Reference electrodes: MMS and SSC- SI Analytics, Germany.

Ultrapurification water system: Evoqua Ultra Clear 10 TWF 30 UV- Evoqua, Germany.


**Materials:**

Ar 5.0- Air Liquide, Germany.

AT-cut Au quartz crystal wafer- $d_{qcw}$: 2.54 cm, $d_{Au}$: 1.37 cm, Stanford Research Systems, USA.

AT-cut ITO quartz crystal wafers- $d_{qcw}$: 2.54 cm, $d_{Au}$: 1.37 cm, MicroVacuum Ltd., Hungary.

AT-cut Pt quartz crystal wafer- $d_{qcw}$: 2.54 cm, $d_{Au}$: 1.37 cm, Stanford Research Systems, USA.

$Au_{pc}$, 99.99%- d: 4 mm, homemade.

$O_2$ 5.0- Air Liquid, Germany.

$Pt_{pc}$, 99.99 %- d: 5 mm, roughness: 30 nm, Mateck, Jülich, Germany.

Pt wire, 99.99 %- d: 0.3 mm, GoodFellow, Germany.


**Chemicals:**

$CoCl_2 \cdot 6H_2O$, 98%, ACS Reagent- Sigma Aldrich, Germany.

$H_2SO_4$, 96 %, Suprapur- Merck, Germany.

$HClO_4$, 70% Suprapur- Merck, Germany.

KOH, i) ≥85%, ACS Reagent- Sigma Aldrich, Germany. ii) 85%- Grüssing, Germany.

$K_2SO_4$, 99.0%- Sigma Aldrich, Germany.

$K_3[Fe(CN)_6]$, 99.0%- Sigma Aldrich, Germany.

$Mn_2O_3$- synthesized in the laboratory of the Indian Institute of Technology Ropar, Punjab, India.

$Na_2SO_4$, 99.0%- Sigma Aldrich, Germany.

NaOH, ≥98%- Sigma Aldrich, Germany.

NaCl, 99.0%- Sigma Aldrich, Germany.

$NaClO_4 \cdot H_2O$, 97%- Alfa Aesar, Germany.

$NiCl_2 \cdot 6H_2O$, 99.3%- Alfa Aesar, Germany.


**Software:**

EC-LAB 10.40- potential control and data collection.

EIS Data Analysis 1.1 and 1.2- fitting of EIS spectra.

Nanoscope 5.31r1- AFM data collection.

OriginPro 2015G- data analysis, treatment, display.

SRS QCM200- EQCM data collection.

WSxM 4.0 Beta 8.3- AFM data analysis.

# 5. Results and Discussion

## 5.1 Surface Charge Determination

As shown in **Section 3.6.3**, the way how the interfacial water molecules orient themselves towards the electrode highly depends on the effective charge accumulated at its surface (see **Figure 5.1A**). The temperature jump at the electrode surface generated by the short laser pulses results in a temporary decrease in the order of the surface water molecules present in the double layer (**Figure 5.1B**).[301] As a consequence, during the relaxation of the interfacial layer, sharp either negative or positive current transients can be observed. The orientation of the transients is, in turn, strictly related to the sign of the charge at the electrode surface. Therefore, the negative net surface charge will result in negative current transients and vice versa.[45]

**Figure 5.1C** shows a typical negatively oriented current transient recorded for a polycrystalline gold electrode immersed in 0.25 M $Na_2SO_4$ at an arbitrarily chosen potential value of -1.50 V vs SSC. Shortly after the laser illumination (at ca. 8 ms), the transient can be seen. Clearly, the excess charge of the electrode surface at the investigated potential is negative. Interestingly, similar responses can be obtained for the other, more positive potential values reaching ca. -0.30 V vs SSC (**Figure 5.1D**). This implies that the net charge accumulated at the surface of the metal stays negative within the investigated potential range. The orientation of the resulting current transients can be seen more clearly in **Figure 5.1E** representing the relation between the recorded maximal current extrema and the electrode potential.[45]
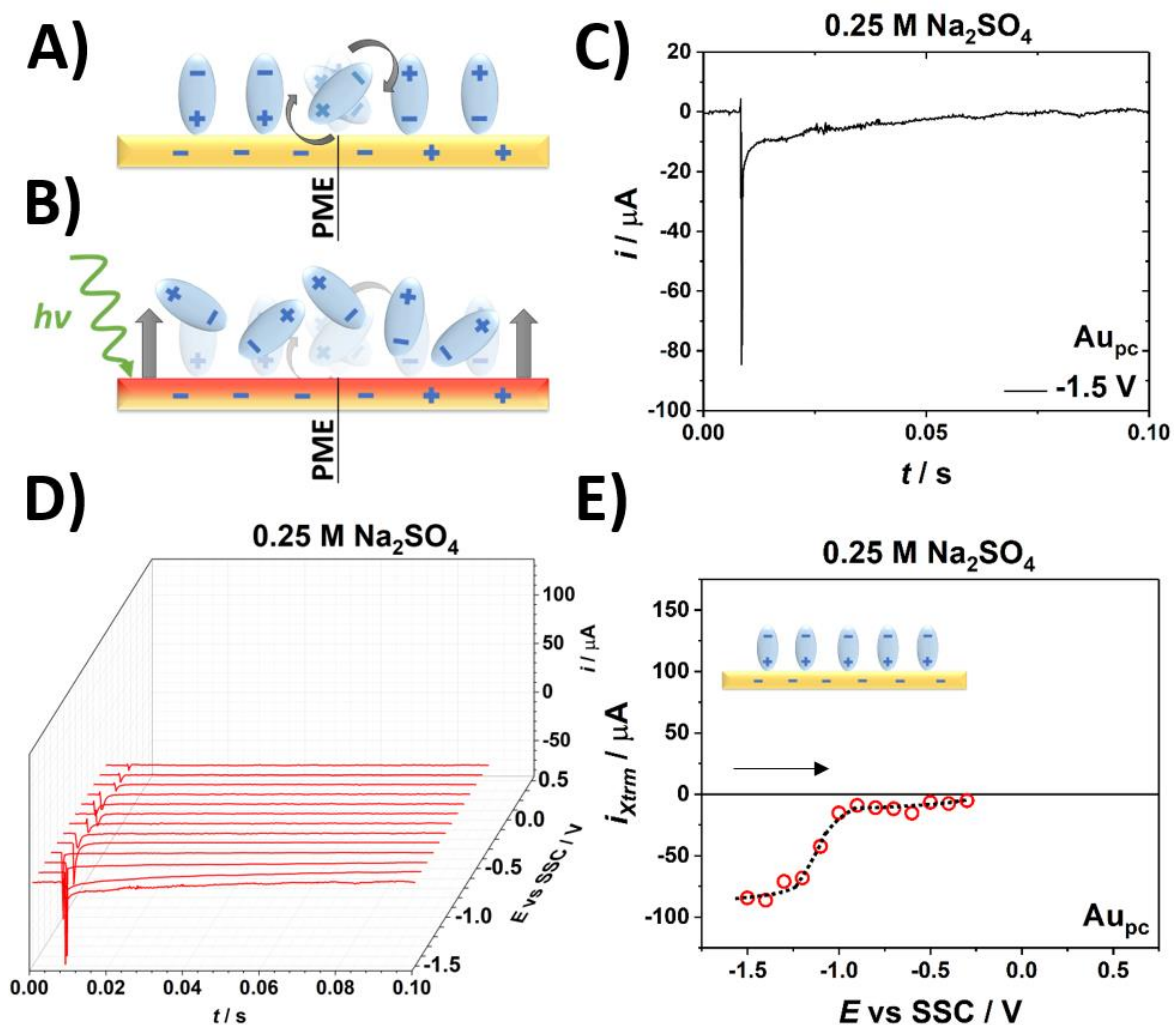
***Figure 5.1***. *(A) Schematic orientation of water molecules towards the electrode according to the surface charge. (B) Disorder introduced by the laser-induced temperature jump at the electrode surface. (C) Single current transient recorded after illuminating the polycrystalline Au electrode in 0.25 M Na₂SO₄ at -1.50 V vs SSC (background corrected curve). (D) 3D plot for the polycrystalline Au electrode representing the change in the orientation of the LICTs obtained within the potential range between -1.50 V and -0.30 V vs SSC. (E) Dependence of the extreme values of the current transients depicted in part D as a function of the WE potential. Inset schematically illustrates corresponding orientation of the surface dipoles at the investigated potential range. Black arrow shows the scan direction.*

Upon the increase in the electrode potential, the structure of the interfacial water layer alters resulting in a decrease in its stiffness. Finally, at -0.20 V vs SSC, the disorder of the molecules reaches the maximum. At this potential, identified as the PME, the system does not show any prominent transient response to the laser illumination (see **Figure 5.2A** and **B**). In turn, at the

91

potential values higher than the PME, the transients change their sign. This indicates that the resulting excess charge of the electrode surface becomes positive, at the same time forcing the interfacial water molecules to reorient (**Figure 5.2C** and **D**).
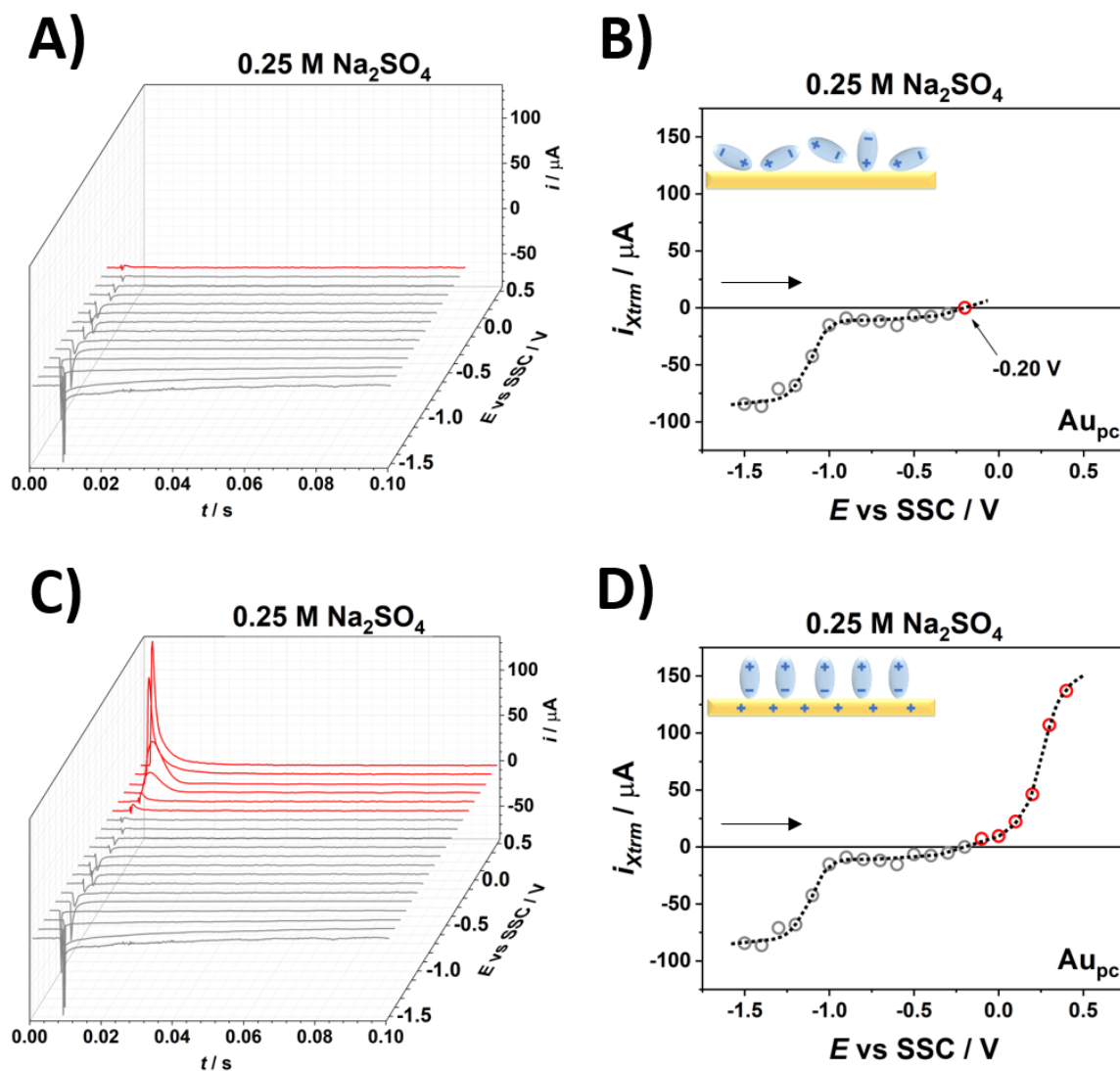


***Figure 5.2.*** *(A) LICTs obtained for the polycrystalline Au electrodes immersed in the 0.25 M Na$_2$SO$_4$ solution within the continuously extended potential range between -1.50 V and -0.20 V vs SSC. The curve corresponding to the PME is depicted in red. (B) 2D graph representing the dependence between the maximal current values of the transients shown in A and the WE potential. (C) LICTs collected for the same system within the potential range of -1.50 V – 0.50 V vs SSC together with the (D) corresponding dependence of the maximal current values of the transients depicted in C shown as a function of the electrode potential. Insets schematically demonstrate the orientation of the water dipoles at the investigated potentials. Black arrows indicate the scan direction.*

## 5.2 Interface Structure and Electrode Activity

In a recently published article, Koper et al. have demonstrated a relation between the charge-dependent structure of the double layer and the rate of the HER.[172] As suggested in that work, the degree of order in the interfacial layer should have a direct influence on the electron transfer through it affecting the electrode activity towards hydrogen evolution. As shown in the previous sections of this work, the reactions vital for a sustainable provision of renewable energy, such as the HER or the ORR, proceed through the initial adsorption of species at the catalyst surface (see **Section 3.4.1** and **Section 3.4.5**). In order to permit these reactions to take place, an electron has to be transferred through the interface. Thus, for a set electrode structure and composition, the reaction kinetics would likely depend on the ability of the double layer to reorient after accommodating such a transfer.[172]
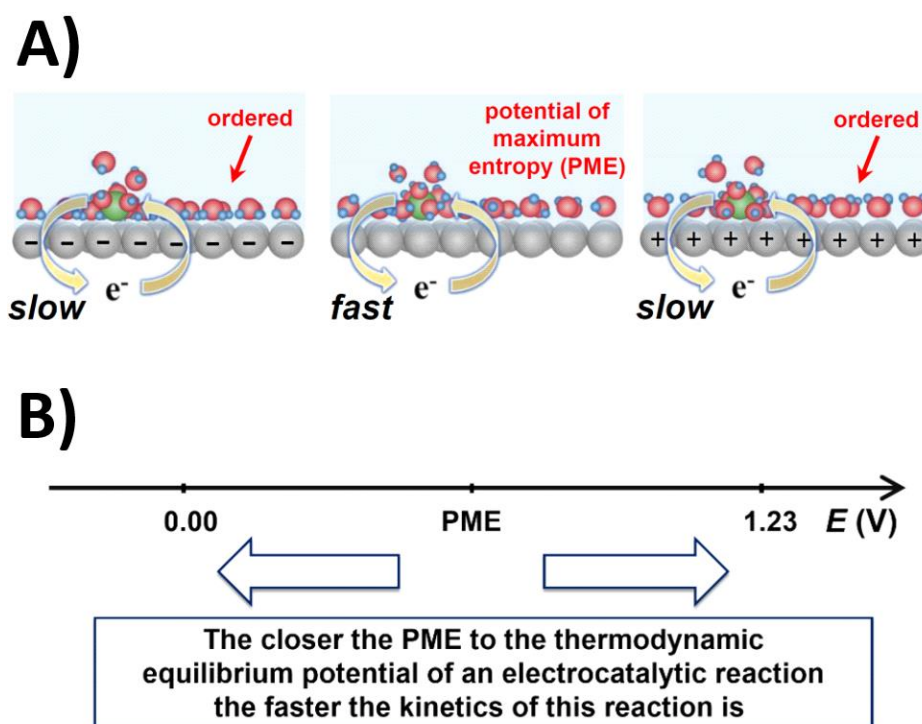


*Figure 5.3. (A) Schematic representation of the electron transfer taking place at the electrode/electrolyte interface according to the charge-dependent structure of the surface water layer. Note that the electron migration is the fastest at the PME, while at the potentials remote from the PME, the process slows down. (B) Graph illustrating the relation between the PME position and the rate of the HER (0.00 V vs RHE) and the ORR (1.23 V vs RHE).*

Following this line of thought, one can expect that the rate of an electrochemical reaction will be the highest at the PME at which the entropy of the double layer formation reaches the maximum. Conversely, at the potentials remote from the PME, the ease of the electrode transfer to occur is supposed to decrease slowing the reaction down (see **Figure 5.3A**). Considering the dependence mentioned above, one could anticipate that the closer the PME to the thermodynamic equilibrium potential of a certain reaction is, the faster this reaction should proceed (**Figure 5.3B**).

In the following sections, experimental validation of the aforementioned hypothesis is presented. For this purpose, the resulting net surface charge of metal electrodes immersed in various electrolytes of different pH and containing different alkali-metal cations is studied using the LICT method. It is shown that the application of the laser technique enables a profound examination of the influence of the electrolyte composition on the interface structure. Afterwards, the acquired LICT data are correlated with the results of the HER and the ORR activity measurement performed in the corresponding systems.

### 5.2.1 pH Effect

In the first step, simple systems consisting of the $Pt_{pc}$ immersed in aqueous $HClO_4$ solutions at different pH levels (pH 0, 1, and 2) were examined. By using aqueous electrolytes containing only $H^+$, and non-adsorbing $ClO_4^-$ anions, it was possible to solely investigate the influence of the electrolyte pH.

**Figure 5.4A**, **B**, and **C** represent typical examples of the LICTs collected in the $HClO_4$ electrolyte with three different $H^+$ concentrations. In each case, the orientation of the resulting transients alters from negative to positive, revealing the PME. The estimated potential values at which the sign of the current spikes changes are located at ~0.31 V, ~0.37 V, and ~0.41 V vs RHE for electrolytes at pH 0, 1, and 2, respectively. One can see that the PME increases (in this case by ca. 50 mV/dec) as a consequence of the pH rise. These findings coincide with the results reported for the basal Pt electrode planes. As shown by Garcia-Araez et al., the PMEs of these surfaces exhibit sensitivity to the electrolyte pH.[170] As further demonstrated by the authors, the potential at which water molecules change their orientation towards the Pt(111) surface shows the pH dependence shifting by ca. 60 mV/dec. Analogously, the PME of Pt(100) and Pt(110)

planes also increases with the decrease in the proton concentration. In these cases, however, the recorded shifts are less significant; for the former, the PME value increases by 30 mV/dec, while for the latter, the recorded change is only 15 mV/dec. Since the polycrystalline surfaces consist of an irregular arrangement of the monocrystalline facets and grains,[348] one can expect that, to a certain extent, trends observed for these types of surfaces will reflect the trends of its individual "surface components". Thus, the PME of $Pt_{pc}$ electrodes should also exhibit a pH dependence with a more or less gentle $\frac{dE_{PME}}{d\text{pH}}$ slope.
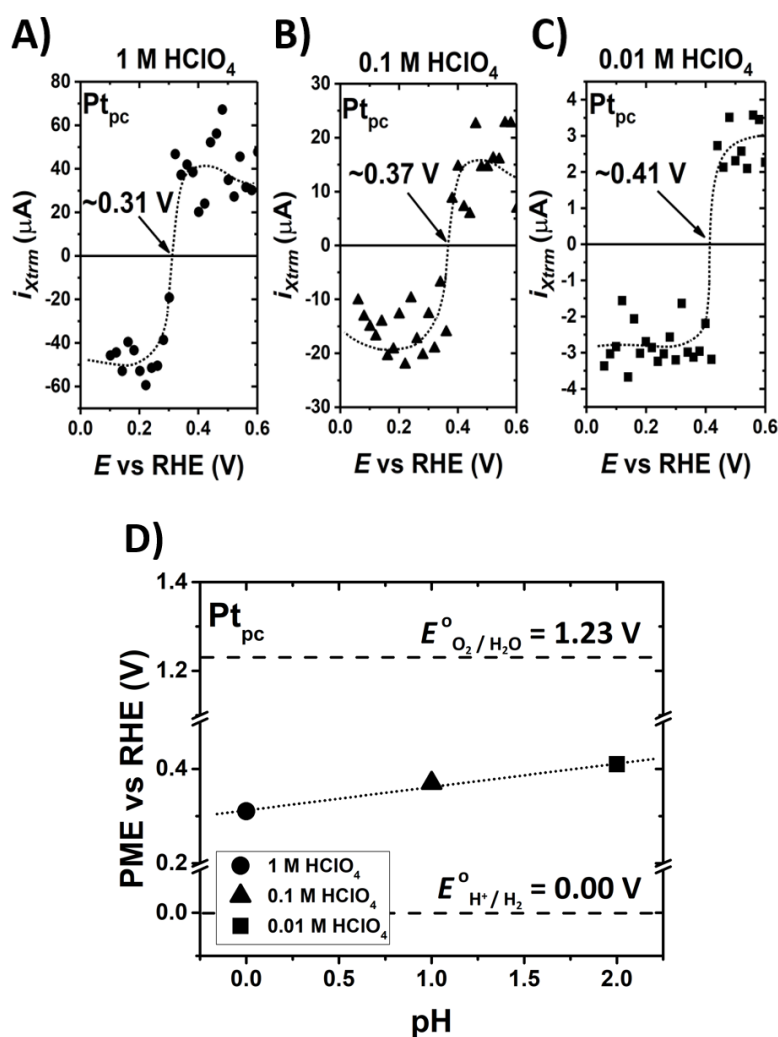


*Figure 5.4.* *Maximal current extrema of the LICTs collected for $Pt_{pc}$ in acidic electrolytes with different pH levels: (A) pH 0, (B) pH 1, and (C) pH 2. The estimated points at which the sign of the current transients changes coincide with the PMEs. Note that each system exhibits the PME. Black dotted lines are used to guide eyes. (D) Dependence of the resulting PME values shown as a function of the pH. Black dashed lines at 0.00 V and 1.23 V vs RHE additionally show the thermodynamic equilibrium potentials of the HER and the ORR, respectively, while the straight dotted line depicts the trend line.*

Interestingly, as displayed in **Figure 5.4D**, upon the increase in the pH, the PME of the Pt electrode moves further away from the thermodynamic equilibrium potential of the HER (0.00 V vs RHE), at the same time, getting closer to the corresponding value of the ORR (1.23 V vs RHE). On the basis of the hypothesis relating the stiffness of the electrochemical interface with its ability to facilitate the electrode transfer, one can anticipate that the modification of the PME will have an impact on the electrocatalytic behavior of the studied systems.[172] In order to check whether these predictions are correct, measurements of the $Pt_{pc}$ activity towards the HER and the ORR have been conducted. The experiments were performed in the corresponding three $HClO_4$ solutions saturated with either $H_2$ (for the HER) or $O_2$ (for the ORR). To additionally increase the efficiency of the diffusion mass transport, and the sensitivity of the activity measurements to potential changes, microelectrodes were used.[349]
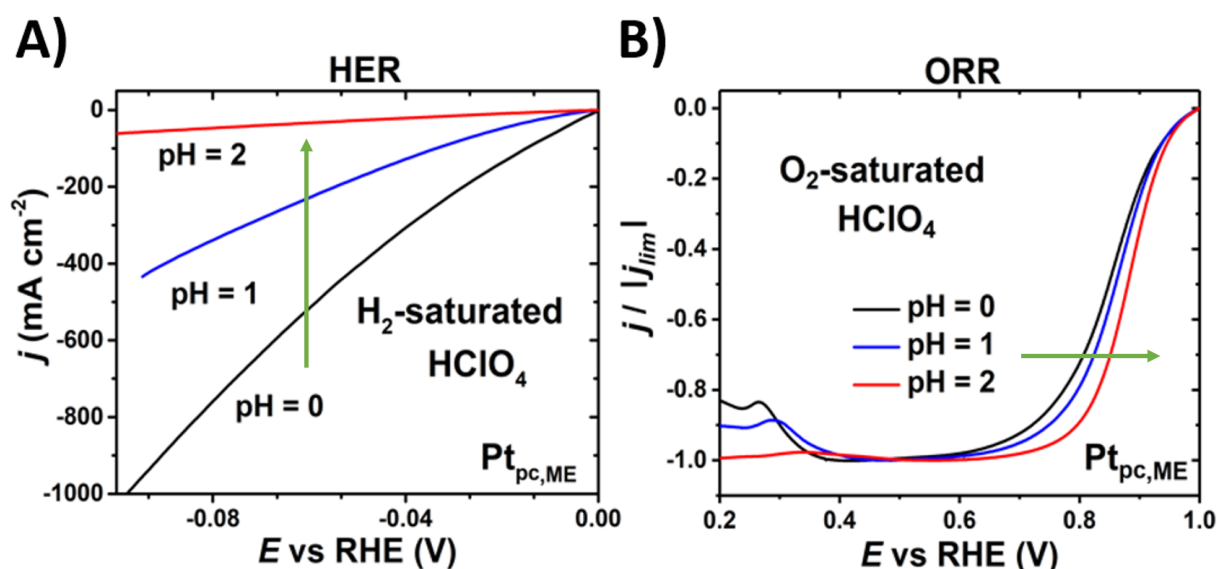


***Figure 5.5***. *Polarization curves for (A) HER and (B) ORR on $Pt_{pc}$ microelectrode in $H_2$- and $O_2$-saturated $HClO_4$ solutions at three different pHs. Both in the case of the HER and the ORR, a clear pH dependence of the electrode activity can be seen. Green arrows depict the pH increase. Scan rate: $dE\ dt^{-1} = 10\ mV\ s^{-1}$.*

**Figure 5.5** shows the resulting polarization curves recorded in the $HClO_4$ solutions at different pHs. One can see that in the examined systems, both the HER and ORR activities exhibit the pH dependence. It should be, however, noted that the increase in the pH has a different effect on the electrode activities towards the investigated reactions. The HER activity of the electrode significantly diminishes with the pH increase (**Figure 5.5A**). The opposite trend is observed for the ORR activity (see **Figure 5.5B**).

The experimental findings show that in the investigated systems the pH-driven modification of the PMEs location indeed leads to the alteration in the electrode activity towards the studied reactions. The pH increase shifts the PME from the values located in the vicinity of the onset potential of the HER towards the potential at which the ORR is supposed to occur (**Figure 5.4D**). As a consequence, the surface water layer at the potentials closer to the 0.00 V vs RHE should become stiffer making the solvent molecules less likely to reorganized after the interfacial electron transfer. This diminishes the HER activity of the Pt electrode (**Figure 5.5A**). In contrast, the activity of the ORR increases (**Figure 5.5B**).

The obtained activity trends are in relatively good agreement with the previous literature reports. As mentioned in **Section 3.7.3**, it had been reported that the rate of the HER at polycrystalline Pt electrode indeed gets higher with the increase in the $H^+$ concentration.[88] A thorough search of the relevant literature yielded no reported studies clearly showing the influence of the $H^+$ concentration on the electrocatalytic activity of a polycrystalline Pt electrode towards the ORR. The obtained results, however, are in line with those published by Briega-Martos et al. presenting the increase of the Pt(111) activity upon the pH rise (see **Section 3.7.3**).[273] It is also worth noting that the PMEs in the investigated systems are located within the potential region of hydrogen adsorption.[170] As the PME value can be influenced by the adsorbing species (see **Section 3.6.3**), one can anticipate that the interface structure should likely exhibit sensitivity to the alteration in the $H^+$ concentration.

### 5.2.2 pH Effect in Presence of Alkali-Metal Cations

Remarkably, electrolytes utilized in electrocatalytic studies of the pH effect often differ from one another not only in the pH level but also in the entire composition.[88] As the resulting behavior of an electrochemical system is most likely related to the hydration energy of all the electrolyte species, it can be expected that electrocatalytic properties of such a system will exhibit sensitivity to the presence of both $H^+$ and other electrolyte ions.[24,242,248] To shed further light on the interplay of these two factors, a series of laser measurements on the $Pt_{pc}$ immersed in 0.5 M solutions of $Na_2SO_4$ and $K_2SO_4$ at various pHs was carried out. In these measurements, a new type of species, namely the alkali-metal cations, was introduced. Furthermore, the perchlorate anions were replaced with (bi)sulfates ones. Unlike the $ClO_4^-$ species (characterized by the hydration energy of 229 kJ mole$^{-1}$), the $SO_4^{2-}$ exhibit much higher hydration energy

(1059 kJ mole$^{-1}$) than the Na$^+$ (409 kJ mole$^{-1}$) and K$^+$ (322 kJ mole$^{-1}$) cations.[350] Therefore, it was less likely for the SO$_4^{2-}$ anions to show an effect competitive to the effect of the other electrolyte species. This, in turn, assured that the alterations in the interface properties were related solely to the changes in the H$^+$ concentration and the nature of the alkali-metal cations.

**Figure 5.6A** depicts the 3D LICT graph recorded for the polycrystalline platinum electrode in the 0.5 M Na$_2$SO$_4$ solution at pH 3. From the obtained results, one can see that at the very low potentials, the surface water dipoles tend to orient themselves with the hydrogen sides towards the metal electrodes. Then, along with the potential increase, the net orientation with the oxygen sides pointing the surface becomes more favorable. As a consequence, the investigated system exhibits the PME. This can be seen more clearly in **Figure 5.6B** representing the corresponding dependence between the maximal current and the applied potential. A very similar trend was observed for all the other investigated pH values. **Figure 5.6C**, **D**, and **E** illustrate sample 2D $i_{Xtrm}$-$E$ plots recorded at pH 5, 8, and 12, respectively. In all these systems, the "potentials of no current response" are very close to one another and do not show a dependence on the pH level (see **Figure 5.6F**). The overall value of the PME of the polycrystalline platinum electrode can be given as:

$$E_{PME} = 0.095 \pm 0.022 \text{ V}$$
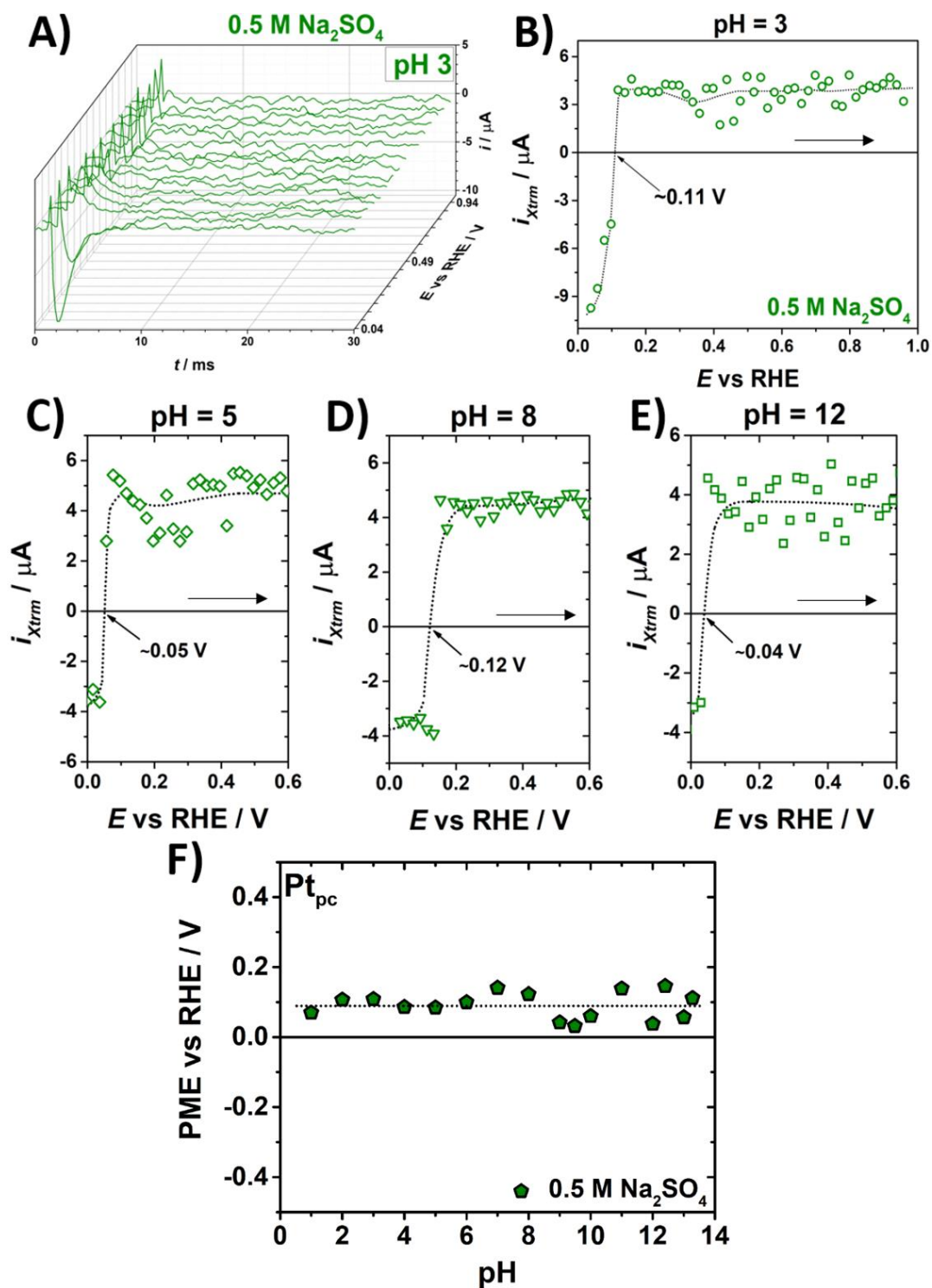
**Figure 5.6.** *(A) Typical 3D LICT plot recorded for polycrystalline Pt electrode in 0.5 M Na₂SO₄ at pH 3 with (B) the corresponding 2D representation of the collected maximal current extrema shown as a function of the WE potential. Analogous 2D LICT plots showing the maximum current values obtained at (C) pH 5, (D) pH 8, and (E) pH 12. The 3D graph depicts every third potential step. Additional black arrows point the scan direction, while the black dotted curves serve as guides for eyes. (E) PME of the $Pt_{pc}$ in 0.5 M Na₂SO₄ depicted as a function of the electrolyte pH. The straight dotted line represents the trend line.*

One can see that in 0.5 M $Na_2SO_4$ the PME of the $Pt_{pc}$ becomes independent of the electrolyte pH. Thus, assuming a dominant effect of the alkali-metal cations, the $Na^+$ cations seem to stabilize the structure of the EDL. Interestingly, the obtained results are consistent with the literature reports. According to Gileadi et al., the PZC of the polycrystalline Pt surface measured in aqueous sodium salt solutions using impedance spectroscopy is indeed independent of the $H^+$ concentration.[351] As the PME of a metal electrode is located in the close vicinity of its PZC, the PME should not change with the electrolyte pH, too.

To further understand the role of the cations for the system behavior at various pHs, analogous measurements for the $Pt_{pc}$ electrode in the 0.5 M $K_2SO_4$ electrolytes with different $H^+$ concentrations were conducted. Quite surprisingly, the electrode immersed in the electrolytes containing $K^+$ cations does not show the PME at most of the investigated pHs. Instead, in these solutions, the sign of the electrode surface charge is constant within the whole examined potential range. **Figure 5.7** shows examples of corresponding 3D (parts A and C) and 2D (parts B and D) LICT graphs collected in 0.5 M $K_2SO_4$ at two different pHs. In the solution containing a higher concentration of $H^+$, the sign of the net charge stays positive within the investigated potential region (**Figure 5.7B**). In contrast, in the alkaline solution, the charge of the surface becomes negative and does not change its sign upon the potential increase (**Figure 5.7D**). The same trend was observed for the very acidic electrolytes (pH 1 to 3) as well as for the electrolytes with the pH ranging from neutral to highly alkaline (pH 7 to 13.70) (see **Figure 5.7E**). In these systems, the PMEs might be located outside of the set potential range; however, in order to avoid the gas generation, the investigated regions were not further extended.[45] As suggested by Huang et al., it is also likely that in some electrolytes the electrode does not exhibit the PME.[352] In such cases, electrolyte species adsorbing at the electrode surface can alter its electronic structure resulting in a constant sign of its surface charge.

**Figure 5.7.** *3D LICT graphs obtained for the polycrystalline platinum electrode immersed in 0.5 M K₂SO₄ at (A) pH 2, and (C) pH 13 together with the (B,D) corresponding 2D plots showing the relation between the extreme current values and the applied potential. For the sake of clarity, the 3D graphs depict every third step. Dotted lines serve as guides to eyes. (E) Trend lines of extreme current values obtained in K⁺-containing solution at various pHs. Note that in most of the electrolytes the sign of the charge does not change within the investigated potential range. Dashed lines represent extrapolated parts of the trend lines. Black horizontal arrows show the scan direction.*

Interestingly, in 0.5 M $K_2SO_4$, the potentials at which the current transients change their orientation were detected only at pH 4, 5, and 6. **Figure 5.8A** depicts the relevant sample 3D graph. The estimated PMEs at all three pHs are equal to ~0.12 V (**Figure 5.8B**), ~0.14 V (**Figure 5.8C**), and ~0.46 V (**Figure 5.8D**) vs RHE, respectively. One can see that dissimilarities between the estimated potentials of no response in the potassium-containing electrolytes are more significant than those observed in sodium salt solutions. This clearly shows that, in the presence of $K^+$ cations, the PME exhibits a higher sensitivity to the $H^+$ concentration than in the presence of $Na^+$ cations.



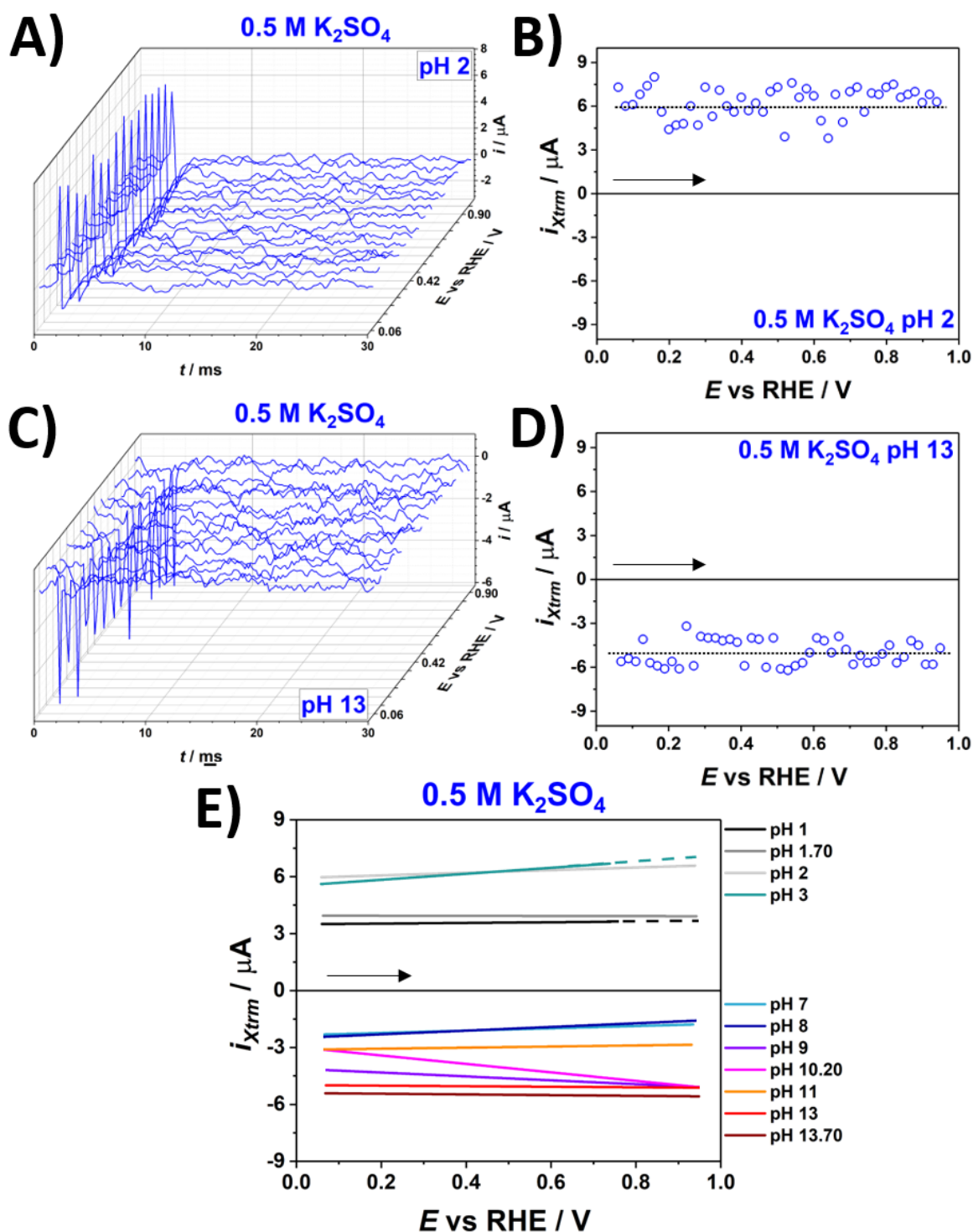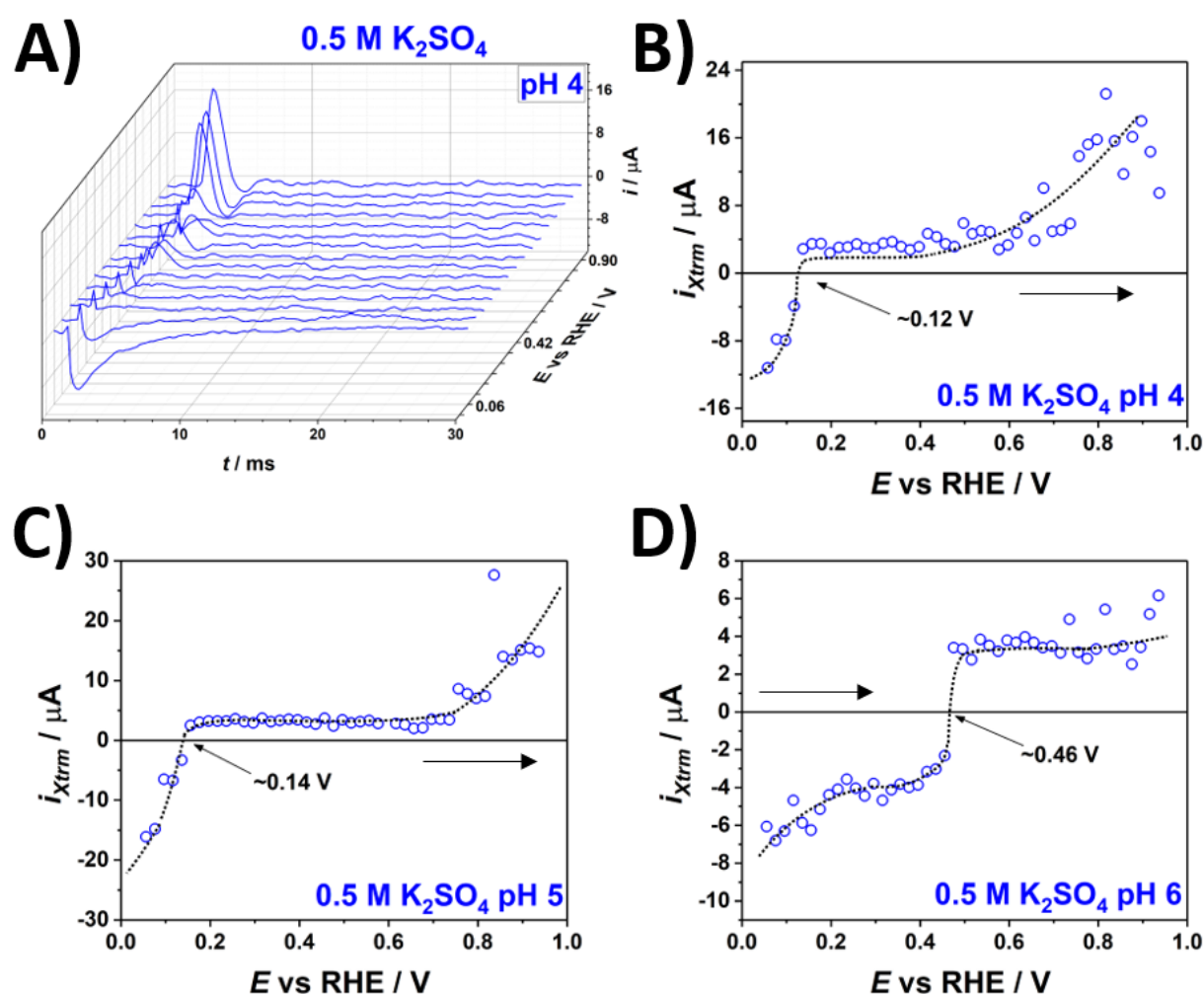***Figure 5.8.*** *3D LICT graphs obtained for the polycrystalline Pt electrodes in 0.5 M $K_2SO_4$ at (A) pH 4 together with the (B) corresponding dependence between the recorded extreme current values and the WE potential. For the sake of clarity, the 3D graphs represent every third potential step. Analogous 2D plots showing the extreme current values obtained at (C) pH 5 and (D) pH 6. Black arrows depict the scan direction, while the dotted lines are used as guides for eyes.*

The non-trivial trends in the investigated systems reveal the complexity of the issue related to the influence of the electrolyte composition on the double layer structure. In the systems containing sodium salt solutions, the nature of the cations appears to play a dominant role in establishing the solid/liquid interface making its structure practically independent from the electrolyte composition. Conversely, in the presence of potassium cations, the interface order can drastically change even with small alterations in the concentration of the electrolyte constituents. Thus, further analysis of the effect of individual species required the use of other model systems. The platinum electrode immersed in the solutions at pH 6 served this purpose. The use of the near-to-neutral pH electrolytes had two main benefits. Firstly, it allowed to maximally lower the effect arising from the excessive amount of the protons or hydroxyl ions on the obtained results without losing an efficient control over the pH. Secondly, the existence of the PMEs in these systems (see **Figure 5.6** and **Figure 5.8**) permitted to investigate the correlation between the properties of the interface and the electrode activity. For these reasons, in the further studies, the focus was narrowed down to the systems using almost neutral electrolytes.

### 5.2.3   Influence of Cations

**Figure 5.9** shows the maximal values of the LICTs obtained for the $Pt_{pc}$ electrode in 0.5 M $Na_2SO_4$ and 0.5 M $K_2SO_4$ solutions at pH 6. The estimated location of the PME in the former electrolyte is ~0.10 V vs RHE, while the PME value in the latter equals to ~0.46 V vs RHE. One can see that, in the examined systems, the sodium cations "move" the PME towards the more negative voltages. Hence, depending on the nature of positively charged species introduced into the system, the interfacial solvent layer gets less stiff and more likely to reorient in the vicinity of the thermodynamic equilibrium potentials of either the HER (0.00 V vs RHE) or the ORR (1.23 V vs RHE). By analogy to the experiments with the $HClO_4$ solutions (see **Section 5.2.1**), the cation-dependent structure of the surface $H_2O$ adlayer should affect the electrode activity towards these reactions.

103
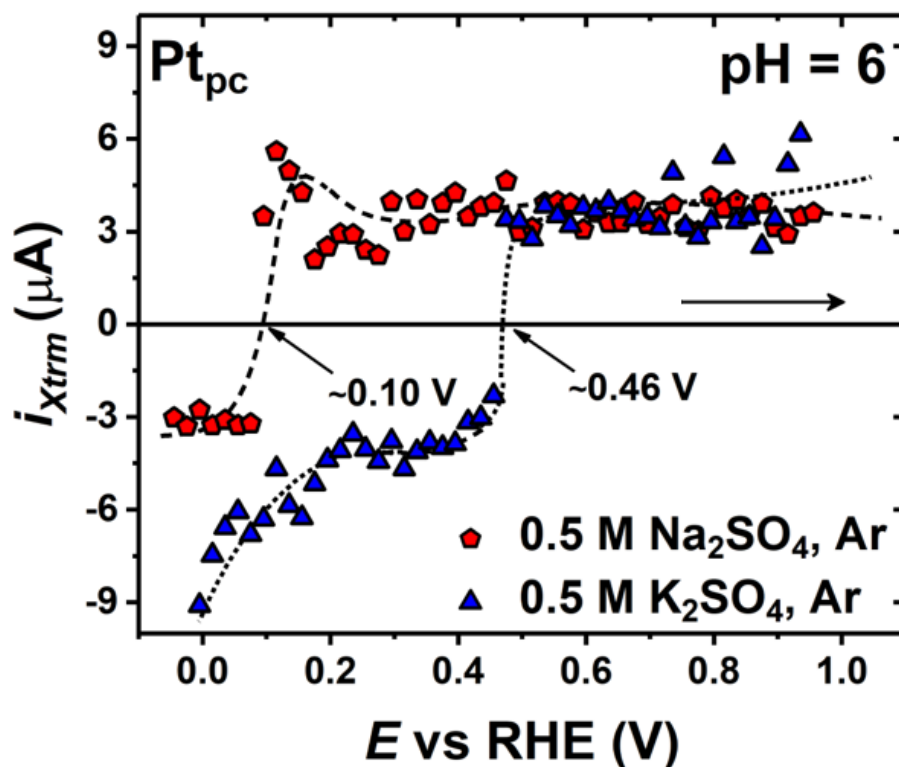
***Figure 5.9***. *Extreme current values of the LICTs collected for the polycrystalline Pt electrode immersed in the near-to-neutral pH electrolytes containing $Na^+$ (depicted in red) and $K^+$ (depicted in blue) cations. Black dashed and dotted lines serve as guides for eyes, while the black horizontal arrow depicts the scan direction. Each system shows the PME; however, the detected PME values differ significantly from each other.*

To check if these predictions have any correspondence to reality, the relevant activity measurements were performed. **Figure 5.10A** and **B** show the polarization curves for the HER and the ORR, respectively, obtained for the $Pt_{pc}$ in different salt solutions at pH 6. One can see that the presence of dissimilar alkali-metal cations indeed influences the electrode activity towards the investigated reactions. The HER is faster in the $Na^+$-containing solutions than in the $K^+$-containing ones (**Figure 5.10A**). In contrast, the rate of the ORR appears to be higher in 0.5 M $K_2SO_4$ than in 0.5 M $Na_2SO_4$ (**Figure 5.10B**). These observations coincide with the trends reported in the literature for Pt(111). As shown by Tymoczko et al., both the HER and the ORR performed on the monocrystalline Pt electrode in presence of (bi)sulfate anions exhibit sensitivity to the nature of alkali-metal cations.[247] Furthermore, depending on the reaction, the presence of some cations is more beneficial than the others. The rate of hydrogen evolution in the electrolyte containing sodium is indeed higher than that measured in the presence of potassium. Conversely, the reduction of oxygen is more favored in the systems containing $K^+$ than in those which contain $Na^+$.
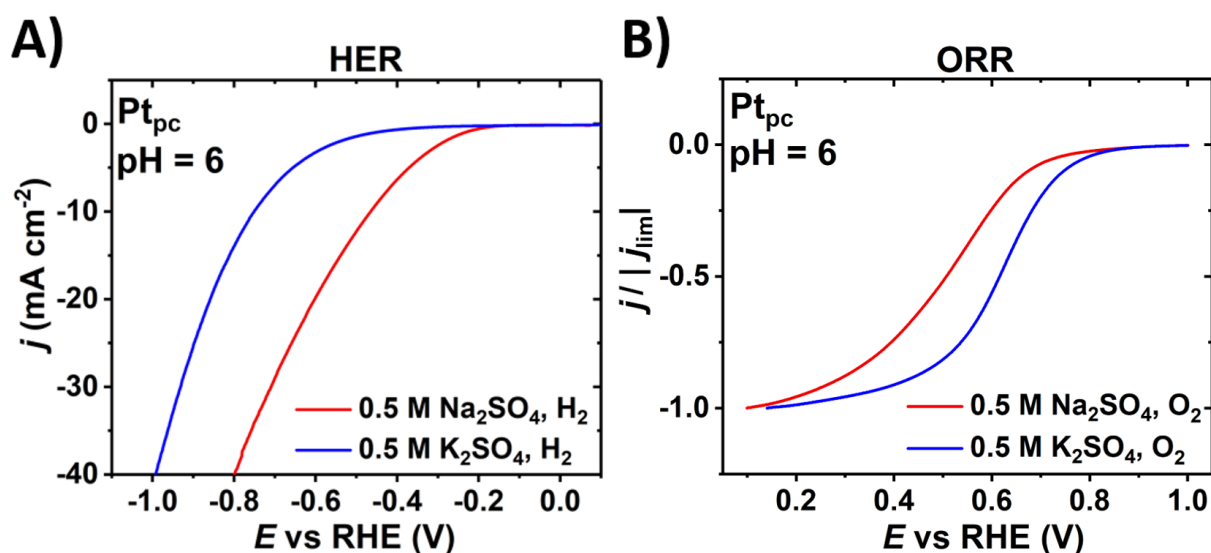
***Figure 5.10.*** *Polarization curves for the (A) HER and the (B) ORR for the $Pt_{pc}$ disk electrode immersed in the $H_2$- and $O_2$-saturated near-to-neutral pH 0.5 M $Na_2SO_4$ (depicted in red) and 0.5 M $K_2SO_4$ solutions (depicted in blue). The electrode activity towards both reactions shows opposite trends in the electrolytes containing different alkali-metal cations. Scan rate: $dE\,dt^{-1} = 50\,mV\,s^{-1}$; rotating speed: 400 rpm. Note that the negative shift in A is due to the change in the surface pH during the reaction, as explained by Auinger et al.[271] However, this does not change the relative activity trend.*

Interestingly, laser experiments performed on the polycrystalline Au electrode revealed similar trends. **Figure 5.11** shows the extreme current values of the LICTs collected in near-to-neutral pH 0.25 M $Na_2SO_4$ (discussed in **Section 5.1**) and 0.25 M $K_2SO_4$ electrolytes. In both systems, the current spikes change their signs upon the potential increase revealing the PMEs. Furthermore, similar as for the Pt electrode, the PME value of the Au electrode is significantly affected by the nature of the cation species present in the electrolyte. The estimated potentials of zero response in the sodium and potassium salt solutions are 0.20 V and ~1.57 V vs RHE, respectively. Again, it can be clearly seen that in the presence of $Na^+$ cations, the PME value is located at the more negative potentials indicating a less ordered array of the interfacial water dipoles at the potentials vicinal to the thermodynamic equilibrium potential of the HER (0.00 V vs RHE). In contrast, in the presence of $K^+$ species, the recorded potential at which the electrode surface charge changes its sign is much more positive, which implies a more chaotic arrangement of the $H_2O$ molecules within the voltage range around the onset potential of the ORR (1.23 V vs RHE).
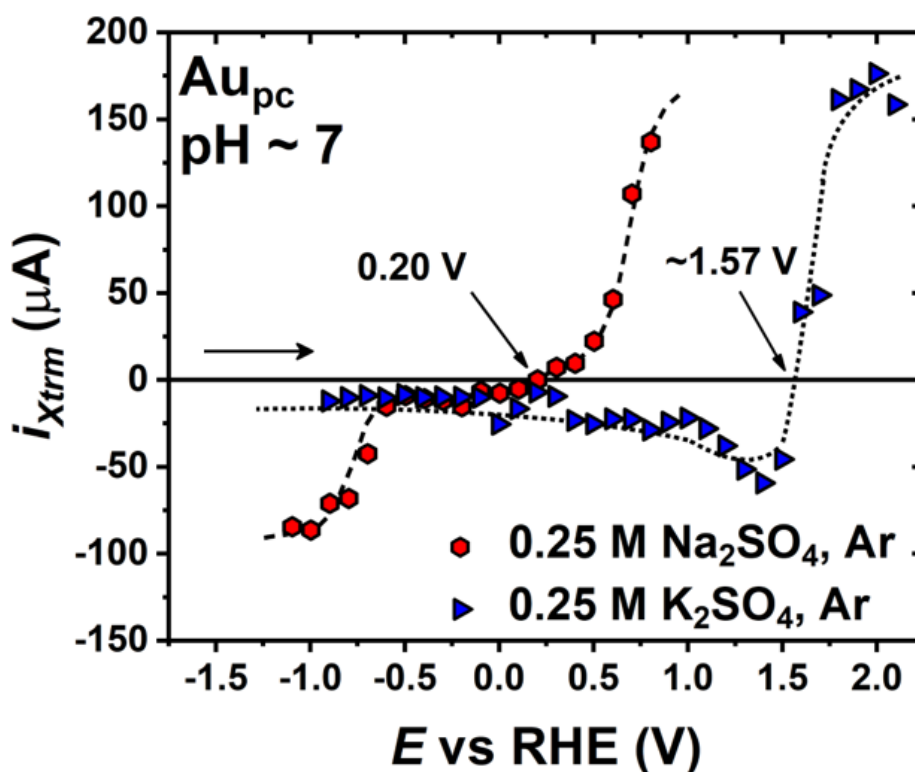
**Figure 5.11.** *Extreme current values of the LICTs recorded for the $Au_{pc}$ electrode in the near-to-neutral pH solutions containing $Na^+$ (depicted in red) and $K^+$ (depicted in blue) cations. Black dashed and dotted lines are used as guides for eyes, while the black horizontal arrow shows the scan direction. Similar to the case with the $Pt_{pc}$ electrode, the systems exhibit single PMEs located remotely from each other.*

In the next step, the activity measurements on $Au_{pc}$ in both the $Na_2SO_4$ and $K_2SO_4$ solutions were performed. By doing so, it was possible to find out whether there is a correlation between the different interface structure and the electrocatalytic activity of the gold electrode towards the reactions mentioned above. **Figure 5.12A** and **B** represent the resulting HER and ORR polarization curves, respectively. The obtained findings show trends similar to the ones recorded for the case of the platinum surface. That is to say, the activity of polycrystalline gold towards the HER is significantly higher in the sodium sulfate than in the potassium sulfate solution. Nonetheless, in the presence of the $K^+$ cations, the electrode activity is higher towards the ORR if compared with the Na-containing electrolytes.
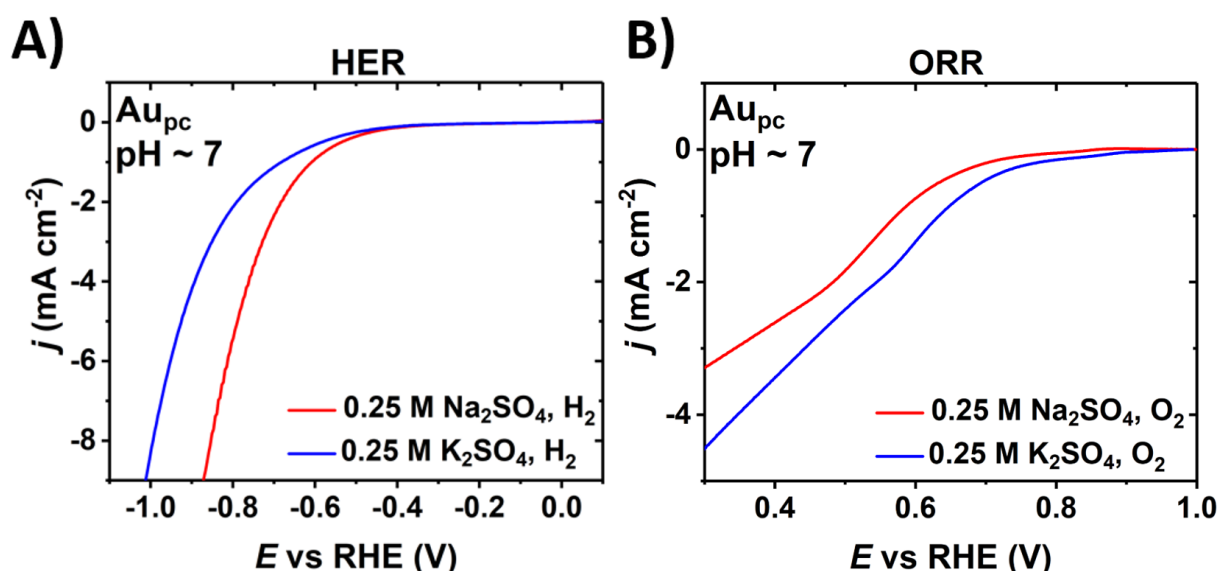
***Figure 5.12***. *Polarization curves for the (A) HER and the (B) ORR recorded for the $Au_{pc}$ bead electrode in the $H_2$- and $O_2$-saturated near-to-neutral pH electrolytes containing different alkali-metal cations: $Na^+$(depicted in red) and $K^+$ (depicted in blue). By analogy with the activity measurements on $Pt_{pc}$, the activities of the investigated reactions on the $Au_{pc}$ electrode also exhibit an opposite dependence on the nature of the alkali-metal cations present in the electrolytes. Scan rate: $dE\ dt^{-1} = 50\ mV\ s^{-1}$; rotating speed: 400 rpm.*

The presented results acquired for both the Pt and the Au electrodes are again consistent with the hypothesis suggesting the explanation of the effect of the surface water structuring on the interfacial electron transfer. They reveal the direct correlation between the PME value of a given electrode in certain electrolytes and its electrocatalytic performance. By analogy with the case shown in **Section 5.2.1**, by changing the electrolyte composition (in this case by introducing different alkali-metal cations), one can alter the location of the PME. The change in the PME, in turn, alters the EDL stiffness at certain potential values, which further influences the electron transfer through the interface making it either easier or more difficult to proceed. The resulting "facility" of the interfacial transport eventually affects the electrode activity increasing or decreasing the rate of a particular electrocatalytic reaction.

As shown before, the cation effect is most likely associated with the different nature of the positively charged ions (see **Section 3.7.3**). Various cations characterized by dissimilar hydration energies interact with the adsorbed species (e.g., water) affecting the structure of the electrified interface and influencing the electrocatalytic activity.[45] Furthermore, the system behavior might also originate from the resulting local concentration of electrolyte species in the vicinity of the electrode surface. As recently presented by Garlyyev et al., the estimated

concentration of alkali-metal cations in the double layer formed between salt electrolytes and metal electrodes consisting both of Pt and Au is up to ~80 times higher than the bulk molarity of the positively charged species.[277] The high amount of the cation species interacting with other constituents of the double layer might intensify the observed effect modifying the interfacial array even more significantly. Thus, the cation effect should rather be seen as an interplay between the nature and the effective concentration of the cations in the electrified solid/liquid interface.

To conclude, profound LICT studies of the interface formed between polycrystalline Pt and Au electrodes and aqueous electrolytes together with the corresponding CV measurements reveal a good correlation between the interface structure and the rate of some electrocatalytic processes. As shown by the example of the HER and the ORR, the electrode activity towards these reactions in perchloric acid solutions and near-to-neutral pH electrolytes containing different alkali-metal cations (i.e., $Na^+$ and $K^+$) indeed appears to depend on the ability of the EDL to reorient after the interfacial electron transfer. Furthermore, the performed experiments show that this particular characteristics of the electrochemical interface strictly depends on the electrolyte composition. A various $H^+$ concentration as well as different types of alkali-metal cations alter the stiffness of the interfacial solvent layer at different potentials, which eventually results in either enhancement or hindrance of electrocatalytic processes. The aforementioned findings once more expose an influence of the different nature of electrolyte constituents on the kinetics of electrocatalyzed reactions. Furthermore, they can explain why electrolytes govern the electrode activity in many systems. Finding an answer for this question should set out a new course in understanding numerous electrochemical processes, enabling optimization and development of systems essential for the sustainable energy provision.

## 5.3 Non-Precious Metal Electrocatalysts

High costs and scarcity of noble metals utilized in WELs and FCs are frequently recognized as the main drawbacks of these technologies. Hence, the identification of new non-precious metal catalysts might be a rational route to overcome these issues.[353] Manganese oxides are an example of such materials. These cheap and earth-abundant compounds can be utilized to catalyze both the OER and ORR.[354,355] Especially promising one is Mn(III) oxide ($Mn_2O_3$)

which, owing to its unique structure, offers the best balance between the activities towards the oxygen reactions among the Mn oxides.[356]

In this part, the interface formed between $Mn_2O_3$ electrodes and an aqueous alkaline electrolyte is examined. As in the previous sections, the LICT method and CV were used to inspect a correlation between the structure of the EDL and the ORR activity of the Mn-catalyst. Furthermore, in order to better understand interfacial processes occurring in the system, the findings acquired from the laser experiments are compared with those obtained from the impedance analysis.

### 5.3.1   Interface Structure and ORR Activity

**Figure 5.13** displays typical LICTs recorded for the $Mn_2O_3$ electrodes in $O_2$-saturated 1 M NaOH at four arbitrarily chosen potential values: 0.91 V, 1.03 V, 1.11 V, and 1.19 V vs RHE. Right after heating the electrode surface, one can see negatively and positively oriented current transients.
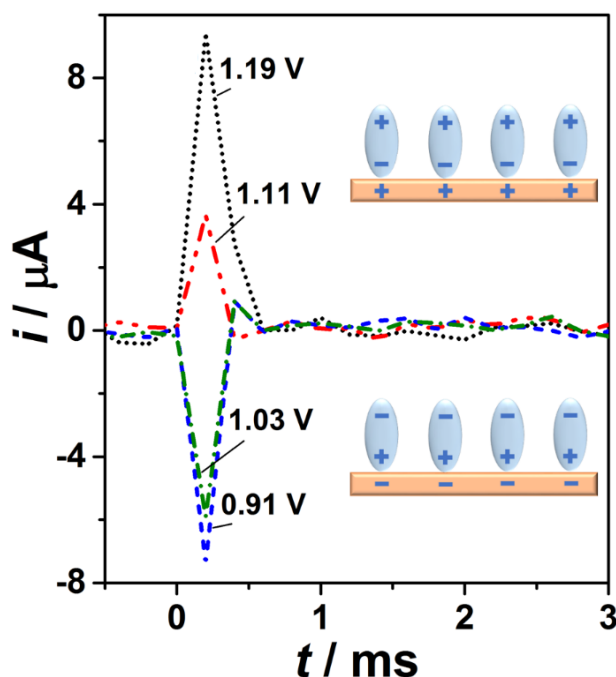


*Figure 5.13. Sample LICTs obtained for the Mn₂O₃ electrode in O₂-saturated 1 M NaOH at different potentials and the schematic illustration of the water molecules arrangement at the electrode surface according to the sign of the excess charge.*

The orientation of the recorded LICTs alters along the investigated potential range revealing the existence of the PME. This can be clearly seen in **Figure 5.14** displaying the relation between the maximal current values and the WE potential. Following the direction opposite to the direction of the performed LICT scan, one can see that at the high potential values the observed current peaks are oriented positively. Then, at ~1.09 V vs RHE (at the PME), their orientation alters and stays negative up to the very low voltages. **Figure 5.14** additionally shows the cathodic scan of the CV for the ORR. Notably, the onset potential of the ORR (~1.07 V vs RHE) is very close to the estimated value of the PME. There is evidence to believe that this close relation is not coincidental. The interfacial solvent dipoles at the PME and in its vicinity are most likely to reorient and facilitate the electron transfer.[172] This is in line with the hypothesis presented at the beginning of **Section 5.2** describing the effect of the interface stiffness on the rate of electrocatalyzed reactions.
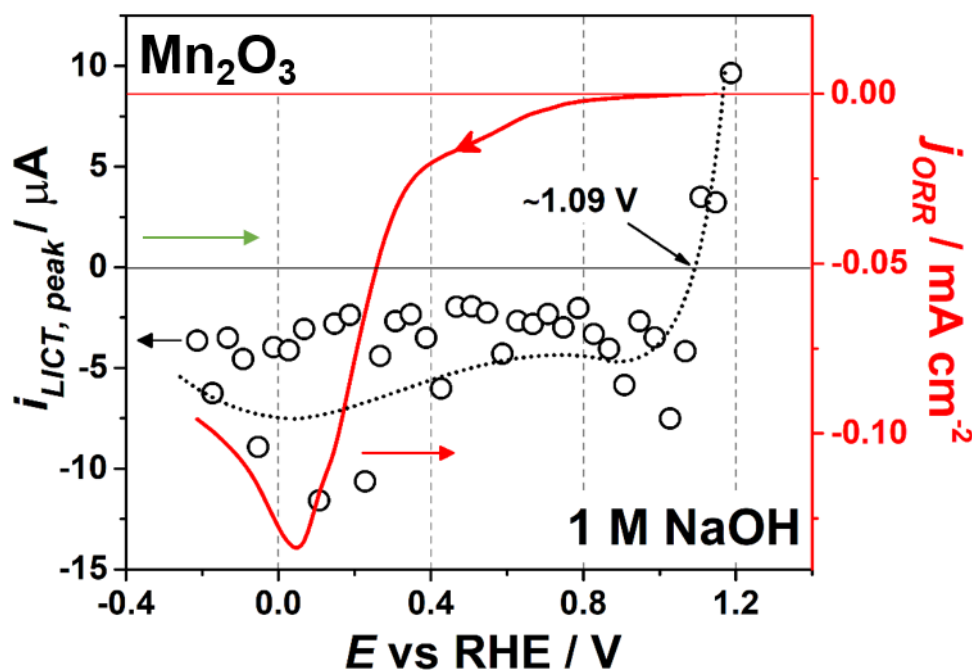


**Figure 5.14**. *2D plot representing all recorded LICTs (depicted in black) as a function of the WE potential together with the cathodic scan of the corresponding CV (depicted in red). Scan rate: dE dt $^{-1}$ = 50 mV s$^{-1}$. Dotted line serves as a guide to eyes. The system exhibits the PME located at ~1.09 V vs RHE, which is very close to the onset potential of the ORR at ~1.07 V vs RHE. The additional horizontal green arrow depicts the scan direction.*

Interestingly, the obtained results suggest that the electrode composition might alter during the ORR. This can be concluded from the unusual shape of the cathodic scan of the CV, particularly, in the curve slope between ~0.05 V and ~0.80 V vs RHE (see **Figure 5.14**). The characteristic change, assigned to the film transition, can be observed at ~0.30 V vs RHE.

### 5.3.2 Impedance Analysis

To gain more information about the system behavior, the $Mn_2O_3$ electrodes were investigated with the EIS. The resulting impedance data together with their fitting curves are displayed in **Figure 5.15A**. **Figure 5.15B** shows the equivalent electric circuit used to fit the impedance spectra.
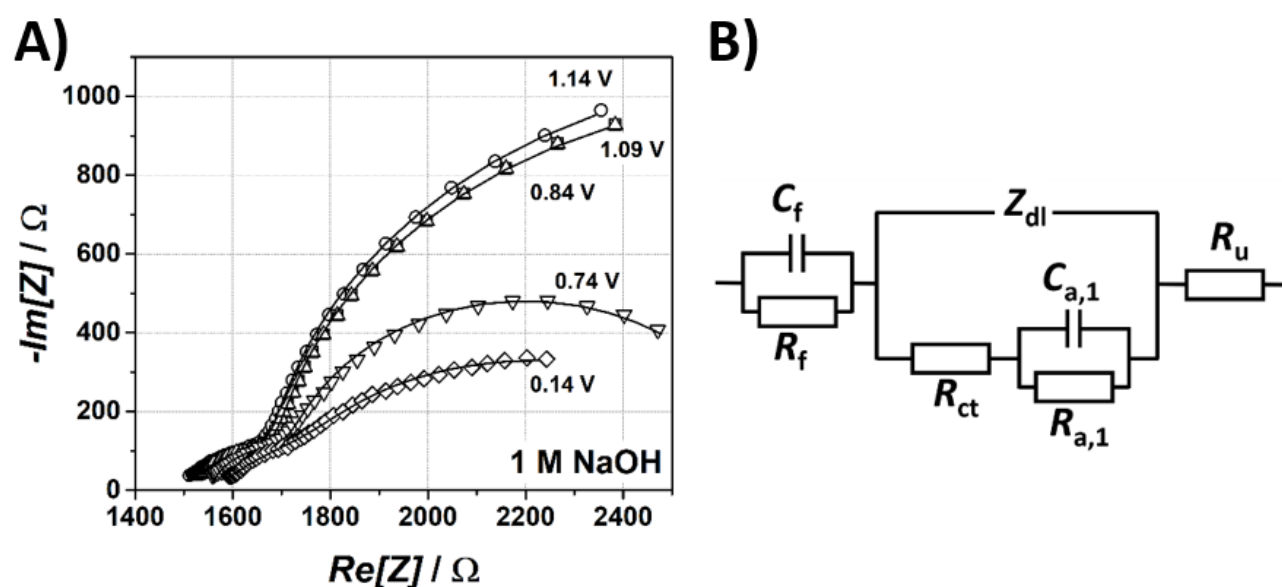


*Figure 5.15. (A) EIS data (depicted as open symbols) of the investigated $Mn_2O_3$ electrodes in $O_2$-saturated 1 M NaOH together with the corresponding fits (depicted as black lines). Fits were performed using the EEC shown in B. The meaning of each EEC parameter can be found in the text.*

The parameter $R_u$ in the presented EEC represents the uncompensated resistance which, generally speaking, arises from the instrumental artifacts.[357,358] In turn, the impedance of the double layer, $Z_{dl}$ is represented by the constant phase element CPE (see **Section 3.9.2**); and it can be expressed as follows:

111

$$Z_{\mathrm{dl}} = \frac{1}{C'_{\mathrm{dl}}}(j\omega)^{-\varphi}$$

where $C'_{\mathrm{dl}} \approx C_{\mathrm{dl}}$ if the exponent $\varphi$, which is associated with the frequency dispersion in the EDL, is close to 1.[359] The remaining resistances $R_{\mathrm{ct}}$ and $R_{\mathrm{a,1}}$ as well as the capacitance $C_{\mathrm{a,1}}$ reflect the response of adsorption processes. Finally, the additional parallel set involving the capacitance of the drop-casted films, $C_{\mathrm{f}}$, and the film resistance, $R_{\mathrm{f}}$, accounts for the alteration in the intrinsic properties of the electrode, such as its composition, during the electrochemical process.[303,359] These changes could also explain why in the high-frequency region the real part of the impedance data gets higher upon the potential decrease (see **Figure 5.15A**).[360]

To conclude, the application of the LICT method can be expanded to the electrochemical systems containing metal oxide catalysts, such as $Mn_2O_3$. As shown above, the results of the LICT analysis reveal the close correlation between the onset potential of the ORR and the PME of the studied system. These findings further emphasize the significance of the surface water structure for the rate of electrocatalytic reactions. Apparently, the hypothesis explaining the dependence between the EDL properties and the rate of a certain reaction is valid also in the systems utilizing the oxide material as the catalyst. Considering the fact that the laser technique was initially developed to probe the electrified interfaces formed between pure metals and electrolytes, these findings appear unique. Moreover, also in this case, the LICT method turns out to be particularly useful in combination with other techniques. By combining it with the CV and the EIS, one can obtain thorough information about the processes taking place not only in the interface but even in the electrode material.

## 5.4 Model Battery Systems

Undeniably, the possibility to apply the laser radiation to probe the surface charge accumulated at electrodes consisting of non-precious metal compounds opens up new avenues for performing in-depth analyses of the whole spectrum of systems crucial for the sustainable energy provision. The findings presented in the previous subchapters served as motivation to utilize the LICT technique in the studies of even more complex interfaces. Thus, the LICT

method was, for the first time, implemented to characterize model aqueous battery systems. In the following sections, the results obtained during the LICT investigation of the interfaces formed between model battery electrodes and aqueous solutions are presented. To perform a more comprehensive analysis, the acquired data were further complemented with those obtained using other electroanalytical methods, namely the CV, EIS, EQCM, and AFM.

### 5.4.1   Initial Characterization of NiHCF Films

Consider the $Na_2[Fe(CN)_6]$ thin films (NiHCF)- typical PBA material suitable as cathodes in Na-ion battery systems.[361] Due to its relatively simple synthesis, easily adjustable composition, non-toxicity, and low costs, this inorganic compound has attracted special attention in the scientific community during the last  years.[133,135,362,363,364,365] These were also the reasons why the NiHCF was chosen to be investigated in this work.

Following electrodeposition of NiHCF thin films on a gold substrate (described and analyzed in detail in reference 12), the electrodes were immersed in two different electrolytes, namely 0.25 M $Na_2SO_4$ and 0.25 M $K_2SO_4$, and characterized during intercalation and deintercalation of the $Na^+$ and $K^+$ cations. **Figure 5.16A** shows the resulting voltammograms. The alterations in the oxidation state of iron atoms present in the structure of the electrode material result in anodic and cathodic peaks visible in the CVs. These changes are also recognized as the main reasons for alkali-metal cation deintercalation and intercalation. In addition, the corresponding increase in the electrode mass during intercalation of sodium and potassium was detected from the analysis of EQCM data (**Figure 5.16B**). The calculated mass changes were ~1.63 $\mu g\ cm^{-2}$ and ~2.66 $\mu g\ cm^{-2}$ for the $Na^+$ and $K^+$ cations, respectively. Considering that the mass of the deposited films was ca. 22 $\mu g\ cm^{-2}$, the mass changes resulting from intercalation of the cations are very close to the expected values determined from the chemical formula assuming that only one cation intercalates per one reacting iron center.[45]
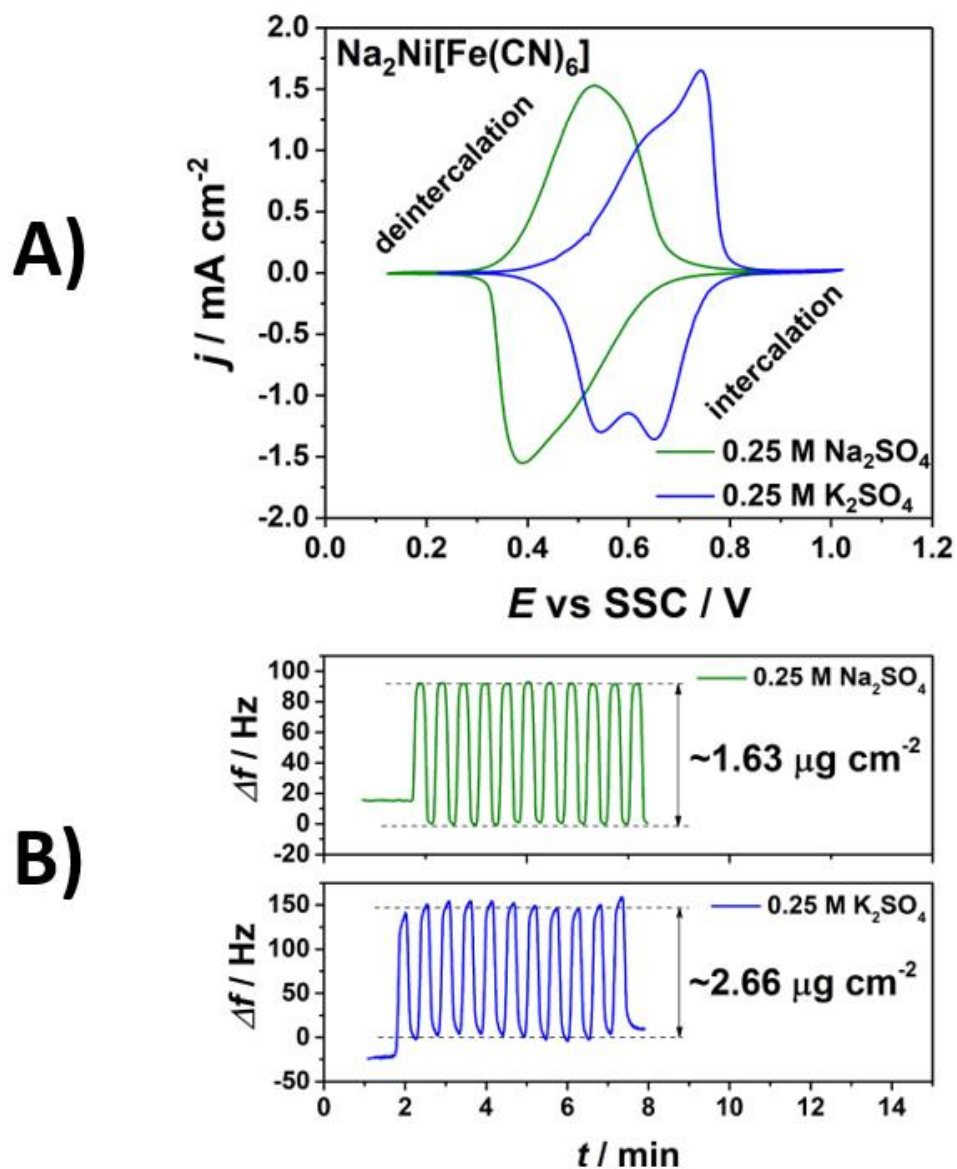
***Figure 5.16.*** *(A) Typical CVs of the NiHCF thin films immersed in the 0.25 M Na₂SO₄ (depicted in green) and 0.25 M K₂SO₄ (depicted in blue) solutions (dE dt $^{-1}$ = 50 mV s$^{-1}$) together with the (B) corresponding background corrected curves representing the change in the electrode mass during (de)intercalation of Na⁺ and K⁺ cations; 1 Hz = 17.7 ng cm$^{-2}$.*

The resulting surfaces were additionally characterized using the AFM. The AFM measurement enabled to check the quality of the produced films. **Figure 5.17A** and **B** show the 2D and 3D image of deposited NiHCF, respectively. The electrodes exhibit relatively high surface evenness and smoothness with the roughness factor of ca. 1.07.
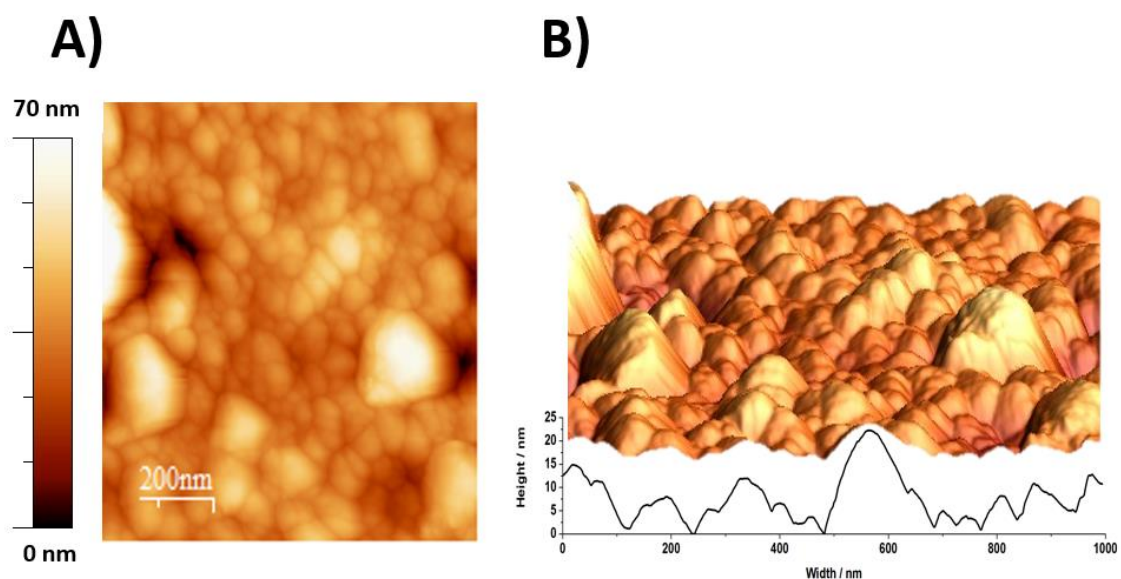
***Figure 5.17.*** *Representative (A) 2D and (B) 3D AFM images of the deposited thin films. The surface is relatively uniform and smooth.*

### 5.4.2    Impedance Characterization of NiHCF Films

The processes occurring at the electrified solid/liquid interface of the electrodes were further investigated using the EIS. **Figure 5.18A** and **B** show typical ''loop-shaped'' EIS spectra obtained for the films together with corresponding fits in 0.25 M $Na_2SO_4$ and 0.25 M $K_2SO_4$, respectively. All the spectra were fitted using an EEC shown in **Figure 5.18C** as proposed by Yun et al.[12] and Ventosa et al.[138] According to this physical model, the alkali-metal intercalation takes place in at least three stages including oxidation/reduction of transition metal centers present in the PBA (in this case iron centers), temporary adsorption/desorption of anions present in electrolytes at the surface of the electrode, as well as the cation intercalation into and deintercalation from the electrode material.[45] The actual mechanism was described in detail in **Section 3.5.3**.
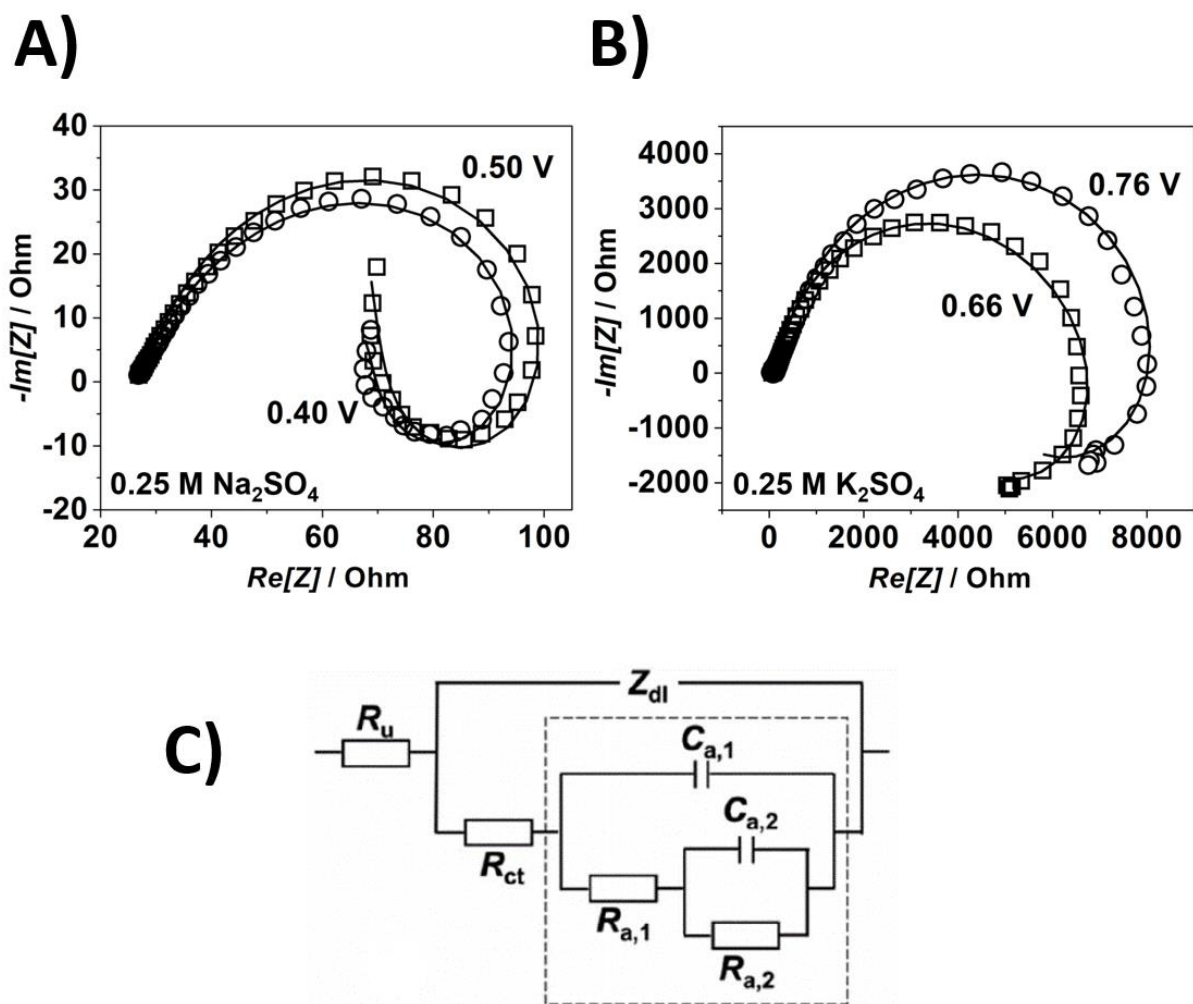
*Figure 5.18.* EIS data (depicted as open symbols) of the NiHCF films in (A) 0.25 M $Na_2SO_4$ and (B) 0.25 M $K_2SO_4$ together with the corresponding fits (depicted as solid lines). The fits were obtained with the use of the EEC presented in part C. The model describes a mechanism involving at least three quasi-reversibly connected steps. $R_u$ - uncompensated resistance; $Z_{dl}$ - impedance of the double layer; $R_{ct}$ - charge transfer resistance; the remaining R and C elements stand for resistances and capacitances of adsorption, respectively.

### 5.4.3   LICT Characterization of NiHCF Films

Following the characterization of the electrodes with the "conventional" electrochemical methods, the formed interfaces were probed using the LICT technique. After a series of experiments, it was revealed that the NiHCF electrodes immersed in 0.25 M $Na_2SO_4$ exhibit the PME. However, in this system, the potential at which surface water molecules change their orientation towards the electrode surface was found outside of the (de)intercalation potential regime at ca. -0.13 V vs SSC (**Figure 5.19A** and **B**). In contrast, the PME in the 0.25 M $K_2SO_4$ solution was not detected at all (**Figure 5.19C** and **D**). In this case, right after the laser illumination, all the obtained transients were positive within the whole investigated range reaching the onset potential of the HER at ca. -1.20 V vs SSC. As discussed in **Section 5.2.2**, in some cases, the PME of the system might be located at very negative potentials. This, however, could have not been verified in this case as the generation of hydrogen bubbles and the probable potential-driven damage of the film made it impossible to perform measurements at more negative potentials. Based on the alternative explanation suggested by Huang et al., it is also possible that the studied system might simply not exhibit the PME (see **Section 5.2.2**).[45,352]
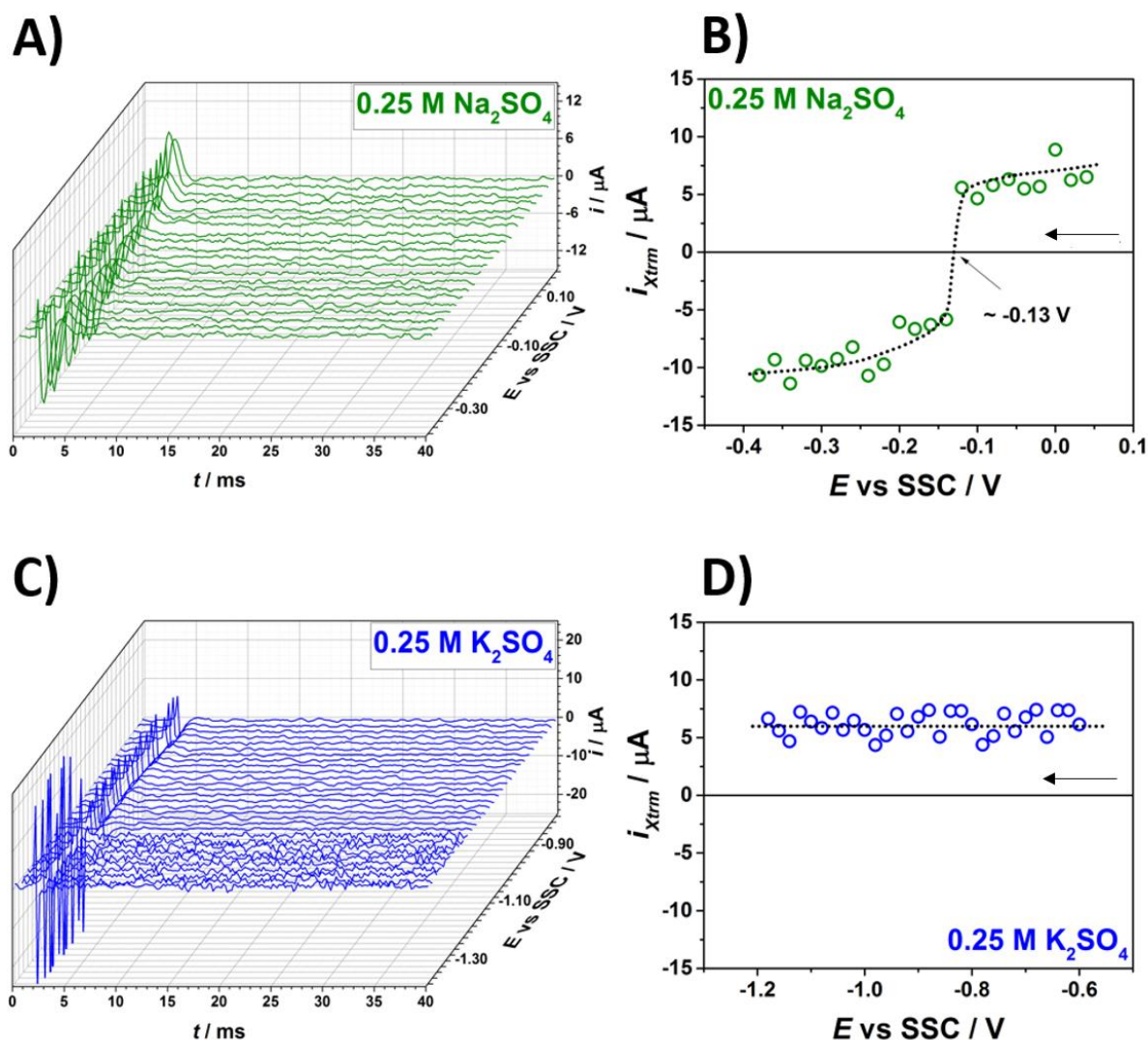
**Figure 5.19.** *LICTs of the NiHCF thin films in (A,B) 0.25 M Na$_2$SO$_4$ and (C,D) 0.25 M K$_2$SO$_4$, respectively. (A) 3D LICT plot obtained in the Na$^+$-containing solution outside of the cation (de)intercalation range. (B) Corresponding 2D plot representing the maximal extrema of the collected current transients as a function of the applied potential. The estimated value of the PME is ca. -0.13 V vs SSC. (C) Analogous 3D LICT graph obtained in the electrolyte containing K$^+$ and the (D) corresponding 2D plot showing the dependence of maximal current extrema as a function of the voltage. One can observe drastic changes in the current transients caused by the HER and/or the modification of the film composition below -1.20 V vs SSC. Black arrows show the scan direction of the performed LICT measurements.*

**Figure 5.20A** and **C** show the current transients collected for the NiHCF films immersed in the 0.25 M Na₂SO₄ and 0.25 M K₂SO₄ solutions within the voltage ranges of sodium and potassium cation (de)intercalation, respectively. Interestingly, in both systems, the sign of the obtained maximal extrema of the current spikes are positive within the whole investigated regimes. This further implies that within these potential ranges, the electrode surface charge is positive. The relations between the recorded current extrema and the applied electrode potentials for both solutions are additionally displayed in **Figure 5.20B** and **D**.
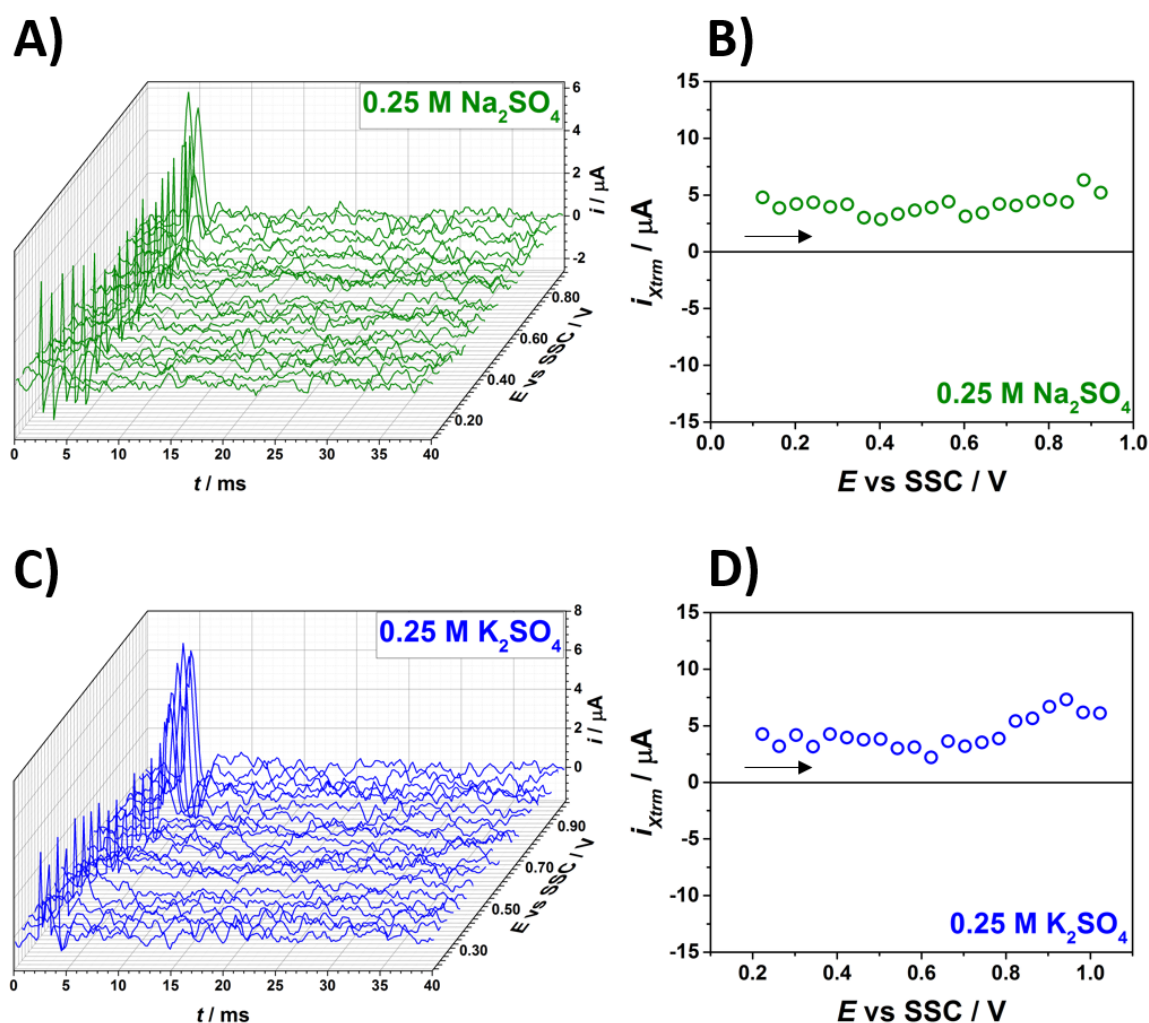


***Figure 5.20***. *LICTs of the NiHCF thin films in (A,B) 0.25 M Na₂SO₄ and (C,D) 0.25 M K₂SO₄, respectively. (A) 3D LICT plot obtained within the Na⁺ (de)intercalation range together with the (B) corresponding 2D plot of the maximal extrema as a function of the electrode potential. (C) Analogous 3D plot in the range of K⁺ cation (de)intercalation and the (D) corresponding 2D representation of maximal current extrema as a function of the potential. Graphs display every second measurement. Black arrows show the scan direction.*

### 5.4.4   LICTs and Impedance Data

On the basis of the aforementioned results, one might expect that, during intercalation, the positively charged ions are attracted by the electrode surface which carries the positive excess charge. This could appear counterintuitive judging from the expected electrostatic repulsion. However, it should be mentioned that intercalation is thermodynamically driven, and the same charge of the electrode and the species, in the first place, would only slow the process down. Interestingly, the vast majority of the current transients collected in the solutions of sodium and potassium sulfate exhibits the characteristic ''tripolar shape''. As shown in **Figure 5.21** representing single sample transients, shortly after the laser illumination, the observed current peaks are positive. Then their orientation changes to negative, eventually getting positive in longer times. Interestingly, the fluctuations were not seen for the pure gold electrodes (presented in **Section 5.1**). For this reason, they cannot be found as artifacts resulting from the hardware. Moreover, owing to the very short time frame of the potentiostat, such artifacts could not have been detected. Instead, the unique shape of the transients shows that in both investigated model battery systems there are most likely at least three different relaxation processes characterized by different ''time constants'' indicated as $\tau_1$, $\tau_2$, and $\tau_3$.[45]

The first current peaks in the resulting LICTs can be solely associated with the double layer response since it is expected to be the quickest.[366] This anodic process can be seen as the reorientation of the interfacial water molecules after illuminating the surface with the laser beam. As a result, the positive charge accumulated at the electrode surface might lead to intensified anion adsorption (in this case adsorption of the $SO_4^{2-}$ anions). Partial temperature-driven intercalation and deintercalation of alkali-metal cations might be other processes possibly contributing to these peaks. The subsequent current alteration likely reflects the interfacial charge and mass transfer. It should be mentioned that during the laser experiments, the electrode potentials at each step were held constant. Therefore, the observed LICTs should be seen as system answers coming from various processes, which are often opposite to each other. As a consequence, one can expect a dynamic equilibrium to occur between, for instance, cation intercalation and deintercalation. In the final step, represented as the broad, positive current peaks, the adsorbed species get desorbed from the electrode surface. Also in this case, the process of anion adsorption can take place in parallel with partial readsorption of the negatively charged species.[45,46]
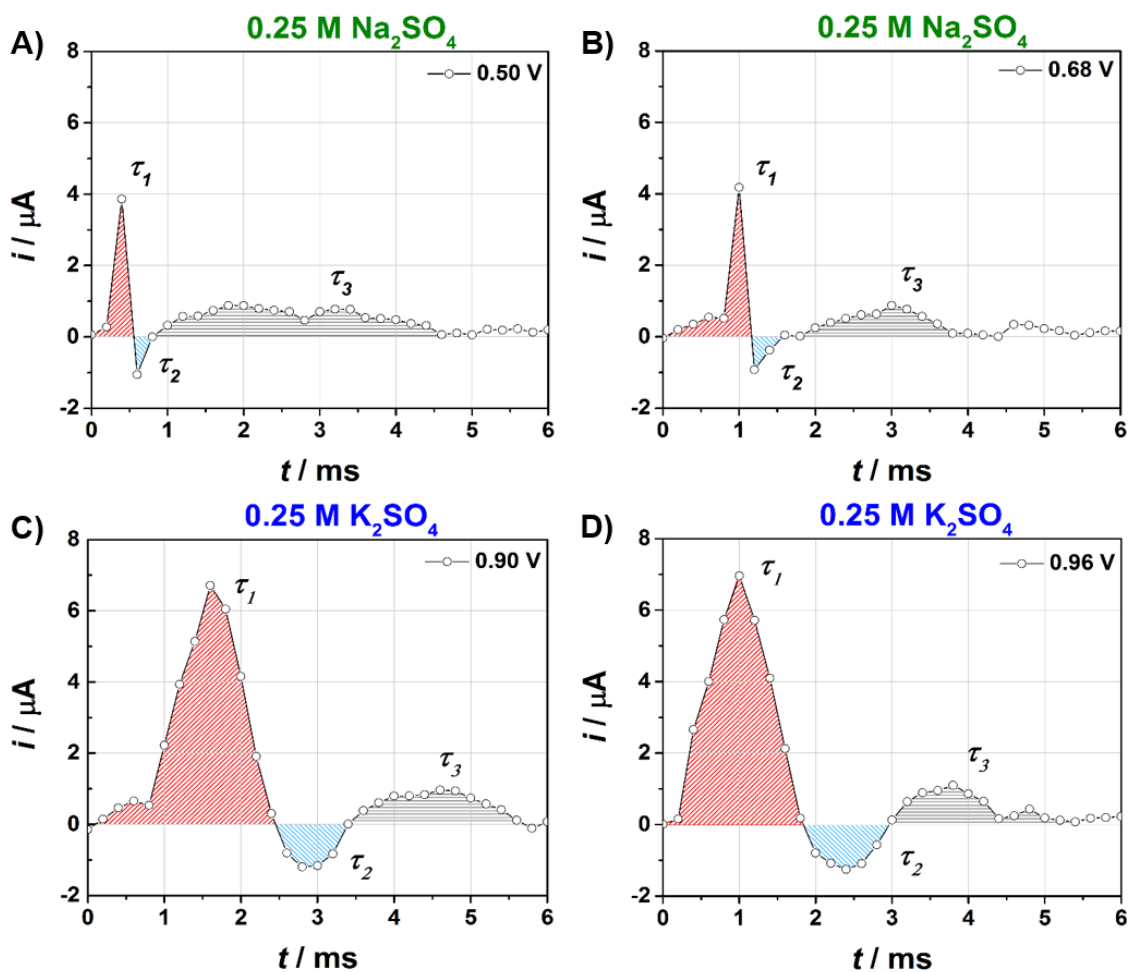
***Figure 5.21.*** *Comparison of the shape of the sample current transients recorded for NiHCF thin films in 0.25 M Na₂SO₄ at (A) 0.50 V, and (B) 0.68 V vs SSC, and in 0.25 M K₂SO₄ at (C) 0.90 V, and (D) 0.96 V vs SSC. One can clearly notice the ''tripolar shape'' of the resulting curves. All three peaks can be related to three different interfacial processes having different time constants: $\tau_1$, $\tau_2$, and $\tau_3$.*

To validate this interpretation, the time constants acquired from the EIS experiments were linked with the ones estimated from the LICT measurements. For this purpose, the time constants obtained from the values of the corresponding parameters belonging to the EEC presented in **Figure 5.18C** (i.e., $Z_{dl}$ and $R_{ct}$, $C_{a,1}$ and $R_{a,1}$, as well as $C_{a,2}$ and $R_{a,2}$; see **Table A.A** in **Appendix A**) were calculated and compared with the corresponding time constants estimated from the LICT plots, i.e., $\tau_1$, $\tau_2$, and $\tau_3$. Interestingly, the resulting $\tau_1$'s were very close to the values representing the response of the EDL determined from the EIS data. Likewise, the estimated values of $\tau_2$ and $\tau_3$ were found to be similar to the time constants obtained from the EEC parameters related to the interfacial charge and mass transfer (acquired from $C_{a,1}$ and $R_{a,1}$,

as well as $C_{a,2}$ and $R_{a,2}$). One can see that the EIS data are consistent with the LICT ones. Nevertheless, the laser experiments offer a benefit over the impedance analysis: they provide information regarding the net cathodic and anodic components of mechanisms occurring in multiple stages.[45]

Moreover, the combination of the LICT and EIS data can support the three-stage mechanism of alkali-metal cations in aqueous electrolytes introduced in **Section 3.5.3**. For the solution containing $Na^+$ and $SO_4^{2-}$, the mechanism can be described as follows:

$$Na_2Ni[Fe^{II}(CN)_6] - e^- \rightleftarrows Na_2Ni[Fe^{III}(CN)_6]^+ \qquad \textit{Eq. 5.2}$$

$$2Na_2Ni[Fe^{III}(CN)_6]^+ + SO_4^{2-} \rightleftarrows (Na_2Ni[Fe^{III}(CN)_6])_2SO_4 \qquad \textit{Eq. 5.3}$$

$$(Na_2Ni[Fe^{III}(CN)_6])_2SO_4 \rightleftarrows 2Na^+ + SO_4^{2-} + 2NaNi[Fe^{III}(CN)_6] \qquad \textit{Eq. 5.4}$$
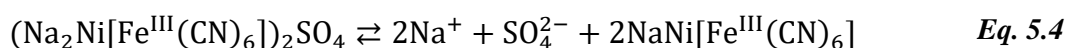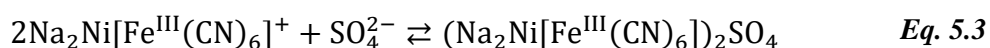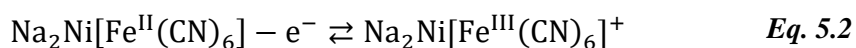
Generally speaking, the alteration in the oxidation state of the iron atoms in the electrode structure designated by **Eq. 5.2** can also occur as a consequence of the laser-induced temperature jump (step I). This should generate the excessive charge at the electrode surface, which can be further compensated by the electrolyte components (e.g., anions) as depicted in **Eq. 5.3** (step II). In the final step, shown schematically by **Eq. 5.4**, slower relaxation of the system without the net charge transfer is supposed to take place (step III).[45]

Noteworthy, the comparison of part A and B with C and D of **Figure 5.21** can additionally reveal notable dissimilarities between the relaxation curves at shorter times, $\tau_1$, obtained in different solutions. The only difference between the two electrolytes is the nature of the cations. Thus, the bigger time constants $\tau_1$'s acquired for the $K_2SO_4$ might result from the lower hydration energy of $K^+$.[350] The lower value of hydration energy might mitigate the order of the $H_2O$ adlayer and, as a consequence, lead to a slower reorganization of the double layer after the laser probing. Although it requires further experimental validation, such an analysis of the relaxation curves could likely provide further information about the influence of the cation nature on the kinetics of the investigated processes.[313] This might be particularly useful in, for instance, understanding the origins of the irreversibilities during charging and discharging of battery cells usually visible as asymmetry in a shape of CVs (see **Figure 5.16A**).[12,45,367]

In conclusion, it is demonstrated that the LICT technique can be successfully used in the investigation of NiHCF-based battery systems. Particularly, the combination of the LICT data

with those obtained using other commonly known methods of electroanalysis can provide unique information regarding the alkali-metal (de)intercalation processes in aqueous PBA battery systems. As presented for the NiHCF material, the laser technique can disclose the effective surface charge of the battery electrodes and reveal their PMEs. By using solutions containing different alkali-metal cations (i.e., $Na^+$ and $K^+$), it was additionally shown how the electrolyte composition can influence the interfacial processes through, for instance, affecting the PME value. Surprisingly, the excess surface charge accumulated at the electrode during (de)intercalation of both the $Na^+$ and $K^+$ cations is positive. However counterintuitive these findings appear, they are in agreement with the hypothesis suggesting the three-stage mechanism of the interfacial processes reported in the literature (and described in **Section 3.5.3**). Additionally, owing to its unique ability to differentiate between the net anodic and cathodic constituents, the LICT technique further confirms the complexity of the (de)intercalation. The aforementioned findings show that the LICT analysis can indeed be a useful method for characterizing aqueous battery systems. Understanding the role of different electrolyte components (in this case cations) in establishing the EDL structure, as well as their effect on the interfacial processes, can be particularly helpful in the development of new models describing mechanisms of alkali-metal cation (de)intercalation.[45]

### 5.4.5 Deposition and Characterization of CoHCF Films

Cobalt hexacyanoferrate (CoHCF) is another example of PBAs. As a compound capable of being used as a battery electrode material, CoHCF is known for its high stability in solutions containing $Na^+$ and $K^+$ cations,[368] and good energy density.[369] In this section, the interfacial processes occurring at the solid/liquid interfaces at model CoHCF-based battery electrodes in aqueous electrolytes are investigated. As in the case of NiHCF, the extensive analysis of the system utilizing the LICT technique augmented by other electrochemical methods is performed.
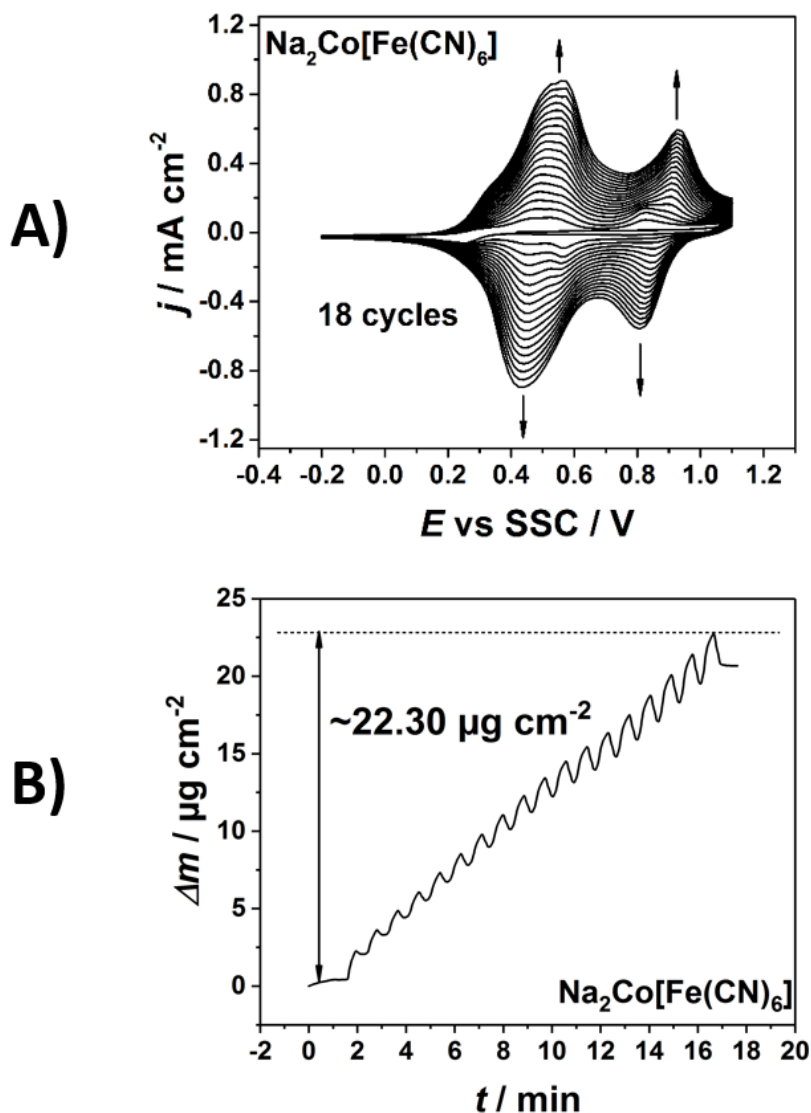
***Figure 5.22.*** *(A) Typical CV obtained during deposition of the CoHCF film (dE dt $^{-1}$ = 50 mV s$^{-1}$) and the (B) corresponding EQCM diagram showing the change of the electrode mass.*

Part A of **Figure 5.22** shows a typical CV obtained during deposition of CoHCF thin films. The recorded current increases with the potential cycles. In the displayed voltammogram, two pairs of oxidation/reduction peaks can be seen. The first, bigger pair is observed at ~0.55/0.45 V. As reported by Wu et al., it can be partially related to the change in the oxidation state of the nitrogen-coordinated Co atoms.[370,371] At the more positive potentials, at ~0.90/0.80 V, another pair of peaks can be seen. As further claimed by the same group, this pair can be associated with an alteration in the oxidation state of the carbon-coordinated Fe. The corresponding change in the electrode mass recorded during the film deposition is presented in **Figure 5.22B**. The resulting mass increase was ~22.30 μg cm$^{-2}$.[46]

The quality of the deposited films was further checked using the AFM. 2D and 3D AFM images of CoHCF electrodes are shown in **Figure 5.23A** and **B**, respectively. The acquired images show a relatively smooth film surface with the roughness factor of ca. 1.23. The deposited films evenly cover the gold support.
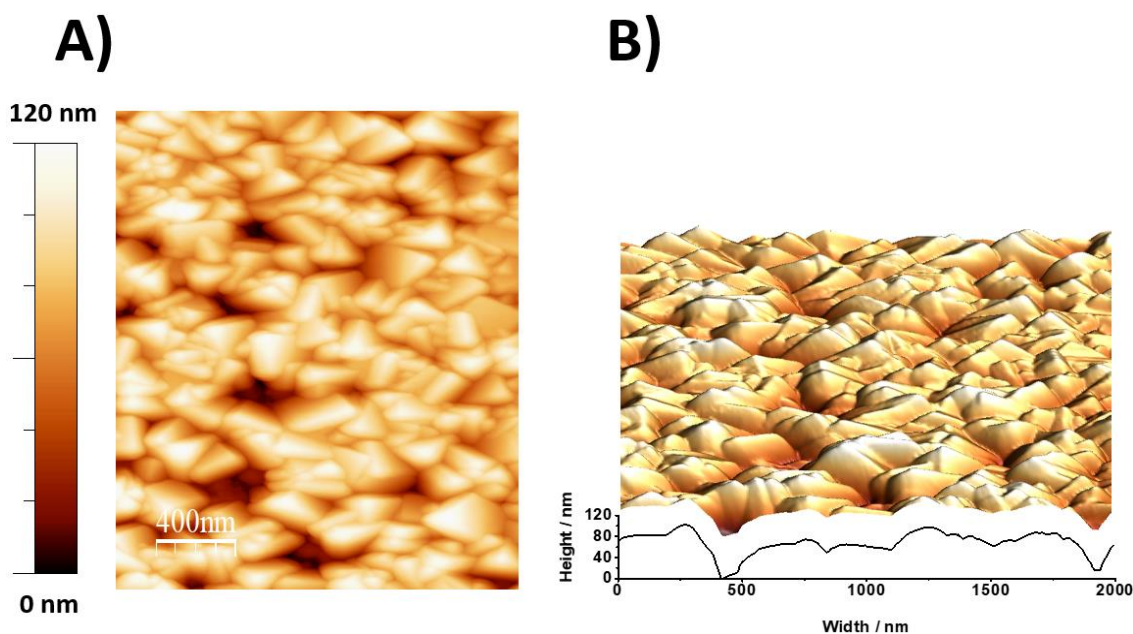


*Figure 5.23. Representative (A) 2D and (B) 3D AFM images of the deposited CoHCF films. The obtained surfaces are relatively smooth and uniform.*

Subsequently, the CoHCF electrodes were characterized in 0.25 M aqueous solutions of three salts, namely $Na_2SO_4$, NaCl, and $NaClO_4$. The resulting CVs are shown in **Figure 5.24A**. The anodic and cathodic peaks are associated with deintercalation and intercalation of $Na^+$ cations, respectively. As in the deposition process, the anodic and cathodic peaks also correlate with the alteration in the oxidation states of Co and Fe atoms in the films. Apparently, for all the investigated solutions, the ''bigger'' current peaks are located at the same potentials. They also exhibit a similar shape. Furthermore, the differences in the position and appearance between the ''smaller'' peaks recorded in the electrolytes containing $SO_4^{2-}$ and $ClO_4^-$ anions are also very small (see **Figure 5.24A**). The change in the electrode mass during (de)intercalation is shown in **Figure 5.24B**. The total mass alteration during intercalation of sodium cations from sulfate and perchlorate solutions was determined as ca. 1 µg cm$^{-2}$. The apparent mass decrease (ca. 20%) in the case of sodium chloride arises from the narrower voltage range chosen in order to avoid chlorine evolution.[46]
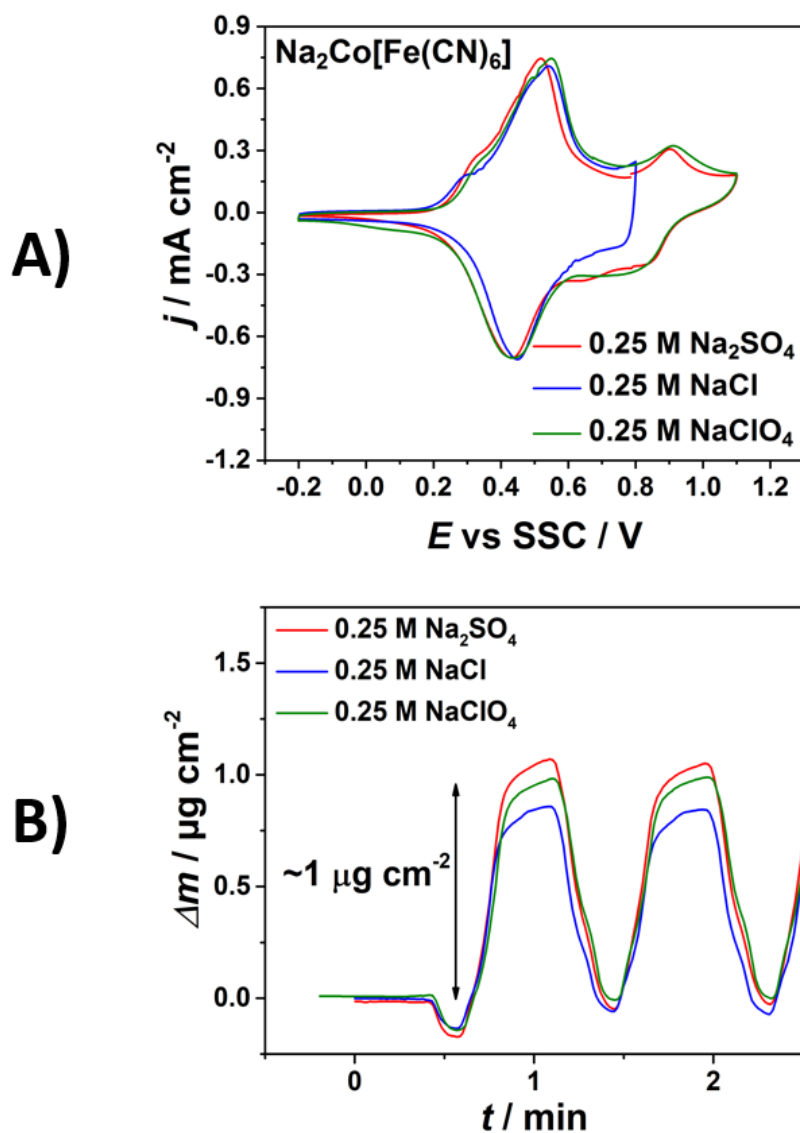
***Figure 5.24.*** *(A) Typical CVs of the CoHCF films immersed in the 0.25 M Na₂SO₄, 0.25 M NaCl, and 0.25 M NaClO₄ solutions (dE dt ⁻¹ = 50 mV s⁻¹), as well as the (B) corresponding EQCM diagram showing the change of the electrode mass during Na⁺ intercalation/deintercalation (background corrected curves). The choice of the narrower potential regime in the case of 0.25 M NaCl was made in order to avoid the chlorine formation.*

### 5.4.6 Impedance Characterization of CoHCF Films

In the next step, the interface formed between the CoHCF thin films and the aqueous electrolytes was examined using the EIS. **Figure 5.25A**, **B**, and **C** display the EIS spectra obtained for the electrodes immersed in the 0.25 M Na₂SO₄, 0.25 M NaClO₄, and 0.25 M NaCl

electrolytes, respectively, together with the corresponding fits. As in the case of the NiHCF films, all the recorded spectra exhibit the typical loop-like shapes. The EECs used to perform the fits of the recorded data are shown in **Figure 5.25D** and **E**.[46]
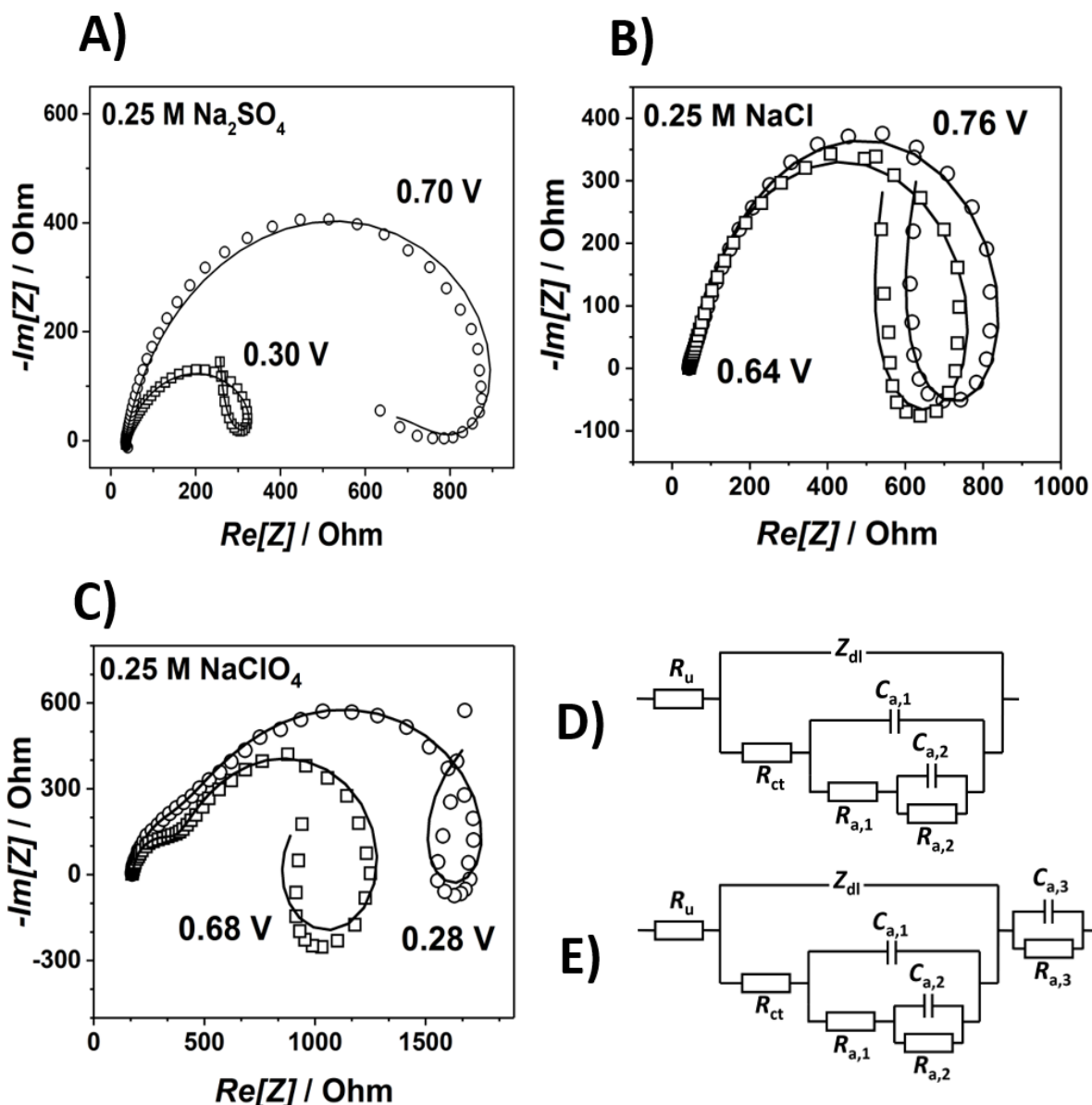


***Figure 5.25.*** *Typical EIS spectra (depicted as open symbols) of the CoHCF films immersed in (A) 0.25 M Na$_2$SO$_4$, (B) 0.25 M NaCl, and (C) 0.25 M NaClO$_4$ together with the corresponding fits (depicted as solid curves). The EECs shown in part D and E were used to perform the fits. The presented models describe a mechanism involving at least three quasi-reversibly connected stages. $R_u$ - uncompensated resistance; $Z_{dl}$ - double layer impedance; $R_{ct}$ - charge transfer resistance; the other R and C parameters stand for resistances and capacitances of adsorption, respectively. As mentioned in the text, the additional parallel set of $R_{a,3}$ and $C_{a,3}$ in E accounts for the additional semicircles visible in the high-frequency regime in part C.*

The EEC shown in **Figure 5.25D** is identical to the one used during the EIS characterization of NiHCF electrodes (see **Figure 5.18C**). Interestingly, it was also successfully applied to fit the data obtained for CoHCF films in the 0.25 M $Na_2SO_4$ and 0.25 M NaCl electrolytes. A slightly modified EEC containing an extra parallel set of capacitance ($C_{a,3}$) and resistance ($R_{a,3}$) was used in the case of 0.25 M $NaClO_4$. The existence of the additional branch might be associated with the capacitive properties of the electrodeposited film itself.[372] Regardless of the aforementioned dissimilarities, both the EECs represent the three-stage scheme of sodium ion intercalation/deintercalation proposed by Yun et al. and Ventosa et al. involving temporary adsorption and desorption of electrolyte anions at the electrode surface (see **Section 3.5.3**).[12,46,138]

### 5.4.7   LICT Characterization of CoHCF Films

In order to reveal the excess surface charge of the CoHCF films, the electrodes were further probed with the laser beam. Sample current transients obtained in all three investigated solutions within the voltage ranges of $Na^+$ (de)intercalation are shown in **Figure 5.26A**, **B**, and **C**. Unexpectedly, in the systems under study, the orientation of the current "spikes" changes more than once within the investigated potential ranges. It can be better visible in **Figure 5.26D** presenting the recorded extreme current values as a function of the applied potential. The recorded data indicate multiple changes of the sign of the charge accumulated at the electrode surface during $Na^+$ cation intercalation. As shown in **Figure 5.26**, the resulting LICTs at the potentials ~0.00 V vs SSC are negative. Then, at ~0.05 V vs SSC, they turn positive, changing their sign again to negative at ~0.15 V vs SSC. At potentials around 0.70 V vs SSC, the transients eventually become positive. Interestingly, all the investigated systems show three potential values at which the orientation of the current transients alters. Obviously, the observed ''flipping potentials'' were identified as the PMEs. As discussed in **Section 3.6.3**, the PME in simple electrochemical systems is closely related to the PZC. Furthermore, a single electrochemical system can likely show only one PZC. Thus, at first glance, the existence of multiple PMEs might seem surprising. Nevertheless, it should not be forgotten that the presented Na-ion battery systems and processes occurring at their interfaces are more complex than the model systems usually presented in the literature. Therefore, their behavior might not entirely follow the basic tenets of conventional surface science.[46]
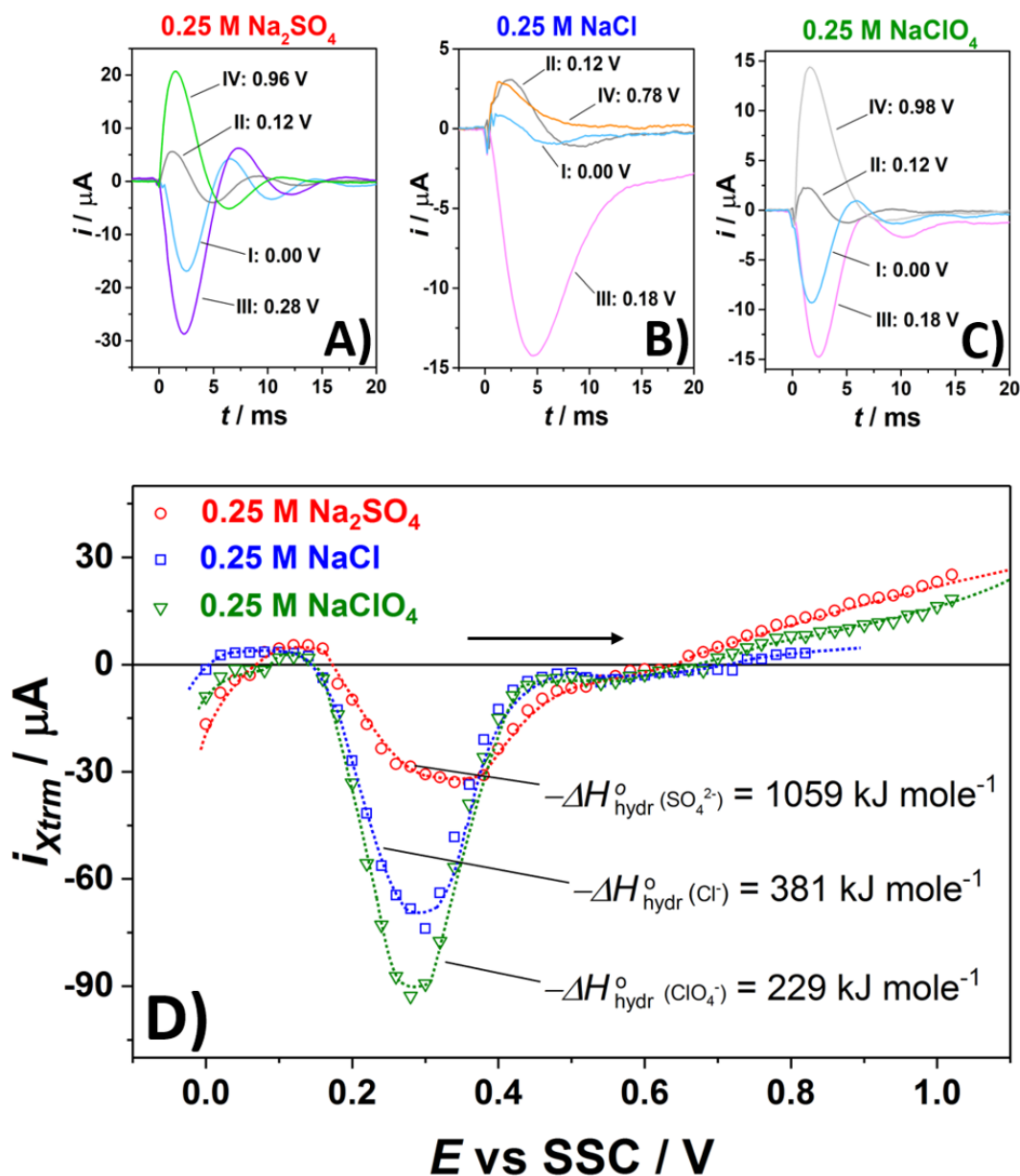
*Figure 5.26. Sample LICTs obtained for the CoHCF films in (A) 0.25 M Na₂SO₄, (B) 0.25 M NaCl, and (C) 0.25 M NaClO₄ at various electrode potentials. The order of the potentials steps is further shown by roman numerals. (D) Corresponding 2D LICT plot depicting the current extrema shown as a function of the electrode potential for all three solutions. Three PMEs were detected in each system. The numerical values of hydration energies are taken from reference 350. The additional black arrow shows the scan direction.*

Interestingly, the direct comparison between the 2D LICT plots (**Figure 5.26D**) and corresponding CVs (**Figure 5.24A**) reveals that the values of the detected PMEs are very close to the onset potentials of sodium cation (de)intercalation. The stiffness of the EDL at the potentials far from the PMEs is high, which makes it difficult for the cations to migrate towards

(**Figure 5.27A**) and from the electrode surface (**Figure 5.27B**). In contrast, at the PMEs and at the potentials close to them, the EDL gets less ordered. As a consequence, at these potential values, the charge and mass transport through the interface can proceed much more easily.[172] This shows the importance of the interface structure for interfacial processes, such as (de)intercalation, occurring in battery systems.[46]
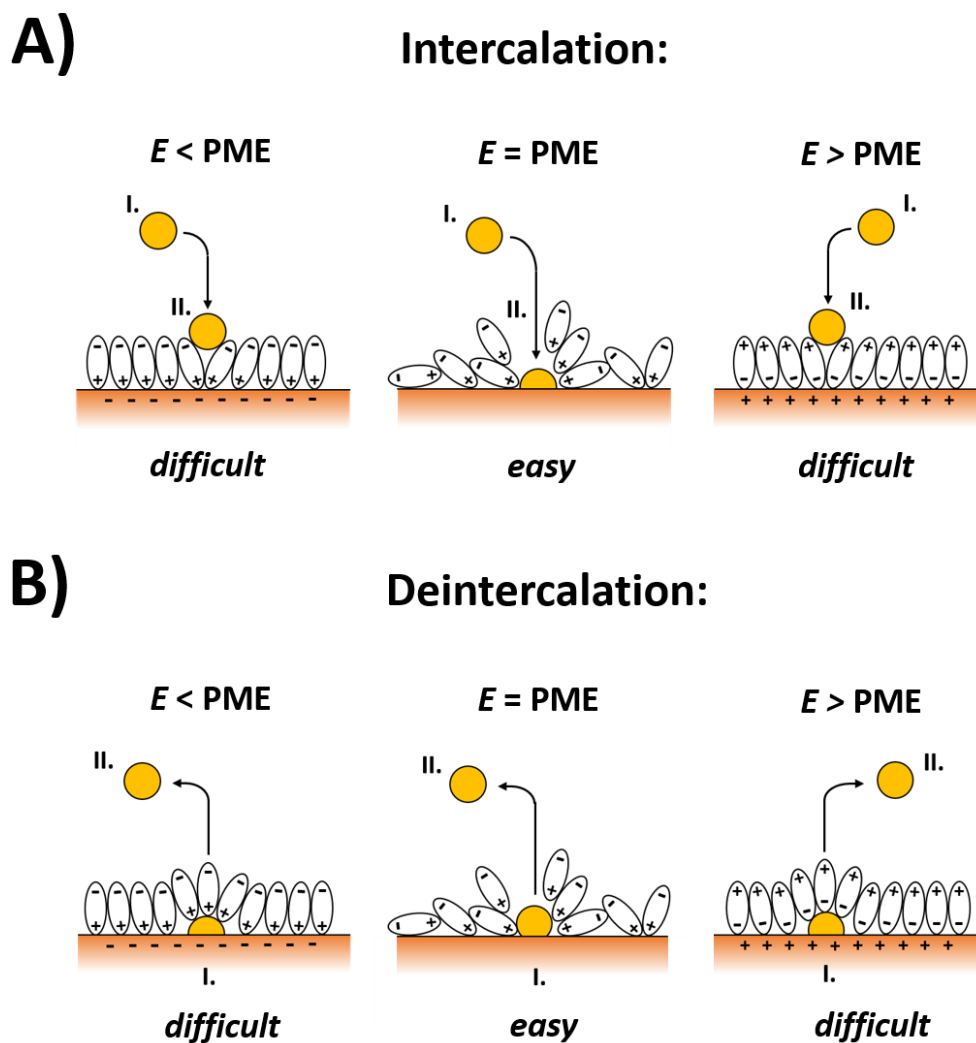


***Figure 5.27.*** *Schematic illustration of the influence of the surface water structuring on alkali-metal cation (represented by yellow circles) (A) intercalation and (B) deintercalation from aqueous solutions at the potential lower than the PME, equal to the PME, and higher than the PME. Note that the ease of the interfacial processes largely depends on the stiffness of the solvent adlayer. The roman numerals depict the order of processing steps.*

It is worth noting that the exact values of the detected PMEs differ for different electrolyte compositions. In the electrolyte containing (bi)sulfate anions, the laser-induced current response of the system is not prominent at ca. 0.07 V (PME$_1$), 0.17 V (PME$_2$), and 0.66 V (PME$_3$) vs SSC; in the Cl$^-$-containing solution, the potentials shift to ca. 0.02 V (PME$_1$), 0.14 V (PME$_2$), and 0.72 V (PME$_3$) vs SSC, while in the presence of ClO$_4^-$ species, the values at which the transients change their orientation are located at ca. 0.09 V (PME$_1$), 0.14 V (PME$_2$), and 0.67 V (PME$_3$) vs SSC (see **Figure 5.26D**). As mentioned before, as a result of keeping the potential constant at each potential step, the obtained current transients should be seen as a superposition of multiple system answers associated with various interfacial processes.[45] This could, for instance, explain the existence of the PME$_1$'s at the beginning of the investigated regimes at the potentials at which (de)intercalation is not supposed to take place. In this particular potential values, the change of the transient orientation is most likely related to alterations in specific adsorption of anions at the electrode surface. This can be further confirmed by the tripolar shape of the LICTs (**Figure 5.28**) representing several processes with different time constants obtained at the low voltages (similar to the case described in **Section 5.4.4**).[46]
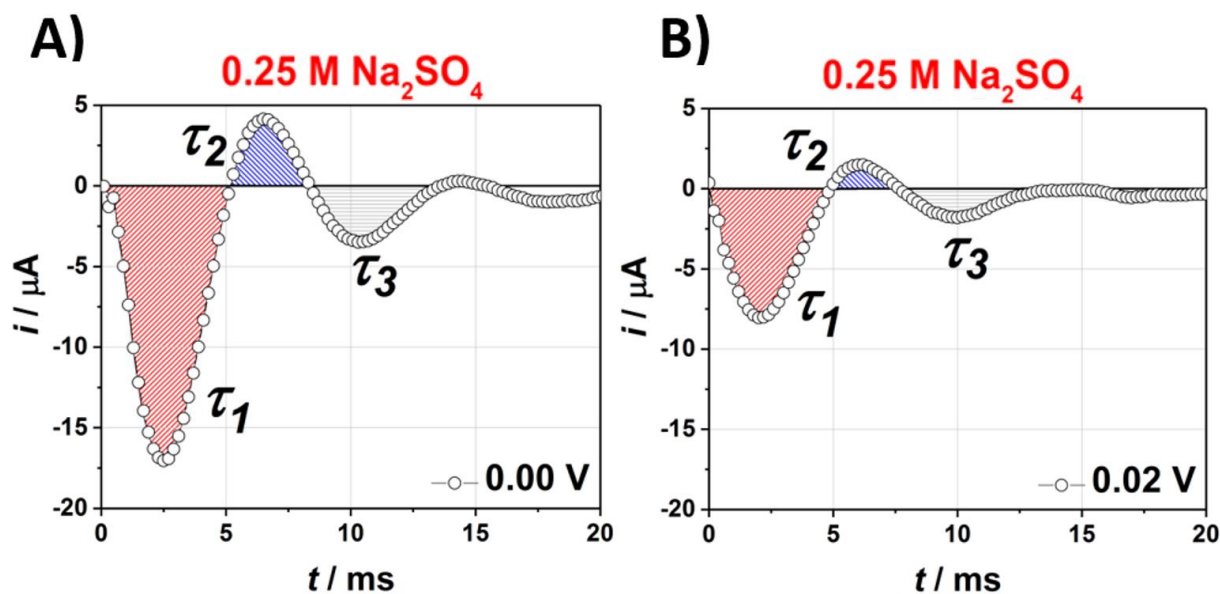


***Figure 5.28.*** *Examples of LICTs obtained for the CoHCF films immersed in 0.25 M Na$_2$SO$_4$ at potential values of (A) 0.00 V and (B) 0.02 V vs SSC. Each of the three peaks can be related to a different process taking place at the interface (including anion adsorption and desorption) and having a different time constant ($\tau_1$, $\tau_2$, or $\tau_3$). Compare with **Figure 5.21**.*

As multiple PMEs were not found in the case of the NiHCF films studied before (see **Section 5.4.3**), their existence seems to be a unique characteristic of CoHCF. The observed behavior might be related to the change in the oxidation state of cobalt in the film occurring at ~0.50 V vs SSC. Nevertheless, although the number of PMEs depends on the electrode material, their location appears to be affected by the composition of the electrolyte. In all the examined CoHCF-battery systems, the alkali-metal cations are the same. The only difference is the nature of the anions. Thus, presumably, the recorded changes might be a consequence of different adsorption strengths of the anions. This, however, would be visible in the shape of the resulting CVs, which does not change significantly in the presence of the dissimilar negatively charged species (**Figure 5.24A**). Therefore, the variations in the system behavior likely originate from different hydration energies of anions (**Figure 5.26D**).[46]

The observed dissimilarities can be explained as follows. The concentration of $Na^+$ cations near the electrode surface increases upon approaching the onset potentials of (de)intercalation. The sodium cations have higher hydration energy (409 kJ $mole^{-1}$) than the chloride (381 kJ $mole^{-1}$) and perchlorate (229 kJ $mole^{-1}$) species, and much lower hydration energy than the (bi)sulfate (1059 kJ $mole^{-1}$) anions.[350] These differences affect the mobility of the species.[373] Thus, after the laser-induced temperature jump, during relaxation, the ''faster'' chloride and perchlorate anions are supposed to reach the electrode surface before the sodium species. This can further influence the response of the system to the laser illumination and, as a consequence, alter the shape of the resulting LICTs. Correspondingly, the sodium cations are expected to move faster than the (bi)sulfate anions. Hence, they will likely reach the surface before the $SO_4^{2-}$ anions. This can influence the overall shape of current transients and change the position of the PMEs.[46]

While the PMEs correlate with the potentials of the minimum energy barriers to (de)intercalation, the potential values at which the system responses are at their maximum are also noteworthy. On the one hand, by using **Eq. 3.38**, one can demonstrate that the formation entropy of the interface is maximal when the potential drop in the interface is minimal. On the other hand, using the same equation, it can be shown that the maximal values of the current responses coincide with the state at which the entropy of the EDL formation reaches its minimum. This means that the potentials of maximum response are likely the potentials at which the order of the interfacial water layer structure is the highest. In all the three systems under study, hydration energies of the anions seem to have an effect also on the position of the

''potentials of minimum entropy''. The current transients reach the highest values at 0.36 V, 0.30 V, and 0.28 V vs SSC in 0.25 M $Na_2SO_4$, 0.25 M NaCl, and 0.25 M $NaClO_4$, respectively. Thus, it can be seen that the order of the surface solvent structure (crucial factor for LICT measurements) decreases as a consequence of an increase in the hydration energy of the negatively charged species present in the electrolyte (**Figure 5.26D**).[46]

To sum up, it is shown that the LICT technique can also be applied to investigate other types of aqueous battery systems- in this particular case the CoHCF-based ones. Interestingly, the examined systems exhibit three PMEs. Taking into account that other known electrochemical systems usually show up to one PME, these results appear surprising. This is, however, in agreement with the theory demonstrating the relationship between the order of the surface water structure and the ease of the interfacial charge and mass transfer to proceed. In all the studied cases, the potentials at which the EDL exhibits the lowest energy barriers correspond to the onset potentials of (de)intercalation in the voltammograms. The further analysis demonstrates the effect of the electrolyte composition (particularly anion species) on processes taking place at the interface. Even though the obtained results might be partly affected by the change in the oxidation/reduction of Co atoms present in the electrode material, exact values of the PMEs seem to depend on the nature of the electrolyte species- most likely on their dissimilar hydration energy.[46]

# 6. Conclusions and Outlook

The focus of this dissertation laid on the in-depth characterization of the electrified solid/liquid interface formed between different types of working electrodes and aqueous electrolytes in electrochemical systems essential for a sustainable provision of renewable energy. For this purpose, the laser-induced current transient (LICT) technique together with other commonly known electrochemical methods was utilized. Such a combination disclosed unique information about the influence of the electrolyte composition on the properties of the electric double layer (EDL) and the course of the interfacial processes.

The first type of the examined systems consisted of polycrystalline Pt and Au electrodes immersed in aqueous solutions of various compositions. The thorough studies using the laser technique together with the cyclic voltammetry (CV) disclosed a direct relationship between the structure of the EDL and the electrode activity towards the hydrogen evolution reaction (HER) and the oxygen reduction reaction (ORR). Furthermore, as revealed from the experiments on the systems containing acidic electrolytes of various pHs and near-to-neutral pH solutions of sodium and potassium salts, the interfacial properties strongly depend on the concentration and nature of individual species. The different $H^+$ concentration as well as the presence of dissimilar alkali-metal cations affect the structure of surface water molecules at certain potentials making them more or less able to reorient after the electron transfer towards and from the metal electrode surface. This, in turn, influences the electrocatalyzed reactions enhancing or hindering their rate.

It should be, however, noted that the utilization of the LICT technique does not have to be limited only to electrocatalytic systems containing noble metal electrodes. The laser illumination can also disclose the surface charge accumulated at the electrodes consisting of $Mn_2O_3$- a bifunctional catalytic material for the oxygen evolution reaction (OER) and the ORR. Interestingly, as obtained from the CV studies, there is a distinct correlation between the so-called potential of maximum entropy (PME) and the potential at which the ORR starts. Thus, also in this type of systems, the kinetics of electrocatalytic processes exhibits sensitivity to the structure of the electrode/electrolyte interface. Moreover, by combining the LICT analysis with impedance studies, one can acquire useful information not only about the phenomena occurring in the interface but also about the processes taking place in the structure of the electrocatalytic material during the reaction course.

In the next step, the studies were extended to the investigation of Na-ion battery systems. The interfaces formed between various aqueous electrolytes and electrodes consisting of $Na_2Ni[Fe(CN)_6]$ thin films deposited on polycrystalline Au electrodes were examined using the laser technique. Also in this case, the LICT appeared as a suitable method to detect the charge accumulated at the electrode surface and, as a consequence, to reveal the PMEs of battery systems. As shown for electrolytes containing sodium and potassium cations, the different electrolyte composition can significantly affect the structure of the electrified solid/liquid interface influencing the processes taking place at it. Notwithstanding, the net charge at the surface of NiHCF was found to be positive during both intercalation and deintercalation of the positively charged species. However surprising these results can seem, they confirm the previously drawn hypothesis regarding the three-stage mechanism of cation (de)intercalation. A careful analysis of the shape of the recorded current transients additionally proved the validity of this interpretation revealing the multistage mechanism of these processes.

Interestingly, the Na-ion battery systems utilizing NiHCF films as the electrode material are not the only ones, which can be investigated with the LICT method. The application of the laser beam can also successfully serve in the examination of the battery systems with Au-supported $Na_2Co[Fe(CN)_6]$ thin film electrodes. Similar as for NiHCF, the LICT unveiled the charge accumulated at the CoHCF electrodes immersed in aqueous electrolytes. Unlike the previous case, the CoHCF-based systems showed three PMEs. As electrochemical systems typically exhibit only up to one PME, the existence of three PME values seems to be surprising. Nevertheless, the presented findings support the theory correlating the EDL arrangement with its ability to facilitate the interfacial charge and mass transfer. In all the battery systems under study containing CoHCF as the cathode material, the potentials at which the entropy of the electrode/electrolyte interface reaches its maximum correspond to the onset potential values of cation intercalation into and deintercalation from the electrode structure. Moreover, the properties of the EDL, as well as the processes taking place at it, exhibit sensitivity to the electrolyte composition. Although the existence of the triple PMEs is a unique characteristic of the electrode material, their values vary according to the nature of anion constituents present in the solution.

The LICT appears to be a versatile method of electroanalysis. Owing to its relative simplicity and ease of combining with other techniques, it can find applications in studying a broad range of electrochemical systems. In spite of its original purpose, it can deliver information about the

interfaces formed not only between aqueous electrolytes and metal surfaces but also between aqueous electrolytes and inorganic electrode materials, such as metal oxides or Prussian Blue Analogs. The results obtained this way fit into the classical perspective emphasizing the importance of the double layer properties for the mechanism of the interfacial processes. Moreover, they underline the role of the electrolyte composition for the electrochemical system performance disclosing the often unclear origins of electrolyte-dependent variations. Comprehension of these effects can play a crucial role in improving and developing electrochemical systems essential for renewable energy provision. This, in turn, can significantly contribute to a decrease in operational expenses of these systems making the generation of green energy more cost-effective.

The presented examples hold a promise of utilizing the laser beam in the investigation of even more complex and "unusual" electrochemical systems. The principle correlating the EDL properties with the mechanism of the interfacial processes can be potentially transferred to other electrocatalytic or battery systems. Furthermore, as the effects associated with the electrolyte composition in these systems often do not follow trivial trends, there are plenty of cases where the application of the LICT could shed light on the origins of the observed variations in the system behavior. Particularly interesting might be the effect of the non-aqueous solutions. As the recorded laser-induced response of a particular system is strictly related to the solvent nature, the implementation of this technique should likely give an insight into the structure and properties of the formed interface. Finally, the laser measurements performed with opposite scan directions might also answer questions about the adsorption strength of particular ions at the electrode surfaces.[374]

# Appendix

## Appendix A: Table A.A and Calculated Time Constants

***Table A.A.*** *Values of the EEC parameters resulting from fitting the impedance spectra depicted in* ***Figure 5.18A*** *and* ***B*** *obtained for the NiHCF electrodes immersed in 0.25 M Na$_2$SO$_4$ and 0.25 M K$_2$SO$_4$ at various potentials. Note that according to the model, the values of adsorption capacitances and resistances can be formally negative.*

| Conditions | $R_u$ [Ω] | $C_{dl}$' [µF] | $n_{dl}$ | $R_{ct}$ [Ω] | $R_{a,1}$ [Ω] | $R_{a,2}$ [Ω] | $C_{a,1}$ [µF] | $C_{a,2}$ [mF] |
|---|---|---|---|---|---|---|---|---|
| at 0.40 V vs RHE in 0.25 M Na$_2$SO$_4$ | 26.902 | 70.297 | 0.744 | 89.383 | -44.996 | -46.173 | -489.93 | 34.084 |
| at 0.50 V vs RHE in 0.25 M Na$_2$SO$_4$ | 27.124 | 65.165 | 0.778 | 92.806 | -46.062 | -221.99 | -516.96 | 17.205 |
| at 0.66 V vs RHE in 0.25 M K$_2$SO$_4$ | 64.622 | 4.347 | 0.792 | 276.9 | 7013.2 | -4935.6 | 5.1998 | -0.197 |
| at 0.76 V vs RHE in 0.25 M K$_2$SO$_4$ | 103.05 | 5.222 | 0.861 | 1090.9 | 7324.2 | -4201.2 | 4.67 | -0.206 |

The impedance of the EDL $C_{dl}$' was determined from the CPE parameters using the software available online.[375]

The calculated time constant, $\tau$, both at 0.40 V and 0.50 V vs RHE in 0.25 M Na$_2$SO$_4$ was ca. 6 ms, while in 0.25 M K$_2$SO$_4$ it was equal to ca. 1.2 ms and ca. 4.5 ms at 0.66 V and 0.76 V vs RHE, respectively. The obtained values are closely related to the $\tau_1$, $\tau_2$, and $\tau_3$ estimated from the LICT graphs (**Figure 5.21**).

# Appendix B: Abbreviations and Symbols

*List of abbreviations:*

| | |
|---|---|
| AC | Alternating Current |
| ads | Adsorbed Species |
| AFC | Alkaline Fuel Cell |
| AFM | Atomic Force Microscopy |
| AM | Alkali-Metal |
| AN | Anion |
| aq | Liquid Phase |
| CE | Counter Electrode |
| CoHCF | Cobalt Hexacyanoferrate |
| CPE | Constant Phase Element |
| CV | Cyclic Voltammetry |
| DC | Direct Current |
| DE | Dummy Electrode |
| dec | Decade |
| DFT | Density Functional Theory |
| DMFC | Direct Methanol Fuel Cell |
| EC-STM | Electrochemical Scanning Tunneling Microscopy |
| EDL | Electric Double Layer |
| EEC | Equivalent Electric Circuit |
| EIS | Electrochemical Impedance Spectroscopy |

| | |
|---|---|
| EQCM | Electrochemical Quartz Crystal Microbalance |
| FC | Fuel Cell |
| fcc | Face Centered Cubic |
| g | Gas Phase |
| HER | Hydrogen Evolution Reaction |
| HMRDE | Hanging Meniscus Rotating Disk Electrode |
| HOPG | Highly Ordered Pyrolytic Graphite |
| HOR | Hydrogen Oxidation Reaction |
| IHL | Inner Helmholtz Layer |
| ITO | Indium Tin Oxide |
| LICT | Laser-Induced Current Transient |
| MMS | Mercury-Mercury Sulfate |
| ME | Microelectrode |
| NiHCF | Nickel Hexacyanoferrate |
| OER | Oxygen Evolution Reaction |
| OHL | Outer Helmholtz Layer |
| ORR | Oxygen Reduction Reaction |
| PAFC | Phosphoric Acid Fuel Cell |
| PBA | Prussian Blue Analog |
| pc | Polycrystal |
| PEM | Polymer Electrolyte Membrane |
| PME | Potential of Maximum Entropy |
| PZC | Potential of Zero Charge |
| PZFC | Potential of Zero Free Charge |

| | |
|---|---|
| PZTC | Potential of Zero Total Charge |
| qcw | Quartz Crystal Wafer |
| RE | Reference Electrode |
| RHE | Reversible Hydrogen Electrode |
| s | Solid Phase |
| SOE | Solid Oxide Electrolyzer |
| SOFC | Solid Oxide Fuel Cell |
| SSC | Silver-Silver Chloride |
| WE | Working Electrode |
| WEL | Water Electrolyzer |

*List of symbols:*

| | |
|---|---|
| $\Delta H^o$ | Hydration Energy |
| $c$ | Thermal Capacity of Metal Electrode |
| $c_1$ | Thermal Capacity of Aqueous Electrolyte |
| $C_a$ | Adsorption Capacitance |
| $C_d$ | Diffuse Layer Capacitance |
| $C_{dl}$ | Double Layer Capacitance |
| $C'_{dl}$ | Factor Related to the Double Layer Capacitance |
| $C_f$ | Film Capacitance |
| $C_i$ | Inner Layer Capacitance |
| $C_S$ | Sensitivity Factor |
| $d$ | Diameter |
| $E$ | Potential |
| $e_0$ | Electron Charge |
| $E_0$ | Potential Amplitude |
| $E^2$ | Potential Drop at Diffuse Layer |
| $E_i$ | Initial Potential |
| $E^o$ | Standard Potential |
| $E_{charge}$ | Electrode Potential Contribution Coming from the Electrode Surface Charge |
| $E_{dipole}$ | Electrode Potential Contribution Coming from the Water Molecules |
| $E_{M-S}$ | Potential between the Electrode and the Solution |
| $E_{PZC}$ | Potential of Zero Charge |
| $E_{TD}$ | Thermo-Diffusion Potential |

| | |
|---|---|
| $E^w$ | Potential Drop due to the Solvent Structuring |
| $E_\lambda$ | Switching Potential |
| $f$ | Frequency |
| $F$ | Faraday Constant |
| $f_0$ | Natural Frequency |
| $i$ | Current |
| $i_0$ | Current Amplitude |
| $i_{Xtrm}$ | Maximal Current Extremum |
| $j$ | Current Density |
| $k$ | Rate Constant |
| $K$ | Equilibrium Constant |
| $K_S$ | Constant Representing the Influence of the Solvent on the $E_{PZC}$ |
| $L$ | Inductance |
| $m$ | Mass |
| $n$ | Harmonic Number of Oscillation |
| $p$ | Power density |
| $q$ | Charge |
| $q_a$ | Adsorption Charge |
| $q_f$ | Final Charge |
| $q_i$ | Initial Charge |
| $q_M$ | Metal Electrode Charge |
| $q_S$ | Charge Carried by the Ions Present in the Solution |
| $q_{dipole}$ | Charge Accumulated at the Surface Water Adlayer |

| | |
|---|---|
| $R$ | Resistance |
| $R_a$ | Adsorption Resistance |
| $R_{ct}$ | Charge Transfer Resistance |
| $R_f$ | Film Resistance |
| $R_u$ | Uncompensated Resistance |
| $S$ | Entropy |
| $\hat{S}$ | Eastman Entropy |
| $T$ | Temperature |
| $t$ | Time |
| $t_0$ | Initial Time |
| $T_0$ | Initial Temperature |
| $W$ | Diffusion Warburg Impedance |
| $Z$ | Impedance |
| $Z_{dl}$ | Double Layer Impedance |
| $Z_{Im}$ | Imaginary Part of Impedance |
| $Z_{Re}$ | Real Part of Impedance |
| $\delta$ | Surface Reflectivity |
| $\epsilon$ | Energy Flux per Unit Area |
| $\theta$ | Phase Angle |
| $\vartheta$ | Transport Number |
| $\kappa$ | Thermal Conductivity of the Metal Electrode |
| $\kappa_1$ | Thermal Conductivity of the Aqueous Electrolyte |
| $\mu$ | Shear Modulus |

| | |
|---|---|
| $\rho$ | Metal Electrode Density |
| $\rho_l$ | Aqueous Electrolyte Density |
| $\rho_Q$ | Quartz Density |
| $\tau$ | Time Constant |
| $\upsilon$ | Scan Rate |
| $\Phi$ | Work Function |
| $\omega$ | Angular Frequency |

# What Do Laser-Induced Transient Techniques Reveal for Batteries? Na- and K-Intercalation from Aqueous Electrolytes as an Example

Daniel Scieszka,[†,‡] Jeongsik Yun,[†,‡] and Aliaksandr S. Bandarenka*[,†,‡] [ID]

[†]Physics of Energy Conversion and Storage (ECS), Physik-Department, Technische Universität München, James-Franck-Straße 1, 85748 Garching, Germany

[‡]Nanosystems Initiative Munich (NIM), Schellingstraße 4, 80799 Munich, Germany

[S] *Supporting Information*

**ABSTRACT:** Technological advancement has been revolutionized by rechargeable batteries, without which the use of various modern devices would not be possible. Aqueous Na ion batteries have lately garnered much attention, being recognized as a promising alternative to the commonly used Li ion batteries for the large-scale energy storage systems. However, further improvement and optimization of such systems require a more detailed understanding of intercalation mechanisms. In this work, we for the first time demonstrate the implementation of the laser-induced current transient (LICT) technique for in situ characterization of battery systems and investigate the interface between $Na_2Ni[Fe(CN)_6]$ model battery electrodes and aqueous electrolytes in contact with aqueous electrolytes. Quite counterintuitively, the LICT method revealed that at the quasi-steady-state the electrode surface stays positively charged within the potential range where the intercalation/deintercalation of sodium as well as of potassium is possible, evidencing that the intercalation mechanism of the alkali-metal cations should be rather complex. Furthermore, the specific shape of the observed current transients indicates that the interfacial processes of intercalation/deintercalation have at least three different relaxation time constants. The relaxation behavior is highly influenced by the nature of the alkali-metal cations—most likely through their different solvation energy. In addition, we outline how the laser-based experiments can intensify detailed in situ investigations of battery systems.

**KEYWORDS:** *laser-induced current transients, aqueous Na ion battery, intercalation, interfacial charge and mass transfer, $Na_2Ni[Fe(CN)_6]$, battery materials*
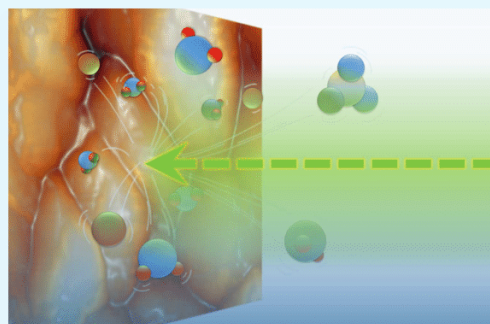
## ■ INTRODUCTION

The energy provision schemes tend nowadays toward renewable resources.[1−4] Among them solar and wind power are well-developed and already share a noticeable portion of sustainable energy provision in various countries.[2,5−7] However, their intermittent energy generation causes the so-called "generation versus consumption" problem. Thus, in order to smooth out the fluctuation of energy generation, effective energy storage systems (ESSs) are necessary.[8,9] Battery systems are considered promising candidates for these purposes, due to their high energy conversion efficiency, flexibility, affordability, and the relatively simple maintenance of these devices.[10−12]

Li ion batteries are among the most advanced types of batteries. They have found applications in various mobile devices due to their high energy density and large operational voltage.[13] However, for the large-scale applications, the abundance and availability of battery materials for Li ion batteries as well as safety issues drawn from the use of flammable electrolytes are problematic. Aqueous Na ion batteries can be an effective solution. The abundance and availability of Na are much higher compared to those of Li.[10,13] Furthermore, the similarity in electrochemical properties of Na

has the advantages of borrowing the developed technology of Li ion batteries. As a result, the use of safer electrolytes will also decrease the costs of the maintenance. For these reasons, sodium ion batteries have recently attracted great interest.

Despite the noticeable progress in the development of electrode materials for aqueous Na ion batteries,[14] the understanding of the intercalation mechanisms is still insufficient. Therefore, elaboration of novel in situ characterization methodologies would provide new insights to investigate battery systems, leading to their further optimization. Probing of the electrode/electrolyte interface with laser beams provides, in many cases, a convenient means to investigate various electrochemical processes.[15,16] This technique utilizes the so-called temperature jump effect.[17−20] One of its biggest benefits is that the high-power illumination results in a sudden temperature change that is too fast for the charge transfer process to occur. Therefore, it is possible to separate the double layer response from the charge transfer processes.[21]
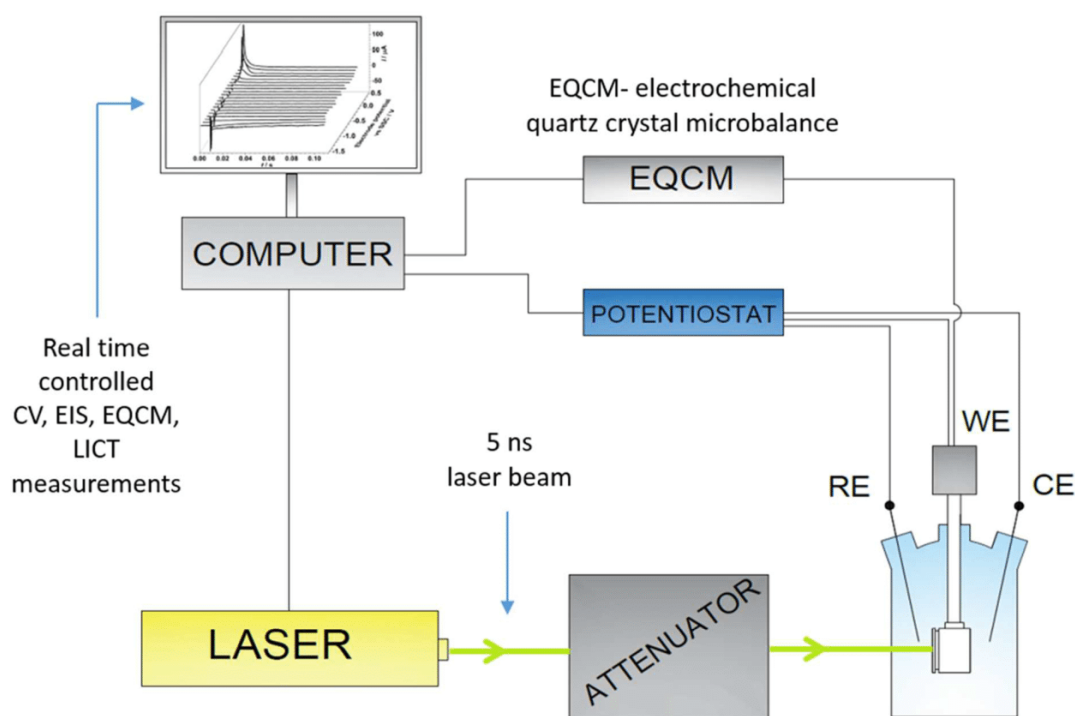
**Figure 1.** Simplified sketch of the experimental setup for simultaneous voltammetric, impedance, nanogravimetric, and laser-induced current transient measurements. RE, reference electrode; WE, working electrode; CE, counter electrode.

As formerly proved, an actual system response to the sudden irradiation reveals the influence of the electrode temperature on the structure of the inner Helmholtz plane of the electric double layer.[22,23] The orientation of water molecules in the first sublayer is determined by the interaction between their dipole moments and the electric field generated by the electrode surface charge ($\Phi_{charge}$).[24−27] Due to their large dipole moment, the solvent molecules mainly contribute to the potential drop ($\Phi_{dipole}$) of the electrode potential. Thus, the potential between the electrode and the solution ($\Phi_{M-S}$) can be expressed as

$$\Phi_{M-S} = \Phi_{charge} + \Phi_{dipole} \qquad (1)$$

The temperature jump introduces randomness in the water layer for a brief period of time. As a result, the influence of $\Phi_{dipole}$ decreases, changing $\Phi_{M-S}$ according to eq 1.[28] The potential jumps can be observed as current transients the sign of which corresponds to the sign of the electrode surface charge.[21] The laser-induced current transient (LICT) technique, which utilizes this phenomenon, is a useful and relatively simple method to evaluate also the kinetics and mechanism of the Faradaic processes, as well as to reveal the potential of maximum entropy (PME) and, related to it, the potential of zero charge (PZC).[29] The PZC and PME are among the key parameters to understand the mechanism of various electrode processes.[21−23,29−31] These parameters can, for example, answer the question about the interfacial energy barriers for the intercalation helping to assess the "looseness" of the interfacial water layer.[21,32] Regardless of their importance, determination of the PZC and PME has never been straightforward.[30] Thus, the application of the LICT might open up new possibilities for more effective studies of the interface of electrode/electrolyte. Furthermore, the LICT technique can be easily combined with other commonly used electrochemical methods (i.e., cyclic voltammetry, electrochemical impedance spectroscopy, and electrochemical nanogravimetry). Such a combination shall be a powerful tool for a detailed characterization of various battery systems.

To the best of our knowledge, no studies of battery systems using the LICT technique have been reported so far. In this work, we applied the LICT method (in combination with other electrochemical techniques) to investigate the electrode/electrolyte interfacial processes in model battery systems. As a model electrode, one of the state-of-the-art cathode materials for aqueous Na ion batteries, namely, $Na_2Ni[Fe(CN)_6]$ thin films, were utilized. It was revealed from the LICT measurements that the $Na_2Ni[Fe(CN)_6]$ electrode surfaces are positively charged within the electrode potentials where intercalation and deintercalation of sodium and potassium are possible. This rather surprising observation, however, supports the hypothesis of a complex mechanism, involving temporary anion adsorption from the electrolyte side.[33,34] Furthermore, we show that the nature of the intercalating alkali-metal cations can significantly affect the behavior of the electrode/electrolyte interface, altering the PME. These changes are likely correlated with the different hydration (solvation) energies of the alkali-metal cations.

## ■ EXPERIMENTAL METHODS

All electrochemical experiments were carried out in a conventional three-electrode cell using a VSP-300 potentiostat (Bio-Logic, France) combined with a QCM 200 (Stanford Research Systems) electrochemical quartz crystal microbalance (EQCM), as depicted in Figure 1. AT-cut Au quartz crystal wafers (Stanford Research Systems) served as working electrodes, while a Pt wire was used as a counter electrode.
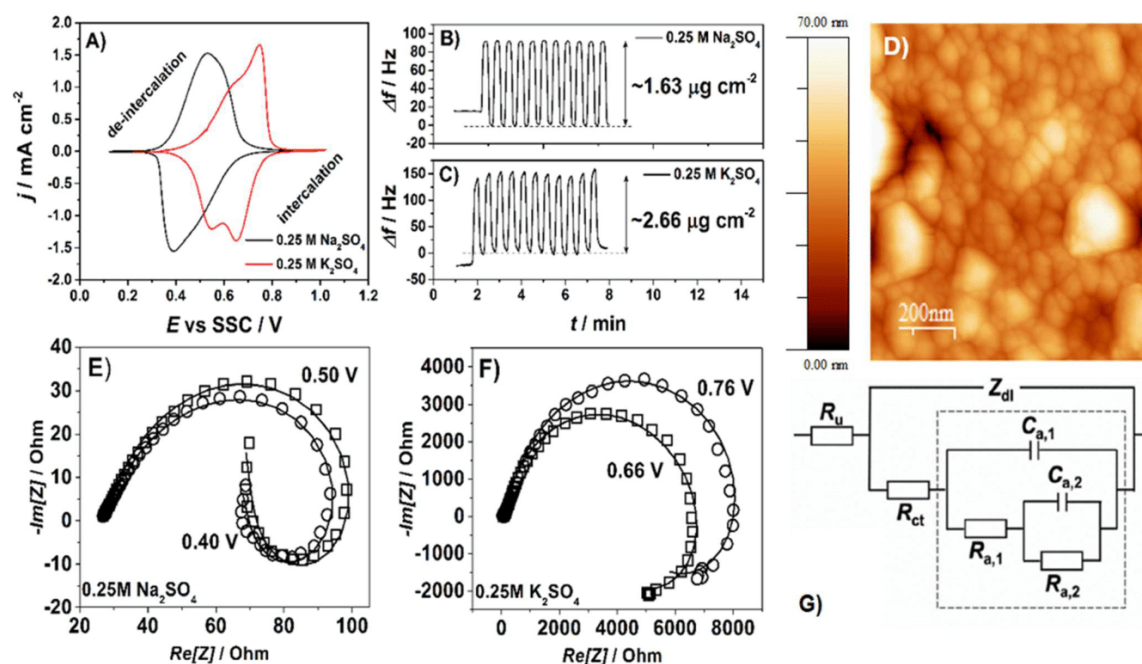
146

**Figure 2.** Characterization of the $Na_2Ni[Fe(CN)_6]$ thin films. (A) Typical cyclic voltammograms of the $Na_2Ni[Fe(CN)_6]$ thin films in 0.25 M $Na_2SO_4$ (black) and 0.25 M $K_2SO_4$ (red) electrolytes and their corresponding electrode mass changes (1 Hz = 17.7 ng cm$^{-2}$) during intercalation of (B) $Na^+$ and (C) $K^+$, respectively (background corrected curves). (D) Representative AFM image of the surface of the resulting $Na_2Ni[Fe(CN)_6]$ thin films. Impedance spectra (open symbols) of the thin films obtained in (E) 0.25 M $Na_2SO_4$ and (F) 0.25 M $K_2SO_4$ electrolytes, respectively, together with the corresponding fittings (solid lines). The fitting was carried out using an equivalent electric circuit shown in part G, which is an impedance model that describes a three-stage mechanism with all the stages being reversible.[33,34] $R_u$, uncompensated resistance; $Z_{dl}$, the double layer impedance; $R_{ct}$, the charge transfer resistance; other R and C elements in the dashed square in part G are pseudo-resistances and pseudo-capacitance of adsorption, respectively. Their meaning is explained in detail in refs 33 and 34 (see the Supporting Information for further details).

All the potentials in this work are reported vs the Ag/AgCl (SSC) reference electrode. A multimode EC-STM/AFM instrument (Veeco VI) with a Nanoscope IIID controller using the Nanoscope 5.31r1 software was utilized for the atomic force microscopy (AFM). AFM measurements were performed in tapping mode (AFM tips, Bruker RTESP-300). The deposition of $Na_2Ni[Fe(CN)_6]$ thin films was performed according to the procedure reported in the previous work.[33] Briefly, the thin films were electrochemically deposited from aqueous solutions containing 0.25 M $Na_2SO_4$, 0.5 mM $NiCl_2·6H_2O$, and 0.5 mM $K_3[Fe(CN)_6]$. All the chemicals utilized in this work are listed with details in the Supporting Information (SI). The electrode potential was cycled in the range between 0.123 and 0.923 V vs SSC at a scan rate of 50 mV s$^{-1}$ until the desired mass (after ca. 60−80 potential cycles) was deposited.

In Figure 2A, $Na_2Ni[Fe(CN)_6]$ electrodes are characterized during sodium and potassium intercalation and deintercalation. Anodic and cathodic peaks in the figure primarily resulted from the change of the oxidation state of Fe in the film, which is formally the first step of the alkali metal cation intercalation/deintercalation. Consequently, those anodic and cathodic peaks are also associated with the induced deintercalation and intercalation of alkali-metal cations, respectively, as can be seen from Figure 2B,C. The net electrode mass change during the (de)intercalation of $Na^+$ and $K^+$ was calculated from the EQCM data as ca 1.63 $\mu$g cm$^{-2}$ ($Na^+$) and ca 2.66 $\mu$g cm$^{-2}$ ($K^+$), respectively (Figure 2B,C). From the comparison of the mass of the deposited thin films (normally ca. 22 $\mu$g cm$^{-2}$ in these cases) to the electrode mass changes during the (de)intercalation, these measured values were very close (within ∼3% of accuracy) to the expected values assuming (de)intercalation of one alkali-metal cation per one Fe atom changing its oxidation state. The morphology of the $Na_2Ni[Fe(CN)_6]$ thin films was characterized using AFM. A relatively smooth and uniform surface of the thin films was observed (Figure 2D).

Potentiodynamic electrochemical impedance spectroscopy (PDEIS)[35,36] measurements were performed using an ac probing signal amplitude of 10 mV in the frequency range between 10 kHz and 0.5 Hz in the potential ranges between 0.123 and 0.923 V for 0.25 M $Na_2SO_4$ electrolytes and 0.223 and 1.023 V for 0.25 M $K_2SO_4$ electrolytes, respectively. The homemade "EIS Data Analysis 1.1" software was used to perform the fitting of the obtained impedance spectra. Figure 2E,F displays the collected impedance spectra for the thin films together with the corresponding fitting curves. Figure 2G shows a physical model, i.e., equivalent electric circuit, used to fit the impedance spectra, which are associated with a three-stage scheme of intercalation of alkali-metal cations, involving temporary adsorption and desorption of anions from the electrolytes at the electrode surface.[33,34] A detailed description of the model, which has been used for the fitting of the "loop-shaped" impedance spectra, is given in the Supporting Information and in refs 33, 34, and 37. The validity of the impedance data was confirmed by the Kramers−Kronig analysis and procedures described in detail elsewhere.[38−40]

A Quanta-Ray INDI-Series pulsed Nd:YAG laser (Spectra Physics Lasers) with a 5−8 ns pulse width, a repetition rate of 10 Hz, and a 532 nm wavelength was used for the LICT measurements. This laser light wavelength is commonly used for the laser-induced transient techniques[16,28,32,41,42] in order to avoid side effects, such as photoemission of electrons. For many electrode materials, the photoemission threshold is at around 200−300 nm.[29] The beam diameter of the laser, ∼9 mm (slightly smaller than the working electrode diameter), along with the distance between the laser source and the working electrode was not changed. In order to reduce the power of a single laser pulse, the beam was passed through a motorized high-energy variable beam splitter (VA-CB-532-CONEX, Newport Corp.) equipped with a passively air-cooled beam dump (BD-7, Newport Corp.) and working as an attenuator. The laser power
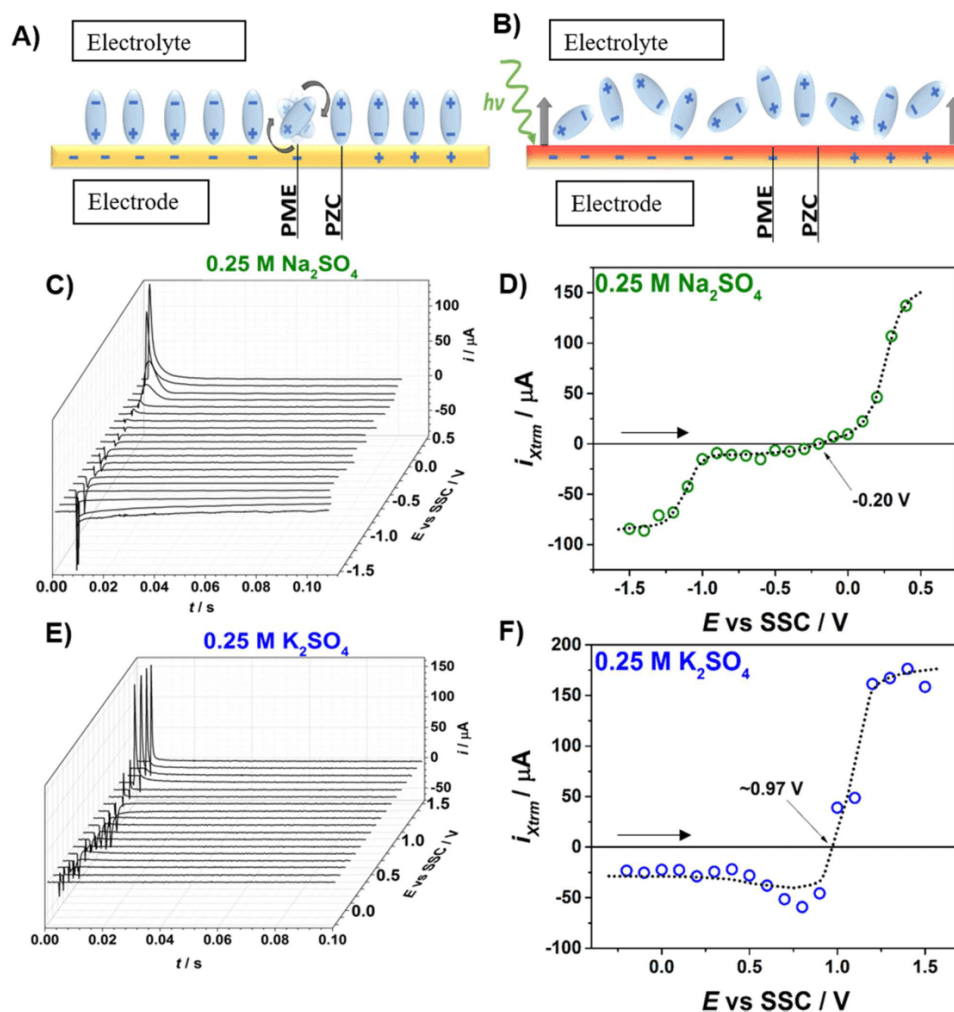
147

**Figure 3.** (A) Schematic of the orientation of water dipoles toward the metal surface according to the surface charge. The potential at which there is a maximum disorder in the interfacial layers corresponds to the PME, while PZC corresponds to the apparent "absence" of the net surface charge. In most cases, PME and PZC are very close to each other. (B) Disorder after the rapid increase in the temperature of the electrode surface induced by the laser illumination. (C) Laser-induced current transients for the Au (polycrystalline) electrodes in 0.25 M $Na_2SO_4$ within the potential range from −1.5 to 0.5 V vs SSC. (D) The corresponding dependence of the maximal extrema of the current transients shown in part C as a function of the potential. (E) Laser-induced current transients for the Au (polycrystalline) electrodes in 0.25 $K_2SO_4$ within the potential range from −0.2 to 1.5 V vs SSC. (F) The corresponding dependence of the maximal extrema of the current transients shown in part E as a function of the potential.

at the output of the attenuator in all experiments was kept at ∼12 mJ (∼19 mJ $cm^{-2}$) per pulse, which is below the damage threshold of the electrode.

All the LICT measurements were performed in the potentiostatic mode monitoring the change of the current in time.[28] In order to investigate the correlation between the PME and hydration energy, the 0.25 M $Na_2SO_4$ and 0.25 M $K_2SO_4$ electrolytes were used in all LICT measurements. For a polycrystalline Au electrode, which served as a support for the $Na_2Ni[Fe(CN)_6]$ films and a benchmark electrode, the LICT measurements were carried out within the potential range from −1.5 to 0.5 V and −0.2 to 1.5 V (both cases 100 mV potential steps) in 0.25 M $Na_2SO_4$ and 0.25 M $K_2SO_4$ electrolytes, respectively. Similar experimental procedures were carried out for $Na_2Ni[Fe(CN)_6]$ films in 0.25 M $Na_2SO_4$ and 0.25 M $K_2SO_4$ within the potential range of the $Na^+$ and $K^+$ ions intercalation/deintercalation (20 mV potential steps). In the next step, the potential ranges were continuously extended for both electrolytes, reaching −0.38 V for $Na_2SO_4$ and −1.20 V for $K_2SO_4$.

## ■ RESULTS AND DISCUSSION

The orientation of the "surface water" molecules at the electrified solid/liquid interface is largely influenced by the resulting electrode surface charge (see schematics in Figure 3A). The rapid increase in temperature at the electrode surface caused by the short laser illumination will lead to the temporary disorder of the adsorbed molecules in the electric double layer (EDL), as schematically illustrated in Figure 3B.[29] The disorder in the EDL induced by the laser pulse results in the sharp either positive or negative current transients (Figure 3C,E), which are closely related to the sign of the surface charge at the electrode and some possible Faradaic processes, related to, for example, specific (re)adsorption/(re)desorption of electrolyte species at the electrode surface. Thus, in the simplest case, the positive net charge will result in positively oriented current transients and vice versa. Figure 3C,E shows representative plots obtained
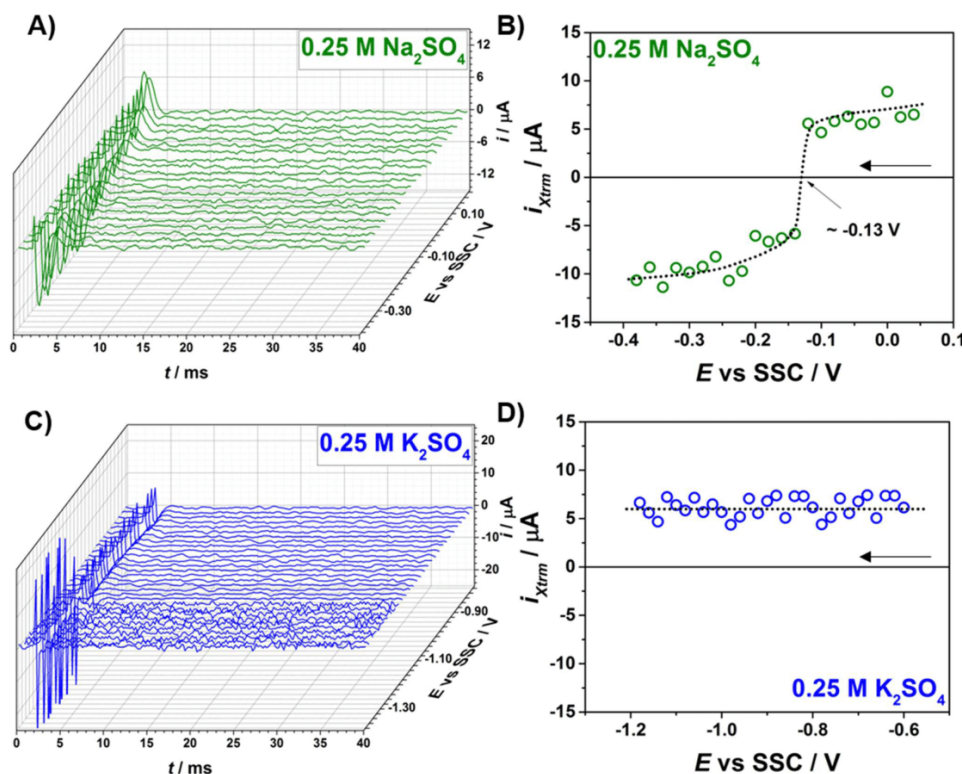
148

**Figure 4.** LICT characterization of the $Na_2Ni[Fe(CN)_6]$ films in aqueous (A, B) 0.25 M $Na_2SO_4$ and (C, D) 0.25 M $K_2SO_4$ electrolytes. (A) 3D LICT plot for the $Na_2Ni[Fe(CN)_6]$ film in 0.25 M $Na_2SO_4$. (B) The corresponding dependence of the maximal extrema of the current transients shown in part A as a function of the electrode potential. The PME is estimated to be near −0.13 V. (C) A similar 3D LICT plot for the $Na_2Ni[Fe(CN)_6]$ film in 0.25 M $K_2SO_4$. Note the drastic changes in the current transients at more negative potentials due to the hydrogen evolution reaction and possible changes in the film composition. (D) The corresponding dependence of the maximal extrema of the current transients shown in part C as a function of the potential. Arrows in parts B and D indicate the scan direction.

for the pure polycrystalline gold electrode (the substrate for the $Na_2Ni[Fe(CN)_6]$ films) immersed in the 0.25 M $Na_2SO_4$ and 0.25 M $K_2SO_4$ solutions. Sharp positive and negative current transients are seen at ca. 8 ms (shortly after illumination) at different potentials, which represent the relaxation of the interfacial layer. The sign of the current transients collected in the 0.25 M $Na_2SO_4$ solution flips at ca. −0.20 V. It can be more clearly seen in Figure 3D, showing the extreme current values obtained for each applied constant potential. At the "flipping potential", the current transient response after the laser illumination is not prominent. Close to the PZC, the contribution of the adsorbed species to the current response is expected to be minimal, which implies the zero surface charge of the Au electrode. In reality, however, due to the natural orientation of water molecules toward the metallic surfaces, the reorientation of the water dipoles takes place at the potential of maximum entropy (PME) located in the vicinity of the PZC.[43,44] Interestingly, the potential of zero response for the system containing potassium cations moves toward more positive values. The Au electrode immersed into the 0.25 M $K_2SO_4$ solution exhibits the potential of zero response at ca. 0.97 V (Figure 3F). It directly indicates that the PME is not only a feature of the material itself but its value can be largely affected by the electrolyte composition. In this case, the potassium cations, having lower hydration energy, interact

more weakly with the water sublayer, which can directly influence the interface charge.

Let us consider a similar system, i.e., the same electrolytes and the same Au-electrode, which is, however, covered by a $Na_2Ni[Fe(CN)_6]$ thin film. Similar LICT experiments were performed in order to investigate the actual sign of the charge of the electrode surface during intercalation and deintercalation of sodium and potassium.

The first series of experiments show that the PME for the $Na_2Ni[Fe(CN)_6]$ thin films in 0.25 M $Na_2SO_4$ is located at the potential of ca. −0.13 V vs SSC, which is outside of the intercalation/deintercalation electrode potential range (Figure 4A,B). Surprisingly, in the case of 0.25 M $K_2SO_4$, the potential at which the current transient changes the sign is not observed at all (Figure 4C,D). Instead, the laser-induced transient peaks are positively oriented (at the shorter time, i.e., after the laser-probing) within the whole electrode potential range up to the onset potential (ca. −1.20 V) of the hydrogen evolution reaction. Thus, the PME might be located at even more negative potentials; however, due to the possible damage to the film and $H_2$ bubble generation, its exact experimental assessment was not possible. Another explanation is that the examined system simply does not exhibit the PME. This result might be correlated with the lower hydration energy of $K^+$ than that of $Na^+$. According to Huang et al., such a situation can indeed take place, and it is closely correlated with the
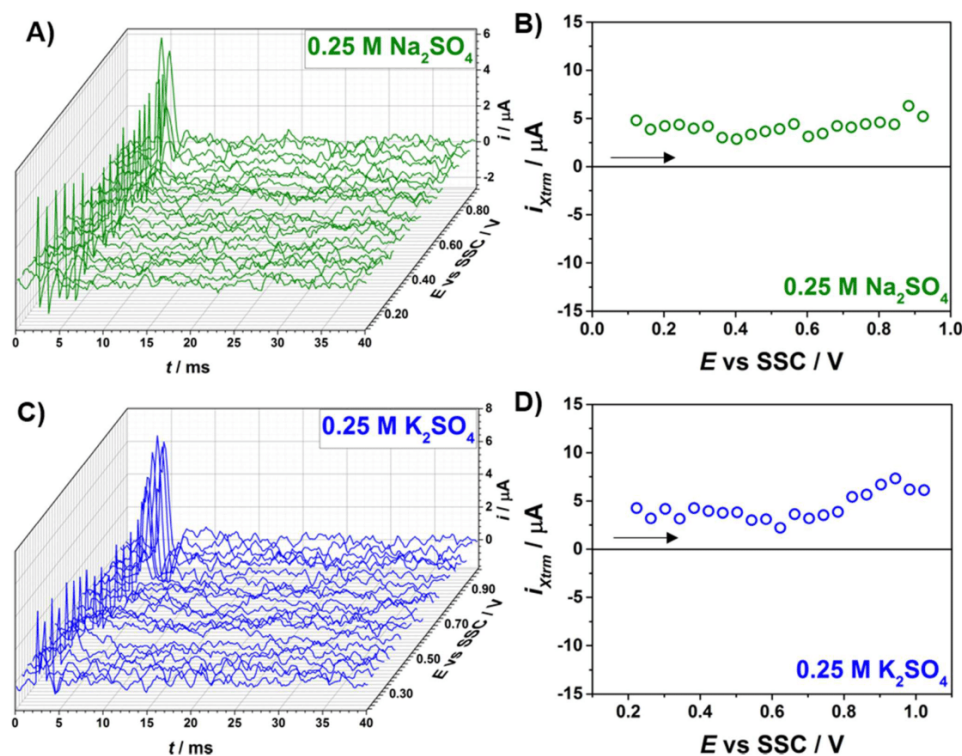
149

**Figure 5.** LICT characterization of the $Na_2Ni[Fe(CN)_6]$ films in aqueous (A, B) 0.25 M $Na_2SO_4$ and (C, D) 0.25 M $K_2SO_4$ electrolytes, respectively. (A) LICT plot obtained in the potential range of sodium intercalation/deintercalation. (B) Corresponding plot of the maximal extrema of the current transients shown in part A as a function of the electrode potential. (C) LICT plot in the potential range of potassium intercalation/deintercalation. (D) Corresponding dependence of the collected positive extrema of the current transients shown in part C as a function of the electrode potential. Arrows in parts B and D indicate the scan direction. Every second step is depicted in the graph (see Supporting Information for the complete sets of transients).

electrolyte composition. Species adsorbed at the electrode surface can change the electronic structure of the electrode surface and result in an apparent constant sign of the surface charge.[45]

Parts A and C of Figure 5 show the results of LICT characterization of the $Na_2Ni[Fe(CN)_6]$ thin films in the 0.25 M $Na_2SO_4$ and 0.25 M $K_2SO_4$ electrolytes within the potential ranges where Na- and K-intercalation take place, respectively. Soon after the electrode illumination, one can observe well-pronounced spikes with the maximal extrema of the current always being positive. As the response of the electric double layer itself should be the fastest, as discussed above, this suggests that the electrode surface remains positively charged at quasi-steady-state at each electrode potential within the whole ranges in which the intercalation takes place for both of $Na^+$- and $K^+$-containing solutions (irrespectively of the scan directions). As a further illustration, Figure 5B,D shows the dependences of the measured maximum current (at the spikes) as a function of the electrode potential for both electrolytes. These results seem to be counterintuitive, considering the fact that during the intercalation process the positively charged alkali-metal cations should be then attracted by the positively charged electrode surface and then inserted into its structure.

It should be, however, noted that the laser-induced relaxation curves in the case of the $Na_2Ni[Fe(CN)_6]$ thin films show "fluctuations", when compared to Au metal electrodes (compare Figure 3C,E with Figures 4A,C and 5A,C). Most of

the observed transients for the $Na_2Ni[Fe(CN)_6]$ thin films in the 0.25 M $Na_2SO_4$ and 0.25 M $K_2SO_4$ electrolytes exhibit "tripolar shapes", with the current peaks being positive at the beginning, changing to slightly or significantly negative values, and becoming again positive afterward (see Figures 5A,C and 6). These trends cannot be explained with artifacts caused by the potentiostat, because they are not observable during the same experiments with the pure Au electrode; they would not be expectable under the conditions of this work, as the time frame of the device is less than a few microseconds in this case.

Therefore, such a fine shape of the transients suggests that there is more than one relaxation time for establishing the resulting potential drop. More specifically, LICT likely reveals at least three different relaxation processes having different "time constants" (designated as $\tau_1$, $\tau_2$, and $\tau_3$ in Figure 6) for the systems containing both $Na^+$ (Figure 6A,B) and $K^+$ ions (Figure 6C,D).

The first (corresponding to shorter times, Figure 6) LICT peaks can be correlated with the response of the electric double layer itself. This process is anodic and can be interpreted as the water sublayer reorientation after the laser-induced temperature jump. The positive charge generated at this step might result in an intensified specific adsorption of $SO_4^{2-}$ anions present in the electrolyte. Other possible contribution to the first peaks might be partial intercalation and deintercalation of cations caused by the rapid temperature jump. The following peaks are most likely associated with the interfacial charge and mass transfer. It
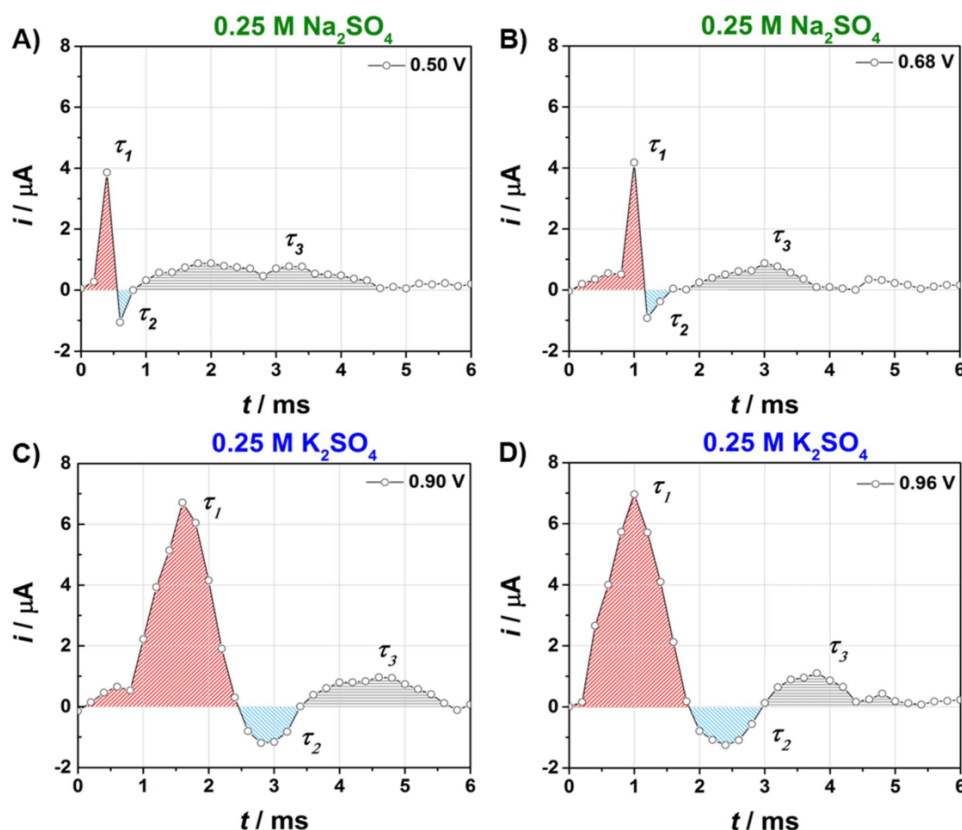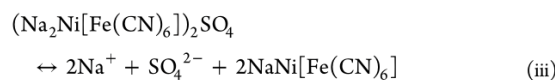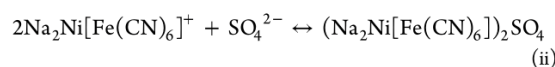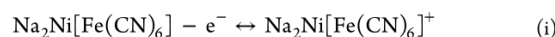
150

**Figure 6.** Examples of current transients for $Na_2Ni[Fe(CN)_6]$ thin films in 0.25 M $Na_2SO_4$ at (A) 0.50 V and (B) 0.68 V, as well as in 0.25 M $K_2SO_4$ at (C) 0.90 V and (D) 0.96 V. Three clearly distinguishable peaks associated with the interfacial processes with three different time constants can be observed (designated as $\tau_1$, $\tau_2$, and $\tau_3$). Solid lines are given as a guide to the eyes.

should be noted here that since the applied potential at each potential step during the LICT measurements was kept constant, the observed peaks might be seen as a superposition of different processes. For instance, during the relaxation, the alkali-metal cations can either intercalate into the film or deintercalate from its structure. At the last step, the excessively adsorbed anions desorb from the surface, which can take place in parallel with their readsorption. In order to prove this hypothesis, one can relate the time constants obtained from the impedance analysis (Figure 2E–G) to those estimated from the LICT experiments. We compared the time constants obtained from the corresponding parameters of the equivalent circuit shown in Figure 2G, i.e., related to $Z_{dl}$ and $R_{ct}$, $C_{a,1}$ and $R_{a,1}$, and $C_{a,2}$ and $R_{a,2}$, with the LICT-estimated time constants, $\tau_1$, $\tau_2$ and $\tau_3$, respectively. They demonstrated a good self-agreement: the smallest $\tau_1$ values were indeed close to those obtained for the "pure" double layer related response using impedance analysis. Similarly, $\tau_2$ and $\tau_3$ were close to those that were estimated from the equivalent circuit parameters accounting for the ac-response of the interfacial charge and mass transfer (represented by $C_{a,1}/R_{a,1}$ and $C_{a,2}/R_{a,2}$, in the model shown in Figure 2G). In other words, the impedance and LICT experiments give, in general, self-consistent results. However, a distinct advantage of the laser technique is that it additionally gives information on the effective electrode surface charge (which determines the energy barriers for intercalation) and the

net anodic and cathodic constituencies of the multistage mechanisms in real time under potentiostatic conditions.

Taking into account LICT and impedance data, one can additionally support the mechanism of (de)intercalation of alkali-metal cations taking place in aqueous (and also in some cases in nonaqueous) media, and which can be schematically described in the case of $Na^+$- and $SO_4^{2-}$-containing electrolytes as follows:[33,34]

$$Na_2Ni[Fe(CN)_6] - e^- \leftrightarrow Na_2Ni[Fe(CN)_6]^+ \qquad (i)$$

$$2Na_2Ni[Fe(CN)_6]^+ + SO_4^{2-} \leftrightarrow (Na_2Ni[Fe(CN)_6])_2SO_4 \qquad (ii)$$

$$(Na_2Ni[Fe(CN)_6])_2SO_4$$
$$\leftrightarrow 2Na^+ + SO_4^{2-} + 2NaNi[Fe(CN)_6] \qquad (iii)$$

The first step in the above-described scheme is associated with the change of the oxidation state of Fe atoms in the film that can be induced by either the electrode potential or the temperature jump. This process creates a temporary uncompensated surface charge. The latter can be compensated by other electrolyte components, such as anions, as schematically designated by step ii. Finally, step iii represents a slower relaxation of the system, which does not involve the net interfacial charge transfer.[34]

151

Interestingly, by comparing parts A,B and C,D of Figure 6 (as well as Figure 5A,C) one can also notice that the relaxation curves at shorter times, $\tau_1$, are drastically different in case of the Na$^+$- and K$^+$-containing electrolytes. While this should be investigated further, we hypothesize that the obviously smaller time constants $\tau_1$ observable for the Na$^+$-containing electrolytes might be associated with the higher hydration energy of the sodium ions. The higher hydration energy might result in a better-ordered water structure leading to the faster reorganization of the double layer. Hydrated Na ions are bigger and heavier:[46] the only difference between the electrolytes is the nature of the alkali-metal cations. A deeper analysis of relaxation curves obtained for different battery systems might help in the investigation of the process kinetics,[47] answering questions about reasons for the irreversibility during charging and discharging.

Summarizing, LICT data, especially those that are combined with other state-of-the-art electrochemical techniques, can uniquely reveal the following facts related to the intercalation of alkali-metal cations (Na$^+$ and K$^+$ in this case) from aqueous electrolytes into the PBA battery systems. In other words, answering the question "what do laser-induced transient techniques reveal for batteries?" one can summarize the following using Na$_2$Ni[Fe(CN)$_6$] as the model material:

(1) The effective surface charge of the battery electrodes (under quasi-steady-state conditions) can be determined. In the particular case of Na$_2$Ni[Fe(CN)$_6$] in the potential region of intercalation of sodium and potassium, the surface charge is positive. This is quite counterintuitive, and this phenomenon should contribute to elucidation of the energy barriers for intercalation of alkali-metal cations.

(2) So-called potentials of maximum entropy can be detected by the LICT technique in the case of battery materials: this is demonstrated for the first time for one of the important battery systems, namely, Na$_2$Ni[Fe(CN)$_6$]. The LICT technique can be effectively used to distinguish the contribution of the nature of the electrolyte components to the change of PME, as demonstrated by replacing Na$^+$ with K$^+$ in the electrolyte.

(3) The laser-induced current transient technique is able to reveal multistage mechanisms of intercalation. It should be relatively easy to interpret the data by taking into account clear anodic and cathodic constituents after the probing. This is an obvious advantage compared to, for example, impedance spectroscopy, where due to the different probing signal, the cathodic/anodic constituents are not straightforwardly distinguishable.

(4) LICT should be a unique tool to explore the influence of the electrolyte components on the interfacial processes related to (de)intercalation. Further theoretical background is necessary, but, for example, the distinguishability of the interface response between Na$^+$ and K$^+$ holds promise to shed light on the intercalation with unprecedented details.

## CONCLUSIONS

In this paper, we report for the first time the application of the in situ laser-induced current transient (LICT) technique to analyze model battery systems, namely, Na$_2$Ni[Fe(CN)$_6$] thin films. We present rather unexpected results showing that the electrode surfaces are positively charged during intercalation/deintercalation of sodium and potassium cations. The observations, however, confirm the previously drawn hypothesis concerning a complex mechanism of the interfacial processes in Na ion battery systems. Moreover, the uncommon tripolar shape of the obtained transients implies that these interfacial processes have at least three different relaxation time constants. The behavior of the electrode/electrolyte interface, however, can be largely affected by the electrolyte composition. By changing the nature of the metal cations, one can modify the relaxation time constants or even alter the so-called potential of maximum entropy (PME). The presented results show that the LICT can be indeed a useful technique for deeper investigations of battery systems. The results obtained in this way could significantly contribute to a better understanding of the actual role of different electrolyte components and finally help to develop more accurate models describing the alkali-metal cation intercalation mechanisms.

## ASSOCIATED CONTENT

### Ⓢ Supporting Information

The Supporting Information is available free of charge on the ACS Publications website at DOI: 10.1021/acsami.7b03923.

Text describing the fitting of electrochemical impedance spectra, the influence of cations on the reversibility of charging/discharging, laser-induced current transient measurements, AFM measurements, and chemicals used (PDF)

## AUTHOR INFORMATION

### Corresponding Author

*E-mail: bandarenka@ph.tum.de. Tel: +49(0) 89289 12531.

### ORCID Ⓞ

Aliaksandr S. Bandarenka: 0000-0002-5970-4315

### Author Contributions

D.S. and J.Y. contributed equally to this work. The manuscript was written through contributions of all the authors.

### Notes

The authors declare no competing financial interest.

## REFERENCES

(1) Armaroli, N.; Balzani, V. *Energy for a Sustainable World: From the Oil Age to a Sun-Powered Future*; WILEY-VCH Verlag GmbH & Co. KGaA: Weinheim, 2011; Preface, pp 15−17.

(2) Yang, Z.; Zhang, J.; Kintner-Meyer, M. C. W.; Lu, X.; Choi, D.; Lemmon, J. P.; Liu, J. Electrochemical Energy Storage for Green Grid. *Chem. Rev.* **2011**, *111*, 3577−3613.

(3) Poizot, P.; Dolhem, F. Clean Energy New Deal for a Sustainable World: from non-CO$_2$ Generating Energy Sources to Greener Electrochemical Storage Devices. *Energy Environ. Sci.* **2011**, *4*, 2003−2019.

(4) Wolfram, C.; Shelef, O.; Gertler, P. How Will Energy Demand Develop in the Developing World? *J. Econ. Perspect.* **2012**, *26*, 119−138.

(5) Ginley, D.; Green, M. A.; Collins, R. Solar Energy Conversion Toward 1 Terawatt. *MRS Bull.* **2008**, *33*, 355−364.

(6) Zervos, A. *Renewables 2016: Global Status Report*; REN21: Paris, 2016.

(7) Ellis, B. L.; Nazar, L. F. Sodium and Sodium-Ion Energy Storage Batteries. *Curr. Opin. Solid State Mater. Sci.* **2012**, *16*, 168−177.

(8) Trieb, F.; Schillings, Ch.; O'Sullivan, M.; Pregger, T.; Hoyer-Klick, C. Global Potential of Concentrating Solar Power. *Proceedings of SolarPaces Conference*, Berlin, Germany, Sept 2009.

(9) Liu, J. Addressing the Grand Challenges in Energy Storage. *Adv. Funct. Mater.* **2013**, *23*, 924−928.

(10) Palomares, V.; Serras, P.; Villaluenga, I.; Hueso, K. B.; Carretero-Gonzalez, J.; Rojo, T. Na-ion batteries, Recent Advances and Present Challenges to Become Low Cost Energy Storage Systems. *Energy Environ. Sci.* **2012**, *5*, 5884−5901.

(11) Dunn, B.; Kamath, H.; Tarascon, J.-M. Electrical Energy Storage for the Grid: A Battery of Choices. *Science* **2011**, *334*, 928−935.

(12) Soloveichik, G. L. Battery Technologies for Large-Scale Stationary Energy Storage. *Annu. Rev. Chem. Biomol. Eng.* **2011**, *2*, 503−527.

(13) Komaba, S.; Murata, W.; Ishikawa, T.; Yabuuchi, N.; Ozeki, T.; Nakayama, T.; Ogata, A.; Gotoh, K.; Fujiwara, K. Electrochemical Na Insertion and Solid Electrolyte Interphase for Hard-Carbon Electrodes and Application to Na-Ion Batteries. *Adv. Funct. Mater.* **2011**, *21*, 3859−3867.

(14) Dell, R. M. Batteries: Fifty Years of Materials Development. *Solid State Ionics* **2000**, *134*, 139−158.

(15) Brennan, J. L.; Forster, R. J. Laser Light and Electrodes: Interaction Mechanisms and Electroanalytical Applications. *J. Phys. Chem. B* **2003**, *107*, 9344−9350.

(16) Climent, V.; Coles, B. A.; Compton, R. G. Laser-Induced Potential Transients on a Au(111) Single-Crystal Electrode. Determination of the Potential of Maximum Entropy of Double-Layer Formation. *J. Phys. Chem. B* **2002**, *106*, 5258−5265.

(17) Smalley, J. F.; Geng, L.; Feldberg, S. W.; Rogers, L. C.; Leddy, J. Evidence for Adsorption of $Fe(CN)_6^{3-/4-}$ on Gold Using the Indirect Laser-Induced Temperature-Jump Method. *J. Electroanal. Chem.* **1993**, *356*, 181−200.

(18) Benderskii, V. A.; Babenko, S. D.; Krivenko, A. G. Investigation of the Charge Relaxation in the Double Layer by a Thermal Jump. *J. Electroanal. Chem. Interfacial Electrochem.* **1978**, *86*, 223−225.

(19) Benderskii, V. A.; Velichko, G. I. Temperature Jump in Electric Double-Layer Study. Part I. Method of Measurements. *J. Electroanal. Chem. Interfacial Electrochem.* **1982**, *140*, 1−22.

(20) Benderskii, V. A.; Velichko, G. I.; Kreituss, I. V. Temperature Jump in Electric Double-Layer Study. Part II. Excess Entropy of EDL Formation at the Interface of Mercury and Electrolyte Solutions of Various Concentrations. *J. Electroanal. Chem. Interfacial Electrochem.* **1984**, *181*, 1−20.

(21) Climent, V.; Coles, B. A.; Compton, R. G. Coulostatic Potential Transients Induced by Laser Heating of a Pt(111) Single-Crystal Electrode in Aqueous Acid Solutions. Rate of Hydrogen Adsorption and Potential of Maximum Entropy. *J. Phys. Chem. B* **2002**, *106*, 5988−5996.

(22) García-Aráez, N.; Climent, V.; Feliu, J. M. Evidence of Water Reorientation on Model Electrocatalytic Surfaces from Nanosecond-Laser-Pulsed Experiments. *J. Am. Chem. Soc.* **2008**, *130*, 3824−3833.

(23) Garcia-Araez, N.; Climent, V.; Feliu, J. M. Potential-Dependent Water Orientation on Pt(111), Pt(100), and Pt(110), As Inferred from Laser-Pulsed Experiments. Electrostatic and Chemical Effects. *J. Phys. Chem. C* **2009**, *113*, 9290−9304.

(24) Toney, M. F.; Howard, J. N.; Richer, J.; Borges, G. L.; Gordon, J. G.; Melroy, O. R.; Wiesler, D. G.; Yee, D.; Sorensen, L. B. Voltage-Dependent Ordering of Water Molecules at an Electrode−Electrolyte Interface. *Nature* **1994**, *368*, 444−446.

(25) Osawa, M.; Tsushima, M.; Mogami, H.; Samjeske, G.; Yamakata, A. Structure of Water at the Electrified Platinum-Water Interface: A Study by Surface-Enhanced Infrared Absorption Spectroscopy. *J. Phys. Chem. C* **2008**, *112*, 4248−4256.

(26) Ataka, K.; Yotsuyanagi, T.; Osawa, M. Potential-Dependent Reorientation of Water Molecules at an Electrode/Electrolyte Interface Studied by Surface-Enhanced Infrared Absorption Spectroscopy. *J. Phys. Chem.* **1996**, *100*, 10664−10672.

(27) Ataka, K.; Osawa, M. In Situ Infrared Study of Water-Sulfate Coadsorption on Gold(111) in Sulfuric Acid Solutions. *Langmuir* **1998**, *14*, 951−959.

(28) Yamakata, A.; Osawa, M. Dynamics of Double-Layer Restructuring on a Platinum Electrode Covered by CO: Laser-Induced Potential Transient Measurement. *J. Phys. Chem. C* **2008**, *112*, 11427−11432.

(29) Climent, V.; Coles, B. A.; Compton, R. G. Laser Induced Current Transients Applied to a Au(111) Single Crystal Electrode. A General Method for the Measurement of Potentials of Zero Charge of Solid Electrodes. *J. Phys. Chem. B* **2001**, *105*, 10669−10673.

(30) Gomez, R.; Climent, V.; Feliu, J. M.; Weaver, M. J. Dependence of the Potential of Zero Charge of Stepped Platinum (111) Electrodes on the Oriented Step-Edge Density: Electrochemical Implications and Comparison with Work Function Behavior. *J. Phys. Chem. B* **2000**, *104*, 597−605.

(31) Frumkin, A. N.; Petrii, O. A.; Damaskin, B. B. In *Comprehensive Treatise of Electrochemistry. The Double Layer*; Bockris, J. O'M., Conway, B. E., Yeager, E., Eds.; Plenum Press: New York, 1980; Vol. *1*, Chapter 5, pp 221−289.

(32) Ledezma-Yanez, I.; Wallace, W. D. Z.; Sebastián-Pascual, P.; Climent, V.; Feliu, J. M.; Koper, M. T. M. Interfacial Water Reorganization as a pH-Dependent Descriptor of the Hydrogen Evolution Rate on Platinum Electrodes. *Nat. Energy* **2017**, *2*, 17031.

(33) Yun, J.; Pfisterer, J.; Bandarenka, A. S. How Simple are the Models of Na Intercalation in Aqueous Media? *Energy Environ. Sci.* **2016**, *9*, 955−961.

(34) Ventosa, E.; Paulitsch, B.; Marzak, P.; Yun, J.; Schiegg, F.; Quast, T.; Bandarenka, A. S. The Mechanism of the Interfacial Charge and Mass Transfer During Intercalation of Alkali Metal Cations. *Adv. Sci.* **2016**, *3*, 1600211.

(35) Ragoisha, G. A.; Bondarenko, A. S. Potentiodynamic Electrochemical Impedance Spectroscopy. *Electrochim. Acta* **2005**, *50*, 1553−1563.

(36) Ragoisha, G. A.; Bondarenko, A. S.; Osipovich, N. P.; Rabchynski, S. M.; Streltsov, E. A. Multiparametric Characterisation of Metal-Chalcogen Atomic Multilayer Assembly by Potentiodynamic Electrochemical Impedance Spectroscopy. *Electrochim. Acta* **2008**, *53*, 3879−3888.

(37) Paulitsch, B.; Yun, J.; Bandarenka, A. S. Electrodeposited $Na_2VO_x[Fe(CN)_6]$ Films as a Cathode Material for Aqueous Na-Ion Batteries. *ACS Appl. Mater. Interfaces* **2017**, *9*, 8107−8112.

(38) Bondarenko, A. S.; Ragoisha, G. A. In *Progress in Chemometrics Research*; Pomerantsev, A. L., Eds.; Nova Science Publishers. Inc.: New York, 2005; pp 89−102.

(39) Bondarenko, A. S. Analysis of Large Experimental Datasets in Electrochemical Impedance Spectroscopy. *Anal. Chim. Acta* **2012**, *743*, 41−50.

(40) Berkes, B. B.; Inzelt, G.; Schuhmann, W.; Bondarenko, A. S. Influence of $Cs^+$ and $Na^+$ on Specific Adsorption of *OH, *O, and *H at Platinum in Acidic Sulfuric Media. *J. Phys. Chem. C* **2012**, *116*, 10995−11003.

(41) Sebastián, P.; Martínez-Hincapié, R.; Climent, V.; Feliu, J. M. Study of the Pt (111) | Electrolyte Interface in the Region Close to Neutral pH Solutions by the Laser Induced Temperature Jump Technique. *Electrochim. Acta* **2017**, *228*, 667−676.

(42) Climent, V.; Garcia-Araez, N.; Compton, R. G.; Feliu, J. M. Effect of Deposited Bismuth on the Potential of Maximum Entropy of Pt(111) Single-Crystal Electrodes. *J. Phys. Chem. B* **2006**, *110*, 21092−21100.

(43) Silva, F.; Sottomayor, M. J.; Martins, A. Temperature Coefficient of the Potential of Zero Charge and Entropies of Formation for the Interface of Stepped Faces of Gold in Contact with Aqueous Perchloric Acid Solutions. *J. Chem. Soc., Faraday Trans.* **1996**, *92*, 3693−3699.

(44) Silva, F.; Sottomayor, M. J.; Hamelin, A. J. The Temperature Coefficient of the Potential of Zero Charge of the Gold Single-Crystal Electrode/Aqueous Solution Interface: Possible Relevance to Gold-

Water Interactions. *J. Electroanal. Chem. Interfacial Electrochem.* **1990**, *294*, 239−251.

(45) Huang, J.; Malek, A.; Zhang, J.; Eikerling, M. H. Non-Monotonic Surface Charging Behavior of Platinum: A Paradigm Change. *J. Phys. Chem. C* **2016**, *120*, 13587−13595.

(46) Dean, J. A. *Lange's Handbook of Chemistry*; McGraw-Hill Book Co.: New York, 1985; Vol. *13*, pp 5−5.

(47) Smalley, J. F. Kinetics of Interfacial Ion-Transfer Reactions Studied Using the Indirect Laser-Induced Temperature Jump Technique: Theory. *J. Electroanal. Chem.* **2010**, *640*, 68−74.

# Multiple Potentials of Maximum Entropy for a Na$_2$Co[Fe(CN)$_6$] Battery Electrode Material: Does the Electrolyte Composition Control the Interface?

Daniel Scieszka,[†,‡] Christian Sohr,[†] Paul Scheibenbogen,[†] Philipp Marzak,[†,‡] Jeongsik Yun,[†,‡] Yunchang Liang,[†] Johannes Fichtner,[†] and Aliaksandr S. Bandarenka*[,†,‡]

[†]Physics of Energy Conversion and Storage (ECS), Physik-Department, Technical University of Munich, James-Franck-Str. 1, 85748 Garching, Germany

[‡]Nanosystems Initiative Munich (NIM), Schellingstraße 4, 80799 Munich, Germany

Ⓢ *Supporting Information*

**ABSTRACT:** Development of efficient schemes of energy storage is crucial for finding a solution for the "generation versus consumption" problem. Aqueous Na-ion batteries have been already recognized as one of the promising candidates for large-scale energy-storage systems. Despite noticeable progress in this field, the actual intercalation mechanisms governing these battery cells are yet to be fully comprehended. In this manuscript, we examine the electrode/electrolyte interface formed between electrodeposited Na$_2$Co[Fe(CN)$_6$] films and aqueous solutions. The investigated systems exhibit up to three potentials of maximum entropy (PMEs). To the best of our knowledge, the existence of multiple PMEs in electrochemical systems has never been reported in the literature. These unexpected results are, however, in line with the theory explaining the correlation between the water structure at the interface and the ease of the interfacial mass and charge transfer. Additionally, the obtained PMEs appear to largely depend on the anions' properties, most probably on the hydration energy of these species. This reveals the impact of the electrolyte composition on the interfacial processes in Na-ion batteries.

**KEYWORDS:** laser-induced current transients, aqueous Na ion batteries, interfacial charge and mass transfer, water plane structure, Na$_2$Co[Fe(CN)$_6$], battery materials
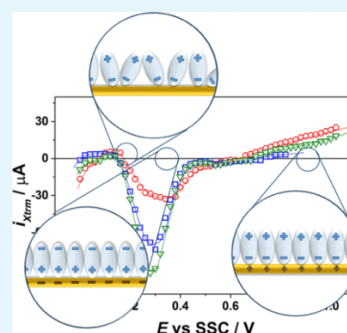
## ■ INTRODUCTION

Energy is a paramount factor in the global economy, society, and politics.[1,2] It is of utmost importance in the sustainable development of many countries.[3] Although different types of conventional and nonconventional energy sources are used, solar and wind power schemes have already become one of the most prominent elements of sustainable energy provision with lower greenhouse gas emission. However, the stochastic nature of solar and wind resources can cause issues regarding the intermittency of energy generation.[4,5] Implementation of effective energy-storage systems, such as battery systems, can help to overcome these problems.[6,7] Particularly interesting are aqueous Na-ion batteries, which, thanks to their comparatively good performance, safe electrolytes, and low material costs, seem to be a very promising choice for grid-scale energy-storage systems.[8−11] There has been a drastically increasing number of research projects on various materials applicable as electrodes in aqueous Na-ion batteries. Oxides, polyanionic compounds, sodium super ionic conductors, and Prussian blue analogues (PBAs) can be mentioned as examples.[12−23] Because of their relatively simple and inexpensive manufacture, high durability, and adequately good energy density, PBAs are especially outstanding.[24−30]

Although most of the studies considering batteries are focused on improving the energy and power densities, material durability, and diffusion barriers of an electrode material structure, the kinetic properties that determine the performance of the batteries are still poorly understood.[31−37] Hence, a better understanding of these properties is needed for further optimization of battery systems. A deeper analysis of interfacial processes can be especially informative. Recent studies have shown that the intercalation/deintercalation mechanism of different cations in various systems is more complex than it had been believed before.[38−41] Intercalation is a quasi-reversible insertion of guest molecules or ions into host solids.[42,43] This implies that the energy barriers of the electric double layer (EDL) to intercalation should have a noticeable impact on the whole process influencing its course. Thus, the rate of charge and mass transfer through the electrode/electrolyte interface of battery systems will be largely governed by the ability of the interfacial water structure to reorganize.[44]

21688

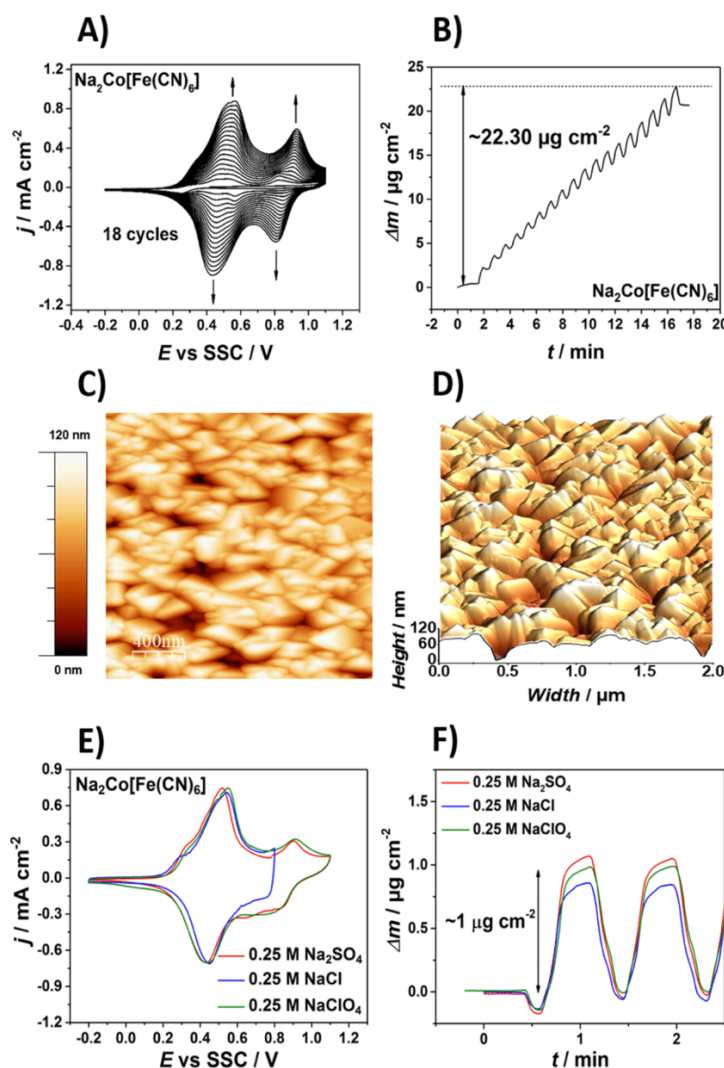**Figure 1.** (A) Representative CV of the $Na_2Co[Fe(CN)_6]$ film obtained during film deposition ($dE/dt$ = 50 mV s$^{-1}$) together with (B) the corresponding EQCM diagram depicting the mass change of the electrode. (C) Typical 2D and (D) 3D AFM images of the $Na_2Co[Fe(CN)_6]$ film deposited. (E) Representative CVs of the CoHCF films in 0.25 M $Na_2SO_4$, 0.25 M NaCl, and 0.25 M $NaClO_4$ together with (F) the corresponding change of the electrode mass during Na$^+$ cation intercalation/deintercalation in these solutions (background corrected curve). A narrower potential range in the presence of 0.25 M NaCl electrolyte was chosen to prevent $Cl_2$ formation (confer Experimental Section).

The knowledge of parameters such as the potential of zero charge (PZC) or the potential of maximum entropy (PME) can be very helpful for the assessment of water layer structurization.[44−46] In the vicinity of the PME, the water molecules can reorient more easily, whereas at potentials more remote from this point, the solvent structure is more rigid. This can be the main reason for the energy barriers influencing a charge and mass transfer.[47]

As it was recently reported, the surface charge and, consequently, the PME in model aqueous Na-ion battery systems can be revealed using the laser-induced current transient (LICT) method.[44] This in situ technique utilizes short laser pulses to rapidly increase the temperature of the electrode surface. The interfacial electric field resulting from the charge separated between the electrode and the electrolyte determines the structure of the solvent adlayer.[48−52] The

temperature jump results in the randomization of the water adlayer structure present at the surface.[52−58] The answer of the system is recorded as current transients. Their orientation coincides with the sign of the excess charge at the electrode surface.[45] The potential at which no response is observed corresponds to the PME.[45,56,57,59]

In this study, we examined the processes taking place at the interface of model battery systems during Na$^+$ intercalation/deintercalation into and from $Na_2Co[Fe(CN)_6]$ (CoHCF) films in aqueous media. By analogy with our previous studies on a comparable system,[44] we used the LICT technique together with other commonly known electrochemical methods [i.e., cyclic voltammetry, electrochemical quartz crystal microbalance (EQCM), and electrochemical impedance spectroscopy (EIS)]. The LICT measurements revealed that the examined systems exhibit up to three PMEs located within electrode

156

potential ranges where sodium cation (de)intercalation takes place. These results are unexpected considering the common assumption that the PME is located in close vicinity of the PZC.[53] On the contrary, the potentials of zero response correspond to the onset potentials of $Na^+$ cation intercalation/deintercalation. This observation further supports the aforementioned assumption regarding the interfacial energy barriers and their significant role in the process of (de)intercalation. Thus, the obtained results can provide information about the interfacial processes as well as unveil their limitations.

## ■ EXPERIMENTAL SECTION

All measurements were performed using a three-electrode configuration in a custom-built electrochemical glass cell. The cell was equipped with a flat, laser-transmittable glass window allowing laser illumination at the working electrode. An AT-cut gold quartz crystal wafer ($A_{electrode}$ = 1.37 cm$^2$, Stanford Research Systems) and a platinum wire were used as the working electrode and the counter electrode, respectively. All potentials in the manuscript are referred to the silver/silver chloride scale. The experimental protocol has been described elsewhere.[44] The cleaned bare gold quartz crystal electrodes were cycled in the deposition solution within the potential range from −0.2 to 1.1 V at a scan rate of 50 mV s$^{-1}$ using a VSP-300 potentiostat (Bio-Logic). $Na_2Co[Fe(CN)_6]$ films were prepared via electrochemical deposition from aqueous deposition solutions containing 0.5 mM $K_3Fe(CN)_6$, 0.5 mM $CoCl_2$, and 0.25 M $Na_2SO_4$ electrolyte. The detailed list of chemicals used in this work is provided in the Supporting Information. The mass change of the working electrode was recorded at the same time with a QCM 200 (Stanford Research Systems) EQCM.

After deposition, the influence of different anions on the electrochemical processes at $Na_2Co[Fe(CN)_6]$ films was studied using aqueous electrolytes ($Na_2SO_4$, NaCl, and $NaClO_4$) with the concentration of 0.25 M. Because of difficulties in controlling the effective cation concentration near the electrode surface,[60] a focus was put on using the same concentration of anions in all experiments. Subsequently, three intercalation/deintercalation cycles were performed within the potential regime of −0.2 to 1.1 V (scan rate 50 mV s$^{-1}$) for the solutions of sodium sulfate and sodium perchlorate, and, to avoid chlorine evolution, in the narrower regime of −0.2 to 0.8 V for the solution of sodium chloride. While cycling the films in the electrolytes, the mass changes due to (de)intercalation were measured using a EQCM. The films were further used for LICT measurements.

EIS of the deposited $Na_2Co[Fe(CN)_6]$ films were carried out using 10 mV amplitude of ac probing frequency range between 250 kHz and 300 mHz in the potential range between 0.0 and 1.0 V. Fits of the impedance data were performed using the homemade software "EIS Data Analysis 1.2".[44,61] The validation of the analysis of the impedance data followed the procedures and concepts introduced elsewhere.[62−64] For instance, the Kramers−Kronig test indicated no issues with the quality of data fitting.

The morphology of the prepared film was imaged by atomic force microscopy (AFM) using a MultiMode EC-STM/EC-AFM microscope with a NanoScope IIID controller (Veeco Instruments Inc.). Nanoscope 5.31r1 was the software used to operate the device. Each AFM image was obtained by the tapping mode of AFM (AFM tips, Bruker RTESP-300) at a scan rate of 0.5 Hz and further analyzed using WSxM 5.0 Develop 8.0 software.[65]

The detailed experimental procedure of the laser measurements has been described elsewhere.[44] LICT experiments were performed using the 5−8 ns laser pulse of a Quanta-Ray INDI pulsed Nd:YAG laser with a repetition rate of 10 Hz and a wavelength of 532 nm. The laser energy was controlled with an attenuator (Newport Corp.). The energy of pulses was kept under the damage threshold of the electrode at 10 mJ, which corresponds to ~16 mJ cm$^{-2}$. The transients were obtained by recording the change in the current over time right after heating up the surface with the laser. To ensure reproducible conditions, the whole process was automated. For evaluation, only

the last transients of each potential were plotted as representative results. The investigated potential range for 0.25 M $Na_2SO_4$ and 0.25 M $NaClO_4$ was between 0 and 1 V, whereas the potential range for 0.25 M NaCl was narrowed to 0−0.8 V. In all LICT measurements, the potential steps used were equal to 20 mV. After the LICT measurements, the morphologies of the $Na_2Co[Fe(CN)_6]$ films were additionally examined with high-resolution field emission scanning electron microscopy. The resulting images are given in the Supporting Information.

## ■ RESULTS AND DISCUSSION

$Na_2Co[Fe(CN)_6]$ films were electrodeposited according to the following reaction scheme

$$2Na_{(aq)}^+ + Co_{(aq)}^{2+} + [Fe(CN)_6]_{(aq)}^{3-} + 1e^-$$
$$\rightarrow Na_2Co[Fe(CN)_6]_{(s)} \tag{1}$$
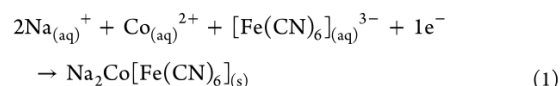
A typical cyclic voltammogram (CV) obtained while depositing CoHCF films is displayed in Figure 1A. One can distinguish two pairs of oxidation/reduction peaks: bigger ones at potentials of ca. 0.55/0.45 V and smaller ones at ca. 0.9/0.8 V. According to Wu et al., the peaks at the lower and higher potentials can be partly associated with the alteration in the oxidation state of the nitrogen-coordinated cobalt and carbon-coordinated iron, respectively.[66,67] The current peaks increase together with the number of cycles depicting the film growth. Figure 1B presents the corresponding change of the electrode mass. The total change of mass resulting from deposition was determined as ~22.30 $\mu$g cm$^{-2}$. Figure 1C,D shows the two-dimensional (2D) and three-dimensional (3D) AFM images of the deposited CoHCF, respectively. The film exhibits a relatively smooth surface, and the substrate is fully covered. Figure 1E depicts the typical CVs for CoHCF films in aqueous 0.25 M $Na_2SO_4$, 0.25 M NaCl, and 0.25 M $NaClO_4$ solutions, respectively. The anodic peak represents deintercalation of $Na^+$, whereas the cathodic one is associated with intercalation of the cations. These two processes can also be related to the change of the oxidation state of cobalt and iron present in the structure of the electrode material. The exact location and shape of the "bigger" peaks are apparently similar for all three electrolytes. Also, the position and appearance of the second pair of peaks in the cases of 0.25 M $Na_2SO_4$ and 0.25 M $NaClO_4$ are very much alike (see Figure 1E). Figure 1F depicts the change of the electrode mass during intercalation/deintercalation. The recorded mass change during intercalation was ~1 $\mu$g cm$^{-2}$ ($Na^+$) for sodium sulfate and sodium perchlorate. The decreased mass (by ~20%) in the case of sodium chloride results from the narrower potential regime of (de)intercalation.

The interfacial processes at the CoHCF films were further investigated with EIS. Figure 2A−C shows the typical "loop-shaped" EIS spectra obtained for the examined films together with corresponding fits. The fits of the measured impedance spectra were performed utilizing two equivalent electric circuits (EECs) presented in Figure 2D,E. The former was used in the case of 0.25 M $Na_2SO_4$ and 0.25 M NaCl, whereas the latter was used in the case of 0.25 M $NaClO_4$. Both the EECs illustrate a mechanism of (de)intercalation of the Na ions consisting of at least three stages. The mechanism involves temporary adsorption/desorption of negatively charged species present in the solution at the electrode surface, followed by desorption/adsorption.[38] An additional parallel set of capacitance and resistance might appear due to, for instance, formation of an additional interface;[68] however, its actual
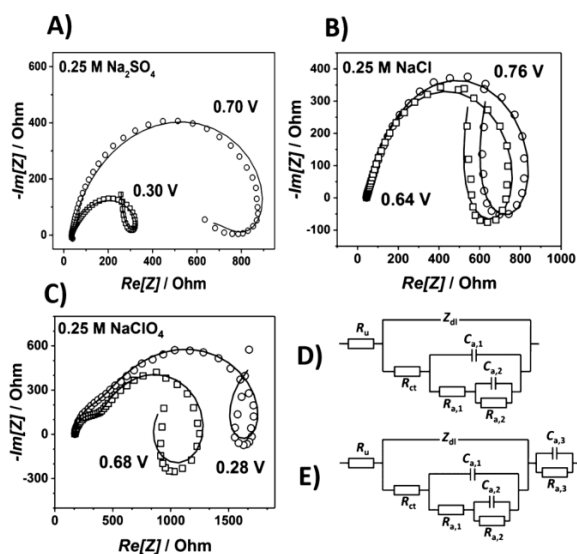
157

**Figure 2.** Impedance data (depicted as open squares and circles) of the CoHCF films collected in (A) 0.25 M $Na_2SO_4$, (B) 0.25 M NaCl, and (C) 0.25 M $NaClO_4$ and their fits (depicted as solid curves). The presented fits were performed using EECs shown in (D,E), which are impedance models describing a mechanism with at least three stages interconnected quasi-reversibly. $R_u$—uncompensated resistance; $Z_{dl}$—impedance of the double layer; $R_{ct}$—resistance of the charge transfer; the remaining $R$ parameters can be identified as pseudoresistances, whereas the $C$ parameters stand for pseudocapacitances of the adsorption process. The added parallel set of $R_{a,3}$ and $C_{a,3}$ in (E) describes the additional semicircles observed in the high-frequency region in (C), see text.



**Figure 3.** LICT plots obtained for the CoHCF films immersed in aqueous (A) 0.25 M $Na_2SO_4$, (B) 0.25 M NaCl, and (C) 0.25 M $NaClO_4$ solutions for different potentials applied. Roman numerals additionally show the order of the potential steps. (D) Corresponding 2D graph representing the maximal current values of the transients obtained for the three different electrolytes as a function of the potential applied, together with hydration enthalpies of the anions. Numerical values of hydration enthalpies are retrieved from the work of Smith[74] The black arrow indicates the scan direction. In each case, three PMEs were found.

origins are not further analyzed, as it is out of the scope of this manuscript. Still, one can assume that the process of cation (de)intercalation follows at least the three-stage mechanism, as proposed by Yun et al.[38]

Figure 3A–C shows examples of LICTs obtained for the examined films in 0.25 M $Na_2SO_4$, 0.25 M NaCl, and 0.25 M $NaClO_4$, respectively, in potential regimes of sodium (de)-intercalation. Shortly after the illumination, the current transients can be observed. The recorded answers of the system to the rapid temperature jumps come mainly from the EDL.[57,58] Therefore, the sign of the maximal current values of the recorded transients will be consistent with the sign of the excess charge of the electrode surface.[45] Interestingly, in the studied battery systems containing different anions, the sign of the current peaks is swapped more than once along the applied potential range. The dependence is well-visible in Figure 3D depicting the collected extreme values of the recorded current.

This implies multiple changes of the excess surface charge of the electrode. At low potential values (∼0 V), the current transients are oriented negatively. Then, within a narrow range, they become positive (∼0.05 V), changing again the orientation to negative (∼0.15 V). Finally, at ∼0.7 V, the current transients turn positive. One can see that all three systems (containing $SO_4^{2-}$, $Cl^-$, or $ClO_4^-$ anions) exhibit three potentials at which the current transients change their orientation. This alteration, in the simplest case, comes from the flipping of the water molecules adsorbed at the electrode and oriented toward its surface according to the net charge. The "flipping potentials," known as the PMEs, represent the potentials at which the
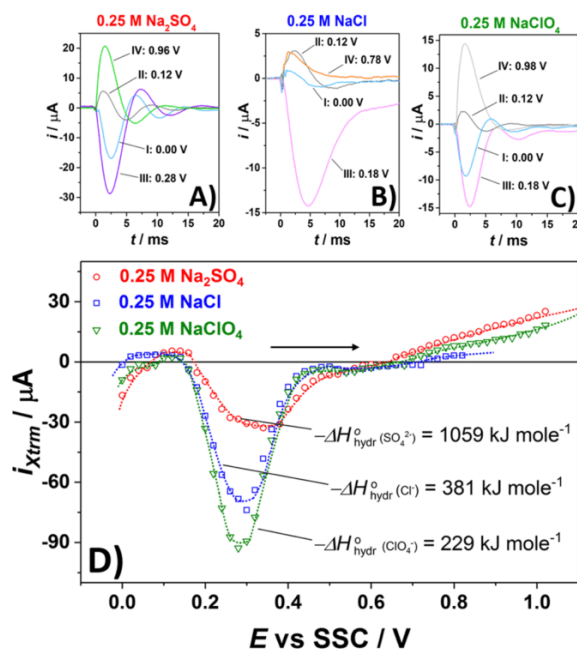
solvent dipoles change their arrangement. It was proven that, for simple electrochemical systems, the PME is closely associated with the PZC, another basic characteristic of the EDL.[69,70] Considering the fact that a system can likely exhibit only one PZC,[71] the existence of three PMEs is surprising. However, comparing the 2D LICT graph (Figure 3D) with the corresponding CVs (Figure 1E), one can notice that the PMEs are located close to the onset potentials of the $Na^+$ cation intercalation into and deintercalation from the film structure. At potentials vicinal to the PMEs, "rigidity" of the double layer reaches its minimum. Consequently, the transport of intercalating ions from the electrolyte to the surface of the electrode through the EDL (and vice versa) can proceed much more easily. This is highly important for the (de)intercalation process.[47] Obviously, the presented model battery systems and the mass- and charge-transfer processes taking place in their interface are more complex than the typical systems consisting of a metal electrode immersed in an aqueous electrolyte, often presented and discussed in the literature. Thus, up to a certain extent, the behavior of the examined battery systems may deviate from the classical surface science perspective.

The exact location of the observed PMEs differs according to the electrolyte composition. In the 0.25 M $Na_2SO_4$ electrolyte, the LICT response is zero at ca. 0.07 V ($PME_1$), 0.17 V ($PME_2$), and 0.66 V ($PME_3$); in 0.25 M NaCl, the values shift to ca. 0.02 V ($PME_1$), 0.14 V ($PME_2$), and 0.72 V ($PME_3$), whereas in 0.25 M $NaClO_4$, the potentials of reorientation are located at ca. 0.09 V ($PME_1$), 0.14 V ($PME_2$), and 0.67 V

158

(PME$_3$) (Figure 3D). Notably, the collected LICTs should be viewed as a superposition of responses coming from different, often opposite, processes.[44] The applied potentials at each step are kept constant. This leads to the establishment of equilibrium between, for instance, intercalation and deintercalation of the metal cations or adsorption and desorption of anions. Furthermore, the rapid laser-induced temperature jump might cause a partial migration of the cations into and from the structure of the electrode material. Therefore, the PME$_1$'s were found at the beginning of the scan range at the potentials at which no (de)intercalation processes occur. In this particular potential regime, the alteration of the current transients' orientation might be mainly associated with the change in the specific adsorption of anions.[45,72,73] The tripolar transients collected at these potentials depicting multiple processes with different time constants can support this statement (Figure 4).[44] Unlike the studied systems, multiple PMEs were not
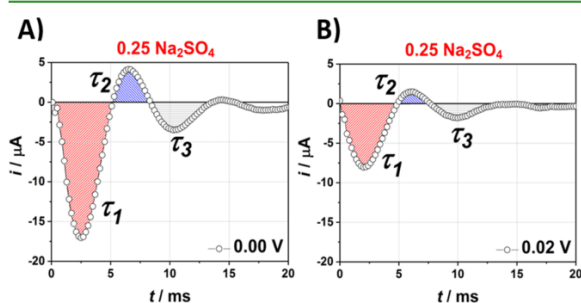


**Figure 4.** Sample LICTs recorded for the Na$_2$Co[Fe(CN)$_6$] films in 0.25 M Na$_2$SO$_4$ solution at low potentials of (A) 0.00 and (B) 0.02 V. Each of the three peaks can be associated with different interfacial processes (including adsorption/desorption of anions). Three "time constants" (depicted as $\tau_1$, $\tau_2$, and $\tau_3$) can be linked with three different processes, including specific adsorption and desorption of anions. For more details, see ref 44.

detected in the systems containing Na$_2$Ni[Fe(CN)$_6$] (NiHCF) films as the electrode.[44] The existence of multiple PMEs appears to be a feature of CoHCF. The aforementioned transition of the oxidation state of the Co atoms present in the structure of Na$_2$Co[Fe(CN)$_6$] (~0.5 V) might be a reason for the observed behavior. Hence, while the number of PMEs can be a matter of the electrode material, their exact location seems to be affected by the electrolyte composition. In the investigated systems, only the nature of the anions changes; the alkali-metal cations are kept the same in all three cases. The variations in the systems' behavior might originate from different adsorption strengths of species present in the electrolyte. The effect of the adsorption strength would be, however, reflected in the shape of CVs. As mentioned above, the change in the CV appearance is not prominent. Thus, the observed results most likely arise from the hydration energy of anions present in the electrolyte (Figure 3D).

While approaching the onset potentials of intercalation/deintercalation, the amount of sodium ions near the electrode surface increases. The hydration energy of the Na$^+$ (409 kJ mol$^{-1}$) cations is higher than the hydration energy of the Cl$^-$ (381 kJ mol$^{-1}$) and ClO$_4^-$ (229 kJ mol$^{-1}$) anions and much lower than the hydration energy of the SO$_4^{2-}$ (1059 kJ mol$^{-1}$) anions.[74] This influences the ions' mobility.[75] During the relaxation after the temperature jump, the "slower" sodium cations will approach the surface after the Cl$^-$ or ClO$_4^-$ anions.

This can affect the system response resulting in a change in the shape of the current transients. A corresponding scenario can be drawn up for the SO$_4^{2-}$-containing electrolyte. The (bi)sulfates should move more slowly than the sodium ions. This, similar to the other two cases, could result in an alteration in the shape of the current transients and shift the potentials of zero response. Whereas the potentials of the lowest energy barriers to intercalation can coincide with the PMEs, the potentials at which the current transient responses reach their maximum are also worth of attention. From the electrocapillary equation[76,77]

$$\left( \frac{\partial E}{\partial T} \right)_q = -\left( \frac{\partial \Delta S}{\partial q} \right)_T \tag{2}$$

it is possible to show that (in the relevant experiments) when the potential drop is minimal, the formation entropy of the EDL is maximal. This is one of the main dependences used in the LICT experiments. On this basis, the potentials of no current response are associated with the PMEs.

Conversely, the maximum value of the current transients can be correlated with the state at which the entropy is at its minimum. In other words, the potentials at which the current transients reach their maximum values likely indicate the highly ordered solvent plane. Interestingly, in all three systems, the location of the "potentials of minimum entropy" also seems to be affected by the hydration energy of the anions present in the electrolyte. The current values are the highest at 0.28, 0.3, and 0.36 V for 0.25 M NaClO$_4$, 0.25 M NaCl, and 0.25 M Na$_2$SO$_4$, respectively. One can see that an increase in the hydration energy results in a decrease in the order of the water structure, a crucial factor for LICT measurements (Figure 3D).

## CONCLUSIONS

In summary, we present the application of the in situ LICT method to investigate the CoHCF-based battery systems. Unlike the other known electrochemical systems, the studied Na-ion battery model systems exhibit up to three PMEs. This surprising result, however, is qualitatively in line with the theory regarding the effect of the interfacial water structuring influencing the mass and charge transfer. In the examined battery systems, the detected potentials of the lowest energy barriers correlate with the onset potentials of the sodium cation (de)intercalation. Whereas the observed change might be partially influenced by the alteration in the oxidation states of cobalt present in the material, the exact location of the PMEs appears to depend on the composition of the electrolytes used. The nature of the anions seems to have a particular impact on the behavior of the interface. It can, for instance, affect the PMEs. In addition, the presented results further demonstrate the usefulness of the LICT analysis in the fundamental studies of aqueous battery systems.

## ASSOCIATED CONTENT

### Supporting Information

The Supporting Information is available free of charge on the ACS Publications website at DOI: 10.1021/acsami.8b03846.

> Quantitative comparison of the influence of the anions on the reversibility of charging/discharging, presentation of complete and detailed LICT results, AFM and SEM measurements, and list of chemicals used (PDF)

# ■ AUTHOR INFORMATION

**Corresponding Author**

*E-mail: bandarenka@ph.tum.de. Phone: +49(0) 89289 12531.

**ORCID** ●

Philipp Marzak: 0000-0003-3372-0816

Aliaksandr S. Bandarenka: 0000-0002-5970-4315

**Author Contributions**

The contribution of D.S. and C.S. to this study was equal. All authors contributed to writing of the manuscript.

# ■ REFERENCES

(1) Nematollahi, O.; Hoghooghi, H.; Rasti, M.; Sedaghat, A. Energy Demands and Renewable Energy Resources in the Middle East. *Renewable Sustainable Energy Rev.* **2016**, *54*, 1172−1181.

(2) Sovacool, B. K. Diversity: Energy Studies Need Social Science. *Nature* **2014**, *511*, 529−530.

(3) Midilli, A.; Dincer, I.; Ay, M. Green Energy Strategies for Sustainable Development. *Energy Policy* **2006**, *34*, 3623−3633.

(4) Khare, V.; Nema, S.; Baredar, P. Solar-wind hybrid renewable energy system: A review. *Renewable Sustainable Energy Rev.* **2016**, *58*, 23−33.

(5) Hoffert, M. I.; Caldeira, K.; Benford, G.; Criswell, D. R.; Green, C.; Herzog, H.; Jain, A. K.; Kheshgi, H. S.; Lackner, K. S.; Lewis, J. S.; Lightfoot, H. D.; Manheimer, W.; Mankins, J. C.; Mauel, M. E.; Perkins, L. J.; Schlesinger, M. E.; Volk, T.; Wigley, T. M. L. Advanced Technology Paths to Global Climate Stability: Energy for a Greenhouse Planet. *Science* **2002**, *298*, 981−987.

(6) Ellis, B. L.; Nazar, L. F. Sodium and Sodium-Ion Energy Storage Batteries. *Curr. Opin. Solid State Mater. Sci.* **2012**, *16*, 168−177.

(7) Ginley, D.; Green, M. A.; Collins, R. Solar Energy Conversion Toward 1 Terawatt. *MRS Bull.* **2008**, *33*, 355−364.

(8) Komaba, S.; Murata, W.; Ishikawa, T.; Yabuuchi, N.; Ozeki, T.; Nakayama, T.; Ogata, A.; Gotoh, K.; Fujiwara, K. Electrochemical Na Insertion and Solid Electrolyte Interphase for Hard-Carbon Electrodes and Application to Na-Ion Batteries. *Adv. Funct. Mater.* **2011**, *21*, 3859−3867.

(9) Palomares, V.; Serras, P.; Villaluenga, I.; Hueso, K. B.; Carretero-González, J.; Rojo, T. Na-Ion Batteries, Recent Advances and Present Challenges to Become Low Cost Energy Storage Systems. *Energy Environ. Sci.* **2012**, *5*, 5884−5901.

(10) Kim, S.-W.; Seo, D.-H.; Ma, X.; Ceder, G.; Kang, K. Electrode Materials for Rechargeable Sodium-Ion Batteries: Potential Alternatives to Current Lithium-Ion Batteries. *Adv. Energy Mater.* **2012**, *2*, 710−721.

(11) Wenzel, S.; Hara, T.; Janek, J.; Adelhelm, P. Room-Temperature Sodium-Ion Batteries: Improving the Rate Capability of Carbon Anode Materials by Templating Strategies. *Energy Environ. Sci.* **2011**, *4*, 3342−3345.

(12) Luo, C.; Langrock, A.; Fan, X.; Liang, Y.; Wang, C. P2-type Transition Metal Oxides for High Performance Na-Ion Battery Cathodes. *J. Mater. Chem. A* **2017**, *5*, 18214−18220.

(13) Ortiz-Vitoriano, N.; Drewett, N. E.; Gonzalo, E.; Rojo, T. High Performance Manganese-Based Layered Oxide Cathodes: Overcoming the Challenges of Sodium Ion Batteries. *Energy Environ. Sci.* **2017**, *10*, 1051−1074.

(14) Kim, H.; Hong, J.; Park, K.-Y.; Kim, H.; Kim, S.-W.; Kang, K. Aqueous Rechargeable Li and Na Ion Batteries. *Chem. Rev.* **2014**, *114*, 11788−11827.

(15) Chen, S.; Wu, C.; Shen, L.; Zhu, C.; Huang, Y.; Xi, K.; Maier, J.; Yu, Y. Challenges and Perspectives for NASICON-Type Electrode Materials for Advanced Sodium-Ion Batteries. *Adv. Mater.* **2017**, *29*, 1700431.

(16) Radha, A. V.; Subban, C. V.; Sun, M. L.; Tarascon, J. M.; Navrotsky, A. Possible correlation between enthalpies of formation and redox potentials in LiMSO4OH (M = Co, Fe, Mn), Li-ion polyanionic battery cathode materials. *J. Mater. Chem. A* **2014**, *2*, 6887−6894.

(17) Asl, H. Y.; Ghosh, K.; Meza, M. P. V.; Choudhury, A. Li3Fe2(HPO3)3Cl: an electroactive iron phosphite as a new polyanionic cathode material for Li-ion battery. *J. Mater. Chem. A* **2015**, *3*, 7488−7497.

(18) Erinmwingbovo, C.; Palagonia, M. S.; Brogioli, D.; La Mantia, F. Intercalation into a Prussian Blue Derivative from Solutions Containing Two Species of cations. *ChemPhysChem* **2017**, *18*, 917−925.

(19) Yun, J.; Schiegg, F. A.; Liang, Y.; Scieszka, D.; Garlyyev, B.; Kwiatkowski, A.; Wagner, T.; Bandarenka, A. S. Electrochemically Formed NaxMn[Mn(CN)6] Thin Film Anodes Demonstrate Sodium Intercalation and Deintercalation at Extremely Negative Electrode Potentials in Aqueous Media. *ACS Appl. Energy Mater.* **2018**, *1*, 123−128.

(20) You, Y.; Yao, H.-R.; Xin, S.; Yin, Y.-X.; Zuo, T.-T.; Yang, C.-P.; Guo, Y.-G.; Cui, Y.; Wan, L.-J.; Goodenough, J. B. Subzero-Temperature Cathode for a Sodium-Ion Battery. *Adv. Mater.* **2016**, *28*, 7243−7248.

(21) You, Y.; Yu, X.; Yin, Y.; Nam, K.-W.; Guo, Y.-G. Sodium Iron Hexacyanoferrate with High Na Content as a Na-Rich Cathode Material for Na-Ion Batteries. *Nano Res.* **2015**, *8*, 117−128.

(22) You, Y.; Wu, X.-L.; Yin, Y.-X.; Guo, Y.-G. A Zero-Strain Insertion Cathode Material of Nickel Ferricyanide for Sodium-Ion Batteries. *J. Mater. Chem. A* **2013**, *1*, 14061−14065.

(23) You, Y.; Wu, X.-L.; Yin, Y.-X.; Guo, Y.-G. High-quality Prussian Blue Crystals as Superior Cathode Materials for Room-Temperature Sodium-Ion Batteries. *Energy Environ. Sci.* **2014**, *7*, 1643−1647.

(24) Pasta, M.; Wessells, C. D.; Liu, N.; Nelson, J.; McDowell, M. T.; Huggins, R. A.; Toney, M. F.; Cui, Y. Full Open-Framework Batteries for Stationary Energy Storage. *Nat. Commun.* **2014**, *5*, 3007.

(25) Wang, L.; Lu, Y.; Liu, J.; Xu, M.; Cheng, J.; Zhang, D.; Goodenough, J. B. A Superior Low-Cost Cathode for a Na-Ion Battery. *Angew. Chem., Int. Ed.* **2013**, *52*, 1964−1967.

(26) Wessells, C. D.; Huggins, R. A.; Cui, Y. Copper Hexacyanoferrate Battery Electrodes with Long Cycle Life and High Power. *Nat. Commun.* **2011**, *2*, 550.

(27) Wessells, C. D.; McDowell, M. T.; Peddada, S. V.; Pasta, M.; Huggins, R. A.; Cui, Y. Tunable Reaction Potentials in Open Framework Nanoparticle Battery Electrodes for Grid-Scale Energy Storage. *ACS Nano* **2012**, *6*, 1688−1694.

(28) Wessells, C. D.; Peddada, S. V.; Huggins, R. A.; Cui, Y. Nickel Hexacyanoferrate Nanoparticle Electrodes for Aqueous Sodium and Potassium Ion Batteries. *Nano Lett.* **2011**, *11*, 5421−5425.

(29) Wessells, C. D.; Peddada, S. V.; McDowell, M. T.; Huggins, R. A.; Cui, Y. The Effect of Insertion Species on Nanostructured Open Framework Hexacyanoferrate Battery Electrodes. *J. Electrochem. Soc.* **2012**, *159*, 98−103.

(30) Wu, X.; Cao, Y.; Ai, X.; Qian, J.; Yang, H. A low-cost and environmentally benign aqueous rechargeable sodium-ion battery based on NaTi2(PO4)3-Na2NiFe(CN)6 intercalation chemistry. *Electrochem. Commun.* **2013**, *31*, 145−148.

(31) Ong, S. P.; Chevrier, V. L.; Hautier, G.; Jain, A.; Moore, C.; Kim, S.; Ma, X.; Ceder, G. Voltage, Stability and Diffusion Barrier Differences Between Sodium-Ion and Lithium-Ion Intercalation Materials. *Energy Environ. Sci.* **2011**, *4*, 3680−3688.

160

(32) Van der Ven, A.; Bhattacharya, J.; Belak, A. A. Understanding Li Diffusion in Li-Intercalation Compounds. *Acc. Chem. Res.* **2013**, *46*, 1216−1225.

(33) Etacheri, V.; Marom, R.; Elazari, R.; Salitra, G.; Aurbach, D. Challenges in the Development of Advanced Li-Ion Batteries: A Review. *Energy Environ. Sci.* **2011**, *4*, 3243−3262.

(34) Islam, M. S.; Fisher, C. A. J. Lithium and Sodium Battery Cathode Materials: Computational Insights into Voltage, Diffusion and Nanostructural Properties. *Chem. Soc. Rev.* **2014**, *43*, 185−204.

(35) Park, Y.-U.; Seo, D.-H.; Kwon, H.-S.; Kim, B.; Kim, J.; Kim, H.; Kim, I.; Yoo, H.-I.; Kang, K. A New High-Energy Cathode for a Na-Ion Battery with Ultrahigh Stability. *J. Am. Chem. Soc.* **2013**, *135*, 13870−13878.

(36) Lee, D. H.; Xu, J.; Meng, Y. S. An Advanced Cathode for Na-Ion Batteries with High Rate and Excellent Structural Stability. *Phys. Chem. Chem. Phys.* **2013**, *15*, 3304−3312.

(37) He, H.; Jin, G.; Wang, H.; Huang, X.; Chen, Z.; Sun, D.; Tang, Y. Annealed NaV3O8 nanowires with good cycling stability as a novel cathode for Na-ion batteries. *J. Mater. Chem. A* **2014**, *2*, 3563−3570.

(38) Yun, J.; Pfisterer, J.; Bandarenka, A. S. How Simple are the Models of Na Intercalation in Aqueous Media? *Energy Environ. Sci.* **2016**, *9*, 955−961.

(39) Ventosa, E.; Paulitsch, B.; Marzak, P.; Yun, J.; Schiegg, F.; Quast, T.; Bandarenka, A. S. The Mechanism of the Interfacial Charge and Mass Transfer during Intercalation of Alkali Metal Cations. *Adv. Sci.* **2016**, *3*, 1600211.

(40) Pham-Cong, D.; Choi, J. H.; Yun, J.; Bandarenka, A. S.; Kim, J.; Braun, P. V.; Jeong, S. Y.; Cho, C. R. Synergistically Enhanced Electrochemical Performance of Hierarchical MoS2/TiNb2O7 Hetero-nanostructures as Anode Materials for Li-Ion Batteries. *ACS Nano* **2017**, *11*, 1026−1033.

(41) Paulitsch, B.; Yun, J.; Bandarenka, A. S. Electrodeposited Na2VOx[Fe(CN)6] films As a Cathode Material for Aqueous Na-Ion Batteries. *ACS Appl. Mater. Interfaces* **2017**, *9*, 8107−8112.

(42) McKinnon, W. R.; Haering, R. R. Physical Mechanism of Intercalation. In *Modern Aspects of Electrochemistry*; White, R. E., Bockris, J. O'M., Conway, B. E., Eds.; Plenum Press: New York, 1983; Vol. 15, pp 235−236.

(43) Schlögl, R. Graphite—A Unique Host Lattice. In *Progress in Intercalation Research*; Müller-Warmuth, W., Schöllhorn, R., Eds.; Springer Science+Business Media: Dordrecht, 1994; pp 83−84.

(44) Scieszka, D.; Yun, J.; Bandarenka, A. S. What Do Laser-Induced Transient Techniques Reveal for Batteries? Na- and K-Intercalation from Aqueous Electrolytes as an Example. *ACS Appl. Mater. Interfaces* **2017**, *9*, 20213−20222.

(45) Climent, V.; Coles, B. A.; Compton, R. G. Coulostatic Potential Transients Induced by Laser Heating of a Pt(111) Single-Crystal Electrode in Aqueous Acid Solutions. Rate of Hydrogen Adsorption and Potential of Maximum Entropy. *J. Phys. Chem. B* **2002**, *106*, 5988−5996.

(46) Climent, V.; Garcia-Araez, N.; Compton, R. G.; Feliu, J. M. Effect of Deposited Bismuth on the Potential of Maximum Entropy of Pt(111) Single-Crystal Electrodes. *J. Phys. Chem. B* **2006**, *110*, 21092−21100.

(47) Ledezma-Yanez, I.; Wallace, W. D. Z.; Sebastián-Pascual, P.; Climent, V.; Feliu, J. M.; Koper, M. T. M. Interfacial Water Reorganization as a pH-Dependent Descriptor of the Hydrogen Evolution Rate on Platinum Electrodes. *Nat. Energy* **2017**, *2*, 17031−17037.

(48) Ataka, K.-i.; Yotsuyanagi, T.; Osawa, M. Potential-Dependent Reorientation of Water Molecules at an Electrode/Electrolyte Interface Studied by Surface-Enhanced Infrared Absorption Spectroscopy. *J. Phys. Chem.* **1996**, *100*, 10664−10672.

(49) Ataka, K.-i.; Osawa, M. In Situ Infrared Study of Water−Sulfate Coadsorption on Gold(111) in Sulfuric Acid Solutions. *Langmuir* **1998**, *14*, 951−959.

(50) Toney, M. F.; Howard, J. N.; Richer, J.; Borges, G. L.; Gordon, J. G.; Melroy, O. R.; Wiesler, D. G.; Yee, D.; Sorensen, L. B. Voltage-dependent ordering of water molecules at an electrode-electrolyte interface. *Nature* **1994**, *368*, 444−446.

(51) Osawa, M.; Tsushima, M.; Mogami, H.; Samjeské, G.; Yamakata, A. Structure of Water at the Electrified Platinum−Water Interface: A Study by Surface-Enhanced Infrared Absorption Spectroscopy. *J. Phys. Chem. C* **2008**, *112*, 4248−4256.

(52) Yamakata, A.; Osawa, M. Dynamics of Double-Layer Restructuring on a Platinum Electrode Covered by CO: Laser-Induced Potential Transient Measurement. *J. Phys. Chem. C* **2008**, *112*, 11427−11432.

(53) Benderskii, V. A.; Babenko, S. D.; Krivenko, A. G. Investigation of the Charge Relaxation in the Double Layer by a Thermal Jump. *J. Electroanal. Chem.* **1978**, *86*, 223−225.

(54) Benderskii, V. A.; Velichko, G. I. Temperature jump in electric double-layer study. *J. Electroanal. Chem.* **1982**, *140*, 1−22.

(55) Benderskii, V. A.; Velichko, G. I.; Kreitus, I. V. Temperature jump in electric double-layer study. *J. Electroanal. Chem.* **1984**, *181*, 1−20.

(56) Climent, V.; Coles, B. A.; Compton, R. G. Laser Induced Current Transients Applied to a Au(111) Single Crystal Electrode. A General Method for the Measurement of Potentials of Zero Charge of Solid Electrodes. *J. Phys. Chem. B* **2001**, *105*, 10669−10673.

(57) García-Aráez, N.; Climent, V.; Feliu, J. M. Evidence of Water Reorientation on Model Electrocatalytic Surfaces from Nanosecond-Laser-Pulsed Experiments. *J. Am. Chem. Soc.* **2008**, *130*, 3824−3833.

(58) Garcia-Araez, N.; Climent, V.; Feliu, J. Potential-Dependent Water Orientation on Pt(111), Pt(100), and Pt(110), as Inferred from Laser-Pulsed Experiments. Electrostatic and Chemical Effects. *J. Phys. Chem. C* **2009**, *113*, 9290−9304.

(59) Sebastián, P.; Martínez-Hincapié, R.; Climent, V.; Feliu, J. M. Study of the Pt (111) | Electrolyte Interface in the Region Close to Neutral pH Solutions by the Laser Induced Temperature Jump Technique. *Electrochim. Acta* **2017**, *228*, 667−676.

(60) Garlyyev, B.; Xue, S.; Watzele, S.; Scieszka, D.; Bandarenka, A. S. Influence of the Nature of the Alkali Metal Cations on the Electrical Double-Layer Capacitance of Model Pt(111) and Au(111) Electrodes. *J. Phys. Chem. Lett.* **2018**, *9*, 1927−1930.

(61) Bandarenka, A. S. Development of Hybrid Algorithms for EIS Data Fitting. In *Lecture Notes on Impedance Spectroscopy*; Kanoun, O., Ed.; Taylor & Francis Group: London, 2014; Vol. 4, pp 29−38.

(62) Bondarenko, A. S.; Ragoisha, G. A. Inverse Problem in Potentiodynamic Electrochemical Impedance. In *Progress in Chemometrics Research*; Pomerantsev, A. L., Ed.; Nova Science Publishers. Inc.: New York, 2005; pp 89−102.

(63) Bondarenko, A. S. Analysis of Large Experimental Datasets in Electrochemical Impedance Spectroscopy. *Anal. Chim. Acta* **2012**, *743*, 41−50.

(64) Berkes, B. B.; Inzelt, G.; Schuhmann, W.; Bondarenko, A. S. Influence of Cs+ and Na+ on Specific Adsorption of *OH, *O, and *H at Platinum in Acidic Sulfuric Media. *J. Phys. Chem. C* **2012**, *116*, 10995−11003.

(65) Horcas, I.; Fernández, R.; Gómez-Rodríguez, J. M.; Colchero, J.; Gómez-Herrero, J.; Baro, A. M. WSXM: A Software for Scanning Probe Microscopy and a Tool for Nanotechnology. *Rev. Sci. Instrum.* **2007**, *78*, 013705.

(66) Wu, X.; Wu, C.; Wei, C.; Hu, L.; Qian, J.; Cao, Y.; Ai, X.; Wang, J.; Yang, H. Highly Crystallized Na2CoFe(CN)6 with Suppressed Lattice Defects as Superior Cathode Material for Sodium-Ion Batteries. *ACS Appl. Mater. Interfaces* **2016**, *8*, 5393−5399.

(67) Li, W.; Zhang, F.; Xiang, X.; Zhang, X. Electrochemical Properties and Redox Mechanism of Na2Ni0.4Co0.6[Fe(CN)6] Nanocrystallites as High-Capacity Cathode for Aqueous Sodium-Ion Batteries. *J. Phys. Chem. C* **2017**, *121*, 27805−27812.

(68) Andre, D.; Meiler, M.; Steiner, K.; Wimmer, C.; Soczka-Guth, T.; Sauer, D. U. Characterization of High-Power Lithium-Ion Batteries by Electrochemical Impedance Spectroscopy. I. Experimental Investigation. *J. Power Sources* **2011**, *196*, 5334−5341.

(69) Silva, F.; Sottomayor, M. J.; Martins, A. Temperature Coefficient of the Potential of Zero Charge and Entropies of

161

Formation for the Interface of Stepped Faces of Gold in Contact with Aqueous Perchloric Acid Solutions. *J. Chem. Soc., Faraday Trans.* **1996**, *92*, 3693−3699.

(70) Silva, F.; Sottomayor, M. J.; Hamelin, A. The temperature coefficient of the potential of zero charge of the gold single-crystal electrode/aqueous solution interface. *Electroanal. Chem.* **1990**, *294*, 239−251.

(71) Emets, V. V.; Damaskin, B. B. The Relation between the Potential of Zero Charge and Work Function for sp-Metals. *Russ. J. Electrochem.* **2009**, *45*, 45−57.

(72) Climent, V.; Coles, B. A.; Compton, R. G. Laser-Induced Potential Transients on a Au(111) Single-Crystal Electrode. Determination of the Potential of Maximum Entropy of Double-Layer Formation. *J. Phys. Chem. B* **2002**, *106*, 5258−5265.

(73) Brennan, J. L.; Forster, R. J. Laser Light and Electrodes: Interaction Mechanisms and Electroanalytical Applications. *J. Phys. Chem. B* **2003**, *107*, 9344−9350.

(74) Smith, D. W. Ionic Hydration Enthalpies. *J. Chem. Educ.* **1977**, *54*, 540−542.

(75) Pratihar, S.; Chandra, A. A First Principles Molecular Dynamics Study of Lithium Atom Solvation in Binary Liquid Mixture of Water and Ammonia: Structural, Electronic, and Dynamical Properties. *J. Chem. Phys.* **2011**, *134*, 024519.

(76) Harrison, J. A.; Randles, J. E. B.; Schiffrin, D. J. The Entropy of Formation of the Mercury-Aqueous Solution Interface and the Structure of the Inner Layer. *Electroanal. Chem.* **1973**, *48*, 359−381.

(77) Silva, A. F. Temperature Effects of Interfacial Properties. In *Trends in Interfacial Electrochemistry*; Silva, A. F., Ed.; ACS Symposium Series; D. Reidel Publishing Company: Amsterdam, 1986; pp 49−70.

162

# References

1. N. Armaroli, V. Balzani, Energy for a Sustainable World: From the Oil Age to a Sun-Powered Future, WILEY-VCH Verlag GmbH & Co. KGaA, Weinheim, 2011.

2. P. Poizot, F. Dolhem, Energy Environ. Sci., 2011, 4, 2003.

3. C. Wolfram, O. Shelef, P. Gertler, J. Econ. Perspect., 2012, 26, 119.

4. M. Ball, M. Weeda, Int. J. Hydrog. Energy, 2015, 40, 7903.

5. IEA (International Energy Agency). Technology roadmap-hydrogen and fuel cells. Paris: OECD/IEA; 2015 (forthcoming).

6. BP Statistical Review of World Energy, Pureprint Group, Ltd., London, 2018.

7. Z. Yang, J. Zhang, M.C.W. Kintner-Meyer, X. Lu, D. Choi, J.P. Lemmon, J. Liu, Chem. Rev., 2011, 111, 3577.

8. Fraunhofer ISE. https://energycharts.de/power.htm?source=conventional&year=2018&week=39, (accessed October 2018).

9. D. Ginley, M.A. Green, R. Collins, MRS Bull., 2008, 33, 355.

10. A. Zervos, Renewables 2016: Global Report; REN21: Paris, 2016.

11. B.L. Ellis, L.F. Nazar, Curr. Opin. Solid State Mater. Sci., 2012, 16, 168.

12. J. Yun, J. Pfisterer, A.S. Bandarenka, Energy Environ. Sci., 2016, 9, 955.

13. S. Dunn, Int. J. Hydrog. Energy, 2002, 27, 235.

14. G.W. Crabtree, M.S. Dresselhaus, M.V. Buchanan, Phys. Today, 2004, 57, 39.

15. Hydrogen Generation via Thermochemical Water-Splitting. http://h2.hiroshima-u.ac.jp/research.html, (accessed October 2018).

16. M.S. Dresselhaus, I.L. Thomas, Nature, 2001, 414, 332.

17. M.G. Walter, E.L. Warren, J.R. McKone, S.W. Boettcher, Q. Mi, E.A. Santori, N.S. Lewis, Chem. Rev., 2010, 110, 6446.

18. J.A. Turner, Science, 2004, 305, 972.

19. N.S. Lewis, D.G. Nocera, PNAS, 2006, 103, 15729.

20. K. Xu, A. Chatzitakis, T. Norby, Photochem. Photobiol. Sci., 2017, 16, 10.

21. I. Roger, M.A. Shipman, M.D. Symes, Nat. Rev. Chem., 2017, 1, 3.

22. J. Yang, J.K. Cooper, F.M. Toma, K.A. Walczak, M. Favaro, J.W. Beeman, L.H. Hess, C. Wang, C. Zhu, S. Gul, J. Yano, C. Kisielowski, A. Schwartzberg, I.D. Sharp, Nat. Mater., 2016, 7, 335.

23. J.K. Norskov, J. Rossmeisl, A. Logadottir, L.R.K.J. Lindqvist, J.R. Kitchin, T. Bligaard, H. Jonsson, , J. Phys. Chem. B, 2004, 108, 17886.

24. V. Colic, M.D. Pohl, D. Scieszka, A.S. Bandarenka, Catal. Today, 2016, 262, 24.

25. F. Trieb, C. Schillings, M. O'Sulivan, T. Pregger, C. Hoyer-Klick, Global Potential of Concentrating Solar Power. Proceedings of Solar Paces Conference, Berlin, 2009.

26. J. Liu, Adv. Funct. Mater., 2013, 23, 924.

27. S. Komaba, W. Murata, T. Ishikawa, N. Yabuuchi, T. Ozeki, T. Nakayama, A. Ogata, K. Gotoh, K. Fujiwara, Adv. Funct. Mater., 2011, 21, 3859.

28. B. Dunn, H. Kamath, J.M. Tarascon, Science, 2011, 334, 928.

29. G.L. Soloveichik, Annu. Rev. Chem. Biomol. Eng., 2011, 2, 503.

30. V. Palomares, P. Serras, I. Villaluenga, K.B. Hueso, J. Carretero-Gonzalez, T. Rojo, Energy Environ. Sci., 2012, 5, 5884.

31. M. Pasta, C.D. Wessells, R.A. Huggins, Y. Cui, Nat. Commun., 2011, 2, 550.

32. M. Pasta, C.D. Wessells, N. Liu, J. Nelson, M.T. McDowell, R.A. Huggins, M.F. Toney, Y. Cui, Nat. Commun., 2014, 5, 3007.

33. D.R. Lide, The 84th Edition CRC Handbook of Chemistry and Physics, CRC Press LLC, 2003.

34. Terrestrial Abundance of Elements. http://www.daviddarling.info/encyclopedia/E/elterr.html, (accessed October 2018).

35. R.M. Hazen, G. Hystad, R.T. Downs, J.J. Golden, A. Pires, E.S. Grew, Am. Mineral., 2015, 100, 2344.

36. C. Luo, A. Langrock, X. Fan, Y. Liang, C. Wang, J. Mater. Chem. A, 2017, 5, 18214.

37. N. Ortiz-Vitoriano, N.E. Drewett, E. Gonzalo, T. Rojo, Energy Environ. Sci., 2017, 10, 1051.

38. S. Chen, C. Wu, L. Shen, C. Zhu, Y. Huang, K. Xi, J. Maier, Y. Yu, Adv. Mater., 2017, 29, 1700431.

39. S.P. Ong, V.L. Chevrier, G. Hautier, A. Jain, C. Moore, S. Kim, X. Ma, G. Ceder, Energy Environ. Sci., 2011, 4, 3680.

40. M.S. Islam, C.A.J. Fisher, Chem. Soc. Rev., 2014, 43, 185.

41. Y. Park, D. Seo, H. Kwon, B. Kim, J. Kim, H. Kim, I. Kim, H. Yoo, K. Kang, J. Am. Chem. Soc., 2013, 135, 13870.

42. D.H. Lee, J. Xu, Y.S. Meng, Phys. Chem. Chem. Phys., 2013, 15, 3304.

43. H. He, G. Jin, H. Wang, X. Huang, Z. Chen, D. Sun, Y. Tang, J. Mater. Chem. A, 2014, 2, 3563.

44. A. Ponrouch, E. Marchante, M. Courty, J. Tarascon, M. Rosa Palacin, Energy Environ. Sci., 2012, 5, 8572.

45. D. Scieszka, J. Yun, A.S. Bandarenka, ACS Appl. Mater. Interfaces, 2017, 9, 20213.

46. D. Scieszka, C. Sohr, P. Scheibenbogen, P. Marzak, J. Yun, Y. Liang, J. Fichtner, A.S. Bandarenka, ACS Appl. Mater. Interfaces, 2018, 10, 21688.

47. A.J. Bard, L.R. Faulkner, Electrochemical Methods: Fundamentals and Applications, Wiley & Sons, New York, 2001.

48. G. Ertl, H. Knözinger, F. Schüth, J. Weitkamp (eds.), Handbook of Heterogeneous Catalysis: Second, Completely Revised and Enlarged Edition, WILEY-VCH Verlag GmbH & Co. KGaA, Weinheim, 2008.

49. A.J.B. Robertson, Platinum Metals Rev., 1975, 2, 64.

50. G. Rothenber, Catalysis: Concepts and Green Applications, WILEY-VCH Verlag GmbH & Co. KGaA, Weinheim, 2017.

51. I. Chorkendorff, J.W. Niemantsverdriet, Concepts of Modern Catalysis and Kinetics, WILEY-VCH Verlag GmbH & KGaA, Weinheim, 2003.

52. A.S. Bandarenka, E. Ventosa, A. Maljusch, J. Masa, W. Schumann, Analyst, 2017, 139, 1274.

53. W.K. Berry, Biochem. J., 1951, 49, 615.

54. P. Muller, PAC, 1994, 66, 1077.

55. R.J. Farrauto, R.M. Heck, Catal. Today, 2000, 55, 179.

56. J.G. McCarty, M. Gusman, D.M. Lowe, D.L. Hildebrand, K.N. Lau, Catal. Today, 1999, 47, 5.

57. D.M. Kolb, Angew. Chem. Int. Ed., 2001, 40, 1162.

58. A.J. Appleby, Catal. Rev., 1971, 4, 221.

59. P. Sabatier, J.B. Senderens, C.R. Acad. Sci., 1902, 134, 514.

60. A.J. Medford, A. Vojvodic, J.S. Hummelshoj, J. Voss, F. Abild-Pedersen, F. Studt, T. Bligaard, A. Nilsson, J.K. Norskov, J. Cat., 2015, 328, 36.

61. A.B. Laursen, I.C. Man, O.L. Trinhammer, J. Rossmeisl, S. Dahl, J. Chem. Edu., 2011, 88, 1711.

62. V. Colic, A.S. Bandarenka, ACS Catal., 2016, 6, 5378.

63. H.S. Taylor, Proc. Roy. Soc. A, 1925, 108, 105.

64. M. Boudart, Adv. Catal. Relat. Subj., 1969, 20, 153.

65. M.D. Pohl, V. Colic, D. Scieszka, A.S. Bandarenka, Phys. Chem. Chem. Phys., 2016, 18, 10792.

66. A.S. Bandarenka, H.A. Hansen, J. Rossmeisl, I.E.L. Stephens, Phys. Chem. Chem. Phys., 2014, 16, 13625.

67. M. Gong, H. Dai, Nano Res., 2015, 8, 23.

68. M. Zeng, Y. Li, J. Mater. Chem. A, 2015, 3, 14942.

69. M.T.M. Koper, J. Electroanal. Chem., 2011, 660, 254.

70. J.O'.M. Bockris, E.C. Potter, J. Electrochem. Soc., 1952, 99, 169.

71. N.M. Markovic, P.N. Ross, Jr, Surf. Sci. Rep., 2002, 45, 117.

72. Y. Matsumoto, E. Sato, Mat. Chem. Phys., 1986, 14, 397.

73. T. Reier, M. Oezaslan, P. Strasser, ACS Catal., 2012, 2, 1765.

74. J. Durst, A. Siebel, C. Simon, F. Hasché, J. Herranz, H.A. Gasteiger, Energy Environ. Sci., 2014, 7, 2255.

75. V.I. Birss, A. Damjanovic, P.G.J. Hudson, Electrochem. Soc., 1986, 133, 1621.

76. B.E. Conway, T.C. Liu, Langmuir, 1990, 6, 268.

77. S. Chen, J. Duan, M. Jaroniec, S. Qiao, Adv. Mater., 2014, 26, 2925.

78. M.S. Burke, L.J. Enman, A.S. Batchellor, S. Zou, S.W. Boettcher, Chem. Mater., 2015, 27, 7549.

79. S. Park, Y. Shao, J. Liu, Y. Wang, Energy Environ. Sci., 2012, 5, 9331.

80. Introduction to Electrolyzer and Fuel Cells. https://www.horizoncurriculum.com/supportmaterial/introduction-to-electrolyzers-and-fuel-cells/, (accessed online February 2019).

81. W. Kreuter, H. Hofmann, Int. J. Hydrogen Energy, 1998, 23, 661.

82. D.M.F. Santos, C.A.C. Sequeira, J.L. Figueiredo, Quim. Nova, 2013, 36, 1176.

83. Hydrogen Production: Electroylsis. https://www.energy.gov/eere/fuelcells/hydrogen-production-electrolysis (accessed online January 2018).

84. A. Brisse, J. Schefold, M. Zahid, Int. J. Hydrog. Energy, 2008, 33, 5375.

85. D. Bessarabov, H. Wang, H. Li, N. Zhao (eds.), PEM Electrolysis for Hydrogen Production: Principles and Applications, Taylor & Francis Group, Boca Raton, London, NY, 2015.

86. D. Strmcnik, M. Uchimura, C. Wang, R. Subbaraman, N. Danilovic, D. van der Vliet, A.P. Paulikas, V.R. Stamenkovic, N.M. Markovic, Nat. Chem., 2013, 5, 300.

87. L. Carrette, K.A. Friedrich, U. Stimming, Fuel Cells, 2001, 1, 5.

88. W. Sheng, Z. Zhuang, M. Gao, J. Zheng, J.G. Chen, Y. Yan, Nat. Commun., 2015, 6, 5848.

89. R.M.Q. Mello, E.A. Ticianelli, Electrochim. Acta, 1997, 42, 1031.

90. P.M. Quaino, J.L. Fernandez, M.R. Gennero de Chialvo, A.C. Chialvo, J. Mol. Catal. A. Chem., 2006, 252, 156.

91. H. Wroblowa, Y.C. Pan, J. Razumney, J. Electroanal. Chem., 1976, 69, 195.

92. N.M. Markovic, T.J. Schmidt, V. Stamenkovic, P.N. Ross, Fuel Cells, 2001, 1, 105.

93. Y. Nie, L. Li, Z. Wei, Chem. Soc. Rev., 2015, 44, 2168.

94. J.X. Wang, F.A. Uribe, T.E. Springer, J. Zhangc, R.R. Adzic, Faraday Discuss., 2008, 140, 347.

95. S. Siahrostami, A. Verdaguer-Casadevall, M. Karamad, D. Deiana, P. Malacrida, B. Wickman, M. Escudero-Escribano, E.A. Paoli, R. Frydendal, T.W. Hansen, I. Chorkendorff, I.E.L. Stephens, J. Rossmeisl, Nat. Mat., 2013, 12, 1137.

96. S.J. Peighambardoust, S. Rowshanzamir, M. Amjadi, Int. J. Hydrog. Energy, 2010, 35, 9349.

97. U. Eberle, R. von Helmholt, Energy Environ. Sci., 2010, 3, 689.

98. F.T. Wagner, B. Lakshamanan, Mathias, M.F.J. Phys. Chem. Lett., 2010, 1, 2204.

99. A. Rabis, P. Rodriguez, T.J. Schmidt, ACS Catal., 2012, 2, 864.

100. R. Bashyam, P. Zelenay, Nature, 2006, 443, 63.

101. Fuel Cell Model. https://www.rtds.com/hot-topic-fuel-cell-model/figure-1-functional-diagram-of-fuel-cell/, (accessed February 2019).

102. X. Cheng, Z. Shi, N. Glass, L. Zhang, J. Zhang, D. Song, Z. Liu, H. Wang, J. Shen, J. Power Sources, 2007, 165, 739.

103. X. Li, Principles of Fuel Cells, , Taylor & Francis Group, NY, 2006.

104. A.J. Bard, G. Inzelt, F. Scholz (eds.), Electrochemical Dictionary. 2nd, Revised and Extended Edition, Springer-Verlag Berlin Heidelberg, 2012.

105. K.E. Aifantis, S.A. Hackney, R.V. Kumar (eds.), High Energy Density Lithium Batteries: Materials, Engineering, Wiley-VCH Verlag GmbH & Co. KGaA, Weinheim, 2010.

106. J. Zhang, Z. Liu, Q. Kong, C. Zhang, S. Pang, L. Yue, X. Wang, J. Yao, G. Cui, ACS Appl. Mater. Interfaces, 2013, 5, 128.

107. F.V. Conte, P. Gollob, H. Lacher, World Electr. Veh. J., 2009, 3, 719.

108. J.F. Manwell, J.G. McGowan, 1993, 50, 399.

109. G.J. May, A. Davidson, B. Monahov, 2018, 15, 145.

110. H. Li, Z. Wang, L. Chen, X. Huang, 2009, 21, 4593.

111. M.M. Huie, D.C. Bock, E.S. Takeuchi, A.C. Marschilok, K.J. Takeuchi, 2015, 287, 15.

112. T. Ishihara, M. Koga, H. Matsumoto, M. Yoshio, 2007, 10, A74.

113. Y. Yue, A.J. Binder, B. Guo, Z. Zhang, Z. Qiao, C. Tian, S. Dai, Angew. Chem. Int. Ed., 2014, 53, 3134.

114. Y. Lu, L. Wang, J. Cheng, J.B. Goodenough, Chem. Commun., 2012, 48, 6544.

115. H.J. Buser, A. Ludi, W. Petter, D. Schwarzenbach, J. Chem. Soc. Chem. Commun., 1972, 0, 1299.

116. K. Tayan, I. Hida, Acc. Chem. Res., 1986, 19, 162.

117. S. Margadonna, K. Prassides, A.N. Fitch, Angew. Chem., 2004, 116, 6476.

118. S. Margadonna, K. Prassides, A.N. Fitch, Angew. Chem. Int. Ed., 2004, 43, 6316.

119. B. Paulitsch, J. Yun, A.S. Bandarenka, ACS Appl. Mater. Interfaces, 2017, 9, 8107.

120. R.E. White, J.O'M. Bockris, B.E. Conway, (eds.), Modern Aspects of Electrochemistry no. 22, Plenum Press, New York, 1992.

121. W. Müller-Warmuth, R. Schöllhorn (eds.), Progress in Intercalation Research, Springer Science+Business Media, Dordrecht, 1994.

122. G. Xu, Q. Wang, J. Fang, Y. Xu, J. Li, L. Huang, S. Sun, J. Mater. Chem. A, 2014, 2, 19941.

123. D. Yang, X. Liao, B. Huang, J. Shen, Y. He, Z. Ma, J. Mater. Chem. A, 2013, 1, 13417.

124. H.J. Buser, D. Schwarzenbach, W. Petter, A. Ludi, Inorg. Chem., 1977, 16, 2704.

125. T. Matsuda, J. Kim, Y. Moritomo, J. Am. Chem. Soc., 2010, 132, 12206.

126. H. Kim, J. Hong, K. Park, H. Kim, S. Kim, K. Kang, Chem. Rev., 2014, 114, 11788.

127. A.V. Radha, C.V. Subban, M. L. Sun, J.M. Tarascon, A. Navrotsky, J. Mater. Chem. A, 2014, 2, 6887.

128. H.Y. Asl, K. Ghosh, M.P.V. Meza, A. Choudhury, J. Mater. Chem. A, 2015, 3, 7488.

129. C. Erinmwingbovo, M.S. Palagonia, D. Brogioli, F. La Mantia, 2017, 18, 917.

130. J. Yun, F.A. Schiegg, Y. Liang, D. Scieszka, B. Garlyyev, A. Kwiatkowski, T. Wagner, A.S. Bandarenka, ACS Appl. Energy Mater., 2018, 1, 123.

131. Y. You, X. Yu, Y. Yin, K. Nam, Y. Guo, Nano. Res., 2015, 8, 117.

132. L. Wang, Y. Lu, J. Liu, M. Xu, J. Cheng, D. Zhang, J. B. Goodenough, Angew. Chem. Int. Ed., 2013, 52, 1964.

133. C.D. Wessells, R.A. Huggins, Y. Cui, Nat. Commun., 2011, 2, 550.

134. C.D. Wessells, M.T. McDowell, S.V. Peddada, M. Pasta, R.A. Huggins, Y. Cui, ACS Nano, 2012, 6, 1688.

135. C.D. Wessells, S.V. Peddada, R.A. Huggins, Y. Cui, Nano Lett., 2011, 11, 5421.

136. C.D. Wessells, S.V. Peddada, M.T. McDowell, R.A. Huggins, Y. Cui, J. Electrochem. Soc., 2012, 159, 98.

137. X. Wu, Y. Cao, X. Ai, J. Qian, H. Yang, Electrochem. Commun., 2013, 31, 145.

138. E. Ventosa, B. Paulitsch, P. Marzak, J. Yun, F. Schiegg, T. Quast, A.S. Bandarenka, Adv. Sci., 2016, 3, 1600211.

139. C.H. Hamann, A. Hamnett, W. Vielstich, Electrochemistry, Second, Completely Revised and Updated Edition, WILEY-VCH Verlag GmbH & Co. KGaA, Weinheim, 2007.

140. H. Du, X. Lin, Z. Xu, D. Chu, J. Mater. Sci., 2015, 50, 5641.

141. V. Climent, N. Garcia-Araez, R.G. Compton, J.M. Feliu, J. Phys. Chem. B, 2006, 110, 21092.

142. H. Ogasawa, B. Brena, D. Nordlund, M. Nyberg, A. Pelmenschikov, L.G.M. Pettersson, A. Nilsson, Phys. Rev. Lett., 2002, 89, 276102.

143. S. Schnur, A. Groß, New J. Phys., 2009, 11, 125003.

144. S. Trasatti, J. Electroanal. Chem., 1974, 54, 437.

145. P.A. Thiel, T.E. Madey, Surf. Sci. Rep., 1987, 7, 211.

146. R. Guidelli, W. Schmickler, Electrochim. Acta, 2000, 45, 2317.

147. M.A. Henderson, Surf. Sci. Rep., 2002, 46, 1.

148. J. Lipkowski, P.H. Ross, Structure of Electrified Interfaces, VCH, New York, 1993.

149. A. Michaelides, Appl. Phys. A, 2006, 85, 415.

150. A. Michaelides, A. Alavi, D.A. King, Phys. Rev. B, 2006, 85, 113404.

151. P.J. Feibelman, Science, 2002, 295, 99.

152. D. Menzel, Science, 2002, 295, 58.

153. G. Materzanini, G.F. Tantardini, P.J.D. Lindan, P. Saalfrank, Phys. Rev. B, 2005, 71, 155414.

154. M. Osawa, J. Phys. Chem., 2008, 112, 4248.

155. J.O'M. Bockris, S.U.M. Khan, Surface Electrochemistry: A Molecular Level Approach, Plenum, New York, 1993.

156. E. Spohr, Chem. Phys., 1990, 141, 87.

157. G. Nagy, K. Heinzinger, 1990, 296, 549.

158. A. Kovalenko, F.J. Hirata, Chem. Phys., 1999, 110, 10095.

159. J.N. Glosli, M.R.J. Philpott, Chem. Phys., 1992, 96, 6962.

160. G. Nagy, K.J. Heinzinger, Electroanal. Chem., 1990, 296, 549.

161. K. Ataka, M. Osawa, Langmuir, 1998, 14, 951.

162. D. Doering, T.E. Madey, Surf. Sci., 1982, 123, 305.

163. J.O.'M. Bockris, B.E. Conway, E. Yeager (eds), Comprehensive Treatise of Electrochemistry, Vol. 1, Plenum Press, New York, 1980.

164. A. Cuesta, Surf. Sci., 2004, 572, 11.

165. V. Climent, R. Gomez, J.M. Feliu, Electrochim. Acta, 1999, 45, 629.

166. A.N. Frumkin, A. Gorodetzkaya, Z. Phys. Chem., 1928, 136, 215

167. V.V. Emets, B.B. Damaskin, Russ. J. Electrochem., 2009, 45, 45.

168. H. Gerischer, C.W. Tobias (eds.), Advances in Electrochemistry and Electrochemical Engineering, Vol. 10, Wiley, New York, 1977.

169. A.N. Frumkin, O.A. Petrii, Electrochim. Acta, 1975, 20, 347.

170. N. Garcia-Araez, V. Climent, J.M. Feliu, J. Am. Chem. Soc., 2008, 130, 3824.

171. V. Climent, B.A. Coles, R.G. Compton, J.M. Feliu, J. Electroanal. Chem., 2004, 561, 157.

172. I. Ledezma-Yanez, W.D.Z. Wallace, P. Sebastián-Pascual, V. Climent, J.M. Feliu, M.T.M. Koper, Nat. Energy, 2017, 2, 17031.

173. D. Strmcnik, D.F. van der Vliet, K. Chang, V. Komanicky, K. Kodama, H. You, V.R. Stamenkovic, N.M. Markovic, J. Phys. Chem. Lett., 2011, 2, 2733.

174. M. Breiter, M. Kleinerman, P. Delahay, J. Am. Chem. Soc., 1958, 80, 5111.

175. A.N. Frumkin, J. Electrochem. Soc., 1960, 107, 461.

176. V. Viswanathan, H.A. Hansen, J. Rossmeisl, J.K. Norskov, ACS Catal., 2012, 2, 1654.

177. J.S. Jirkovsky, M. Busch, E. Ahlberg, I. Panas, P. Krtil, J. Am. Chem. Soc., 2011, 133, 5882.

178. C. Zhang, Y. Yu, M.E. Grass, C. Dejoie, W. Ding, K. Gaskell, N. Jabeen, Y.P. Hong, A. Shavorskiy, H. Bluhm, W. Li, G.S. Jackson, Z. Hussain, Z. Liu, B. Eichhorn, J. Am. Chem. Soc., 2013, 135, 11572.

179. A.P. O'Mullane, Nanoscale, 2014, 6, 4012.

180. T.F. Jaramillo, K.P. Jorgensen, J. Bonde, J.H. Nielsen, S. Horch, I. Chorkendorf, Science, 2007, 317, 100.

181. M.T.M. Koper, Nanoscale, 2011, 3, 2054.

182. A.S. Bandarenka, M.T.M. Koper, J. Catal., 2013, 308, 11.

183. T. Jiang, D.J. Mowbray, S. Dobrin, H. Falsig, B. Hvolbaek, T. Bligaard, J.K. Norskov, J. Phys. Chem. C, 2009, 113, 10548.

184. N. Job, M. Chatenet, S. Berthon-Fabry, S. Hermans, F. Maillard, J. Power Sources, 2013, 240, 294.

185. F. Calle-Vallejo, M.D. Pohl, D. Reinisch, D. Loffreda, P. Sautet, A.S. Bandarenka, Chem. Sci., 2017, 8, 2283.

186. G. Hoogersy (ed.), Fuel Cell Technology Handbook, CRC Press, Boca Raton, 2002.

187. L.M.C. Pinto, P. Quaino, M.D. Arce, E. Santos, W. Schmickler, ChemPhysChem, 2014, 15, 2003.

188. G.S. Karlberg, Ohys. Rev. B, 2006, 74, 153414.

189. A. Michaelides, P. Hu, J. Am. Chem. Soc., 2001, 123, 4235.

190. A. Michaelides, P. Hu, J. Chem. Phys., 2001, 114, 513.

191. F. Calle-Vallejo, J. Tymoczko, V. Colic, Q.H. Vu, M.D. Pohl, K. Morgenstern, D. Loffreda, P. Sautet, W. Schumann, A.S. Bandarenka, Science, 2015, 350, 185.

192. I.E.L. Stephens, A.S. Bondarenko, U. Gronbjerg, J. Rossmeisl, I. Chorkendorff, Energy Environ. Sci., 2012, 5, 6744.

193. J. Greeley, I.E.L. Stephens, A.S. Bondarenko, T.P. Johnsson, H.A. Hansen, T.F. Jaramillo, J. Rossmeisl, I. Chorkendorff, J.K. Norskov, Nat. Chem., 2009, 1, 552.

194. A. Kuzume, E. Herrero, J.M. Feliu, J. Electroanal. Chem., 2007, 599, 333.

195. J.-F. Paul, P. Sautet, J. Phys. Chem., 1994, 98, 10906.

196. M.D. Macia, J.M. Campina, E. Herrero, J.M. Feliu, J. Electroanal. Chem., 2004, 564, 141.

197. A. Hitotsuyanagi, S. Kondo, M. Nakamura, N. Hoshi, J. Electroanal. Chem., 2011, 657, 512.

198. A. Hitotsuyanagi, M. Nakamura, N. Hoshi, Electrochim. Acta, 2012, 82, 512.

199. H.S. Casalongue, S. Kaya, V. Viswanathan, D.J. Miller, D. Friebel, H.A. Hansen, J.K. Norskov, A. Nilsson, H. Ogasawara, Nat. Commun., 2013, 4, 2817.

200. M.D. Pohl, S. Watzele, F. Calle-Vallejo, A.S. Bandarenka, ACS Omega, 2017, 2, 8141.

201. F. Calle-Vallejo, M.D. Pohl, A.S. Bandarenka, ACS Catal., 2017, 7, 4355.

202. V. Rosca, M.T.M. Koper, Electrochim. Acta, 2008, 53, 5199.

203. V. Rosca, M.T.M. Koper, Phys. Chem. Chem. Phys., 2006, 8, 2513.

204. F. Maillard, G.-G. Lu, A. Wieckowski, U. Stimming, J. Phys. Chem., 2005, 109, 16230.

205. R. Chattot, T. Asset, P. Bordet, J. Drnec, L. Dubau, F. Maillard, ACS Catal., 2017, 1, 398.

206. C. Wang, M. Chi, D. Li, D. Strmcnik, D. van der Vliet, G. Wang, V. Kamanicky, K. Chang, A.P. Paulikas, D. Tripkovic, J. Pearson, K.L. More, N.M. Markovic, V.R. Samenkovic, J. Am. Chem. Soc., 2011, 133, 14396.

207. P. Strasser, S. Koh, T. Anniyev, J. Greeley, K. Moore, C. Yu, Z. Liu, S. Kaya, D. Nordlund, H. Ogasawara, M.F. Toney, A. Nilsson, Nat. Chem., 2010, 2, 454.

208. H.A. Gasteiger, N.M. Markovic, Science, 2009, 324, 48.

209. P. Malacrida, H.G. Sanchez Casalongue, F. Masini, S. Kaya, P. Hernandez-Fernandez, D. Deiana, H. Ogasawara, I.E.L. Stephens, A. Nilsson, I. Chorkendorff, Phys. Chem. Chem. Phys., 2015, 17, 28121.

210. C. Wang, N.M. Markovic, V.R. Stamenkovic, ACS Catal., 2012, 2, 891.

211. C. Wang, M. Chi, D. Li, D. van der Vliet, G. Wang, Q. Lin, J.F. Mitchell, K.L. More, N.M. Markovic, V.R. Stamenkovic, ACS Catal., 2012, 1, 1355.

212. U.A. Paulus, A. Wokaun, G.G. Scherer, T.J. Schmidt, V.R. Stamenkovic, N.M. Markovic, R.N. Ross, Electrochim. Acta, 2002, 47, 3787.

213. V. Stamenkovic, T.J. Schmidt, P.N. Ross, N.M. Markovic, J. Phys. Chem. B, 2002, 106, 11970.

214. T. Asset, R. Chattot, M. Fontana, B. Mercier-Guyon, N. Job, L. Dubau, F. Maillard, ChemPhysChem, 2018, 13, 1552.

215. E. Antolini, J.R.C. Salgado, E.R. Gonzalez, J. Power Sources, 2006, 160, 957.

216. J. Wu, X.Z. Yuan, J.J. Martin, H. Wang, J. Zhang, J. Shen, S. Wu, W. Merida, J. Power Sources, 2008, 184, 104.

217. L. Dubau, T. Asset, R. Chattot, C. Bonnaud, V. Vanpeene, J. Nelayah, F. Maillard, ACS Catal., 2015, 5, 5333.

218. T. Yoshida, K. Kojima, Electrochem. Soc. Interface, 2015, 24, 45.

219. M. Escudero-Escribano, P. Malacrida, M.H. Hansen, U.G. Vej-Hansen, A. Velázquez-Palenzuela, V. Tripkovic, J. Schiøtz, J. Rossmeisl, I.E.L. Stephens, I. Chorkendorff, Science, 2016, 352, 73.

220. A. Serov, T. Asset, M. Padilla, I. Matanovic, U. Martinez, A. Roy, K. Artyushkova, M. Chatenet, F. Maillard, D. Bayer, C. Cremers, P. P. Atanassov, Appl. Catal., B, 2016, 191, 76.

221. J. Erlebacher, M.J Aziz, A. Karma, N. Dimitrov, K. Sieradzki, Nature, 2001, 410, 450.

222. F.U. Renner, A. Stierle, H. Dosch, D.M. Kold, T. Lee, J. Zegenhagen, Nature, 2006, 439, 707.

223. J. Durst, M. Chatenet, F. Maillard, Phys. Chem. Chem. Phys., 2012, 14, 13000.

224. J. Sun, S. Zhang, T. Kou, J. Xu, Z. Zhang, ACS Appl. Mater. Interfaces, 2012, 4, 6038.

225. I. Heller, S. Chatoor, J. Männik, M.A.G. Zevenbergen, C. Dekker, S.G. Lemay, J. Am. Chem. Soc., 2010, 132, 17149.

226. W. Yao, Q. Dai, P. Chen, S. Zhong, Z. Yan, RSC Adv., 2015, 5, 19145.

227. X. Liu, L. Wang, L. Wan, D. Wang, ACS Appl. Mater. Interfaces, 2015, 7, 9573.

228. M.M. Collinson, D.A. Higgins, R. Kommidi, D. Campbell-Rance, Anal. Chem., 2008, 80, 651.

229. L. Liu, J. Hu, J. Zhang, C. Cao, Anal. Chem., 2009, 81, 3199.

230. R. Matthessen, J. Fransaer, K. Binnemansc, D.E. De Vos, RSC Adv., 2013, 3, 4634.

231. R. Naegeli, J. Redepenning, F.C. Anson, J. Phys. Chem., 1986, 90, 6227.

232. T.H. Silva, V. Garcia-Morales, C. Moura, J.A. Manzanares, F. Silva, Langmuir, 2005, 21, 7461.

233. S. Santi, A. Bisello, R. Cardenaa, A. Donoli, Dalton Trans., 2015, 44, 5234.

234. M. Wang, L. Chen, L. Sun, Energy Environ. Sci., 2012, 5, 6763.

235. A.A. AlZahrani, I. Dincer, Int. J. Hydrog. Energy, 2017, 42, 21404.

236. M. Grotheer, R. Alkire, R. Varjian, Electrochem. Soc. Interface, 2006, 15, 52.

237. L.D. Burke, J.F. O'Neill, J. Electroanal. Chem., 101, 1979, 341.

238. P. Herasymenko, I. Slendyk, Z. Phys. Chem. A, 1930, 149, 230.

239. M. Tokuoka, Czech. Chem. Commun., 1932, 4, 444.

240. A.N. Frumkin, Faraday Soc., 1959, 55, 156.

241. J. Heyrovsky, Actualites Sci. et Ind., 1933, 90, 4.

242. M. Nakamura, N. Sato, N. Hoshi, O. Sakata, ChemPhysChem, 2011, 12, 1430.

243. M. Escudero-Escribano, M.E. Zoloff Michoff, E.P.M. Leiva, N.M. Markovic, C. Gutierrez, A. Cuesta, ChemPhysChem, 2011, 12, 2230.

244. D. Strmcnik, K. Kodama, D. van der Vliet, J. Greeley, V.R. Stamenkovic, N.M. Markovic, Nat. Chem., 2009, 1, 466.

245. G.A. Ragoisha, T.A. Auchynnikava, E.A. Streltsov, S.M. Rabchynski, Electrochim. Acta, 2014, 122, 218.

246. C. Stoffelsma, P. Rodriguez, G. Garcia, N. Garcia-Araez, D. Strmcnik, N.M. Markovic, M.T.M. Koper, J. Am. Chem. Soc., 2010, 132, 16127.

247. J. Tymoczko, V. Colic, A. Ganassin, W. Schumann, A.S. Bandarenka, Cat. Today, 2014, 244, 96.

248. I. Katsounaros, K.J.J. Mayrhofer, Chem. Commun., 2012, 48, 6660.

249. J. Suntivich, E.E. Perry, H.A. Gasteiger, Y. Shao-Horn, Electrocatalysis, 2013, 4, 49.

250. S. Xue, B. Garlyyev, S. Watzele, Y. Liang, J. Fichtner, M.D. Pohl, A.S. Bandarenka, ChemElectroChem, 2018, 5, 2326.

251. J. Greeley, T.F. Jaramillo, J. Bonde, I.B. Chorkendorff, J.K. Norskov, Nat. Mater., 2006, 5, 909.

252. J.K. Norskov, T. Bligaard, A. Logadottir, J.R. Kitchin, J.G. Chen, S. Pandelov, U. Stimming, J. Electrochem. Soc., 2005, 152, J23.

253. M. Wasisaka, H. Suzuki, S. Mitsui, H. Uchida, M. Watanabe, Langmuir, 2009, 25, 1897.

254. M.A. Omole, V.A. Okello, V. Lee, L. Zhou, O.A. Sadik, ACS Catal., 2011, 1, 139.

255. D. Pillay, M.D. Johannes, Y. Garsany, K.E. Swider-Lyions, J. Phys. Chem. C, 2010, 114, 7822.

256. J.D. Froehlich, C.P. Kubiak, J. Am. Chem. Soc., 2015, 137, 3565.

257. R.E. Rettew, N.K. Allam, F.M. Alamgir, ACS Appl. Mater. Interfaces, 2011, 3, 147.

258. O. Diaz-Morales, T.J.P. Hersbach, D.G.H. Hetterscheid, J.N.H. Reek, M.T.M. Koper, J. Am. Chem. Soc., 2014, 136, 10432.

259. J. Rodriguez-Lopez, A.J. Bard, J. Am. Chem. Soc., 2010, 132, 5121.

260. H.N. Sharma, V. Sharma, A.B. Mhadeshwar, R. Ramprasad, J. Phys. Chem. Lett., 2015, 6, 1140.

261. J. Tymoczko, W. Schuhmann, A.S. Bandarenka, ChemElectroChem, 2014, 1, 213.

262. J. Tymoczko, F. Calle-Vallejo, V. Colic, M.T.M. Koper, W. Schuhmann, A.S. Bandarenka, ACS Catal., 2014, 4, 3772.

263. V. Colic, J. Tymoczko, A. Maljusch, A. Ganassin, W. Schuhmann, A.S. Bandarenka, ChemElectroChem, 2015 2, 143.

264. A. Ganassin, V. Colic, J. Tymoczko, A.S. Bandarenka, W. Schuhmann, Phys. Chem. Chem. Phys., 2015, 17, 8349.

265. T. Takashima, K. Hashimoto, R. Nakamura, J. Am. Chem. Soc., 2012, 134, 1519.

266. F. Prieto, I. Navarro, M. Rueda, J. Phys. Chem., 1996, 100, 16346.

267. Y. Zhong, K. Ueno, Y. Mori, T. Oshikiri, H. Misawa, J. Phys. Chem. C, 2015, 119, 8889.

268. M.R. Tarasevich, O.V. Korchagin, Russ. J. Electrochem., 2013, 49, 600.

269. B.J. Murphy, F. Sargent, F.A. Armstrong, Energy Environ. Sci., 2014, 7, 1426.

270. C. Wildi, G. Cabello, M.E. Zoloff Michoff, P. Vélez, E.P.M. Leiva, J.J. Calvente, R. Andreu, A. Cuesta, J. Phys. Chem. C, 2016, 120, 15586.

271. M. Auinger, I. Katsounaros, J.C. Meier, S.O. Klemm, P.U. Biedemann, A.A. Topalov, M. Rohwerder, K.J.J. Mayrhofer, Phys. Chem. Chem. Phys., 2011, 13, 16384.

272. M.F. Li, L.W. Liao, D.F. Yuan, D. Mei, Y. Chen, Electrochim. Acta, 2013, 110, 780.

273. V. Briega-Martos, E. Herrero, J.M. Feliu, Electrochim. Acta, 2017, 241, 497.

274. R. Rizo, E. Herrero, J.M. Feliu, Phys. Chem. Chem. Phys., 2013, 15, 15416.

275. J. Rossmeisl, K. Chan, R. Ahmed, V. Tripkovic, M.E. Bjorketun, Phys. Chem. Chem. Phys., 2013, 15, 10321.

276. K.B. Oldham, J. Electroanal. Chem., 2008, 613, 131.

277. B. Garlyyev, S. Xue, S. Watzele, D. Scieszka, A.S. Bandarenka, J. Phys. Chem. Lett., 2018, 9, 1927.

278. Y. Yu, G. Jin, J. Colloid Interface Sci., 2005, 283, 477.

279. J. Clavilier, R. Albalat, R. Gomez, J.M. Orts, J.M. Feliu, J. Electroanal. Chem., 1992, 330, 489.

280. M.J. Weaver, Langmuir, 1998, 14, 3932.

281. V. Climent, G.A. Attard, J.M. Feliu, J. Electroanal. Chem., 2002, 532, 67.

282. J. Clavilier, R. Albalat, R. Gomez, J.M. Orts, J.M. Feliu, J. Electroanal. Chem., 1993, 14, 3932.

283. R. Gomez, V. Climent, J.M. Feliu, M.J. Weaver, J. Phys. Chem. B, 2000, 104, 597.

284. C. Korzeniowski, B.E. Conway (eds.), The Electrochemical Society Proceedings, Pennington, NJ, 1997.

285. H. Ebert, R. Parsons, G. Ritzoulis, T. Vandernoot, J. Electroanal. Chem., 1989, 264, 181.

286. G.A. Attard, A. Ahmadi, J. Electroanal. Chem., 1995, 389, 175.

287. N.R. Avery, Surf. Sci., 1983, 131, 501.

288. R.J. Bowling, R.T. Packard, R.L. McCreery, J. Am. Chem. Soc., 1989, 111, 1217.

289. E. Hershenhart, R.L. McCreery, R.D. Knight, Anal. Chem., 1984, 56, 2256.

290. R.J. Rice, N.M. Pontikos, R.L. McCreery, J. Am. Chem. Soc., 1990, 112, 4617.

291. R.K. Jaworski, R.L. McCreery, J. Electrochem. Soc., 1993, 140, 1360.

292. W. Huang, R.L. McCreery, J. Electroanal. Chem. 1992, 326, 1.

293. T. Hinoue, N. Kuwamoto, I.J. Watanabe, Electroanal. Chem., 1999, 466, 31.

294. J.L. Brennan, R.J. Forster, J. Phys. Chem. B, 2003, 107, 9344.

295. V. Climent, B.A. Coles, R.G. Compton, J. Phys. Chem. B, 2002, 106, 5258.

296. V.A. Benderskii, S.D. Babenko, A.G. Krivenko, J. Electroanal. Chem. Interfacial Electrochem., 1978, 86, 223.

297. V.A. Benderskii, G.I. Velichko, J. Electroanal. Chem. Interfacial Electrochem., 1982, 140, 1.

298. V.A. Benderskii, G.I. Velichko, I.V. Kreitus, J. Electroanal. Chem. Interfacial Electrochem., 1984, 181, 1.

299. J.F. Smalley, L. Geng, S.W. Feldberg, L.C. Rogers, J. Leddy, J. Electroanal. Chem., 1993, 356, 181.

300. J.F. Smalley, C.V. Krishnan, M. Goldman, S.W. Feldberg, I. Ruzic, J. Electroanal. Chem., 1988, 248, 255.

301. V. Climent, B.A. Coles, R.G. Compton, J. Phys. Chem. B, 2001, 105, 10669.

302. V. Climent, B.A. Coles, R.G. Compton, J. Phys. Chem. B, 2002, 106, 5988.

303. E. Sibert, R. Faure, R. Durand, J. Electroanal. Chem., 2001, 515, 71.

304. A.F. Silva (ed.), ACS Symposium Series, D. Reidel Publishing Company, 1986.

305. J.A. Harrison, J.E.B. Randles, D.J.J. Schiffrin, Electroanal. Chem., 1973, 48, 359.

306. P. Sebastián, R. Martínez-Hincapié, V. Climent, J.M. Feliu, Electrochim. Acta, 2017, 228, 667.

307. R. Guidelli, G. Aloisi, E. Leiva, W. Schmickler, J. Phys. Chem. B, 1988, 92, 6671.

308. M. Kaack, D. Fick, Surf. Sci., 1995, 342, 111.

309. M. Osawa, M. Tsushima, H. Mogami, G. Samjeske, A. Yamakata, J. Phys. Chem. C, 2008, 112, 4248.

310. M.F. Toney, J.N. Howard, J. Richer, G.L. Borges, J.G. Gordon, O.R. Melroy, D.G. Wiesler, D. Yee, L.B. Sorensen, Nature, 1994, 368, 444.

311. J.O'.M. Bockris, A.K.N. Reddy, M. Gamboa-Aldeco, Modern Electrochemistry; 2nd Edition, Kluwer Academic/Plenum Publishers, New York, 2000.

312. A. Yamakata, M. Osawa, J. Phys. Chem. C, 2008, 112, 11427.

313. J.F. Smalley, J. Electroanal. Chem., 2010, 640, 68.

314. Cyclic Voltammetry. http://www.rsc.org/publishing/journals/prospect/ontology.asp?id=CMO:0000025&MSID=B802363H, (accessed online February 2019).

315. G.A. Mabbott, J. Chem. Educ., 1983, 60, 697.

316. P.T. Kissinger, W.R. Heineman, J. Chem. Educ., 1983, 60, 702.

317. J.J. Van Benschoten, J.Y. Lewis, W.R. Heineman, D.A. Roston, P.T. Kissinger, J. Chem. Educ., 1983, 60, 772.

318. E. Barsoukov, J.R. Macdonald (eds), Impedance Spectroscopy. Theory, Experiment, and Applications: Fundamentals of Impedance Spectroscopy, Wiley & Sons, New Jersey, 2005.

319. W. Nernst, Z. Elektrochem., 1894, 14, 622.

320. E. Warburg, Ann. Phys. Chem., 1899, 67, 493.

321. A. Lasia, Electrochemical Impedance Spectroscopy and its Applications, Springer Science+Business Media, New York, 2014.

322. A. Sacco, Renew. Sust. Energ. Rev. 2017, 79, 814 and references therein.

323. Basics of Electrochemical Impedance Spectroscopy. https://www.gamry.com/application-notes/EIS/basics-of-electrochemical-impedance-spectroscopy/, (accessed online February 2019).

324. F. Scholz (ed.), Electroanalytical Methods: Electrochemical Impedance Spectroscopy, Springer-Verlag, Berlin, Heidelberg, 2010.

325. G.B. Kauffman, Angew. Chem. Int. Ed., 2009, 48, 1532.

326. K.A. Marx, Biomacromolecules, 2003, 4, 1099.

327. D.A. Buttry, Electroanalytical Chemistry, 1989.

328. M. Rodahl, B. Kasemo, Sens. Actuators A, 1996, 54, 448.

329. E. Shouji, D.A. Buttry, Electrochim. Acta, 2000, 45, 3757.

330. M.R. Deakin, D.A. Buttry, Anal. Chem., 1989, 61, 1147.

331. P. Eaton, P. West, Atomic Force Microscopy, Oxford University Press Inc., NY, 2010.

332. F.J. Giessibl, Rev. Mod. Phys., 2003, 75, 949.

333. Q. Zhong, D. Inniss, K. Kjoller, V.B. Elings, Surf. Sci. Lett., 1993, 290, 688.

334. D. Rugar, P. Hansma, Phys. Today, 1990, 43, 23.

335. E. Jensen, Anat. Rec., 2013, 296, 179.

336. M. Tello, R. Garcia, Appl. Phys. Lett., 2001, 79, 424.

337. N. Jalili, K. Laxminarayana, Mechatronics, 2004, 14, 907.

338. K. Tokuda, T. Gueshi, K. Aoki, H. Matsuda, 1985, 132, 2390.

339. J. Tymoczko, W. Schumann, A.S. Bandarenka, Phys. Chem. Chem. Phys., 2013, 15, 12998.

340. W. Xing, G. Yin, J. Zhang, Rotating Electrode Methods and Oxygen Reduction Electrocatalysts, Elsevier, 2014.

341. H. Kim, C.M. Gilmore, A. Pique, J.S. Horwitz, H. Mattoussi, H. Murata, Z.H. Kafafi, D.B. Chrisey, J. Appl. Phys., 1999, 86, 6451.

342. H.Y. Yu, X.D. Feng, D. Grozea, Z.H. Lu, R.N.S. Sodhi, A-M. Hor, H. Aziz, Appl. Phys. Lett., 2001, 78, 2595.

343. H. Kim, A. Pique, J.S. Horwitz, H. Murata, Z.H. Kafafi, D.B. Chrisey, Appl. Phys. Lett., 1999, 74, 3444.

344. J.C.C. Fan, F.J. Bachner, J. Electrochem. Soc., 1975, 122, 1719.

345. A.S. Bondarenko, Anal. Chim. Acta, 2012, 743, 41.

346. B.B. Berkes, G. Inzelt, W. Schuhmann, A.S. Bondarenko, J. Phys. Chem. C, 2012, 116, 10995.

347. I. Horcas, R. Fernandez, J.M. Gomez-Rodriguez, J. Colchero, J. Gomez-Herrero, A.M. Baro, Rev. Sci. Inst., 2007, 78, 013705.

348. A.P. Mouritz, Introduction to Aerospace Materials, Woodhead Publishing Limited, PA, 2012.

349. R.J. Foster, Chem. Soc. Rev., 1994, 4, 289.

350. D.W. Smith, J. Chem. Educ., 1977, 54, 540.

351. E. Gileadi, S.D. Argade, J.O'M. Bockris, J. Phys. Chem., 1966, 70, 2044.

352. J. Huang, A. Malek, J. Zhang, M. Eikerling, J. Phys. Chem. C, 2016, 120, 13587.

353. F. Cheng, Y. Su, J. Liang, Z. Tao, J. Chen, Chem. Mater., 2010, 22, 898.

354. A. Ramirez, P. Hillebrand, D. Stellmach, M.M. May, P. Bogdanoff, S. Fiechter, J. Phys. Chem. C, 2014, 118, 14073.

355. J.E. Post, Proc. Natl. Acad. Sci. USA, 1999, 96, 3447.

356. Y. Gorlin, T.F. Jaramillo, J. Am. Chem. Soc., 2010, 132, 13612.

357. J.D.E. McIntyre, W.F. Peck, Jr., J. Electrochem. Soc., 1970, 6, 747.

358. R. Bezman, Anal. Chem., 1972, 44, 1781.

359. A.S. Bondarenko, I.E.L. Stephens, H.A. Hansen, J.J. Perez-Alonso, V. Tripkovic, T.P. Johansson, J. Rossmeisl, J.K. Norskov, I. Chorkendorff, Langmuir, 2011, 27, 2058.

360. B.N. Grgur, P. Zivkovic, M.M. Gvozdenovic, Prog. Org. Coat., 2006, 56, 240.

361. S. Yu, Y. Li, Y. Lu, B. Xu, Q. Wang, M. Yan, Y. Jiang, J. Power Sources, 2015, 275, 45.

362. M. Takachi, T. Matsuda, Y. Moritomo, Appl. Phys. Express, 2013, 6, 025802.

363. M. Matsuda, M. Takachi, Y. Moritomo, Chem. Commun., 2013, 49, 2750.

364. H. Lee, Y.I. Kim, J.K. Park, J.W. Choi, Chem. Commun., 2012, 48, 8416.

365. M. Okubo, C.H. Li, D.R. Talham, Chem. Commun., 2014, 50, 1353.

366. C. Lin, E. Laborda, C. Batchelor-McAuley, R.G. Compton, Phys. Chem. Chem. Phys., 2016, 18, 9829.

367. C. Chen, K. Matsumoto, T. Nohira, R. Hagiwara, Y. Orikasa, Y. Uchimoto, J. Power Sources, 2014, 246, 783.

368. P.J. Kulesza, M.A. Malik, K. Miecznikowski, A. Wolkiewicz, S. Zamponi, M. Berrettoni, R. Marassi, J. Electrochem. Soc., 1996, 143, L10.

369. F. Zhao, Y. Wang, X. Xu, Y. Liu, R. Song, G. Lu, Y. Li, ACS Appl. Mater. Interfaces, 2014, 6, 11007.

370. X. Wu, C. Wu, C. Wei, L. Hu, J. Qian, Y. Cao, X. Ai, J. Wang, H. Yang, ACS Appl. Mater. Interfaces, 2016, 8, 5393.

371. W. Li, F. Zhang, X. Xiang, X. Zhang, J. Phys. Chem., 2017, 121, 27805.

372. D. Andre, M. Meiler, K. Steiner, C, Wimmer, T. Soczka-Guth, D.U. Sauer, J. Power Sources, 2011, 196, 5334.

373. S. Pratihar, A. Chandra, J. Chem. Phys., 2011, 134, 024519.

374. P. Sebastian, A.P. Sandoval, V. Climent, J.M. Feliu, Electrochem. Commun., 2015, 55, 39.

375. Capacitance Value from CPE, $R_{Parallel}$: A Calculator.
http://www.consultrsr.net/resources/eis/cpecalc.htm, (accessed online February 2019).